

AD-A265 056

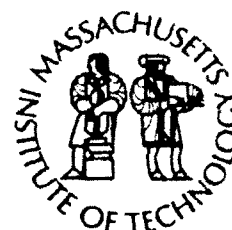


WHOI-92-38

Woods Hole Oceanographic Institution Massachusetts Institute of Technology



Joint Program
in Oceanography/
Applied Ocean Science
and Engineering



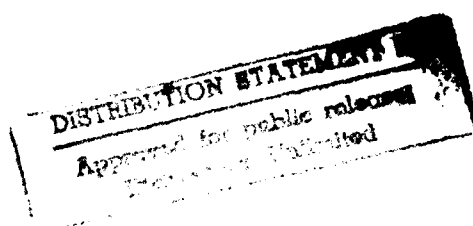
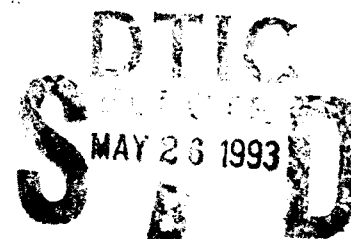
DOCTORAL DISSERTATION

Vortex-Induced Forces on Oscillating Bluff Cylinders

by

Ramnarayan Gopalkrishnan

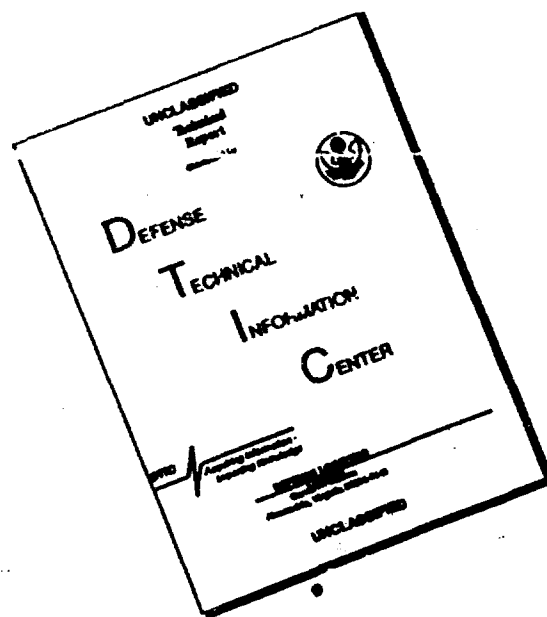
February 1993



93-11658



DISCLAIMER NOTICE



THIS DOCUMENT IS BEST
QUALITY AVAILABLE. THE COPY
FURNISHED TO DTIC CONTAINED
A SIGNIFICANT NUMBER OF
PAGES WHICH DO NOT
REPRODUCE LEGIBLY.

WHOI-92-38

Vortex-Induced Forces on Oscillating
Bluff Cylinders

by

Ramnarayan Gopalkrishnan

Woods Hole Oceanographic Institution
Woods Hole, Massachusetts 02543

and

The Massachusetts Institute of Technology
Cambridge, Massachusetts 02139

February 1993

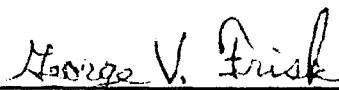
DOCTORAL DISSERTATION

Funding was provided by the National Science Foundation, the Office of Naval Technology,
the Sea Grant Program and the Office of Naval Research.

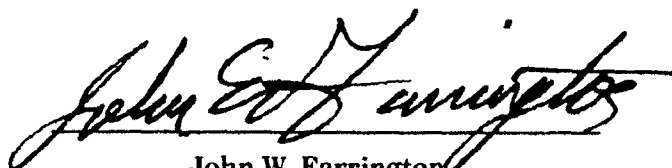
Reproduction in whole or in part is permitted for any purpose of the United States
Government. This thesis should be cited as: Ramnarayan Gopalkrishnan, 1992.
Vortex-Induced Forces on Oscillating Bluff Cylinders. Ph.D. Thesis. MIT/WHOI,
WHOI-92-38.

Approved for publication; distribution unlimited.

Approved for Distribution:



George V. Frisk, Chairman
Department of Applied Ocean Physics and Engineering



John W. Farrington
Dean of Graduate Studies

Vortex-Induced Forces on Oscillating Bluff Cylinders

by

Ramnarayan Gopalkrishnan

Bachelor of Technology, Indian Institute of Technology Madras

Submitted to the

Department of Ocean Engineering, MIT

and the

Department of Applied Ocean Physics and Engineering, WHOI

in partial fulfillment of the requirements for the degree of

Doctor of Science in Oceanographic Engineering

at the

MASSACHUSETTS INSTITUTE OF TECHNOLOGY

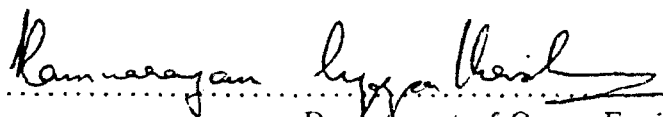
and the

WOODS HOLE OCEANOGRAPHIC INSTITUTION

February 1993

© Massachusetts Institute of Technology 1993. All rights reserved.

Author

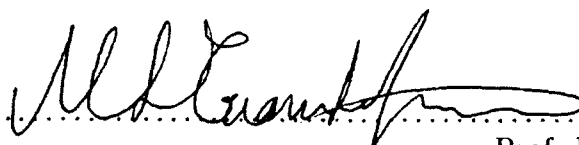


Department of Ocean Engineering, MIT

Department of Applied Ocean Physics and Engineering, WHOI

September 11, 1992

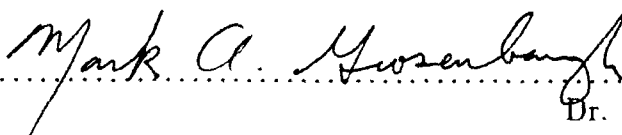
Certified by



Prof. Michael S. Triantafyllou

Thesis Supervisor

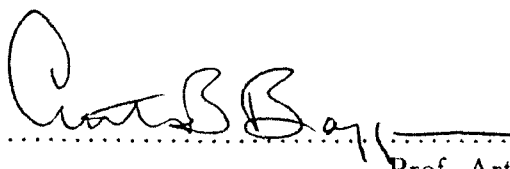
Certified by



Dr. Mark A. Grosenbaugh

Thesis Supervisor

Accepted by



Prof. Arthur B. Baggeroer

Chairman, Joint Committee on Oceanographic Engineering



Vortex-Induced Forces on Oscillating Bluff Cylinders

by

Ramnarayan Gopalkrishnan

Submitted to the

Department of Ocean Engineering, MIT

and the

Department of Applied Ocean Physics and Engineering, WHOI

on September 11, 1992, in partial fulfillment of the requirements for the degree of

Doctor of Science in Oceanographic Engineering

Abstract

Vortex-induced forces and consequent vibration of long cylindrical structures are important for a large number of engineering applications, while the complexity of the underlying physical mechanisms is such that this is one of the canonical problems of fluid mechanics. In the case of a marine tubular exposed to a shear flow, the situation is particularly difficult since the vortex shedding force varies in frequency and magnitude along the length of the structure, causing the response at any point to be amplitude-modulated in space and time.

In this thesis, the focus is on the measurement, via forced-oscillation experiments, of the vortex-induced lift and drag forces acting on circular cylinders undergoing sinusoidal and amplitude-modulated oscillations. Basic concepts on vortex formation and vortex-induced vibrations, a review of the existing literature, and details of the experimental apparatus and data processing methods are all introduced early in the thesis. A comprehensive program of stationary and sinusoidal oscillation tests is presented. Several novel properties are described, among them the role of the lift force phase angle in causing the amplitude-limited nature of VIV, and use of the lift force "excitation region" in contrast with the often-quoted but quite different lift force "lock-in region". Next, a comprehensive data error analysis, and a simple VIV prediction scheme are described. New data on amplitude-modulated oscillations are presented, with an analysis of the behavior of the fluid forces in response to beating excitation. Finally, the concept of control of the mean wake velocity profile via the control of the major vortical features is explored, with the possible applications being the reduction of the in-line wake velocity and the alteration of the wake signature. The thesis concludes with the principal findings of this research as well as suggestions for future work.

Thesis Supervisor: Prof. Michael S. Triantafyllou

Thesis Supervisor: Dr. Mark A. Grosenbaugh

RECEIVED 5

| | |
|--------------------|--|
| Accession For | |
| NTIS CEA&I | <input checked="checked" type="checkbox"/> |
| DTIC TAB | <input type="checkbox"/> |
| Unannounced | <input type="checkbox"/> |
| Justification | |
| By | |
| Distribution/ | |
| Availability Codes | |
| Dist | Avail and/or Special |
| A-1 | |

1
2
3
4
5
6
7
8
9
10
11
12
13
14
15
16
17
18
19
20
21
22
23
24
25
26
27
28
29
30
31
32
33
34
35
36
37
38
39
40
41
42
43
44
45
46
47
48
49
50
51
52
53
54
55
56
57
58
59
60
61
62
63
64
65
66
67
68
69
70
71
72
73
74
75
76
77
78
79
80
81
82
83
84
85
86
87
88
89
90
91
92
93
94
95
96
97
98
99
100

Dedicated to the FAH.

Acknowledgments

Having just completed my doctoral thesis. I feel like I have accomplished one of the major tasks of my life. I turn to contemplate the five years that it took to achieve this enterprise, and I realize that without all of those encouraging words, helping hands, and material assistance, I would never have made it up this hill.

For technical vision, guidance, and support, I am deeply indebted to the members of my committee, Prof. Michael Triantafyllou, Dr. Mark Grosenbaugh, and Prof. Kim Vandiver. This thesis was inspired by their ideas. Both professionally and personally, I feel grateful to have had such good supervisors.

For engineering assistance, I would like to thank Mr. Clifford Goudey of MIT Sea Grant, Mr. William Upthegrove of the MIT Testing Tank, and Mr David Barrett, a fellow student. Cliff's and Dave's mechanical wizardry and Bill's fabrication skills went a long way towards ensuring the success of my experiments. (To Bill, I owe a special debt of gratitude for all that coffee that fueled our many long days in the laboratory!)

For moral support, I am grateful to my family and friends. To my parents, because without their help I would not have been here in the first place. To my wife, whom I met and married during the course of my graduate work, and who has been an endless source of strength. And to my friends at MIT and Woods Hole, ("you know who you are") who made graduate school not only bearable, but fun.

And finally, for financial support of the research in this thesis, I would like to gratefully acknowledge:

- The National Science Foundation, under grant number OCE-8511431.
- The Office of Naval Technology, under grant number N00014-89-C-0179
- The Sea Grant Program, under grant number NA90AA-D-SG424.
- The Defense Advanced Research Projects Agency, through the Office of Naval Research, under grant number N00014-92-J-1726.

Ram Gopajkrishnan
September 1992.

Contents

| | | |
|----------|--|-----------|
| 1 | Intr oduction | 21 |
| 1.1 | The phenomenon of vortex shedding | 21 |
| 1.2 | Vortex shedding and marine cables: the problem at hand | 24 |
| 1.3 | Chronology of this work | 28 |
| 1.4 | A review of the literature | 28 |
| 1.4.1 | Forced-oscillation force-measurement experiments | 28 |
| 1.4.2 | Other references | 37 |
| 1.5 | A preview of the chapters that follow | 39 |
| 2 | Experimental and Data Processing Methods | 41 |
| 2.1 | Preliminary remarks | 41 |
| 2.2 | The experimental system | 41 |
| 2.2.1 | General description | 41 |
| 2.2.2 | Testing tank and carriage | 43 |
| 2.2.3 | Test models, yoke, and oscillating system | 44 |
| 2.2.4 | Force and motion sensors | 47 |
| 2.2.5 | Signal conditioning and data acquisition | 49 |
| 2.2.6 | Miscellaneous system effects | 50 |
| 2.2.7 | Flow considerations | 51 |
| 2.2.8 | Overall accuracy of the experimental apparatus | 52 |
| 2.3 | Formulation and definitions | 53 |
| 2.3.1 | Stationary cylinder | 53 |
| 2.3.2 | Sinusoidal cylinder oscillations | 54 |
| 2.3.3 | Beating cylinder oscillations | 56 |

| | | |
|----------|---|------------|
| 2.4 | Data processing | 58 |
| 3 | Stationary and Sinusoidal Oscillation Tests | 63 |
| 3.1 | The purpose of these tests | 63 |
| 3.2 | Stationary results | 64 |
| 3.3 | Forced sinusoidal oscillations | 67 |
| 3.3.1 | Results for amplitude ratio 0.30 | 69 |
| 3.3.2 | Results for other amplitude ratios | 74 |
| 3.4 | The behavior of the lift force phase angle | 82 |
| 3.5 | The behavior of the oscillating drag force | 89 |
| 3.5.1 | Large amplification at high oscillation frequencies | 89 |
| 3.5.2 | Higher harmonics of the oscillating drag | 93 |
| 3.6 | Lock-in behavior and excitation | 96 |
| 3.7 | Time-domain analysis of the wake response | 100 |
| 4 | Error Analysis and Application to VIV Predictions | 109 |
| 4.1 | Preliminary remarks | 109 |
| 4.2 | Error analysis | 109 |
| 4.2.1 | Introduction | 109 |
| 4.2.2 | Wet calibrations and long-term stability | 111 |
| 4.2.3 | Statistical properties of the sinusoidal data | 111 |
| 4.2.4 | Comparisons with published results | 114 |
| 4.2.5 | The "bottom line" | 120 |
| 4.3 | Applying our data to VIV predictions | 123 |
| 4.3.1 | General principles | 123 |
| 4.3.2 | A simple method of estimating response | 124 |
| 4.3.3 | Long tubulars in shear flow | 130 |
| 4.4 | Cross-sectional effects | 133 |
| 4.4.1 | Preliminary remarks | 133 |
| 4.4.2 | Defining an "effective diameter" | 134 |
| 4.4.3 | Multiple cylinder interference effects | 137 |
| 4.4.4 | Evaluating a vortex-suppression device | 144 |

| | | |
|----------|--|------------|
| 5 | Beating Oscillation Tests | 149 |
| 5.1 | Introduction | 149 |
| 5.1.1 | Background | 149 |
| 5.1.2 | A summary of related research | 152 |
| 5.2 | Force coefficient measurements | 157 |
| 5.2.1 | Mean drag coefficient | 157 |
| 5.2.2 | Oscillating drag coefficients | 162 |
| 5.2.3 | Oscillating lift coefficients | 172 |
| 5.3 | Analysis of the wake response | 181 |
| 5.3.1 | Preliminary remarks | 181 |
| 5.3.2 | Classification of wake response modes | 181 |
| 5.3.3 | Comparisons with published results. | 189 |
| 5.4 | Discussion and Summary | 191 |
| 6 | A Paradigm of Vorticity Control: Cylinder-Foil Vortex Interaction | 195 |
| 6.1 | Introduction | 195 |
| 6.1.1 | Preliminary remarks | 195 |
| 6.1.2 | Background and motivation | 196 |
| 6.1.3 | The parameters of the problem | 199 |
| 6.2 | Flow visualization experiments | 202 |
| 6.2.1 | The Kalliroscope tank | 202 |
| 6.2.2 | Initial experiments | 204 |
| 6.2.3 | Successful experiments | 205 |
| 6.2.4 | Conclusions from the flow visualization experiments | 215 |
| 6.3 | Force measurement experiments | 220 |
| 6.3.1 | The apparatus and methods | 220 |
| 6.3.2 | Experimental results | 222 |
| 6.3.3 | Conclusions from the force measurement experiments | 224 |
| 7 | Conclusions | 227 |
| 7.1 | The essential conclusions of this thesis | 227 |
| 7.2 | Principal contributions of each chapter | 228 |

| | | |
|---------------------|--|------------|
| 7.2.1 | Stationary and sinusoidal oscillation tests | 228 |
| 7.2.2 | Error analysis and application to VIV predictions | 229 |
| 7.2.3 | Beating oscillation tests | 230 |
| 7.2.4 | Cylinder-foil vortex interaction | 231 |
| 7.3 | Recommendations for future work | 231 |
| 7.3.1 | Achieving higher Reynolds numbers. | 232 |
| 7.3.2 | Combined in-line and transverse oscillations. | 233 |
| 7.3.3 | Combined flow visualization and force measurements. | 233 |
| 7.3.4 | Tests with multiple cylinders | 234 |
| 7.3.5 | Comparative evaluation of vortex-suppression devices | 235 |
| 7.3.6 | Further research on vortex interaction | 235 |
| Bibliography | | 237 |

List of Figures

| | | |
|-----|---|----|
| 1-1 | Laminar vortex street behind a circular cylinder at $Re = 140$. Photograph by S. Taneda, from Van Dyke (1982). | 22 |
| 1-2 | The dependence of Strouhal number on Reynolds number for a circular cylinder, from Blevins (1990) | 23 |
| 1-3 | Mean in-line drag coefficient versus nondimensional frequency; from Sarpkaya (1977) | 33 |
| 1-4 | Lift coefficient magnitude \hat{C}_{LO} and phase ϕ as functions of nondimensional oscillation frequency S_O and amplitude ratio $\hat{\xi}$; from Staubli (1983) | 35 |
| 1-5 | Map of vortex synchronization patterns near the fundamental lock-in region; from Williamson and Roshko (1988) | 38 |
| 2-1 | The experimental apparatus used in the Testing Tank. | 42 |
| 2-2 | A typical experimental run (drag force trace). | 43 |
| 2-3 | Design torque versus speed factors and the manufacturer's curve for the SEIBERCO H3430 Sensorimotor. | 46 |
| 2-4 | The force sensor assembly and model attachment. | 47 |
| 2-5 | A typical static force calibration curve. | 49 |
| 3-1 | Power spectrum of a typical stationary lift force trace. | 64 |
| 3-2 | Histogram of the mean drag coefficient; stationary runs. | 66 |
| 3-3 | Histogram of the oscillating lift coefficient; stationary runs. | 66 |
| 3-4 | A time segment of a typical stationary drag force trace. | 68 |
| 3-5 | The time segment of the stationary lift force trace corresponding to the previous figure. | 68 |
| 3-6 | Mean and oscillating drag coefficients; sinusoidal oscillations; $Y_0/d = 0.30$ | 69 |

| | | |
|------|---|-----|
| 3-7 | Lift coefficient magnitude; sinusoidal oscillations; $Y_0/d = 0.30$ | 71 |
| 3-8 | Phase angle of lift wrt motion; sinusoidal oscillations; $Y_0/d = 0.30$ | 71 |
| 3-9 | Lift coefficient in phase with velocity; sinusoidal oscillations; $Y_0/d = 0.30$ | 73 |
| 3-10 | Lift coefficient in phase with acceleration; sinusoidal oscillations; $Y_0/d = 0.30$ | 75 |
| 3-11 | Added mass coefficient; sinusoidal oscillations; $Y_0/d = 0.30$ | 75 |
| 3-12 | Contours of the mean drag coefficient; sinusoidal oscillations. | 76 |
| 3-13 | Contours of the oscillating drag coefficient; sinusoidal oscillations. | 77 |
| 3-14 | Contours of the lift coefficient in phase with velocity; sinusoidal oscillations. | 78 |
| 3-15 | Contours of the lift coefficient in phase with acceleration; sinusoidal oscillations. | 79 |
| 3-16 | Contours of the added mass coefficient; sinusoidal oscillations. | 80 |
| 3-17 | Vector diagram of the cylinder oscillation, velocity and acceleration; and vortex-induced lift force. | 83 |
| 3-18 | Variation of phase angle with nondimensional frequency for "small" ampli- tude ratios 0.15, 0.30 and 0.50. | 84 |
| 3-19 | Variation of phase angle with nondimensional frequency for "large" amplitude ratios 0.75, 1.00 and 1.20. | 85 |
| 3-20 | Vector diagram showing "small" and "large" amplitude phase transition be- havior. | 86 |
| 3-21 | Variation of ϕ_0 for $Y_0/d = 0.50$ by both frequency-domain and time-domain methods. | 88 |
| 3-22 | Variation of ϕ_0 for $Y_0/d = 0.75$ by both frequency-domain and time-domain methods. | 88 |
| 3-23 | Mean and oscillating drag coefficients for amplitude ratio 0.75. | 90 |
| 3-24 | Time segment of the drag force; $Y_0/d = 0.75$; $\hat{f}_0 = 0.132$ | 91 |
| 3-25 | Time segment of the drag force; $Y_0/d = 0.75$; $\hat{f}_0 = 0.285$ | 91 |
| 3-26 | Time segments of the motion (LVDT) and the drag force; $Y_0/d = 0.75$; $\hat{f}_0 = 0.157$ | 93 |
| 3-27 | Higher harmonic oscillating drag coefficients; $Y_0/d = 0.75$ | 95 |
| 3-28 | Higher harmonic oscillating drag coefficients; $Y_0/d = 1.20$ | 95 |
| 3-29 | Motion and lift spectra for $Y_0/d = 0.50$ and four oscillation frequencies. | 98 |
| 3-30 | Experimentally determined lock-in region for sinusoidal oscillations. | 99 |
| 3-31 | Excitation and lock-in regions for sinusoidal oscillations. | 100 |

| | | |
|------|---|-----|
| 3-32 | Time-domain processing applied to $Y_0/d = 0.50$, $\hat{f}_0 = 0.107$ | 102 |
| 3-33 | Time-domain processing applied to $Y_0/d = 0.50$, $\hat{f}_0 = 0.152$ | 103 |
| 3-34 | Time-domain processing applied to $Y_0/d = 0.50$, $\hat{f}_0 = 0.203$ | 104 |
| 3-35 | Wake response state diagrams from time-domain processing. | 106 |
| 3-36 | Motion and lift for increasing linear amplitude, $\hat{f}_0 = 0.132$ | 107 |
| 4-1 | Realizations of the mean drag coefficient; stationary runs. | 112 |
| 4-2 | Realizations of the oscillating lift coefficient; stationary runs. | 113 |
| 4-3 | Lift coefficient magnitude for $Y_0/d = 0.15$, with error bars. | 114 |
| 4-4 | Lift coefficient phase angle for $Y_0/d = 0.50$, with error bars. | 115 |
| 4-5 | Histogram of C_{D_m} ; sinusoidal oscillations at $Y_0/d = 0.75$ and $\hat{f}_0 = 0.203$. . | 116 |
| 4-6 | Histogram of C_{L_0} ; sinusoidal oscillations at $Y_0/d = 0.75$ and $\hat{f}_0 = 0.203$. . | 116 |
| 4-7 | Drag amplification ratio as a function of amplitude ratio, various data sources. | 117 |
| 4-8 | Comparing our $-C_{L_{A_0}}$ results with those from Staubli (1983) | 118 |
| 4-9 | Comparing our $C_{L_{V_0}}$ results with those from Staubli (1983) | 119 |
| 4-10 | Comparing our $-C_{L_{A_0}}$ results with those from Sarpkaya (1977) | 121 |
| 4-11 | Comparing our $-C_{L_{V_0}}$ results with those from Sarpkaya (1977) | 122 |
| 4-12 | Simple structural model of a rigid cylinder. | 125 |
| 4-13 | Resonant nondimensional frequency \hat{f}_n and lift coefficients $C_{L_{V_0}} _n$ and $C_{L_{A_0}} _n$ against resonant amplitude ratio Y_n/d ; smooth circular cylinder. | 127 |
| 4-14 | Graphical illustration of the simple predictive scheme $2S_G Y_n/d \rightleftharpoons C_{L_{V_0}} _n$ | 129 |
| 4-15 | Performance of the predictive scheme compared to various experimental data from Griffin (1985). | 129 |
| 4-16 | Illustrating a long flexible cylinder in sheared flow. | 132 |
| 4-17 | Cross-sectional and flow geometries of the models tested. | 135 |
| 4-18 | C_{D_m} and $C_{L_{V_0}}$ for the wire-rope, $Y_0/d = 0.30$, and circular cylinder data. . | 136 |
| 4-19 | C_{D_m} and $C_{L_{V_0}}$ for the wire-rope, effective diameter 77%, and circular cylinder data. | 137 |
| 4-20 | C_{D_m} and $C_{L_{V_0}}$ for the chain, $Y_0/d = 0.30$, and circular cylinder data. . . . | 138 |
| 4-21 | $C_{L_{V_0}}$ for the riser at 0° , $Y_0/d = 0.30$, and circular cylinder data. | 139 |
| 4-22 | $C_{L_{V_0}}$ for the riser at 90° , $Y_0/d = 0.30$, and circular cylinder data. | 140 |
| 4-23 | $C_{L_{V_0}}$ for the riser at 45° , $Y_0/d = 0.30$, and circular cylinder data. | 140 |

| | | |
|------|--|-----|
| 4-24 | Variation of $C_{L-V_0} _n$ against amplitude ratio for the riser at different angles, and circular cylinder data. | 141 |
| 4-25 | Suppression of vortex shedding using a "control" cylinder, from Strykowski and Sreenivasan (1990). | 143 |
| 4-26 | Contours of the lift coefficient in phase with velocity; haired-fairing. | 146 |
| 4-27 | Contours of the mean drag coefficient; haired-fairing. | 146 |
| 4-28 | The predictive scheme $2S_G Y_n/d \iff C_{L-V_0} _n$ applied to the haired-fairing. | 147 |
| 4-29 | Performance of the predictive scheme applied to the haired-fairing. | 147 |
| 5-1 | Waveforms at constant modulation ratio and varying modulation depth. | 150 |
| 5-2 | Waveforms at varying modulation ratio and constant modulation depth. | 151 |
| 5-3 | States of response of near-wake as a function of dimensionless modulation frequency f_m/f_e and amplitude Y_e/d at $f_e/f_s = 0.95$; from Nakano and Rockwell (1991). | 155 |
| 5-4 | C_{D_m} for beating motion with $2Y_1/d = 0.75$ (open circles), and for peak-matched sinusoidal motion (solid lines). | 157 |
| 5-5 | C_{D_m} for beating motion of RMS amplitude ratio $Y_{RMS}/d = 0.53$ (asterisks), and for RMS-matched sinusoidal motion (solid lines). | 158 |
| 5-6 | Motion and drag for a typical 1:10 beating case; $\hat{f}_c = 0.160$, $2Y_1/d = 0.50$ | 159 |
| 5-7 | Results from the quasistatic C_{D_m} model (dashed lines) and measured data (open circles); beating motion with $2Y_1/d = 0.50$ | 161 |
| 5-8 | Results from the linear C_{D_m} model (dashed lines) and measured data (asterisks); beating motion with $2Y_1/d = 0.30$ | 162 |
| 5-9 | Contours of C_{D_m} ; 1:20 beating motion. | 163 |
| 5-10 | Contours of C_{D_m} ; 1:10 beating motion. | 163 |
| 5-11 | Contours of C_{D_m} ; 1:3 beating motion. | 164 |
| 5-12 | C_{D_1} and C_{D_2} for beating motion with $Y_1/d = 0.50$, and C_{D_0} for component-matched sinusoidal motion. | 165 |
| 5-13 | $C_{D_{RMS}}$ calculated from actual data, as well as $C_{D_{RMS}}^{calc.}$ from C_{D_1} and C_{D_2} ; beating motion with $2Y_1/d = 0.75$ | 166 |
| 5-14 | Measured values of $C_{D_{mod}}$ (crosses) and results from quasistatic model (dashed lines); beating motion with $2Y_1/d = 0.75$ | 167 |

| | | |
|------|--|-----|
| 5-15 | $C_{D_{RMS}}$ calculated from from actual data, as well as $C_{D_{RMS}}^{calc.}$ from C_{D_1} , C_{D_2} and $C_{D_{mod}}$; beating motion with $2Y_1/d = 0.75$ | 168 |
| 5-16 | Power spectrum of a high frequency, 1:3 ratio, beating drag force trace. . . | 169 |
| 5-17 | Contours of $C_{D_{RMS}}$; 1:20 beating motion. | 170 |
| 5-18 | Contours of $C_{D_{RMS}}$; 1:10 beating motion. | 171 |
| 5-19 | Contours of $C_{D_{RMS}}$; 1:3 beating motion. | 171 |
| 5-20 | $C_{D_{RMS}}$ for beating motion with $2Y_1/d = 0.75$ (open circles), and for RMS- matched sinusoidal oscillations (solid lines). | 172 |
| 5-21 | C_{L_1} and C_{L_2} for beating motion with $Y_1/d = 0.15$, and C_{L_0} for component- matched sinusoidal motion. | 173 |
| 5-22 | $C_{L_{RMS}}$ calculated from from actual data, as well as $C_{L_{RMS}}^{calc.}$ from C_{L_1} and C_{L_2} ; beating motion with $2Y_1/d = 0.75$ | 174 |
| 5-23 | Power spectrum of a high frequency, 1:3 ratio, beating lift force trace. . . . | 175 |
| 5-24 | ϕ_1 and ϕ_2 for beating motion with $Y_1/d = 0.50$, and ϕ_0 for component- matched sinusoidal motion. | 176 |
| 5-25 | Contours of $C_{L_{Vc}}$; 1:20 beating motion. | 178 |
| 5-26 | Contours of $C_{L_{Vc}}$; 1:10 beating motion. | 178 |
| 5-27 | Contours of $C_{L_{Vc}}$; 1:3 beating motion. | 179 |
| 5-28 | Contours of $C_{L_{Ac}}$; 1:20 beating motion. | 179 |
| 5-29 | Contours of $C_{L_{Ac}}$; 1:10 beating motion. | 180 |
| 5-30 | Contours of $C_{L_{Ac}}$; 1:3 beating motion. | 180 |
| 5-31 | An example of periodic nonlock-in; 1:10 beats with $2Y_1/d = 0.15$, $\hat{f}_c = 0.144$. . . | 183 |
| 5-32 | An example of frequency-switching; 1:20 beats with $2Y_1/d = 0.75$, $\hat{f}_c = 0.1302$. . . | 184 |
| 5-33 | An example of random phase modulations; 1:10 beats with $2Y_1/d = 0.50$, $\hat{f}_c = 0.1547$ | 185 |
| 5-34 | An example of periodic phase modulations; 1:10 beats with $2Y_1/d = 0.50$, $\hat{f}_c = 0.208$ | 186 |
| 5-35 | Wake response state diagram for 1:20 beats. | 188 |
| 5-36 | Wake response state diagram for 1:10 beats. | 188 |
| 5-37 | Wake response state diagram for 1:3 beats. | 189 |
| 5-38 | An example of "period-doubling"; 1:3 beats with $2Y_1/d = 0.30$, $\hat{f}_c = 0.184$. . . | 190 |

| | | |
|------|--|-----|
| 6-1 | The vortex wakes of a bluff body and an oscillating foil. | 197 |
| 6-2 | Illustrating the concept behind our experimental investigation. | 199 |
| 6-3 | The oscillating mechanism used in the Kalliroscope-tank. | 204 |
| 6-4 | Measured Strouhal number versus Reynolds number for a D-section cylinder. | 206 |
| 6-5 | The locations of the three interaction modes observed. | 208 |
| 6-6 | Wake interaction mode 1: Vortex pairing. Views I and II. | 209 |
| 6-7 | Wake interaction mode 1: Vortex pairing. Views III and IV. | 210 |
| 6-8 | Wake interaction mode 2: Destructive vortex merging. Views I and II. | 213 |
| 6-9 | Wake interaction mode 2: Destructive vortex merging. Views III and IV. | 214 |
| 6-10 | Wake interaction mode 3: Constructive vortex merging. Views I and II. | 216 |
| 6-11 | Wake interaction mode 3: Constructive vortex merging. Views III and IV. | 217 |
| 6-12 | Photographs of the wake downstream of the oscillating foil. | 219 |
| 6-13 | The double-yoke force measurement apparatus. | 222 |
| 6-14 | Overall in-line drag force as a function of spacing. $A_C/d = 0.833$ and $\theta = 45^\circ$ | 225 |
| 6-15 | Apparent foil efficiency as a function of spacing. $A_C/d = 0.833$ and $\theta = 45^\circ$ | 225 |

List of Tables

| | | |
|-----|--|-----|
| 2.1 | Details of the various models tested in the oscillating apparatus. | 45 |
| 3.1 | Summary of results for the stationary circular cylinder; $Re = 10,000$ | 65 |
| 4.1 | Summary of results for the stationary haired-fairing model. | 144 |
| 6.1 | Heave and pitch amplitude combinations tested. | 207 |

Chapter 1

Introduction

1.1 The phenomenon of vortex shedding

One of the classical open-flow problems in fluid mechanics concerns the flow around a circular cylinder, or more generally, a bluff (i.e. non-streamlined) body. At very low Reynolds numbers (based on cylinder diameter) the streamlines of the flow are perfectly symmetric: coincidentally, they resemble the solution obtained from inviscid potential flow theory, although the viscous effect predominates. As Reynolds number is increased, at first, two attached vortices appear behind the cylinder, and grow in size with Reynolds number. As the Reynolds number increases further, the wake becomes unstable. The boundary layers on either side of the cylinder separate and discrete vortices are formed in the near wake region behind the cylinder. New vortices form alternately from either side of the cylinder and move downstream, generating a periodic asymmetric flow, which is the celebrated *von Kármán vortex street*. Figure 1-1, from the cover of Van Dyke's photographic collection [13], is an example of a laminar vortex street revealed via flow visualization.

From a historical perspective, the first known observations of the formation of eddies due to a flow obstacle are attributed to Leonardo da Vinci during the Renaissance period. (See the excellent work by Lugt [42] for a more complete historical discussion.) The systematic study of cylinder wakes did not commence until the end of the nineteenth century, when Strouhal and Rayleigh began investigations into the production of "Aeolian tones" generated by wires in a wind. Strouhal demonstrated that the frequency of these tones was proportional to wind speed divided by wire thickness, and the constant of proportionality

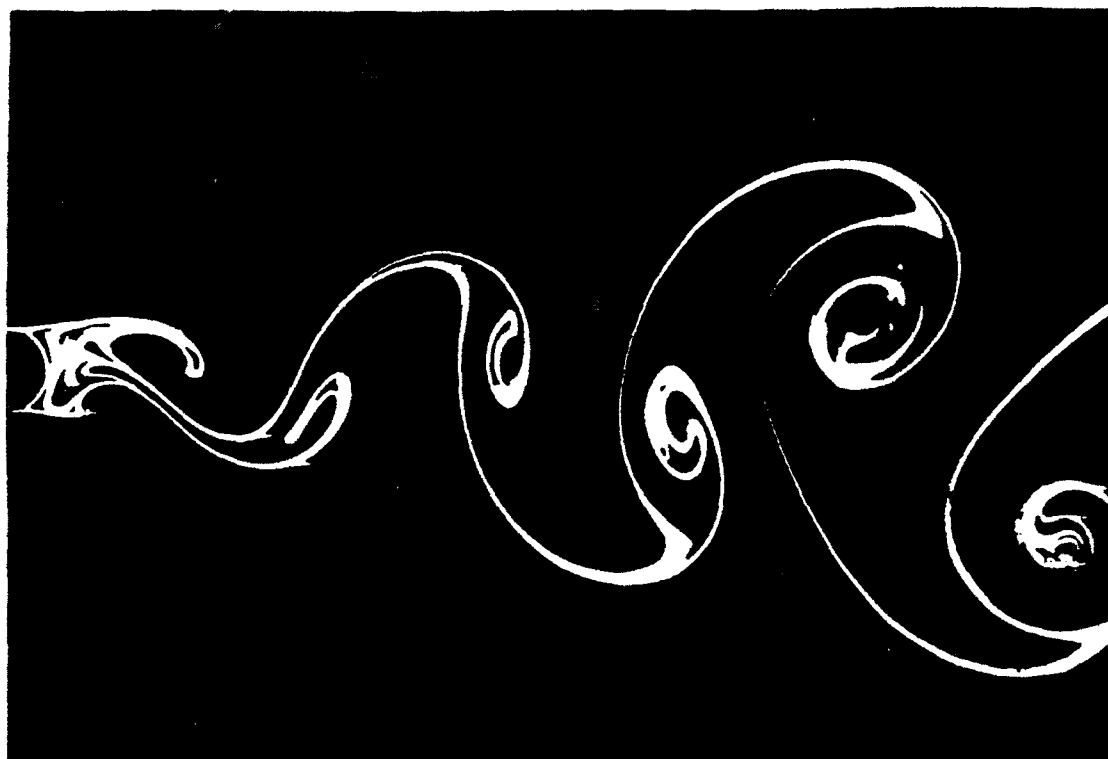


Figure 1-1: Laminar vortex street behind a circular cylinder at $Re = 140$. Photograph by S. Taneda, from Van Dyke (1982).

in this relationship came to be known as the Strouhal number. In 1908, Bénard associated the production of the Aeolian tones with vortex formation; and this advance was followed in 1912 by von Kármán's suggestion of the stable, staggered arrangement of vortices which now bears his name (except in the French literature where it carries the name of Bénard).

In the last three-quarters of the century, a very large number of researchers have investigated the phenomena associated with vortex shedding and vortex-induced vibrations; some of the important references will be mentioned later in this chapter. A few of the important features that have resulted from these investigations are briefly summarized below.

Strouhal number. The Strouhal number S mentioned above is defined as

$$S = \frac{f_s d}{U} \quad (1.1)$$

where f_s is the frequency of vortex shedding, U the free-stream flow velocity, and d the diameter of the body under consideration. It has been found that the Strouhal number is a function of Reynolds number for any given body cross-section. For the case of a circular cylinder, Figure 1-2 shows that the Strouhal number is approximately constant at 0.2 for a wide range of Reynolds numbers.

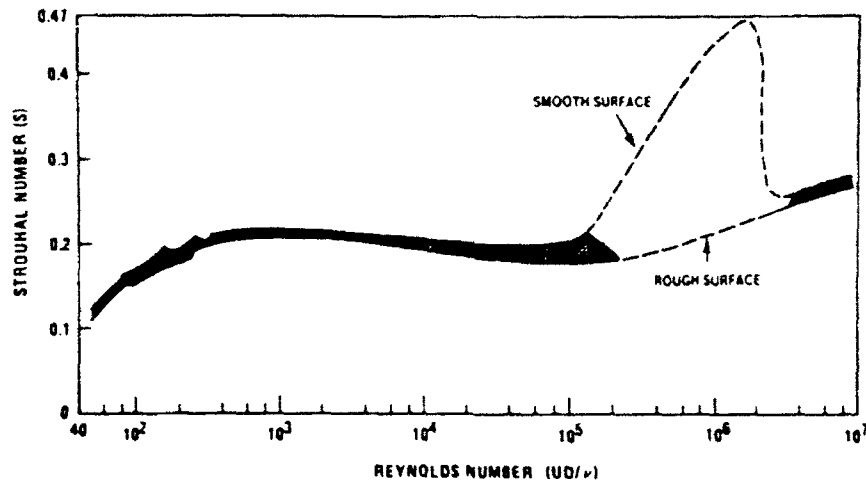


Figure 1-2: The dependence of Strouhal number on Reynolds number for a circular cylinder, from Blevins (1990)

Vortex-induced forces and vibration. Bluff body vortex shedding might well be relegated to the status of a scientific curiosity were it not for the profound engineering consequences of vortex-induced vibrations. The alternate shedding of vortices in the near wake causes fluctuating velocities and pressures in the vicinity of the cylinder, which in turn cause oscillating lift and drag forces to be imposed on the body. The oscillating lift forces are predominant, and if the body is free to move, it responds to the oscillating lift and vibrates in a direction transverse to the ambient flow. These vibrations are referred to variously as "vortex-induced vibrations", "VIV", "vortex strumming", or "cable strumming" (if a cable is involved). An important feature is that the oscillations do not grow indefinitely, but are amplitude-limited to about one diameter. Thus, in an engineering sense, vortex-induced vibrations do not produce catastrophically large oscillation amplitudes, but rather have an important effect on the fatigue life of the structure.

Lock-in. The phenomenon of "lock-in", also called "synchronization" or "wake-capture", is an interesting observation from the study of vortex shedding. If a body experiences vortex-induced vibrations as mentioned above, the motion excites a second mode in the wake that competes with the natural Strouhal shedding process. The interaction between the "natural", or Strouhal frequency and the "forced", or body motion frequency is nonlinear; when the two frequencies are close together, the body motion can take control of the shedding process in an apparent violation of the Strouhal relationship. The frequency of vortex shedding then collapses onto the oscillation frequency of the body; the strength of the shed vortices, transverse lift force, and body response can all greatly increase.

Several comprehensive reviews exist that cover vortex shedding and associated phenomena in considerably more detail. Some of these reviews are referenced in the literature survey section that appears later in this chapter.

1.2 Vortex shedding and marine cables: the problem at hand

The properties and consequences of flow around circular cylinders, as introduced in the previous section, find a special application in the analysis of long marine cables used in towing and mooring situations. The extremely large aspect ratio and flexible nature of these structures make them particularly susceptible to vortex-induced vibrations. From both design and operational points of view, it is important to be able to predict the forces (primarily the drag) acting on the cable, as well as its resultant configuration and motions. Although a value of 1.20 is widely accepted as the mean drag coefficient C_{D_m} for the case of flow normal to a stationary circular cylinder, it is also well known that any motion of the cylinder can significantly alter the flow pattern and amplify the vortex-induced forces. In the case of marine cables, this means that the selection of the proper drag coefficient remains a contentious issue.

Due to the complexity of the hydroelastic cylinder/wake problem, theoretical models remain incomplete, and numerical solutions are as yet not feasible except for very low Reynolds numbers. As a result, most of our knowledge of circular cylinder flows is derived from physical experiments conducted over the last several decades. Both free-oscillation

tests (in which an elastically-mounted cylinder is exposed to a flow and allowed to vibrate) and forced-oscillation tests (in which a cylinder is mounted in a flow and driven externally) have been conducted by generations of researchers. The first type of experiments had as their objective the measurement of displacement response, and the second focused on the measurement of the hydrodynamic forces. In addition, in both types of tests, other quantities have been measured as well, such as surface pressure or wake-velocity measurements, flow visualization, etc. The accumulated results have given us reasonably good insight into the behavior of bluff bodies oscillating in a flow, with one important limitation; almost all of the tests reported thus far have been for pure harmonic oscillations.

In the case of rigid structures exposed to uniform flow, vortices are shed harmonically into the wake and the assumption of a pure sinusoidal response is reasonably valid; however, in the case of marine cables and other similarly long structures exposed to shear flow, this assumption is questionable. Due to the combined effect of varying ocean currents and the static angle of the cable, the normal velocity varies along the cable length. As a result, if one assumes that the sheared current is suddenly "switched on", it must be expected that the flow sets up a vortex-induced loading that is "local", in that the frequency and magnitude of the loading is constant only over a very limited extent. For a cable longer than a few hundred meters, the hydrodynamic damping is such that the end conditions are not felt over most of its length, and the cable responds primarily as one of infinite length. This results in a large number of participating natural modes, and the cable responds at every point along its length primarily to the local forcing at that point and a small neighboring region. In fact, employing the concept of natural modes offers no additional insight. Instead, it is better to view the cable response as traveling waves caused by distributed excitation; these waves are damped out as they move away from the source that produced them, but affect substantially the cable motion at neighboring points. The net result of this scenario is that each point on the cable has a motion that is not simple harmonic, but rather is amplitude-modulated in both space and time.

The presence of such large scale amplitude modulations in the strumming behavior of marine cables has been noticed and commented on in the past by several researchers, for example see Alexander [1] or Kim [36]. The first detailed observations reported in the public literature were made via a full-scale experiment conducted by the Woods Hole Oceanographic Institution and reported by Grosenbaugh *et al.* [28, 27] and Yoerger *et al.*

[99]. Regular beating patterns were observed in the cable motion, characterized by two primary peaks in the power spectra. The period of the beats varied along the length of the cable, and could be related to the current shear prevalent at the corresponding depths. In addition, the overall drag coefficient for the cable was calculated at different instants of time, and was shown to be less than the values commonly assumed for pure harmonic oscillations of equivalent amplitude.

Consequent to the above full-scale tests, Engebretsen [14] and Howell [31] attempted to simulate the beating motions of the cable using a Green's function approach, with the response at any point being the superposition of responses due to varying point loads along the cable. The use of force coefficient magnitude and phase data from standard harmonic results proved to be inadequate, and the authors had to resort to randomly distributed phase angles in order to obtain reasonable results. In related research, Triantafyllou and Karniadakis [79] used a direct Navier Stokes simulation code to numerically simulate, at low Reynolds number, the flow around a circular cylinder undergoing amplitude-modulated motion. They were able to demonstrate that the beating motion caused the lift and drag forces, expected on the basis of sinusoidal results, to be modified in unpredictable ways, and they concluded that sinusoidal test data could not be applied, in a linear superposition sense, to calculations or simulations of beating motion.

The previous paragraphs have attempted to lay out a flow of logic that is summarized as follows:

- the bulk of our knowledge of vortex-induced loads and body motions comes from laboratory experiments with harmonically oscillating cylinders;
- marine cables and similar structures of extreme aspect ratio exposed to shear flows respond with complex, amplitude-modulated vortex-induced vibrations; and
- pure harmonic results cannot be applied directly to calculations involving beating motions.

Thus, there emerges a need for new data quantifying the vortex forces on cylinders undergoing amplitude-modulated motion, and/or new methods to accurately extrapolate the existing data to these more complex cases.

The experiments described in this thesis have as their primary purpose the presentation

of new data and methods for the beating motion mentioned above. We have attempted to extend the classical forced-oscillation experimental approach by driving a circular cylinder with double-frequency beating motion in the presence of a cross-flow, and measuring the lift and drag forces acting on the cylinder. Our data is presented with comparison to sinusoidal test results taken with the same apparatus. (Many of our sinusoidal results represent new findings in themselves and have been presented in some detail.) In the context of related research, our efforts lie in between the full-scale sea tests of Grosenbaugh *et al.* [28, 27] and the low-Reynolds number computer simulations of Triantafyllou and Karniadakis [79].

Before concluding this section, two points must be made about the experiments described herein.

Firstly, our experiments do not bear any resemblance to shear-flow tests conducted by Maull and Young [45], Mair [43], Stansby [73], or others of that period. In those tests, the researchers subjected small aspect ratio fixed and harmonically vibrating cylinders to axial shear flows and recorded their findings with respect to vortex-shedding in "cells", cell length, and base pressure variation. Although a principal motivation for our present efforts is the effect of axial shear in the flow incident on a cable, we make the important simplification that we study the forces on a small local section of the cable over which the flow is essentially uniform. We thus attempt to isolate the effects of amplitude-modulated body motion in a local or "two-dimensional" manner.

Secondly, it will be noticed that in all of our experiments, the test cylinder is externally forced. Much has been written in the literature about the relative advantages and disadvantages of forced- versus free-oscillation experimental methods, and for the general case, there is little to add to the discussion. However we believe that in the case under study, forced experiments are the correct approach. Since the response of the cable at any given location is determined by both the fluid forcing at that location as well as structural interactions along the cable, it is possible for that response to contain spectral components that would normally have been damped out by the flow at that location. Put differently, it is possible for energy to be extracted by the cable from the fluid at one axial location, transmitted via the cable to a different axial location, and lost to the fluid (damped out) there. In the absence of extensive full-scale tests or expensive, large-scale experiments, it would appear that the only viable way of recreating such a scenario is through a systematic forced-oscillation experimental schedule.

1.3 Chronology of this work

Efforts to conduct experiments along the lines of those described in this thesis commenced shortly after the results from the full-scale sea trials became available, in the Fall of 1987. The first experiments were conducted during July 1988, using a vertically mounted cylinder (2.54 cm dia., 30 cm length) in a current flume at the Coastal Research Laboratory of the Woods Hole Oceanographic Institution. A computer controlled motor driving a lead-screw positioning table was used to provide the beating oscillations, and lift and drag forces were measured using strain gages. While conducting the experiments, problems were experienced with the operation and calibration of the strain gages. Several runs were conducted and the data recorded, but data processing efforts were hampered by the lack of reliable calibrations, and the collected data were abandoned.

Learning from the successes and failures of our first effort, a second set of experiments was conducted during January and February of 1990. The venue was shifted to the newly refurbished Ocean Engineering Testing Tank at the Massachusetts Institute of Technology. The motor and lead-screw mechanism were retained, but force measurement was accomplished with a highly accurate and mechanically stiff piezoelectric force sensor. A horizontally mounted cylinder (2.54 cm dia., 60 cm length) was used. Results from this set of experiments [21, 20] were presented at the ISOPE-91 conference held at Edinburgh, U.K., during August 1991.

The bulk of the results presented in this thesis are based on further experiments conducted at MIT during February 1991 and January 1992, using a setup similar to that used in 1990. Many improvements were made to the apparatus, and the experimental method was largely automated. Thus it became possible to test a greater variety of parameters and with a higher resolution than before. Some of these newer results have been published in Gopalkrishnan *et al.* [19].

1.4 A review of the literature

1.4.1 Forced-oscillation force-measurement experiments

Ever since the systematic investigation of vortex-shedding was started by Strouhal and Raleigh in the late nineteenth century, a large body of knowledge has been accumulated.

Any investigation in this field would be incomplete without a careful survey of the existing literature. Since our work is an extension to the forced-oscillation, force-measurement experiments conducted in the past, we will focus our review on important contributions in this particular area. The following paragraphs cite research material in an approximately chronological fashion.

Bishop and Hassan. Our review begins with the seminal work of R.E.D. Bishop and A.Y. Hassan, published during 1964 in a pair of papers, "The lift and drag forces on a circular cylinder in a flowing fluid" [5] and "The lift and drag forces on a circular cylinder oscillating in a flowing fluid" [6]. With these papers, Bishop and Hassan were the first to report on a comprehensive treatment of force coefficient measurements on stationary and oscillating circular cylinders. They used a 1 in. dia., 5 in. long cylinder mounted horizontally to a skotch yoke mechanism in a water channel. Forces were measured on a 3 in. center section by means of strain gages, which could be arranged to measure either the lift or the drag force. The first paper [5] sets out the basic definitions and characteristics of vortex-induced forces; and contains values of Strouhal number S , lift coefficient C_L , mean drag coefficient C_{D_m} , and oscillating drag coefficient C_{D_o} for stationary cylinders at various Reynolds numbers $3,600 < Re < 11,000$. The second paper [6] contains measurements of the force coefficients acting on the cylinder forced to oscillate sinusoidally transverse to the flow. The authors report on the wake synchronization phenomenon and the changes in the magnitudes of the forces and phase angles as the cylinder-oscillation frequency traverses the natural Strouhal shedding frequency. That their work was of high quality is evident in that Bishop and Hassan report on phenomena that other researchers would give prominence to only in later years; phenomena such as hysteresis, frequency demultiplication, and the modification of the "critical nondimensional frequency" as a function of oscillation amplitude.

Two major drawbacks exist in these papers. Firstly, the bulk of the data on lift and drag forces are given in the form of "arbitrary units", and thus can be used only for qualitative comparisons. Secondly, and perhaps more importantly, the method used to deduce the lift coefficient magnitudes from the total measured lift force is questionable. For forced-oscillation experiments of this nature, the total force measured in the lift direction consists of the sum of inertial force due to the cylinder mass, inertial force due to the "added mass"

effect of the water, and the vortex-induced lift force (which may itself have components in the inertial (acceleration) and velocity directions). The first of these components, the inertial force in air, is relatively easy to subtract. However, since the added mass of water does not necessarily remain constant with cylinder motion or fluid flow, the second inertial component is harder to determine. Bishop and Hassan have assumed that the added mass of water does not change with flow velocity; they subtract the inertial lift force measured in still water from the total force measured in flow for each oscillation run. Most researchers today do not attempt to remove the added mass force, and instead treat the sum of this and the vortex-induced force as one holistic fluid force that has both inertial and velocity components.

Toebe et al. Several experiments relating to the vortex-induced forces on cylinders of various cross-sections were conducted during the mid-1960's by Prof. G. H. Toebe and his group at Purdue University, and one of the publications that resulted is reference [60] by Protos, Goldschmidt, and Toebe. This work describes the results of lift force measurements made on circular and triangular cylinders forced to oscillate at small amplitudes in a flow of Reynolds number 45,000. Only the lift forces were measured. The authors present results for the lift coefficient calculated in a manner similar to that of Bishop and Hassan, with the improvement that actual physical values are given. A valuable contribution is in showing the importance of the phase angle between the lift force and the cylinder motion, in the context of determining the sign of the energy transfer between the cylinder and the fluid (whether exciting or damping).

Jones, Cincotta, and Walker. The large majority of experimental results available in the literature relate to flows around cylinders that have Reynolds numbers in the range of a few hundred to a few thousand. The report by Jones *et al.* [34] presents results of tests conducted on a 3 ft. dia. cylinder forced to vibrate in Reynolds numbers up to 1.9×10^7 and Mach numbers up to 0.6, with the motivation being to study the response of Saturn V rockets to wind gusts while on the launch pad. Air and Freon were used in a closed circuit wind tunnel at the NASA Langley Research Center, with a massive hydraulic shaker assembly employed to provide the oscillations. Values of lift and drag coefficients and Strouhal number are given as functions of Reynolds number, Mach number, and oscillation

amplitude and frequency. The trends of lift coefficient against nondimensional frequency are qualitatively very similar to our own results, a very interesting observation given the huge difference in Reynolds number regime.

Mercier. One of the most comprehensive sets of forced-oscillation experiments was conducted by John Mercier at the Stevens Institute of Technology during the early 1970s, and reported in his doctoral thesis "Large Amplitude Oscillations of a Circular Cylinder in a Low-Speed Stream" [47]. The author conducted tests on cylinders forced to oscillate both transversely as well as in-line to the flow in a recirculating water channel. Most of the results are for the range $4000 < Re < 8000$, with amplitude-to-diameter ratios A/D up to three. The experimental method used was rather "modern", in that the force measurements were recorded on magnetic tape, and later digitized and analyzed on a digital computer for Fourier series coefficients and the like. A variety of graphs are presented for mean and oscillatory drag coefficients, lift force magnitudes and phase angles, and lift force drag and inertia coefficients, as functions of reduced velocity and amplitude of oscillation. Several oscillograph time traces are also provided to illustrate the variety of lift and drag waveforms observed.

Mercier's thesis was and remains unique in several ways. He was the first researcher to conduct tests on cylinders oscillating in-line with the flow, and to give results for the large mean drag amplification seen for these cases. Prior to our own work reported herein, he appears to have been the only researcher to report on the very large values of oscillatory drag coefficient that arise for certain ranges of transverse oscillation. He was also one of the first to attempt to combine force measurements with flow visualization of the vortex formation in the cylinder wake, although his efforts in this were not very successful.

Sarpkaya. For practical design applications or estimation of vortex-induced forces and body response, the most complete set of data available is due to Turgut Sarpkaya, as reported in [65] and summarized in [64]. The purpose of Prof. Sarpkaya's work was to conduct forced-oscillation cylinder experiments and use the measured force coefficients to predict the amplitude response of an elastically mounted cylinder subjected to a uniform flow. His experiments were performed in relatively narrow recirculating water tunnels, using very low aspect-ratio circular cylinder models ($L/D \approx 3$). The Reynolds number of the flow

was varied in the range $7,000 < Re < 11,000$, and lift and drag forces were measured using strain gages. In addition to a great deal of valuable experimental data, both references cited above contain excellent discussions of the hydrodynamic and structural issues involved, such as Strouhal number, correlation length, added mass, damping coefficient, and natural frequency.

Sarpkaya formulates the lift force, on the basis of a first-order series expansion of Morison's equation, in terms of an inertial coefficient C_m (component of lift in phase with cylinder acceleration) and a "drag" coefficient C_d (component of lift in phase with cylinder velocity). Curves of these force coefficients (normalized with respect to the amplitude of the cylinder velocity, as well as with respect to the freestream flow velocity) are presented as functions of oscillation amplitude and reduced velocity (reciprocal of nondimensional oscillation frequency). These data were then used in a linear equation of motion in order to predict the maximum amplitudes of vibration of an elastically mounted, linearly damped cylinder. Good agreement was found between these predictions and the experimental data of Griffin and Koopman [25].

In addition to the lift force coefficients, Sarpkaya presents results for the mean drag coefficient plotted against nondimensional oscillation frequency, with each curve representing a particular value of amplitude ratio A/D . These curves (Figure 1-3) dramatically illustrate the amplification of mean drag at frequencies near the Strouhal shedding frequency.

One significant omission in Sarpkaya's work appears to be the lack of quantitative information regarding the oscillating component of the drag force. The author asserts that the magnitude of the oscillating drag force in no case exceeds 7% of the mean drag, a statement which contradicts the results in Mercier's thesis [47] as well as our own measurements. He does mention, however, that the oscillating drag force increases sharply after a certain critical value of oscillation frequency.

Schargel. As mentioned earlier in the introduction, the great majority of experimental results reported thus far have been for the case of cylinders oscillating with pure harmonic motion. To the best of our knowledge, the only laboratory-scale experimental program that focused on random oscillations was that conducted by Robert Schargel at MIT and reported in his M.S. thesis [68]. Schargel used a massive Brüel and Kjaer electromagnetic vibration exciter mounted over a water tunnel to cause a 0.5 in. dia. circular cylinder to oscillate

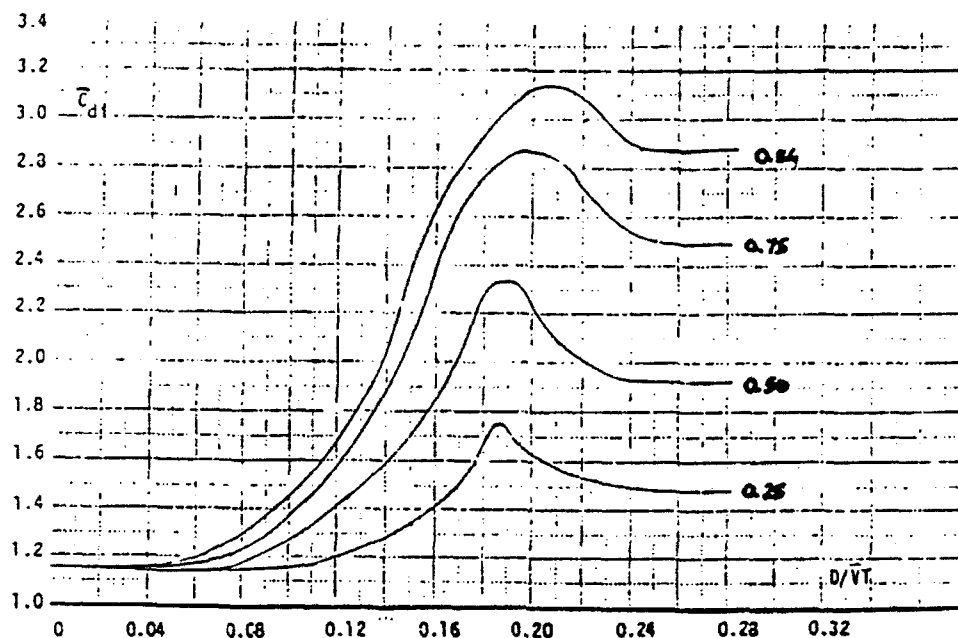


Figure 1-3: Mean in-line drag coefficient versus nondimensional frequency; from Sarpkaya (1977)

transversely to the flow. The electromagnetic shaker tracked an input signal which could be provided by a custom built pseudorandom noise generator, with its output suitably band-pass filtered. Only the drag force was measured, with tests conducted in the range $4,000 < Re < 7,000$, and $0.05 < A_{RMS}/D < 0.38$. Also evaluated were the drag coefficients for pure harmonic oscillations, of comparable RMS amplitudes, using the same apparatus with a sinusoidal signal generator providing the tracking signals. Schargel's results are presented in the form of plots of drag coefficients against nondimensional oscillation frequency (center frequency in the case of random oscillations). The principal conclusions are that the random oscillations cause a "smearing out" of the sinusoidal drag force peaks (to result in "plateau" values); and that these plateau values for the random oscillations were generally lower than the peak values for the corresponding sinusoidal oscillations.

In a later report [69], Schargel and J. Kim Vandiver reported on wake velocity measurements made behind the randomly oscillating cylinder, using a noninvasive laser Doppler anemometer. For pure harmonic oscillations in the lock-in regime, they found that the cylinder motion and wake velocity were strongly correlated, as was to be expected. A small

degree of randomness was sufficient to reduce this correlation, and a broadband cylinder motion virtually eliminated any motion-velocity correlation. From these observations, and the reduction in the drag coefficient mentioned above, the authors concluded that lock-in was a relatively fragile process, that could be interrupted by frequency components not at the lock-in frequency.

Alexander. A limited number of forced-oscillation experiments were conducted by C. M. Alexander [1] at the Scripps Institution of Oceanography, and are reviewed here principally because the author attempted to combine in-line as well as transverse excitation of the test cylinder. Alexander's motivation was very similar to our own, i.e. the characterization of the vortex forces on, and the motions of, an oceanographic cable of large length to diameter ratio. An ingenious test apparatus was designed that could impress a "figure-8" motion on a cylinder suspended in a towing tank. Several tests at different towing velocities were conducted, but unfortunately, the oscillation frequencies were selected such that only a single nondimensional frequency of 0.18 was tested. In addition, a severe drawback was that oscillation amplitude was not separately controllable, but rather depended on the oscillation frequency. Alexander reported a constant value of drag coefficient $C_D \approx 1.8$, but his results must be regarded as inconclusive due to the difficulties noted above. However, the descriptions of his apparatus could provide a convenient starting point for any researcher attempting to combine forced in-line and transverse oscillations.

Staubli. One of the more recent investigations along the "classical" lines of Bishop and Hassan, Mercier, and Sarpkaya, was conducted in the early 1980s by Thomas Staubli of the Swiss Federal Institute of Technology, and reported in his thesis [75] and a related paper [74]. Staubli's work was essentially similar to Sarpkaya's efforts mentioned above, although his Reynolds number was somewhat higher ($Re \approx 60,000$). The lift and drag coefficients on an oscillating cylinder were evaluated experimentally, and then used to predict the response of an elastically mounted cylinder. Generally good agreement was achieved with the experimental data of Feng [16], including the observed hysteresis effects.

Staubli's work is important on two counts. Firstly, his experimental apparatus and methods were well conceived, especially his use of sensitive quartz piezoelectric force transducers to measure the induced forces. Secondly, his treatment of the lift forces emphasizes

their magnitude and phase angle (with respect to cylinder motion), rather than the “inertial” and “drag” components of Sarpkaya. Figure 1-4 shows the author’s 3-dimensional curves of lift coefficient magnitude \hat{C}_{LO} and phase ϕ as functions of nondimensional oscillation frequency S_0 and amplitude ratio $\hat{\xi}$. It is important to note that the two approaches of

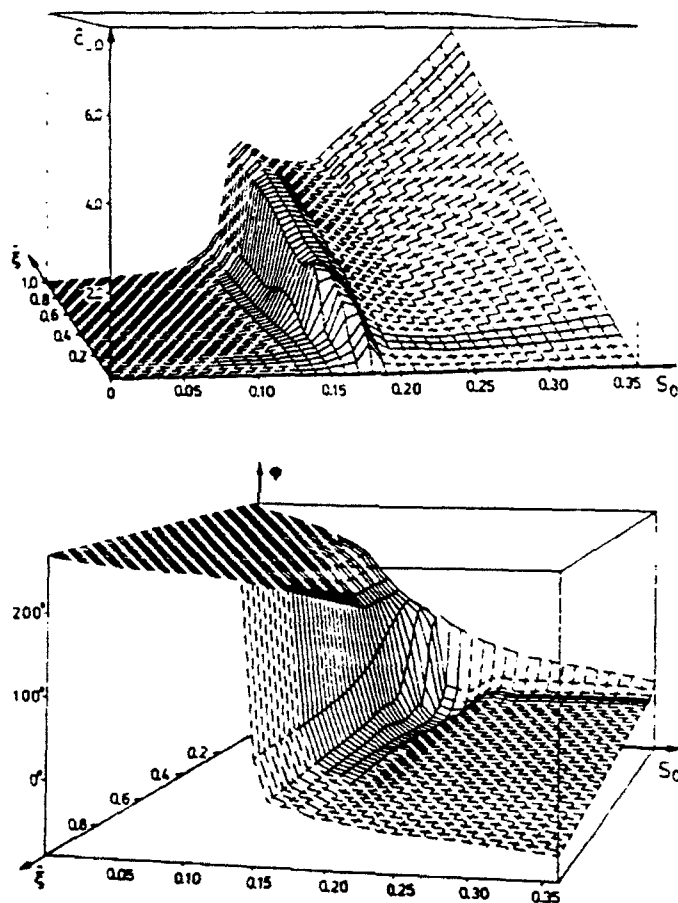


Figure 1-4: Lift coefficient magnitude \hat{C}_{LO} and phase ϕ as functions of nondimensional oscillation frequency S_0 and amplitude ratio $\hat{\xi}$; from Staubli (1983)

Staubli and Sarpkaya with regard to the lift forces are essentially similar, and can easily be derived from each other. However, an emphasis on force magnitude and phase angle makes it easier to relate the changes in the lift force to the wake dynamics and vortex shedding patterns, thus contributing to an understanding of *why* these changes occur. A great deal of our own approach in this thesis is based on Staubli’s contribution.

Moe and Wu. We have seen in the above paragraphs that Sarpkaya [65, 64] and Staubli [75, 74] have each measured the fluid forces via forced-oscillation experiments, and compared predictions based on these measurements to data from free-oscillation experiments available in the literature. Differences between the predicted values and the free-oscillation data could in part be due to the fact that the forced- and free- data were collected by different researchers under different circumstances. An important effort to conduct both forced- and free-oscillations tests with the same apparatus has been undertaken at the Norwegian Institute of Technology, with preliminary results reported by G. Moe and Z. J. Wu in [49]. The authors used an apparatus wherein a circular cylinder was suspended on springs so as to allow elastic vibration in both transverse and in-line directions; the cylinder could also be clamped in place and/or forced to vibrate transversely. Thus four distinct types of experiments could be conducted, with the cylinder being

1. free to vibrate both transversely and in-line
2. clamped in-line but free to vibrate transversely
3. clamped in-line and forced to vibrate transversely
4. free to vibrate in-line and forced to vibrate transversely.

Local lift and drag forces were measured with two ring-type force transducers, and results are presented for the different types of oscillation.

A very important result from this paper is the authors' explanation for the observation that free-oscillation tests conducted in the past have predicted much wider lock-in ranges than have forced-oscillation experiments. Moe and Wu report that during their free tests, the in-water natural frequency of the oscillating cylinder varied by as much as 50% through the lock-in range, presumably due to strong variation of the added mass component. Reduced velocities calculated on the basis of a single natural frequency are thus in error, and falsely indicate wide lock-in regions. If reduced velocities were calculated on the basis of an "instantaneous natural frequency", the authors show that the resulting lock-in range is much narrower and closely resembles forced-oscillation data. It is interesting to note that this variation of natural frequency has also been observed by Vandiver in his analysis of full-scale experimental data [88].

1.4.2 Other references

In the preceding pages we have surveyed several of the important contributions in the area of forced-oscillation force measurement experiments on circular cylinders. This, however, is but a single method used to study the problem of vortex-induced vibrations. Experiments have been conducted to study several other aspects of the cylinder/wake problem, such as pressure distributions, the effects of end conditions, shear flows, turbulence, surface roughness, Reynolds number, aspect ratio, proximity to other bodies, etc. Empirical models have been constructed (with varying degrees of success), and various inviscid schemes formulated in attempts to simulate the flow. In addition, recent theoretical advances in the area of wake stability have contributed to our understanding. For further information on any of these topics the reader is urged to refer to such comprehensive reviews as Blevins [7], King [37], Sarpkaya [66], Bearman [4], Griffin [23, 24], or theoretical contributions such as those of Triantafyllou *et al.* [80, 81] or Karniadakis and Triantafyllou [35].

In addition to measurements of such properties as fluid-induced force and pressure, experiments designed to visualize the flow in the cylinder wake have also been very important to our understanding. The nature of the oscillating lift and drag forces, and the manner in which they vary with cylinder oscillation, can be related to the patterns of vortex shedding that develop in the wake. It has been found that the classical Kármán vortex street (with a staggered array of single vortices) is but one of a variety of "modes" that the wake can sustain under different conditions. Before closing this chapter, we shall briefly review the work of two sets of researchers in this area of cylinder vortex patterns. Additional information may be found in the recent and very comprehensive review of Coutanceau and Defaye [11].

Williamson and Roshko. A particularly novel set of flow visualization results was reported by C.H.K. Williamson and A. Roshko in their paper "Vortex Formation in the Wake of an Oscillating Cylinder" [95]. The authors used aluminum particles on the surface of water in a towing tank to visualize the wake behind a vertically oriented cylinder. A wide range of oscillation frequencies and amplitudes (up to five times the diameter) were tested, in the Reynolds number range $300 < Re < 1000$. The authors' principal hypothesis is that the acceleration of the cylinder causes the formation of *four* regions of vorticity per cycle,

instead of the two that were previously supposed to occur. Depending on the oscillation amplitude and frequency, these four regions of vorticity combine to form different vortex patterns in the near wake, which are classified variously as 2S, 2P, 2P+2S, etc., where S denotes a single vortex and P a pair of vortices. Figure 1-5 shows some of these vortical

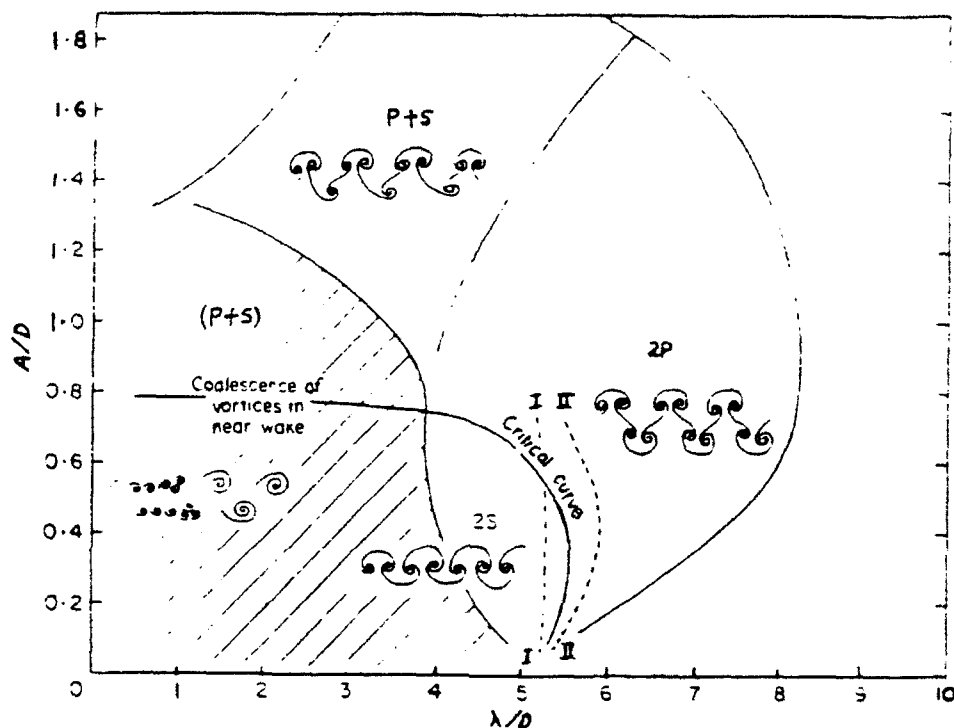


Figure 1-5: Map of vortex synchronization patterns near the fundamental lock-in region: from Williamson and Roshko (1988)

patterns and the regions of oscillation wherein they occur. As the schematic diagrams show, the 2S mode corresponds to the classical Kármán wake with two vortices per cycle of oscillation. The 2P mode corresponds to a pattern with two pairs of vortices per cycle, arranged in a staggered fashion on each side of the wake centerline. The P+S mode is an asymmetric pattern with one pair and one single vortex per cycle. For low wavelengths (high frequencies), coalescence of the near wake vortices can occur to form large scale vortices which may themselves be organized in either a 2S or P+S mode. Note that the X-axis on this figure is in terms of the 'normalized wavelength' $\lambda/d (= UT/d)$, which is more commonly known as the reduced velocity V_R .

As mentioned previously, the classification of various wake vortex patterns assumes

importance when used to explain the variation of the hydrodynamic forces acting on the cylinder. Williamson and Roshko use their data to advance plausible explanations for the variations in lift force magnitude and phase as measured by Bishop and Hassan [5, 6]. As we shall see later, some of our own data are compatible with these patterns as well.

Rockwell *et al.* For several years, Professor Donald Rockwell and his associates at Lehigh University have conducted flow visualization studies on cylinders of various cross-section undergoing various types of oscillation; we shall mention but two of the several publications that have resulted from this work.

Ongoren and Rockwell [53] report on experiments conceptually similar to the work of Williamson and Roshko, designed to visualize the "flow structure" behind an oscillating cylinder. They used a single amplitude ratio of 0.13, but tested circular, triangular, as well as square cylinder cross-sections. At this small amplitude no evidence of 2P or P+S patterns were found, although the authors report a sharp change in the timing of vortex formation as the cylinder frequency traversed the natural shedding frequency. An interesting point was that this change in timing, or jump in phase, was detected for the circular and triangular sections but not for the square section, thus indicating the importance of afterbody shape in determining the wake pattern.

More recently, Nakano and Rockwell [51] have performed visualization and wake velocity studies on the wakes of cylinders undergoing amplitude- and frequency-modulated sinusoidal oscillations. Various combinations of carrier frequency f_c and modulation frequency f_m were tested, and the authors report on the different vortex patterns detected. In many ways it would appear that this work is the flow visualization counterpart to our own experiments reported herein, although the context and motivation are considerably different. Further comparisons between our force measurements and the visualization and velocity data of Nakano and Rockwell will be made in Chapter 5.

1.5 A preview of the chapters that follow

This thesis has been organized into seven chapters. The introductory material and literature survey presented thus far comprise the first chapter. The contents of each of the following chapters are briefly summarized below.

Chapter Two contains extensive descriptions of the experimental apparatus and systems, as well as the data processing techniques and important formulations used in the succeeding material.

Chapter Three presents the results of our stationary and sinusoidal oscillation tests. The use of "contour maps" to depict the variation of force coefficients with oscillation amplitude and frequency is introduced. Novel results on the behavior of the lift force phase angle and oscillating drag force are discussed. The concept of the lift force "excitation region" is compared to the quite different lift force "lock-in region".

Chapter Four surveys some of the important considerations in the application of our data. These include a comprehensive error analysis, a simple VIV prediction scheme, and the results of some tests on typical "real-world" cross-sections that are often idealized as circular cylinders.

Chapter Five presents our beating oscillation data. The measured results of the lift and drag force coefficients are illustrated and then compared to the sinusoidal results. Methods of extrapolating these sinusoidal results to the beating case are discussed. The response of the wake to beating excitation is investigated via time-domain analyses of our data.

Chapter Six investigates a novel concept: the alteration of the mean wake velocity profile via the control of the major vortical features. Results of experiments are presented wherein an oscillating foil is placed in the wake of circular and D-section cylinders. One application of this research is the reduction of the mean in-line wake velocity.

Finally, Chapter Seven presents the principal conclusions of this research. The major benefits and shortcomings are highlighted. Avenues for future work are suggested.

Chapter 2

Experimental and Data Processing Methods

2.1 Preliminary remarks

In this chapter we shall set forth the experimental and data reduction methods by which we obtained our results. In particular, we shall provide an extensive description of our physical apparatus and the various proving tests and calibrations undertaken. This is done with two motives: firstly, to establish the reliability and accuracy of our data, and secondly, because much of the difficulty in interpreting the data available in the literature stems from an inadequate knowledge of the conditions under which they were acquired.

2.2 The experimental system

2.2.1 General description

Our experiments were conducted at the newly refurbished Testing Tank facility of the Department of Ocean Engineering at the Massachusetts Institute of Technology. The tank consists of a 30 m long rectangular channel, equipped with an overhead towing carriage. Our test model was a polished aluminum cylinder, 2.54 cm in diameter and 60 cm in length, installed in a streamlined yoke, which was in turn suspended from the towing carriage. The yoke was oscillated vertically, transverse to the towing direction, using a lead-screw assembly driven by a microprocessor-controlled servomotor. The lift and drag forces acting

on the cylinder were measured simultaneously, and recorded in digital form by a PC-class computer. The vertical motion of the yoke was measured and recorded as well. Figure 2-1 is a diagram of the experimental apparatus used. Detailed descriptions of the various experimental components and procedures are contained in the subsections that follow.

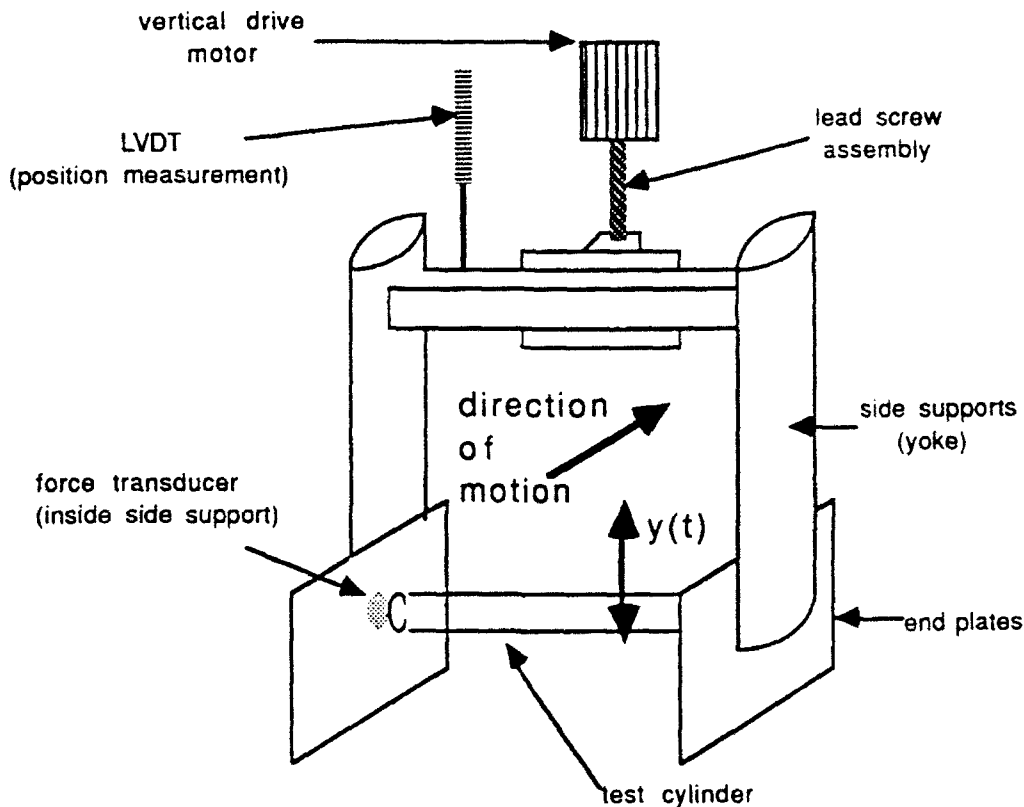


Figure 2-1: The experimental apparatus used in the Testing Tank.

In terms of experimental “strategy”, most of the results reported in this thesis pertain to tests conducted at a towing velocity of 0.4 m/s, corresponding to a Reynolds number (based on cylinder diameter) of approximately 10,000. This towing velocity was selected to give the best compromise between the conflicting requirements of force measurement (larger velocities leading to larger and more easily measured forces) and experimental accuracy (smaller velocities leading to longer experimental run times in the limited tank length). Each experimental run lasted for 75 seconds, during which time the force transducers were switched on and data was acquired. A 10 second initial zero period was followed by a 5

second allowance for carriage motion transients, a 50 second cylinder oscillation time, and a 10 second final zero period. Figure 2-2 illustrates the drag force trace for a typical sinusoidal oscillation (in this case, with amplitude $Y_0/d = 0.50$ and frequency $\dot{f}_0 = 0.203$), and shows the various times comprising the test. A total of about 3,000 runs were conducted.

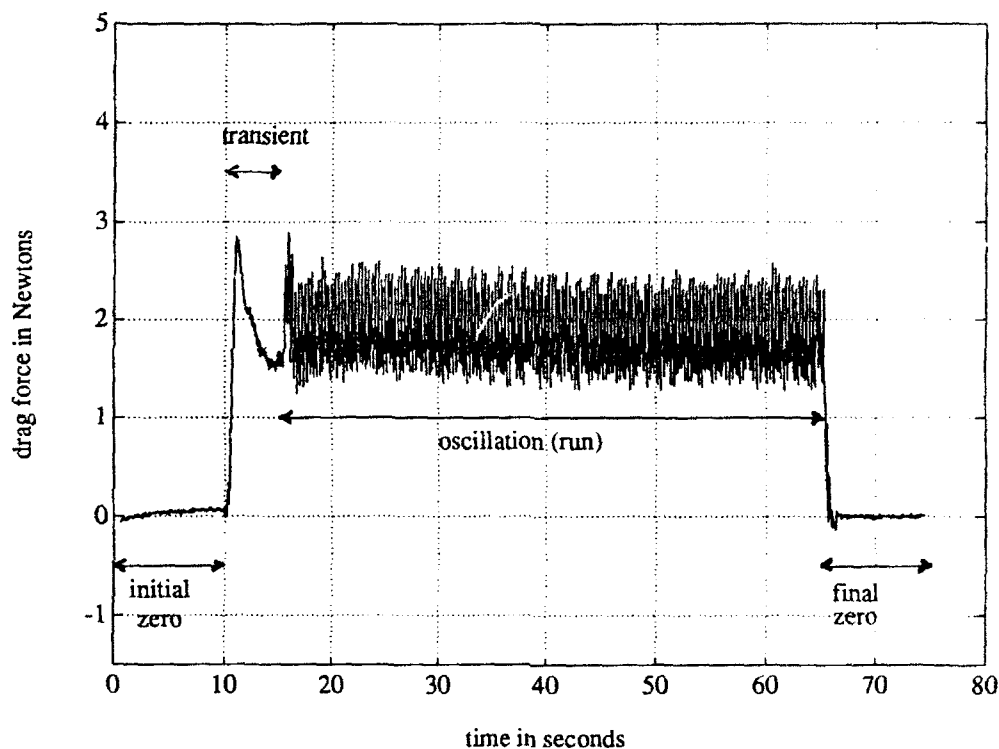


Figure 2-2: A typical experimental run (drag force trace).

2.2.2 Testing tank and carriage

The Ocean Engineering Testing Tank at MIT is the latest incarnation of the venerable Ship Model Towing Tank, first commissioned in 1950. The basic tank remains the same, consisting of a rectangular water channel of dimensions 30 m long x 2.6 m across. The depth of the water in the tank is variable up to a maximum of about 1.8 m, but for these experiments the depth was maintained at 1.3 m. In recent years, the towing carriage and drive systems have seen a complete refit. The present carriage consists of a 1.8 m long aluminum box-beam structure rolling via Polyurethane skateboard wheels on a cylindrical stainless steel overhead rail. An outrigger arm from the box-beam structure rides on a secondary rail along the wall of the tank, and serves to stabilize the carriage. The carriage

drive system consists of an endless steel tape that loops over two flywheels at each end of the tank, and is connected to the rolling box beam. A pulley and weight system maintains tension in the steel tape. An AC induction motor located at one end of the tank provides the motive force, and is in turn controlled by a closed-loop microprocessor based device. All carriage functions are controlled and monitored from the main laboratory office overlooking the tank; setting the carriage speed involves merely entering the desired value (in knots) on a numeric keypad. In addition, the microprocessor controller can be interfaced to a PC-class computer, and thereby all carriage functions can be controlled via user-written software. The drive carriage system is capable of speeds between 0.2 and 8.00 knots. In the range of interest to us (1 knot and less), the calibrated speed error was less than 0.2%, and there were minimal vibrations.

2.2.3 Test models, yoke, and oscillating system

The test cylinder used in the majority of these experiments was a polished aluminum tube of 2.54 cm diameter, 60 cm length, and 0.24 kg mass. The cylinder was plugged at both ends to keep out the water, and was suspended from the yoke structure by means of stainless steel pins embedded in the end plugs. The yoke structure consisted of two streamlined aluminum sections welded together via a box-beam at their upper ends, to form an inverted "U" shape. Rectangular end-plates extending five diameters downstream were designed according to Stansby's specifications [72], and mounted to the lower ends of the yoke arms. One of these arms contained the force transducer used to measure the loads acting on the model, while the opposite arm contained a "dummy" spacing block similar in size to the force transducer. The cylinder specimen to be tested could be assembled in the yoke by momentarily spreading apart the yoke arms, so allowing the model to "click" into place. A very small annular clearance of less than 1 mm was maintained between the cylinder and the end-plates.

The apparatus described above was specifically designed with the objective that several different cylinder models could be tested with the minimum of retooling effort. Chapter 4 describes the results of tests conducted on models of a "haired-fairing" cable, a six-strand wire rope, a chain, and an oil production riser. All of these models had identical lengths and end fittings, and similar diameters and masses. The haired-fairing cable model was

| <i>Model</i> | <i>Construction</i> | <i>Diameter (cm)</i> | <i>Mass (kg)</i> |
|----------------|---------------------|----------------------|------------------|
| Cylinder | Aluminum | 2.54 | 0.24 |
| D-Section | Wood/Epoxy | 5.08 | 0.37 |
| Wire Rope | Carbon-fiber | 2.70 | 0.32 |
| Chain | Aluminum | 2.30 | 0.23 |
| Riser | Aluminum | 2.54 | 0.37 |
| Haired-fairing | Aluminum/Kevlar | 3.05 | 0.56 |

Table 2.1: Details of the various models tested in the oscillating apparatus.

constructed with an actual sample of the haired-fairing cover wrapped around an aluminum tube. The wire rope model consisted of carbon-fiber reinforced plastic, and was made from a mold of an actual specimen of steel wire rope. The chain model was constructed from lightweight aluminum chain welded at the links to provide a single, stiff structure. The riser model consisted of the original 2.54 cm aluminum tube, with two smaller 0.635 cm tubes arranged in a diametrically opposed fashion so as to represent "kill" and "choke" lines. Table 2.1 summarizes the pertinent details of the models built for the oscillating apparatus.

Vertical oscillations of the yoke structure were obtained with the use of a LINTECH lead-screw positioning table, of total stroke length 17.8 cm. The base of this device was mounted vertically on the test tank carriage, with the yoke in turn bolted to the movable plate. The lead-screw was driven in a reciprocating manner by a SEIBERCO H3430 Sensorimotor, which was selected after a careful survey of the available motor products. A program was developed to calculate the desired motor characteristic (torque versus speed curve) for the maximum desired oscillation amplitude and frequency, considering such factors as inertial loads, fluid drag, gravity, etc. An unanticipated outcome from these calculations was that the limiting factor in motor capability was the rotor inertia of the motor, with the result that larger motors were not necessarily more suitable for our application. The Sensorimotor was selected so as to combine the benefits of step motors (high torque in a small package) with those of DC servo motors (high speeds and acceleration, and inherent closed-loop control). Figure 2-3 shows the calculated torque versus speed curves for the design condition (3.05 cm amplitude, 5.6 Hz frequency) as well as the manufacturer's motor characteristic for the SEIBERCO H3430.

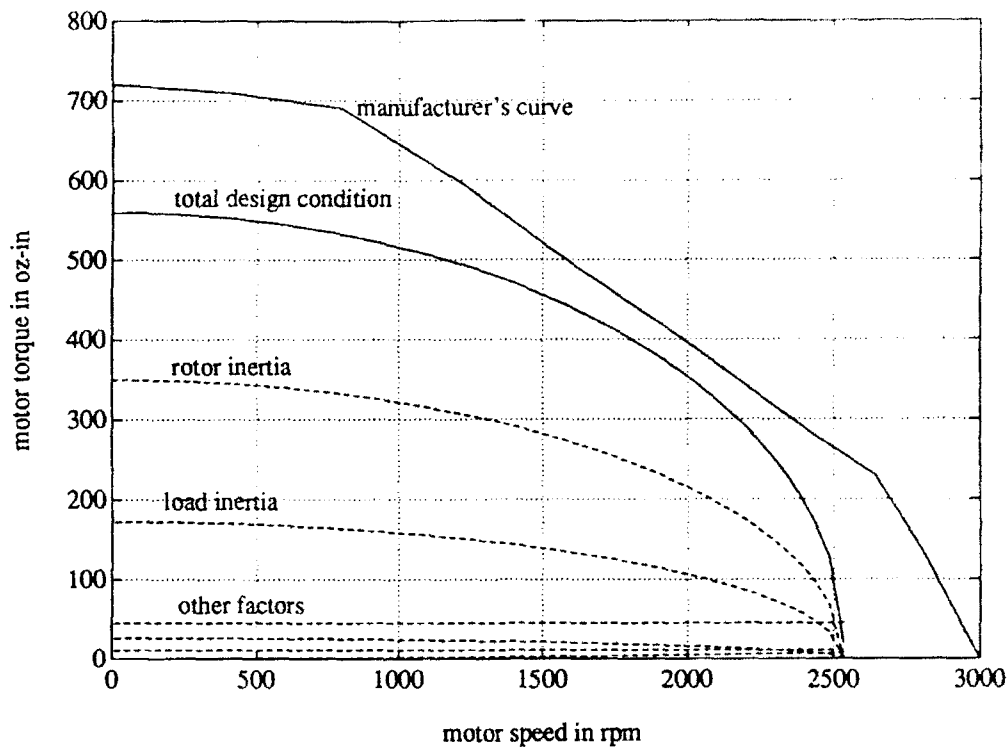


Figure 2-3: Design torque versus speed factors and the manufacturer's curve for the SEIBERCO H3430 Sensorimotor.

Control of the SEIBERCO motor was straightforward since its microprocessor based servo controller was custom-built by the manufacturer so as to track an analog input signal, with a given signal voltage corresponding to a particular absolute position of the motor shaft. Thus oscillations of any shape could be achieved simply by supplying the desired (appropriately scaled) waveform to the motor controller. In our implementation, the desired position waveform was calculated in real time by an NEC Powermate 286 PC-class computer (located in the laboratory office) from an initial user-specified set of parameters, generated with the help of an onboard 12-bit D/A converter, and communicated to the motor via the tank's data cable. The "master" program used to generate the waveform was developed by this author, and in addition to motion control, provided the main timing sequence for all experimental operations such as carriage motion switching and data-acquisition triggering.

2.2.4 Force and motion sensors

The lift and drag forces acting on the model were measured using a highly accurate and mechanically stiff piezoelectric force transducer, borrowing this concept from the experimental work of Staubli [74, 75]. The specific sensor we used was a KISTLER Model 9117 3-axes force transducer, constructed from quartz piezoelectric material that builds up an electric charge in response to an externally applied force. The sensor was connected via specially developed low capacitance cables to a charge amplifier, which converted the electrical charge to a conveniently measurable analog voltage. The Model 9117 is designed to measure force along 3 axes; for our experiments we utilized two of these to measure the lift and drag forces. The principal advantage of such a transducer is that unlike strain-gage-based devices, there is no physical displacement (strain) in response to the applied forces. Hence the transducer can be used in a relatively rigid assembly to measure a relatively small force, and natural frequencies of the test apparatus can be kept well above the range of interest.

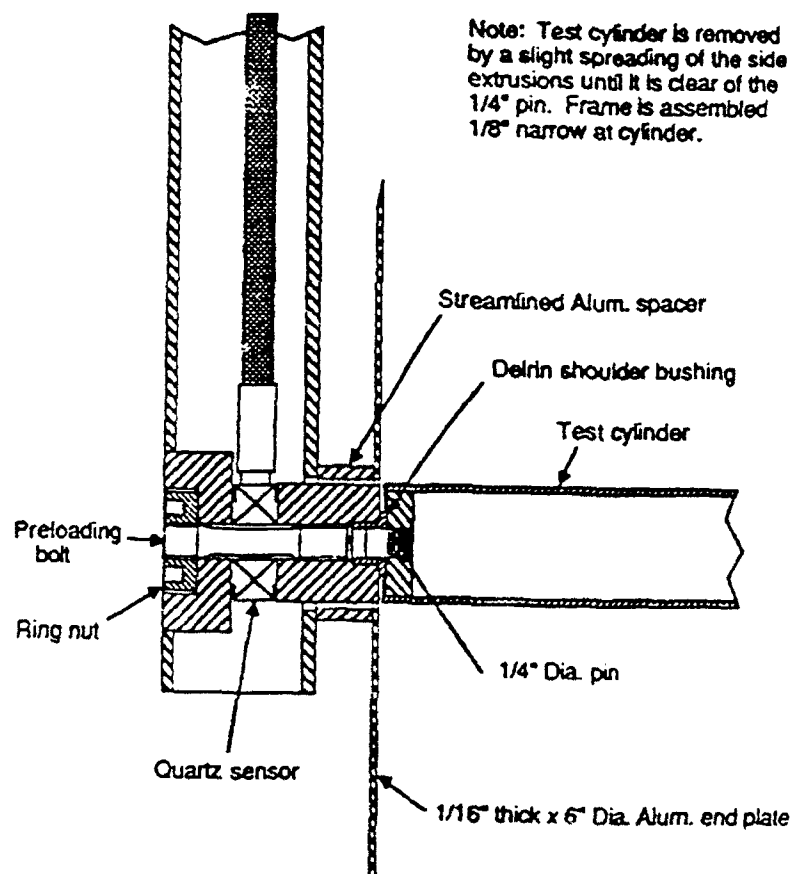


Figure 2-4: The force sensor assembly and model attachment.

Piezoelectric force transducers are expensive, delicate devices, and great care was required in the utilization of the KISTLER 9117. Electrical insulation was of paramount importance, and hence we carefully waterproofed the entire length of the sensor leads with a combination of silicone RTV compound and shrink-wrap tubing. Prior to installation in the yoke, the waterproofed sensor was repeatedly tested by submersion in 1 m of water for periods up to eight hours; no deterioration in performance was detected. The 9117 was installed in one of the yoke arms, rigidly bolted in place. Figure 2-4 is a diagram of the force transducer assembly, and shows details of the model attachment as well.

Following the assembly of the KISTLER 9117 in the yoke and the installation of the model, extensive static calibrations were carried out in both drag (X) and lift (Y) directions by hanging known weights from the center of the model. The remarkable linearity of the sensor is demonstrated by the typical calibration curve shown in Figure 2-5. In addition to static force calibration, the spatial linearity of the assembly and the dynamic characteristics were also determined. Known weights were attached at various points along the length of the cylinder, and the measured force compared with the calculated reaction force assuming linear simply-supported beam behavior. The deviation from this ideal behavior was found to be less than 1.5% over the range of loads expected. Dynamic oscillation tests were conducted in air at typical frequencies and amplitudes of interest, and the frequency response of the force sensor / charge amplifier system was verified to be unity in this range.

Force calibrations as outlined above were carried out prior to the experimental runs. While the experiments were in progress, the behavior of the system was monitored by conducting stationary drag tests at periodic intervals. The results of these "wet calibrations" indicated that there was no calibration drift with time. Further details are provided in Chapters 3 and 4, in the sections on stationary results.

In addition to the lift and drag forces, a third data channel was utilized to record the instantaneous displacement of the cylinder yoke. A SCHAEVITZ Linear Variable Differential Transformer (LVDT) Model HR 3000, with a linear range of $\pm 7.62\text{cm}$ was used to measure the displacement. The response of the LVDT was calibrated both on the laboratory bench, against a finely graduated scale, as well as after installation, using the vertical lead-screw actuator to move known distances. In order to test the dynamic phase characteristics of the LVDT, a contact switch was rigged so as to provide a momentary pulse when the yoke was at the top-dead-center while oscillating at a given amplitude. By comparing a train

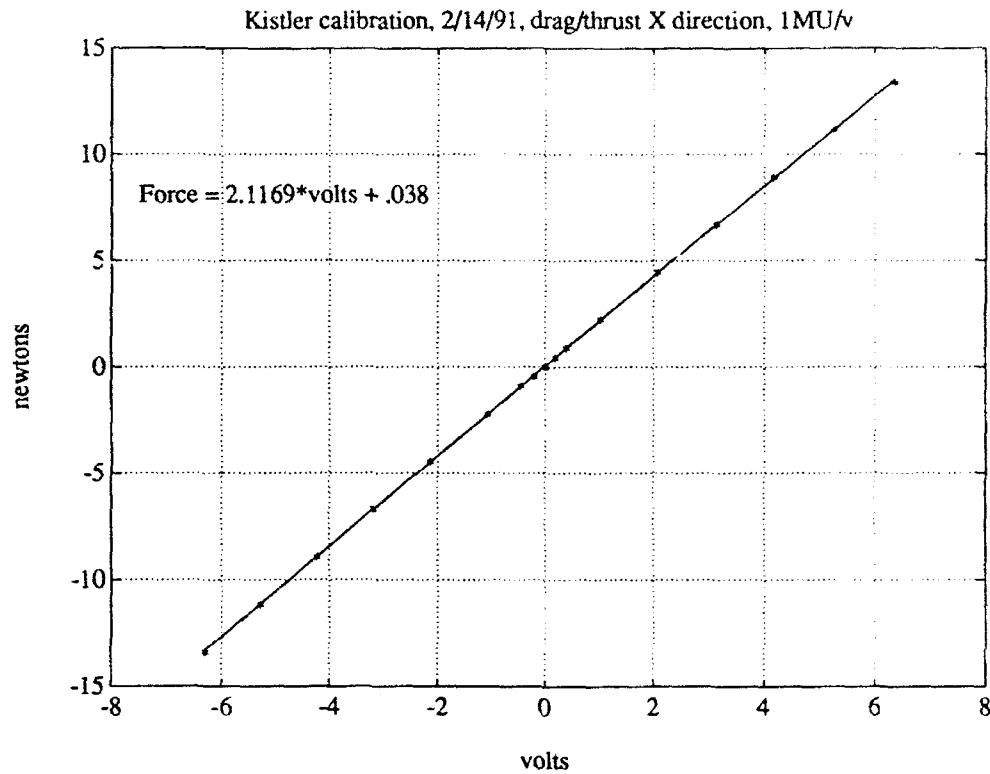


Figure 2-5: A typical static force calibration curve.

of these pulses with the output of the LVDT, it was verified that the device provided an accurate representation of the oscillation over the desired frequency range.

2.2.5 Signal conditioning and data acquisition

Both the KISTLER force transducer and the SCHAEVITZ LVDT were operated with their respective dedicated signal conditioning devices, the charge amplifiers (KISTLER Model 5004) in the case of the force transducer, and a detector/amplifier model ATA 101 in the case of the LVDT. These amplifiers were located on the test tank carriage, so as to be as close as possible to the sensors. The high level analog voltages output from the amplifiers were sent back to the laboratory control room, through the test tank data cable connecting the control room to the carriage. From the data cable termination in the control room, the signals were passed through a set of precision matched lowpass analog filters so as to prevent aliasing. The filters used were built from FREQUENCY DEVICES 4-pole butterworth lowpass modules with a cutoff frequency of 100 Hz, and specifically rigid tolerances on phase- and amplitude- matching.

Following the analog filtering stage, the signals were led to an HP Vectra ES/12 PC-class computer equipped with a COMPUTER BOARDS type CIO-AD16 analog-to-digital accessory plug-in board. A COMPUTER BOARDS type CIO-SSH16 simultaneous sample and hold front end accessory package was used with the plug-in board so as to avoid any contaminating channel-to-channel phase shifts. A commercially available software package, STREAMER, was used to perform the A/D conversions and "stream" the data directly to the hard disk of the ES/12. Each data run lasted for 75 seconds, during which time each channel was sampled at 500 Hz. As mentioned in section 2.2.3, the triggering for each run was controlled by the "master" program running on a separate computer.

In addition to the computer-based data acquisition system, an HP 54501A digital storage oscilloscope was used during the experimental setup and actual runs to monitor the signals at various locations in order to ensure proper operation of the different components.

2.2.6 Miscellaneous system effects

With the yoke assembled to the carriage and the model mounted in the yoke, the natural frequency (in water) of the overall system was determined. Spectral analysis of the measured forces was performed while the carriage, yoke and test specimen were repeatedly excited with a rubber mallet. This revealed that the principal natural frequency component of the structure was at 110 Hz, well out of our region of interest. Other spectral components were detected as low as 17 Hz, but these were 3 to 4 orders lower in magnitude, and spectral analysis of actual experimental data showed no effect from these lower structural frequencies.

In order to evaluate the effect of water flowing up and down *inside* the yoke arm supporting the force transducer, as well as the dynamic effect of the transducer mass, a number of runs were conducted in still water with the model removed. These tests revealed that there was, in fact, a substantial spurious force contribution from these effects. Tests at various amplitudes and frequencies indicated that this extraneous force was entirely in the inertial lift direction, and could be represented very well as an additional "virtual mass" of 0.188 kg. Thus this value was taken into consideration in the calculation of an additional inertial force to be subtracted from each lift force trace during post-processing.

Due to the fact that the KISTLER piezoelectric force transducer used in the experimental setup was essentially a dynamic measuring instrument, the mean drag force traces

exhibited a small, yet definite, drift. To correct for this effect, careful zero measurements were taken at both start and finish of every run. These zero measurements were utilized during post-processing to evaluate the drift and compensate for it.

2.2.7 Flow considerations

End effects

In order to avoid three-dimensional effects stemming from the finite length of the cylinder, thin aluminum end-plates of dimension 21 cm square were installed at the ends of the model. The end-plates were structurally attached to the yoke, with a small annular gap maintained between the plates and the cylinder, so as to not interfere with the measurement of the fluid forces. As mentioned in section 2.2.3, the end-plates were asymmetric fore-and-aft, extending about three diameters upstream and about five diameters downstream of the model.

In order to evaluate the efficacy of the end-plates in maintaining two-dimensionality of the flow, runs were conducted to measure the stationary (no cylinder oscillation) mean drag with and without the end-plates. The removal of the end-plates caused a 20% decrease in the mean drag coefficient, consistent with the conclusion of Stansby [72] that an increase of the (negative) base pressure occurs when the two-dimensionality of the flow around a circular cylinder is destroyed. With the end-plates installed, the stationary mean drag coefficient was constant at a value near the classical 1.20.

Free-surface effects

During these experimental runs, care was taken in the selection of the carriage towing speeds and yoke oscillation amplitudes to avoid the effects of free-surface interactions. In a series of tests conducted during 1990 in connection with oscillating hydrofoils [85], force measurements and visual observations were used to evaluate the regions of significant free-surface wave effects. The towing speed and vertical motions used in the present investigation were well below the critical ranges found earlier.

Bishop and Hassan [5] have used the criterion that the maximum Froude number

$$F_{max} = \frac{U_{max}}{\sqrt{gh_{min}}}$$

be much less than unity, for free-surface effects to be neglected. Here U_{max} is the maximum flow (towing) velocity, g the acceleration due to gravity, and h_{min} the minimum depth of submergence of the model. In their experiments, F_{max} was calculated to be 0.375, which Bishop and Hassan felt was sufficiently low. In our experiments, the maximum Froude number F_{max} was 0.181, so we are indeed justified in neglecting the effect of the free-surface.

Blockage effects

"Blockage" refers to the fact that the force coefficients measured on a cylinder model in a finite body of water is different from the values expected in an infinite stream, due to the presence of the walls of the channel around the model. Empirical blockage corrections are applied to the measured forces, and these corrections are a function of the equivalent blocking ratio d/h , or the ratio of the cylinder diameter to the total depth. In our case, this blocking ratio was only of the order of 2%, and so no corrections have been applied.

2.2.8 Overall accuracy of the experimental apparatus

In order to evaluate the error bounds on our data, it would be desirable to estimate the accuracy of the experimental apparatus, and hence the accuracy of the raw data. However, due to the large number of variables involved, such a value is impossible to determine. Each of the individual components in the experimental system described in the preceding sections has a nominal error bound which is usually 1-2%, and in no case exceeds 5%. The manner in which these combine to give an overall system error bound is unknown, and thus the overall system accuracy cannot be calculated from a knowledge of the individual component specifications. This situation has not changed much since the days of Bishop and Hassan [5], when they said:

"It would be extremely difficult, and probably not very sensible, to specify an overall accuracy, since this depended on so many factors. Thus it depended on the accuracy of hydraulic measurements, of the transducer-amplifier-pen recorder system, of the blockage correction, the evenness of fluid flow, variations in velocity along the cylinder, variations in the speed of the driving motor, length of oscillograph record used and on several other factors. The difficulty has been experienced by all the workers already mentioned; it can only be said

that due care was taken in the design of the apparatus, and in making and recording the results."

In fact, we did carry out an error analysis based on the statistical properties of the data spread and comparisons with published literature, this analysis is given in Chapter 4. As noted in that chapter, the overall *precision* of our data was of the order of 3-8%, and the overall *accuracy* was of the order of 10-15%.

2.3 Formulation and definitions

As mentioned earlier, our experiments are essentially an extension to the pure harmonic tests conducted in the past. As such, the mathematical statements and definitions formulating the problem are straightforward. The essential equations are developed here, with refinements and additional details provided as necessary in later chapters.

2.3.1 Stationary cylinder

For a *stationary* cylinder exposed to a flow, vortices are shed at the Strouhal frequency f_s given by the relation

$$f_s = \frac{SU}{d} \quad (2.1)$$

where U is the velocity of the flow and d is the diameter of the cylinder. The Strouhal number S , is essentially a nondimensional frequency approximately equal to 0.2 over the Reynolds numbers of interest to us. Due to the vortex shedding, the cylinder experiences an oscillating lift force at the frequency of shedding, an oscillating drag force at twice the frequency of shedding, and a mean drag force. Thus the lift force is given by

$$L = L_s \sin(2\pi f_s t + \phi_s) \quad (2.2)$$

and the drag force by

$$D = D_m + D_s \sin(2\pi(2f_s)t + \psi_s) \quad (2.3)$$

where L_s and D_s are the magnitudes of the oscillating Strouhal lift and drag forces respectively, D_m is the magnitude of the mean drag force, and ϕ_s and ψ_s are arbitrary phase angles. Each of the force components can be nondimensionalized in the usual manner by

the dynamic pressure head factor $\frac{1}{2}\rho l d U^2$ (where ρ is the density of water, and l is the length of the cylinder) to give the associated force coefficient. Thus the lift coefficient is

$$C_{L_s} = \frac{L_s}{\frac{1}{2}\rho l d U^2} \quad (2.4)$$

and the mean drag coefficient is

$$C_{D_m} = \frac{D_m}{\frac{1}{2}\rho l d U^2} \quad (2.5)$$

and the oscillating drag coefficient is

$$C_{D_s} = \frac{D_s}{\frac{1}{2}\rho l d U^2} \quad (2.6)$$

2.3.2 Sinusoidal cylinder oscillations

When a cylinder responds with or is externally subjected to *sinusoidal* oscillations, the body motion introduces an additional frequency component in the wake that competes with the Strouhal frequency. Depending on the amplitude and frequency of the cylinder oscillations, the wake response may be *locked-in*, a state wherein the cylinder motion controls the shedding process and the Strouhal frequency disappears. In general, however, the forces experienced by the body will have components at both the Strouhal and body oscillation frequencies. Thus if the body oscillation $y(t)$ at the frequency f_0 is given by

$$y(t) = Y_0 \sin(2\pi f_0 t) \quad (2.7)$$

we may model the lift force by

$$L = L_0 \sin(2\pi f_0 t + \phi_0) + L_s \sin(2\pi f_s t + \phi_s) \quad (2.8)$$

and the drag force by

$$D = D_m + D_0 \sin(2\pi(2f_0)t + \psi_0) + D_s \sin(2\pi(2f_s)t + \psi_s) \quad (2.9)$$

where L_0 and D_0 are the magnitudes of the oscillating lift and drag forces at frequencies f_0 and $2f_0$ respectively. For our purposes, we shall ignore the Strouhal components $L_s \sin(2\pi f_s t + \phi_s)$ and $D_s \sin(2\pi(2f_s)t + \psi_s)$ in equations 2.8 and 2.9. There are two reasons

by which we may justify this omission; firstly, we are interested in the response of the cable that is "locally locked-in" everywhere, and hence these Strouhal components disappear; secondly, since there is no body oscillation at the frequency f_s , these components do not participate in any *power transfer* between the body and the fluid. It may be argued that if the Strouhal lift force L_s exists and is of sufficient magnitude, the cable may begin to respond to both the frequencies f_s as well as f_0 ; the counter to this argument is that this scenario is precisely a case of the beating oscillations that will be treated next.

Equations 2.8 and 2.9 thus give us the following force coefficients in addition to the mean drag coefficient of Equation 2.5:

$$C_{L_0} = \frac{L_0}{\frac{1}{2}\rho l d U^2} \quad (2.10)$$

and

$$C_{D_0} = \frac{D_0}{\frac{1}{2}\rho l d U^2} \quad (2.11)$$

In the case of the lift coefficient, the phase angle ϕ_0 between the lift force and the body motion is crucial in determining the precise action of the lift force; whether it acts to excite or damp the body motion, and the magnitude of the inertial force or "added mass" effect. The component of the lift coefficient in phase with body velocity, given by

$$C_{L-V_0} = C_{L_0} \sin \phi_0 \quad (2.12)$$

determines the exciting or damping effect. Positive values of C_{L-V_0} denote an exciting effect, or power transfer from the fluid to the body, while negative values denote a damping effect, or power transfer from the body to the fluid. Likewise, the component of the lift coefficient in phase with body acceleration, given by

$$C_{L-A_0} = C_{L_0} (-\cos \phi_0) \quad (2.13)$$

determines the inertial added mass force; with positive values of C_{L-A_0} denoting negative added mass and *vice versa*. It should be noted that the coefficients C_{L-V_0} and C_{L-A_0} are precisely the negative of the coefficients C_{dh} and C_{mh} derived by Sarpkaya from a consideration of the Morison's equation for the forces acting on an oscillating cylinder [65].

Further details on the derivation and use of these coefficients are given in Chapter 3.

In the case of the oscillating drag, the coefficient C_{D_0} at the frequency $2f_0$ is often very small, and comparable in magnitude to other frequency components of less obvious origin. Thus several researchers have found it convenient to express the oscillating drag force in term of the RMS value of the fluctuating drag, thus leading to a coefficient $C_{D_{RMS}}$ instead of C_{D_0} .

In addition, it should be noted that the body oscillation frequency f_0 (expressed in Hz) is conveniently nondimensionalized in a manner analogous to equation 2.1 defining the Strouhal frequency. Thus

$$f_0 = \frac{\hat{f}_0 U}{d} \quad (2.14)$$

where \hat{f}_0 is the nondimensional oscillation frequency. The reciprocal of \hat{f}_0 is equivalent to the *reduced velocity* V_R , commonly used in studies of flow-induced vibrations.

2.3.3 Beating cylinder oscillations

The simplest case of *amplitude-modulated* cylinder oscillations is dual-frequency *beating*, which can be expressed in two mathematically equivalent ways. The first is a superposition of two sinusoids at different frequencies f_1 and f_2 (hence the term “dual-frequency beating”):

$$y(t) = Y_1 \sin(2\pi f_1 t) + Y_2 \sin(2\pi f_2 t) \quad (2.15)$$

If $Y_1 = Y_2$, the above equation 2.15 can be written as the product of a rapidly varying sinusoid at the “carrier frequency” f_c modulated by a slowly varying sinusoid at the “modulation frequency” f_m as

$$y(t) = 2Y_1 \sin(2\pi f_c t) \cos(2\pi f_m t) \quad (2.16)$$

The frequency components in the above equations 2.15 and 2.16 are related to each other as follows:

$$f_c = \frac{f_2 + f_1}{2} \quad (2.17)$$

$$f_m = \frac{f_2 - f_1}{2} \quad (2.18)$$

$$f_1 = f_c - f_m \quad (2.19)$$

$$f_2 = f_c + f_m \quad (2.20)$$

The rate of modulation is expressed in terms of the *modulation ratio*, which is defined here as the ratio of unity to “the number of oscillations at the carrier frequency contained in one beat packet”. Thus if the modulation ratio is equal to $1:N$, N is given by

$$N = \frac{1}{2} \frac{f_c}{f_m} \quad (2.21)$$

As an aside, it may be noted that the waveforms defined by equations 2.15 or 2.16 are referred to in electrical engineering parlance as examples of “Suppressed Carrier Amplitude Modulation”, or SC-AM. Details of the creation, manipulation and use of such waveforms may be found in basic Signals and Systems texts such as the one by Siebert [70].

For a cylinder oscillating with a waveform given by equations 2.15 or 2.16, the challenge is to define the induced lift and drag forces in terms of force coefficients that are consistent with experimental observations, and in addition, can be estimated from available sinusoidal data. As we shall see, meeting these two requirements, especially the second, is often not possible.

In the case of the lift force acting on a beating cylinder, a straightforward extrapolation of equation 2.8 to the dual-frequency situation gives the following expression for lift coefficient:

$$C_L = C_{L1} \sin(2\pi f_1 t + \phi_1) + C_{L2} \sin(2\pi f_2 t + \phi_2) \quad (2.22)$$

where we have already performed the nondimensionalization with $\frac{1}{2}\rho l d U^2$ and ignored the Strouhal term in accordance with the discussion in the previous section. The phase angles ϕ_1 and ϕ_2 determine the components of C_{L1} and C_{L2} in phase with cylinder velocity and cylinder acceleration, yielding two exciting/damping coefficients C_{L-V1} and C_{L-V2} , and two inertial coefficients C_{L-A1} and C_{L-A2} , in a manner exactly equivalent to equations 2.12 and 2.13. As we shall see, it turns out that these lift coefficients and phase angles at the frequencies f_1 and f_2 are very difficult to estimate from pure sinusoidal data. In order to simplify the position by reducing the number of variables involved, we can define “equivalent lift coefficients” C_{L-Vc} and C_{L-Ac} at the carrier frequency f_c , based on equating the time-averaged power transfer and inertial force. More details on these coefficients will be given in the chapter on beating oscillations.

In the case of the beating drag force coefficient, an extrapolation of equation 2.9 gives the following expression for C_D :

$$C_D = C_{D_m} + C_{D_1} \sin(4\pi f_1 t + \psi_1) + C_{D_2} \sin(4\pi f_2 t + \psi_2) \quad (2.23)$$

where, as before, the nondimensionalization has been carried out and the Strouhal terms ignored. As it happens, an examination of the experimental data indicates that in addition to the oscillating drag coefficient components C_{D_1} at frequency $2f_1$ and C_{D_2} at frequency $2f_2$, there is a strong oscillating component at the modulation frequency f_m . The multiplicity of frequency components also indicates that the use of an RMS coefficient $C_{D_{RMS}}$ to quantify the fluctuating drag may be useful.

2.4 Data processing

As mentioned in section 2.2.5, the lift and drag force traces and cylinder motion trace were sampled at 500 Hz each by an HP Vectra ES/12 computer equipped with an analog-to-digital conversion board. The software used to accomplish this conversion stored the data in binary form on the hard disk of the ES/12. From here, the next step was to transfer the binary data files to a larger and more capable computer, either the laboratory's HP Vectra RS/20C 386 or HP Vectra EISA 486. All of the binary data files were backed up onto magnetic tape for precautionary storage prior to processing.

The first stage in data reduction involved translating the binary data to ASCII numbers; this was accomplished with software accompanying the data acquisition package. The ASCII files were then passed through a digital time-domain noncausal lowpass filter in order to remove unwanted high frequency noise. This filter consisted of a Finite Impulse Response sinc function convolved with the input data according to the algorithm used by Triantafyllou [82]. The FIR parameters were calculated to provide a cutoff frequency of $2.2f$, where f , the "significant frequency" was one of the following:

1. The (estimated) Strouhal shedding frequency f_s for stationary runs.
2. The externally imposed oscillating frequency f_0 in the case of sinusoidal oscillations.
3. The higher of the two component frequencies, f_2 , in the case of beating oscillations.

Time-domain rather than frequency-domain filtering was employed because of the length of the data traces involved, and the filter resolution desired. Following the lowpass filtering, the data records were resampled at the lower sampling rate of 100 Hz in order to reduce storage and processing requirements.

Beyond the above initial data reduction, all further processing was accomplished using the software package MATLAB. Extensive batch programs and MATLAB functions were created so as to provide for semiautomatic processing with the minimum of subjective decision making. Some of the important steps in the data processing are detailed in the following paragraphs.

Calibration. A function was written to determine automatically whether data files loaded into MATLAB were pre- or post- calibration, and based on this decision, to calibrate the records according to the calibration values determined as in section 2.2.4. During this process, the data were also "de-trended" (to remove any sensor drift), and the mean zero values subtracted.

Lock-in determination. In order to determine whether or not a given cylinder oscillation led to lock-in, and to provide a qualitative understanding of the induced forces, power spectra of the data traces were calculated. In each case, a single 4096 point Fast Fourier Transform was used, with Hanning-window tapering employed to reduce spectral leakage. Since this method was not used to determine quantitatively the force coefficients, no further attempt was made to optimize the spectral estimation technique, nor to estimate the errors involved. In addition to power spectra, time-domain histogrammic analysis was used in a few cases to determine the lock-in behavior. Thus the points of upcrossing of the motion and lift force traces were determined, and histograms were created of the "instantaneous" frequencies. Further details on these methods are provided in Chapters 3 and 5, in the sections on histogrammic analysis.

Removal of inertial force. Prior to the calculation of the oscillating lift coefficient magnitude and phase angle, we subtracted the (in air) inertial force of the test cylinder from the lift force time trace. The inertial force trace was calculated by performing a double-differentiation of the motion (LVDT) signal to obtain the cylinder acceleration, and

then multiplying this acceleration trace by the cylinder mass in air. A centered-difference scheme was used to perform the differentiation. The lack of extraneous noise in the motion time traces (after the digital filtering step) allowed the double-differentiation to take place reliably and accurately.

Oscillating force coefficients. Quantitative determinations of the oscillating force coefficients and phase angles were made via individual Fourier-coefficient analyses. From basic Fourier series theory, a waveform $x(t)$ can be represented as a series

$$x(t) = a_0 + \sum_{n=1}^{\infty} a_n \cos\left(\frac{2\pi nt}{T}\right) + \sum_{n=1}^{\infty} b_n \sin\left(\frac{2\pi nt}{T}\right) \quad (2.24)$$

where the coefficients a_0 , a_n and b_n are given by

$$a_0 = \frac{1}{T} \int_0^T x(t) dt \quad (2.25)$$

$$a_n = \frac{2}{T} \int_0^T x(t) \cos\left(\frac{2\pi nt}{T}\right) dt \quad (2.26)$$

$$b_n = \frac{2}{T} \int_0^T x(t) \sin\left(\frac{2\pi nt}{T}\right) dt \quad (2.27)$$

In our case, one example is the lift force for sinusoidal oscillations, which, by expanding the first term on the RHS of equation 2.8 can be written as:

$$L = L_0 \cos(\phi_0) \sin(2\pi f_0 t) + L_0 \sin(\phi_0) \cos(2\pi f_0 t) \quad (2.28)$$

By constructing reference sine and cosine waveforms with period

$$T = \frac{1}{f_0} \quad (2.29)$$

we can readily identify the quantity $(L_0 \cos(\phi_0))$ with the coefficient b_1 given by equation 2.27, and the quantity $(L_0 \sin(\phi_0))$ with the coefficient a_1 given by equation 2.26. Thus if we calculate a_1 and b_1 , we can find L_0 and ϕ_0 from

$$L_0 = \sqrt{a_1^2 + b_1^2} \quad (2.30)$$

and

$$\phi_0 = \arctan \left(\frac{a_1}{b_1} \right) \quad (2.31)$$

Note that it is not necessary for the reference waveforms to have zero phase relative to the cylinder motion: if we carry out the above procedure for the motion trace as well as the lift force trace, we can readily find the actual phase angle ϕ_0 as the difference between the phase angles calculated between the lift force and the reference, and that calculated between the motion and the reference.

In determining the oscillating force coefficients and phase angles according to the procedure outlined above, a key factor was the number of cycles of the waveform over which the integrations given by equations 2.26 and 2.27 were carried out. Ideally, one would have liked to have performed these evaluations over as many cycles as possible, but in practice it was found that very small errors in frequency led to unacceptably large errors in the calculated coefficients. Thus a "time-gating" method was devised whereby the coefficients were calculated over a smaller number of cycles and averaged over as many gates as were available in the trace. A gate length of 20 cycles was found to give good results with both the harmonic and beating data traces. In passing, it should be noted that this time-gating Fourier series analysis was very similar to that performed by Mercier [47] in the analysis of his data.

Mean drag coefficient. The mean drag coefficient for each record was estimated by calculating the mean value of the drag force trace, relative to the zero values established at the start and finish of each run. As mentioned in section 2.2.6, these zero values were used to subtract out the drag force drift over the length of the data run, prior to the calculation of the mean drag coefficients. In the calculation of the mean drag value, care was taken to average the data over an integer number of oscillation cycles (or beat "packets", in the case of amplitude-modulated data).

Chapter 3

Stationary and Sinusoidal Oscillation Tests

3.1 The purpose of these tests

One of the principal frustrations besetting the researcher investigating vortex shedding phenomena is the sensitive dependence of measurable quantities on the experimental conditions. Thus the values of lift and drag force coefficients, pressure coefficients, and vortex shedding frequency all depend on experimental factors such as aspect ratio (l/d , where l is the length of the model and d its diameter), end conditions, blockage ratio (d/H , where H is the transverse dimension of the test facility), surface finish of the model, and so on. As a result of this situation, several researchers have spent a great deal of effort on attempts to quantify the effects of these experimental factors; this is not an undesirable research goal in itself, but is not one that is directly connected with the basic problem of vortex shedding and vortex-induced vibrations. In our case, we decided to conduct a thorough investigation of stationary and sinusoidal oscillations in order to provide a basis for comparison that could be used to relate the more ambitious beating motion program (conducted with the same apparatus) to standard sinusoidal results available in the literature. As we proceeded with our sinusoidal tests, it became clear that we had noticed and interpreted certain features of the vortex-induced forces that had not been reported in the literature thus far. Hence, we believe that our sinusoidal results include novel findings, in addition to providing experimental "ground-truthing" of the amplitude-modulated results.

3.2 Stationary results

Tests were conducted to measure the lift and drag force coefficients and the natural Strouhal shedding frequency on the stationary (non-oscillating) model cylinder towed through the water. In addition to the scientific benefit of this data, the stationary runs proved to be a valuable way of monitoring the performance of the experimental apparatus and systems, while the apparatus was in the water. One or two of these "wet calibrations" were conducted at the start and finish of each day's experimental schedule, and as presented in Chapter 4, the accumulated results provided a strong boost to our confidence in the overall process.

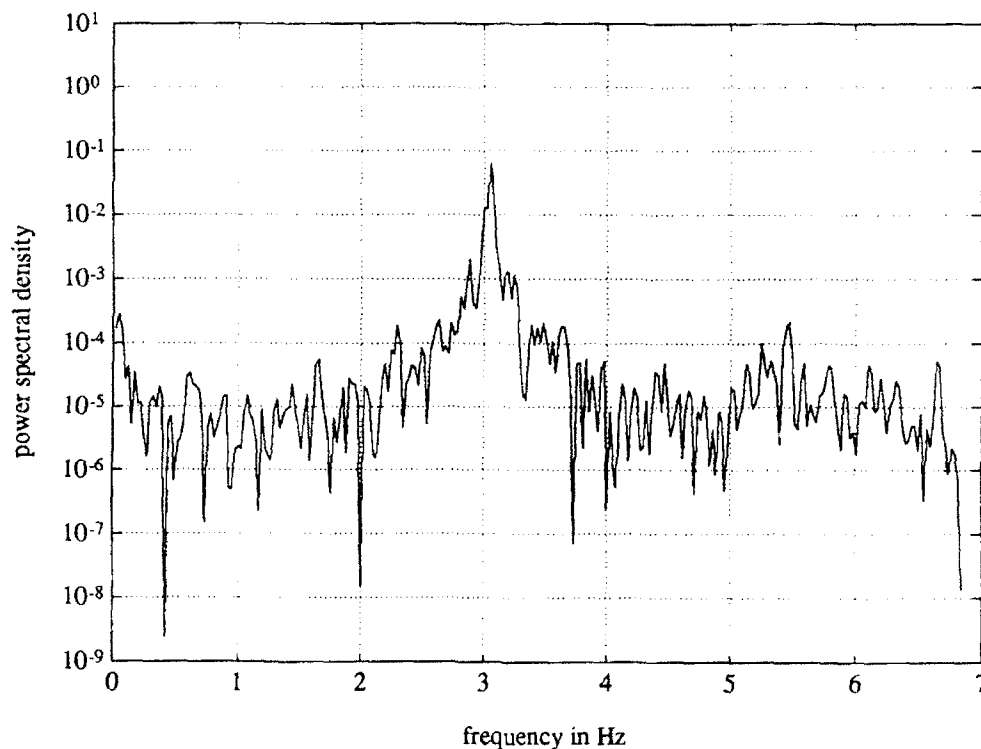


Figure 3-1: Power spectrum of a typical stationary lift force trace.

Data processing for the stationary runs was relatively straightforward. After initial data reduction (consisting of translation of the raw binary data to ASCII, lowpass filtering, decimation, and calibration), a spectral analysis was performed on each lift force time trace in order to determine the natural shedding frequency. The MATLAB routine "spectrum" was used to perform a 4096-point FFT with Hanning-window tapering. A power spectrum for a typical lift force trace is shown in Figure 3-1, where the sharp peak in the spectrum (over 3 orders of magnitude above the background noise) is identified with the natural

shedding frequency. The average nondimensional natural shedding frequency (Strouhal number) calculated from 122 stationary runs was found to be 0.1932, with a standard deviation of less than 1%.

In addition to the Strouhal number, the magnitudes of the mean and oscillating drag coefficients and the oscillating lift coefficient were estimated from the time traces. The mean drag coefficient C_{D_m} was calculated as being the (normalized) difference between the mean value of the drag force during the run period and the mean value during the final zero period. Figure 3-2 shows a histogram of the mean drag coefficient obtained for all the stationary realizations. This figure can be approximated as a normal distribution, with a mean of 1.1856 and a standard deviation of 0.0315, or under 3%. To compute the oscillating lift coefficient C_{L_s} , the experimentally obtained natural shedding frequency f_s was used to generate reference sine and cosine waveforms which were then used to estimate the Fourier coefficients of the lift force, as outlined in Chapter 2. Figure 3-3 is a histogram of the oscillating lift coefficient magnitude for the stationary runs; this can also be modeled as a normal distribution (mean 0.3842, standard deviation 0.0873), but with a much larger spread than that for the mean drag coefficient. In addition to C_{D_m} and C_{L_s} , the oscillating drag coefficient C_{D_s} was evaluated in a manner similar to the above, using twice the natural shedding frequency. Table 3.1 summarizes the results for the stationary (smooth circular) cylinder.

| | S | C_{D_m} | C_{L_0} | C_{D_0} |
|----------|--------|-----------|-----------|-----------|
| Mean | 0.1932 | 1.1856 | 0.3842 | 0.0215 |
| σ | 0.0014 | 0.0315 | 0.0873 | 0.0076 |

Table 3.1: Summary of results for the stationary circular cylinder; $Re = 10,000$

The explanation for the relatively large scatter of the oscillating lift and drag force coefficients, compared to the scatter of the mean drag coefficient, was found to be that these oscillating forces (integrated over the length of the model) were more sensitive to the three-dimensionality of the flow than was the mean drag force. It is well established that the correlation length of vortex shedding (the length over which the shedding process could be considered to be two-dimensional) for a *stationary* circular cylinder is of the order of 3 to 5 cylinder diameters (Blevins [7]). In our case, the aspect ratio of our models was

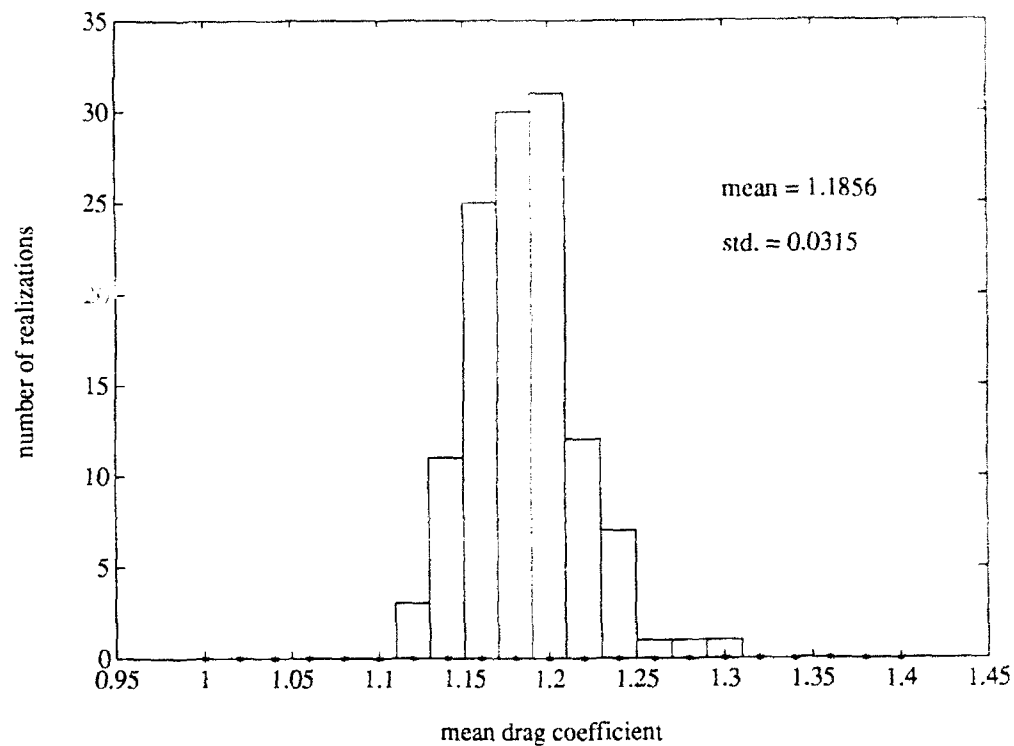


Figure 3-2: Histogram of the mean drag coefficient; stationary runs.

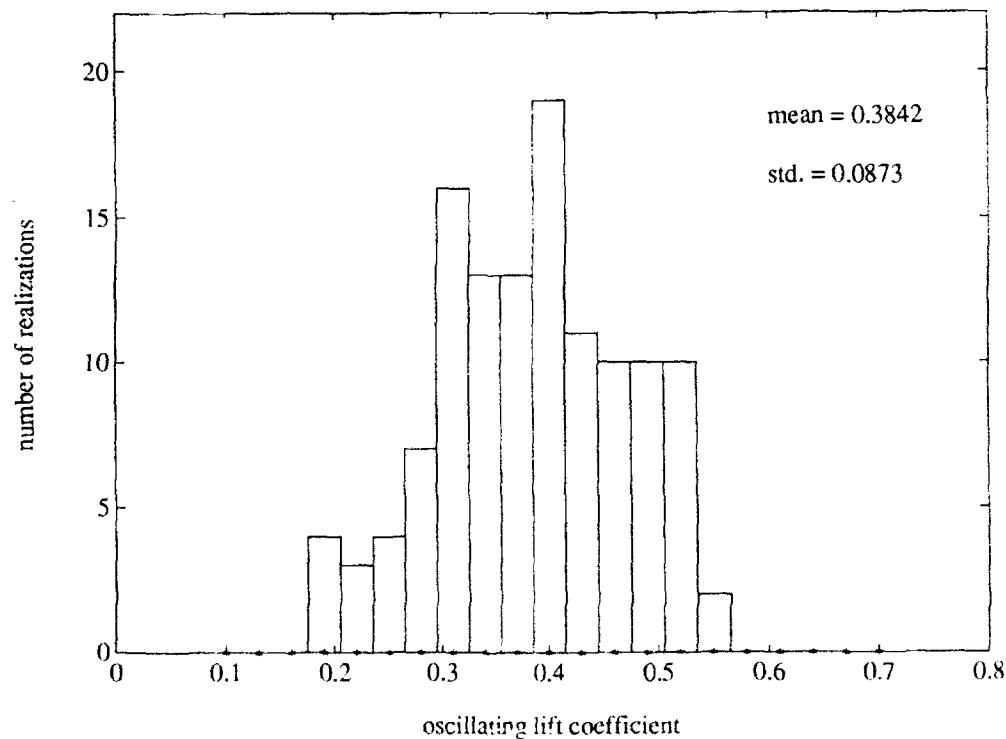


Figure 3-3: Histogram of the oscillating lift coefficient; stationary runs.

approximately 24, so the vortex shedding process *for the stationary runs* could not have been fully correlated along the model span. Figures 3-4 and 3-5 show time segments of a typical stationary drag force trace and the corresponding lift force trace. The segments have been chosen to include a few seconds of run data and a short bit of the final zero period. It is clear from Figure 3-4 that the oscillating drag force appears as relatively small scale fluctuations superimposed on the mean drag. The three-dimensionality of the flow appears as random, low-frequency modulations, which do not have a significant impact on the value of the mean drag. By contrast, Figure 3-5 shows that these random three-dimensional modulations have a relatively large effect on the amplitude of the oscillating lift force. The natural Strouhal shedding frequency is clearly evident; however the amplitude of the lift force at this frequency is widely scattered. As we shall see later in this chapter, forced oscillations of the model cylinder near the natural Strouhal frequency have the effect of dramatically reducing the random fluctuations of the oscillating vortex-induced forces.

3.3 Forced sinusoidal oscillations

Tests involving forced sinusoidal oscillations of the model cylinder were conducted at a large number of frequency and amplitude combinations. Fifty-one values of nondimensional oscillation frequency $\hat{f}_0 (= f_0 d/U)$ ranging from 0.05 to 0.35 were selected so as to bracket the natural Strouhal number. The actual oscillation frequencies f_0 were in the range from 0.80 Hz to 5.33 Hz. Each of these 51 oscillation frequencies were tested at 6 nondimensional amplitude ratios Y_0/d from 0.15 to 1.20, yielding actual oscillation amplitudes ranging from 0.381 cm to 3.048 cm. As mentioned in earlier chapters, the high degree of automation and reliability of our experimental apparatus and procedures enabled us to test this relatively large parameter space in a relatively timely fashion.

As in the case of the stationary run data, the analysis of the sinusoidal oscillation data consisted of initial data reduction followed by further analysis using MATLAB. As before, the mean drag coefficient was calculated as the difference between the mean value of the drag force trace during the run period and that during the final zero period, suitably nondimensionalized. Using the (known) external oscillation frequency, reference sine and cosine waveforms were created and used to calculate the magnitudes of the oscillating lift and drag forces. (As mentioned in Chapter 2, the oscillating force coefficients at the Strouhal

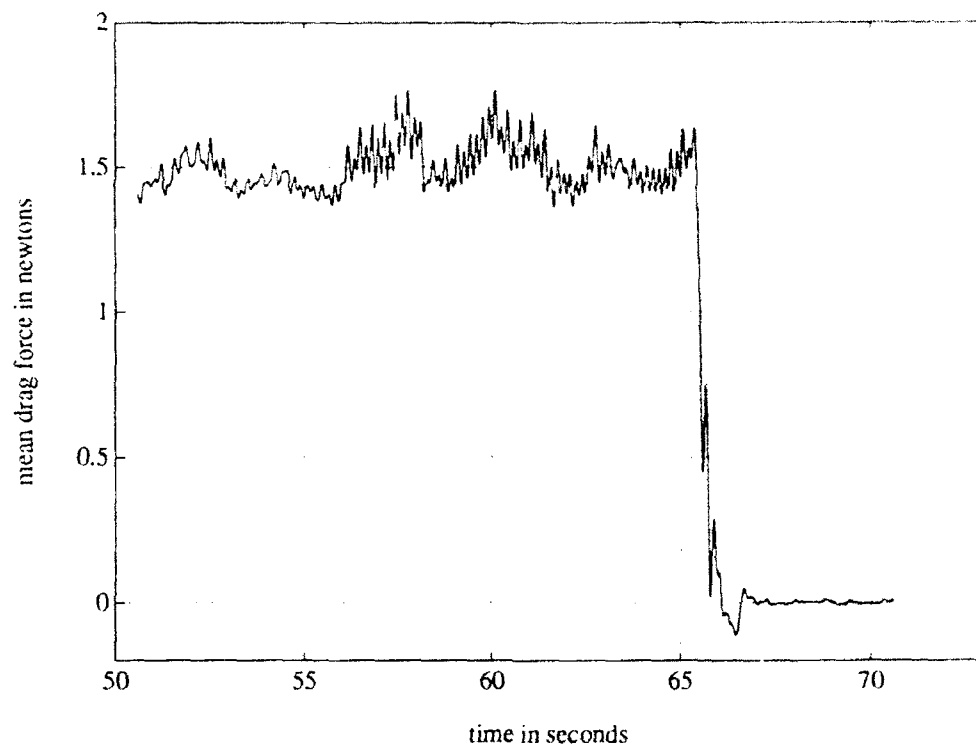


Figure 3-4: A time segment of a typical stationary drag force trace.

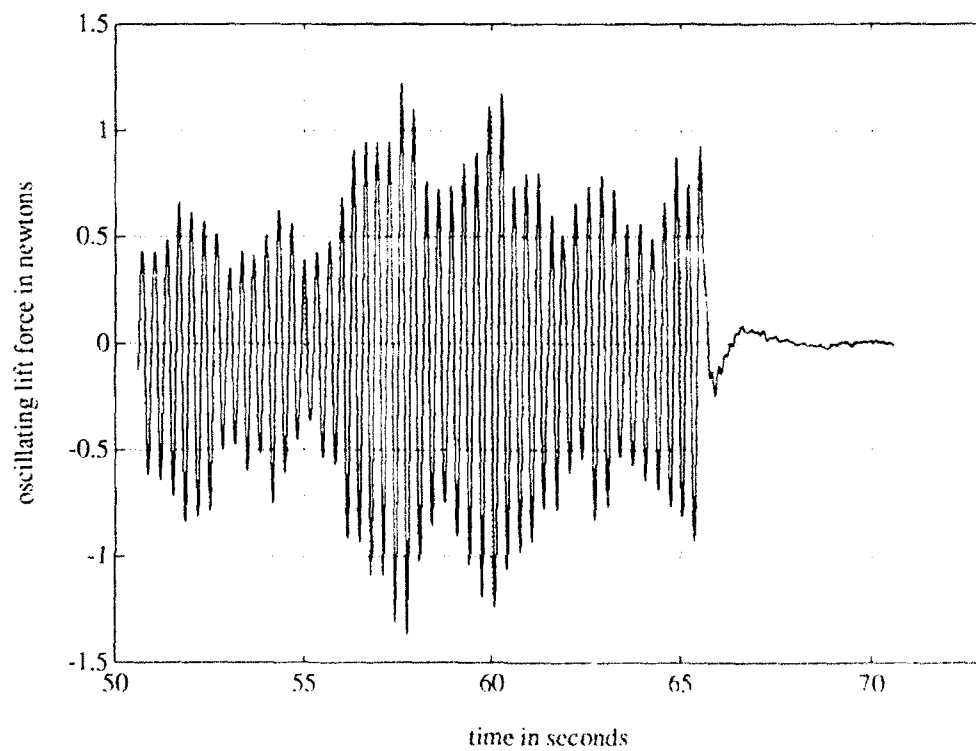


Figure 3-5: The time segment of the stationary lift force trace corresponding to the previous figure.

shedding frequency were not considered.) The phase angle of the oscillating lift force with respect to the externally imposed oscillating motion was calculated as the difference between the phase angle of the lift force (with respect to the reference sine waveform) and the phase angle of the motion (with respect to the same reference sine waveform). As described in the later sections of this chapter (Sections 3.4 - 3.7), certain of the sinusoidal oscillation cases were reprocessed using additional techniques.

In all of the data processing, several methods were used to minimize the risk of error. A comprehensive analysis of the errors in our data and results is presented in the next chapter.

3.3.1 Results for amplitude ratio 0.30

In order to illustrate the principal effects of sinusoidal oscillations, results are presented first for the moderate amplitude ratio of 0.30.

The variations of the mean drag coefficient C_{Dm} and the oscillating drag coefficient C_{Do} against nondimensional oscillation frequency \hat{f}_0 for $Y_0/d = 0.30$ are presented in Figure 3-6. At low oscillation frequencies, the mean drag coefficient is near the stationary cylinder value

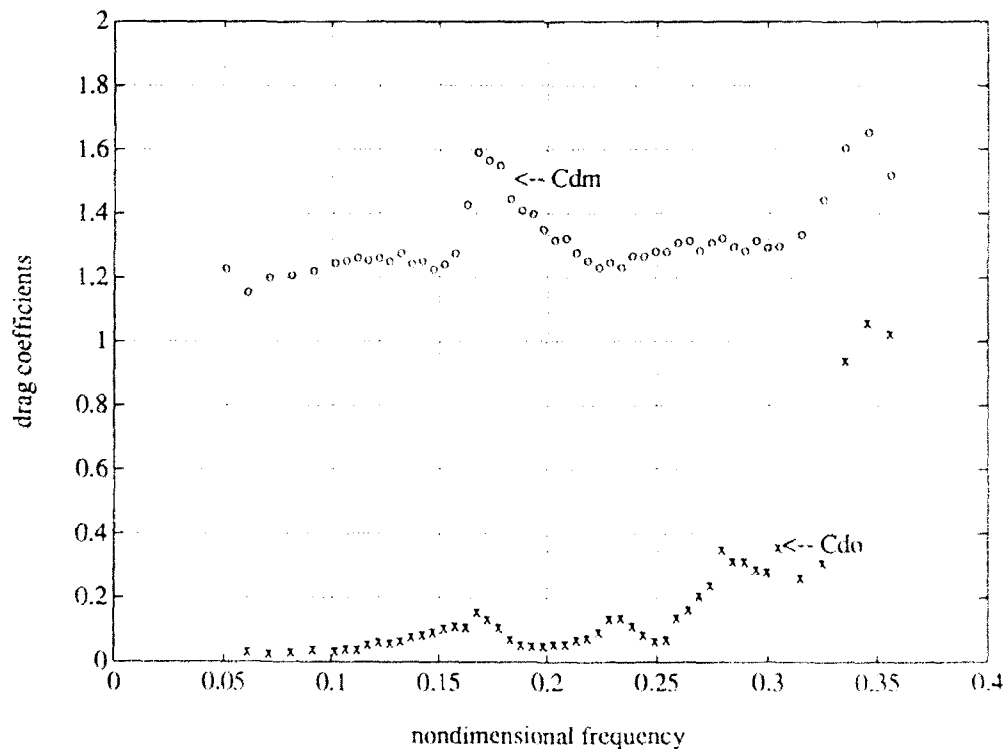


Figure 3-6: Mean and oscillating drag coefficients; sinusoidal oscillations; $Y_0/d = 0.30$.

of 1.20. A sharp amplification peak occurs at a nondimensional frequency of 0.17, slightly below the natural Strouhal frequency of 0.20. There is evidence of a second amplification peak near a frequency of 0.35. The oscillating drag coefficient C_{D_0} is less than 10% of the mean drag coefficient at the lowest oscillation frequencies, but rises rapidly at the higher end.

The behavior of the lift force for the same amplitude $Y_0/d = 0.30$ is illustrated in Figures 3-7 and 3-8. Figure 3-7 shows the dependence of the *magnitude* of the oscillating lift coefficient on oscillation frequency. At low frequencies, this lift coefficient magnitude is very small, but rises sharply and peaks (at a frequency of 0.18) due to resonance between the imposed oscillations and the natural Strouhal shedding process. As seen in the previous drag coefficient illustration, this resonance occurs at a nondimensional frequency slightly below the stationary Strouhal number. At higher frequencies the lift coefficient magnitude begins a steady rise, with the increase in this range being attributed to the effect of added mass. The behavior of the *phase angle* of the oscillating lift force is illustrated in Figure 3-8, where as defined in Chapter 2, this phase angle ϕ_0 is the angle by which the oscillating lift force leads the imposed oscillating motion. The importance of the lift force phase angle is that it determines the *sign of the power transfer between the cylinder and the fluid*. Values of ϕ_0 in the range $0 < \phi_0 < +\pi$ correspond to *power transfer from the fluid to the cylinder*, i.e. the cylinder could get excited into motion by the fluid flow. For an oscillation amplitude $Y_0/d = 0.30$, the phase angle is between 0 and $+\pi$ for the frequency ranges $0.125 < \hat{f}_0 < 0.182$ and $0.223 < \hat{f}_0 < 0.271$. These ranges define the primary and secondary excitation (resonant) regions respectively.

While the previous paragraph illustrated that the phase angle ϕ_0 could be used to find the *sign* of the power transfer between the fluid and the cylinder, the *magnitude* of this power transfer depends on both the phase angle as well as the lift coefficient magnitude. Specifically, the power transfer between the cylinder and the fluid is determined by the inner product of the lift force vector with the cylinder velocity vector. If the cylinder motion is given by $y(t) = Y_0 \sin(2\pi f_0 t)$ and the total lift force by $L(t) = L_0 \sin(2\pi f_0 t + \phi_0)$, then the power transfer $P(t)$ will be given by:

$$\begin{aligned} P(t) &= L_0 \sin(2\pi f_0 t + \phi_0) \cdot \frac{d}{dt} \{Y_0 \sin(2\pi f_0 t)\} \\ &= \{L_0 \sin(\phi_0) \cos(2\pi f_0 t) + L_0 \cos(\phi_0) \sin(2\pi f_0 t)\} \cdot 2\pi f_0 Y_0 \cos(2\pi f_0 t) \end{aligned}$$

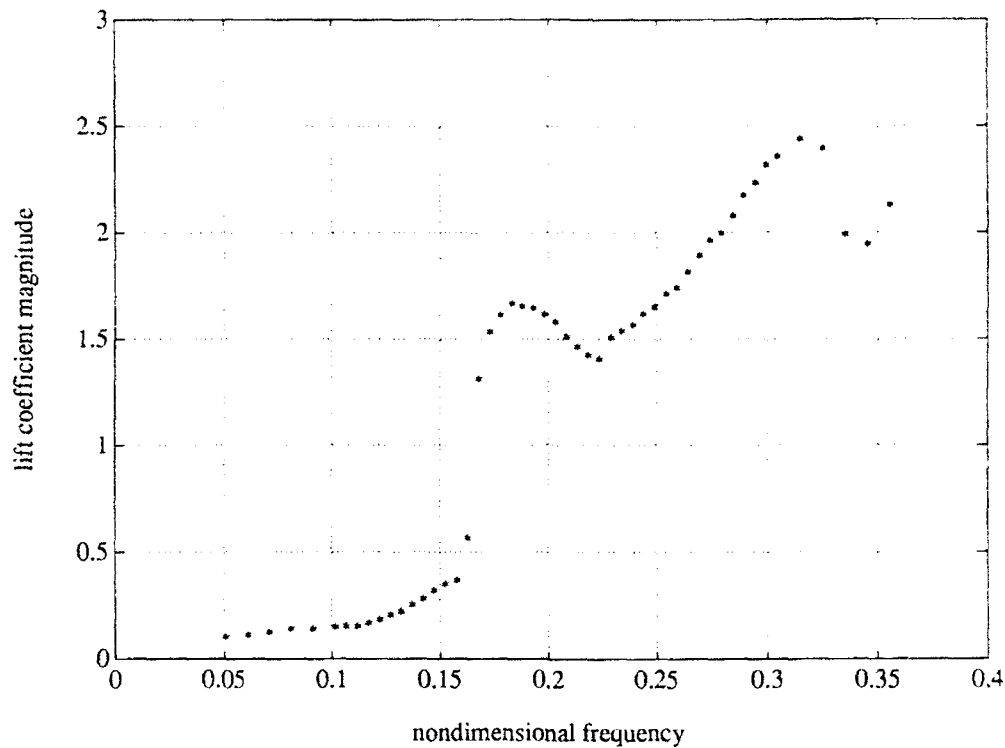


Figure 3-7: Lift coefficient magnitude; sinusoidal oscillations; $Y_0/d = 0.30$.

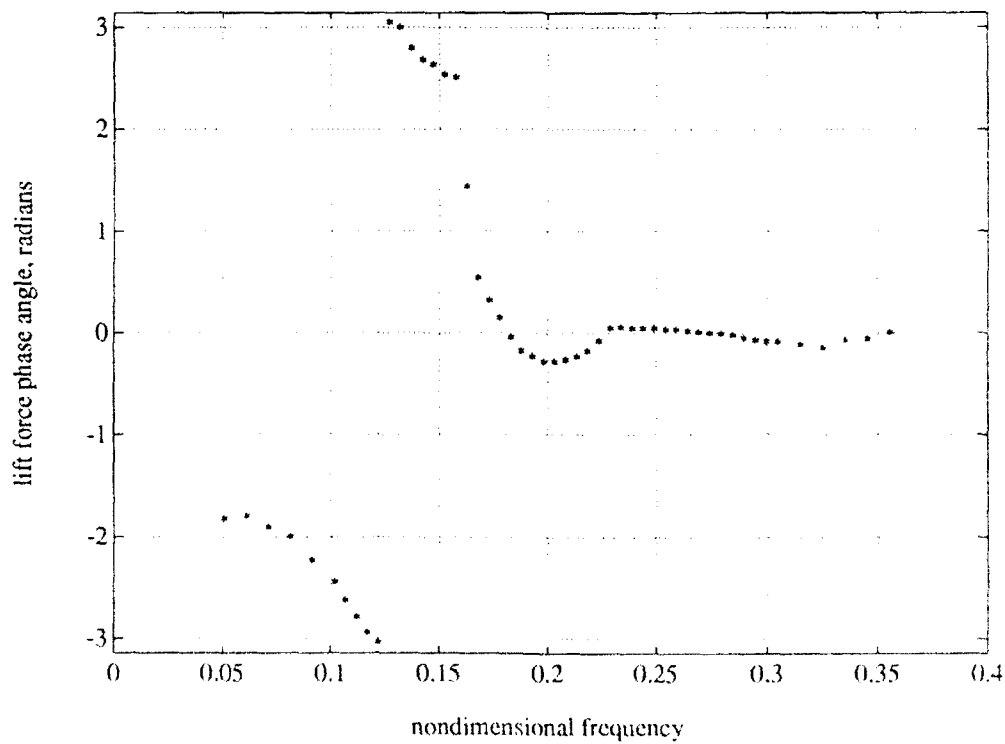


Figure 3-8: Phase angle of lift wrt motion; sinusoidal oscillations; $Y_0/d = 0.30$.

$$= 2\pi f_0 Y_0 L_0 \sin(\phi_0) \cos^2(2\pi f_0 t) + 2\pi f_0 Y_0 L_0 \cos(\phi_0) \sin(2\pi f_0 t) \cos(2\pi f_0 t) \quad (3.1)$$

The average value of the power transfer (over one or more cycles of oscillation) is given by

$$\begin{aligned} \langle P \rangle &= 2\pi f_0 Y_0 L_0 \frac{1}{nT_0} \int_0^{nT_0} \left\{ \sin(\phi_0) \cos^2(2\pi f_0 t) + \cos(\phi_0) \sin(2\pi f_0 t) \cos(2\pi f_0 t) \right\} dt \\ &= 2\pi f_0 Y_0 L_0 \left\{ \frac{1}{2} \sin(\phi_0) \right\} \\ &= \pi f_0 Y_0 \left\{ \frac{1}{2} \rho l d U^2 C_{L-V_0} \right\} \end{aligned} \quad (3.2)$$

where T_0 is the period of oscillation corresponding to the frequency f_0 , and n is an integer number of cycles. The nondimensional coefficient C_{L-V_0} , which determines the magnitude of the power transfer, is the lift coefficient in phase with cylinder oscillation velocity, i.e.

$$C_{L-V_0} = \frac{L_0 \sin(\phi_0)}{\frac{1}{2} \rho l d U^2} = C_{L_0} \sin(\phi_0) \quad (3.3)$$

The variation of C_{L-V_0} against nondimensional frequency \hat{f}_0 for the amplitude ratio $Y_0/d = 0.30$ is shown in Figure 3-9. Positive values of this coefficient denote positive power transfer to the cylinder, i.e. the cylinder extracts energy from the fluid. This power transfer serves to amplify the motion of the cylinder. As we shall see shortly, increased cylinder motion amplitude causes a reduction in the value of C_{L-V_0} , leading to eventual limit-cycle behavior of the cylinder oscillations. From Figure 3-9, the primary positive range of C_{L-V_0} ($0.125 < \hat{f}_0 < 0.182$) delineates the primary resonant region of the cylinder-wake interaction.

An analysis similar to Equations 3.1 – 3.3 can be performed to determine the *added mass* effect of the vortex-induced lift force. As we discussed in Chapter 1, early researchers (Bishop and Hassan [6], Protos *et al.* [60]) assumed a constant added mass coefficient (from potential flow theory) to account for the inertial component of the lift force. This, however, is an incorrect assumption, since the added mass coefficient varies with cylinder oscillation (Sarpkaya [65]). The correct value of the added mass (as a function of oscillation frequency and amplitude) must be determined by calculating the component of the measured lift coefficient in phase with cylinder acceleration.

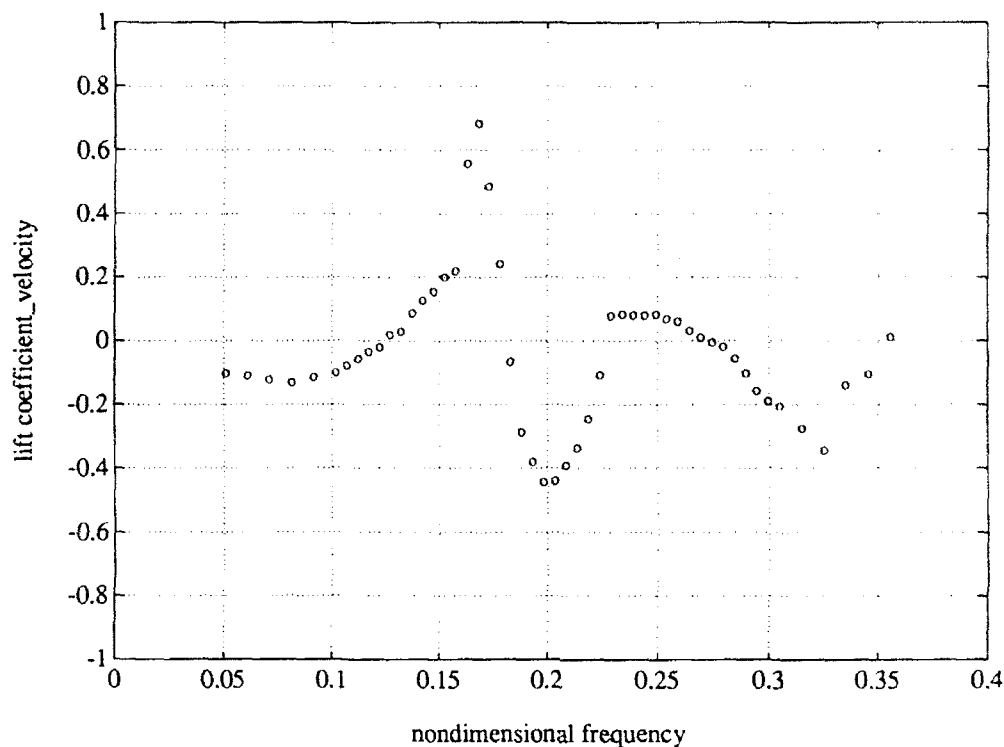


Figure 3-9: Lift coefficient in phase with velocity; sinusoidal oscillations; $Y_0/d = 0.30$.

Using our previous formulations, the cylinder acceleration is given by

$$\frac{d^2}{dt^2} y(t) = -Y_0 (2\pi f_0)^2 \sin(2\pi f_0 t) \quad (3.4)$$

Hence, the component of the lift coefficient in phase with acceleration, which then determines the magnitude of the added mass effect, is given by

$$C_{L-A_0} = \frac{L_0 (-\cos(\phi_0))}{\frac{1}{2} \rho l d U^2} = -C_{L_0} \cos(\phi_0) \quad (3.5)$$

The magnitude of the added mass, M_{A_0} , is given by the total lift force in phase with acceleration divided by the magnitude of the acceleration, i.e.

$$M_{A_0} = \frac{\frac{1}{2} \rho l d U^2 C_{L-A_0}}{Y_0 (2\pi f_0)^2} \quad (3.6)$$

The conventional method of representing the added mass of a body is via an added mass

coefficient C_{M_0} , written as a fraction of the displaced mass of the surrounding fluid, i.e.

$$C_{M_0} = \frac{M_{A_0}}{\rho V} \quad (3.7)$$

where V is the volume of the body in consideration (and hence the volume of the displaced fluid). Some algebraic manipulations of Equations 3.6 and 3.7 finally yield the following convenient representation of the added mass coefficient (in terms of C_{L-A_0} , and nondimensional frequency and amplitude ratio):

$$C_{M_0} = - \frac{1}{2\pi^3} \frac{C_{L-A_0}}{(Y_0/d) \hat{f}_0^2} \quad (3.8)$$

Plots of the lift coefficient in phase with acceleration C_{L-A_0} , and added mass coefficient C_{M_0} , for the amplitude ratio 0.30, are shown in Figures 3-10 and 3-11. These coefficients illustrate that there is a sharp variation of the inertial fluid force in the vicinity of the resonant point. From Figure 3-11, it is seen that the classical value of unity for the cylinder added mass coefficient is true only for frequencies of oscillation that are high relative to the shedding frequency, i.e. at low values of reduced velocity $V_R (= 1/\hat{f}_0)$. At low nondimensional frequencies (high reduced velocities), the effective fluid inertial force must be represented by a *negative* added mass coefficient. Thus it is clear that C_{M_0} *cannot be assumed to have a constant value*.

3.3.2 Results for other amplitude ratios

In the previous section, a detailed set of results were presented for the constant amplitude ratio of $Y_0/d = 0.30$, with the intention of illustrating typical sinusoidal results in some depth. In total, five additional values of amplitude ratio were tested, Y_0/d being 0.15, 0.50, 0.75, 1.00, and 1.20. As can be readily imagined, the graphical depiction of the results for all of these amplitude ratios is very confusing when plotted together in graphs such as Figures 3-6 – 3-11. Hence we opted to show the variation of the combined sinusoidal results by using contour “maps”, presented in Figures 3-12 through 3-16. In these plots, the X axis corresponds to the nondimensional oscillation frequency \hat{f}_0 and the Y axis to nondimensional amplitude ratio Y_0/d , with the contour lines depicting lines of equal force coefficient magnitude. The numbers marked on the contour lines represent the values of

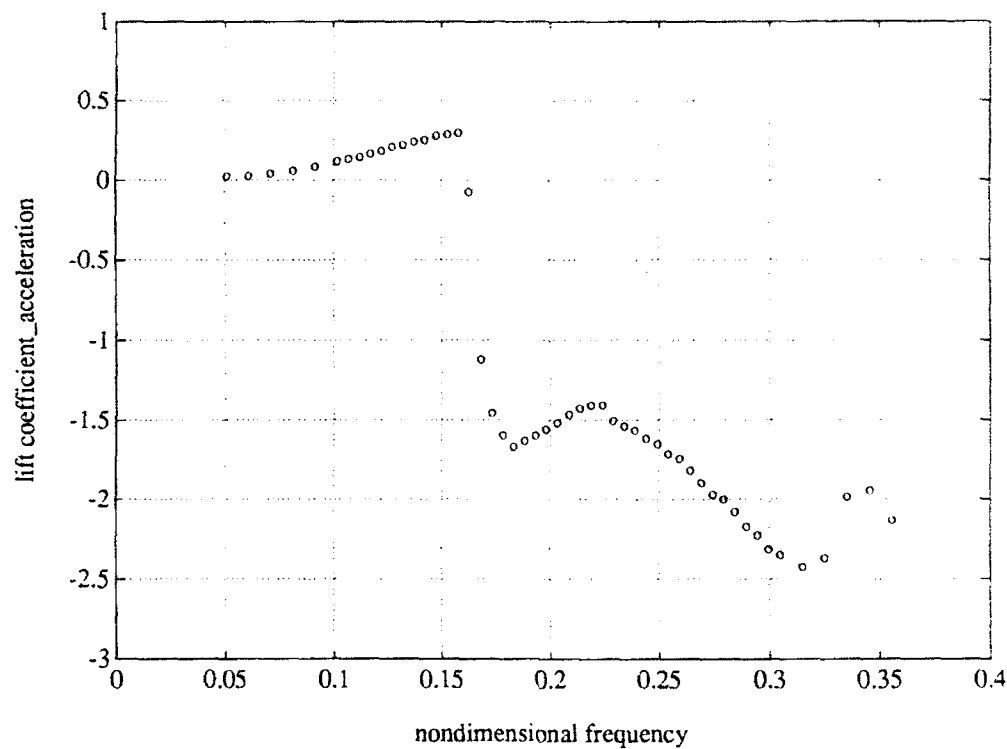


Figure 3-10: Lift coefficient in phase with acceleration; sinusoidal oscillations; $Y_{C_1}/d = 0.30$.

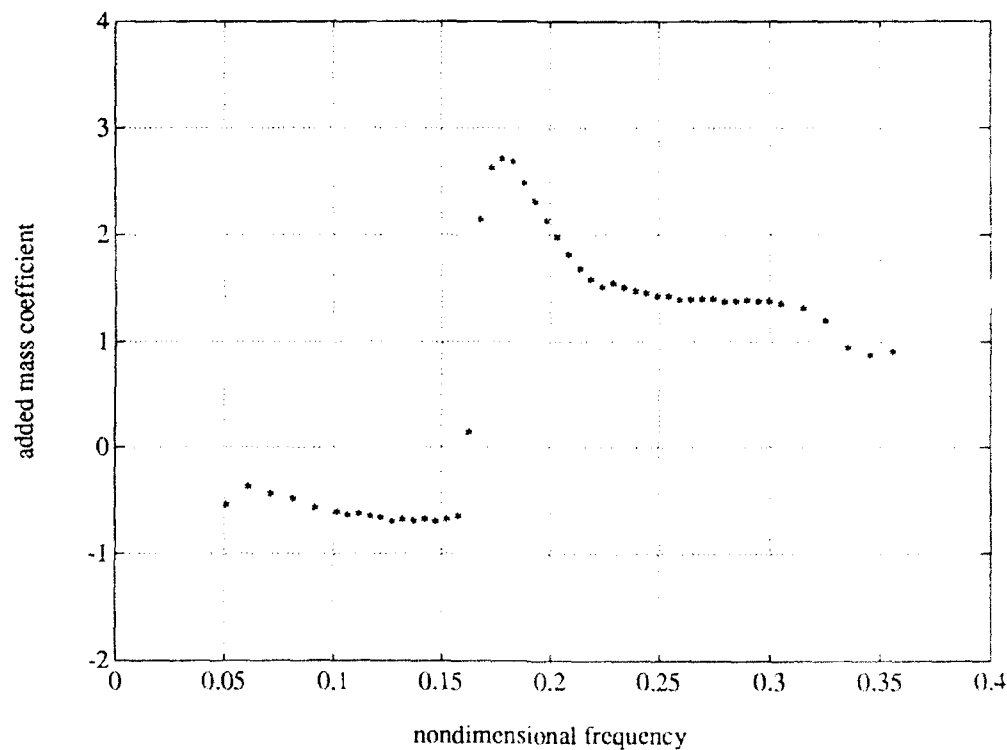


Figure 3-11: Added mass coefficient; sinusoidal oscillations; $Y_0/d = 0.30$.

Figure 3-12: Contours of the mean drag coefficient; sinusoidal oscillations.

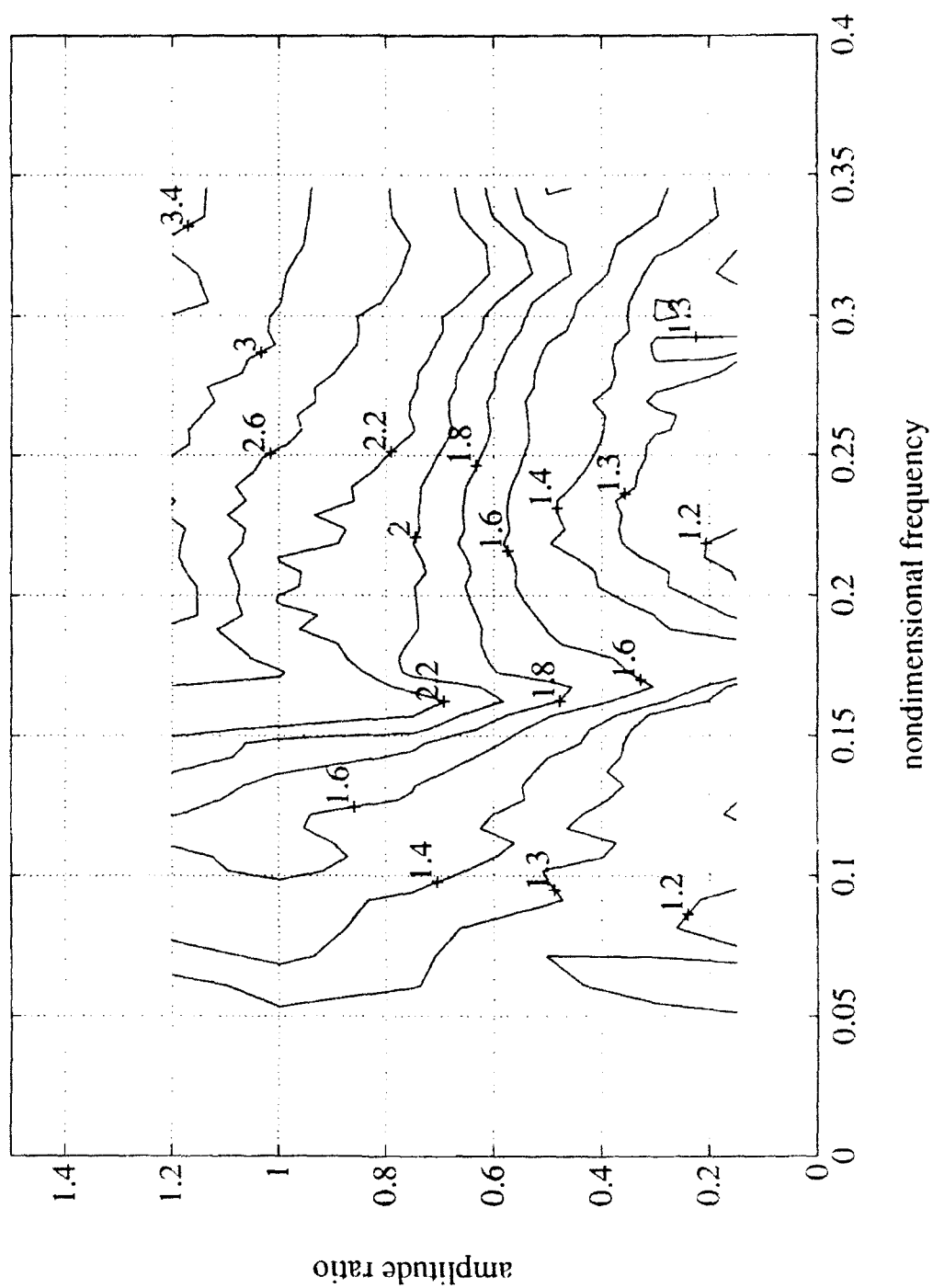


Figure 3-13: Contours of the oscillating drag coefficient; sinusoidal oscillations.

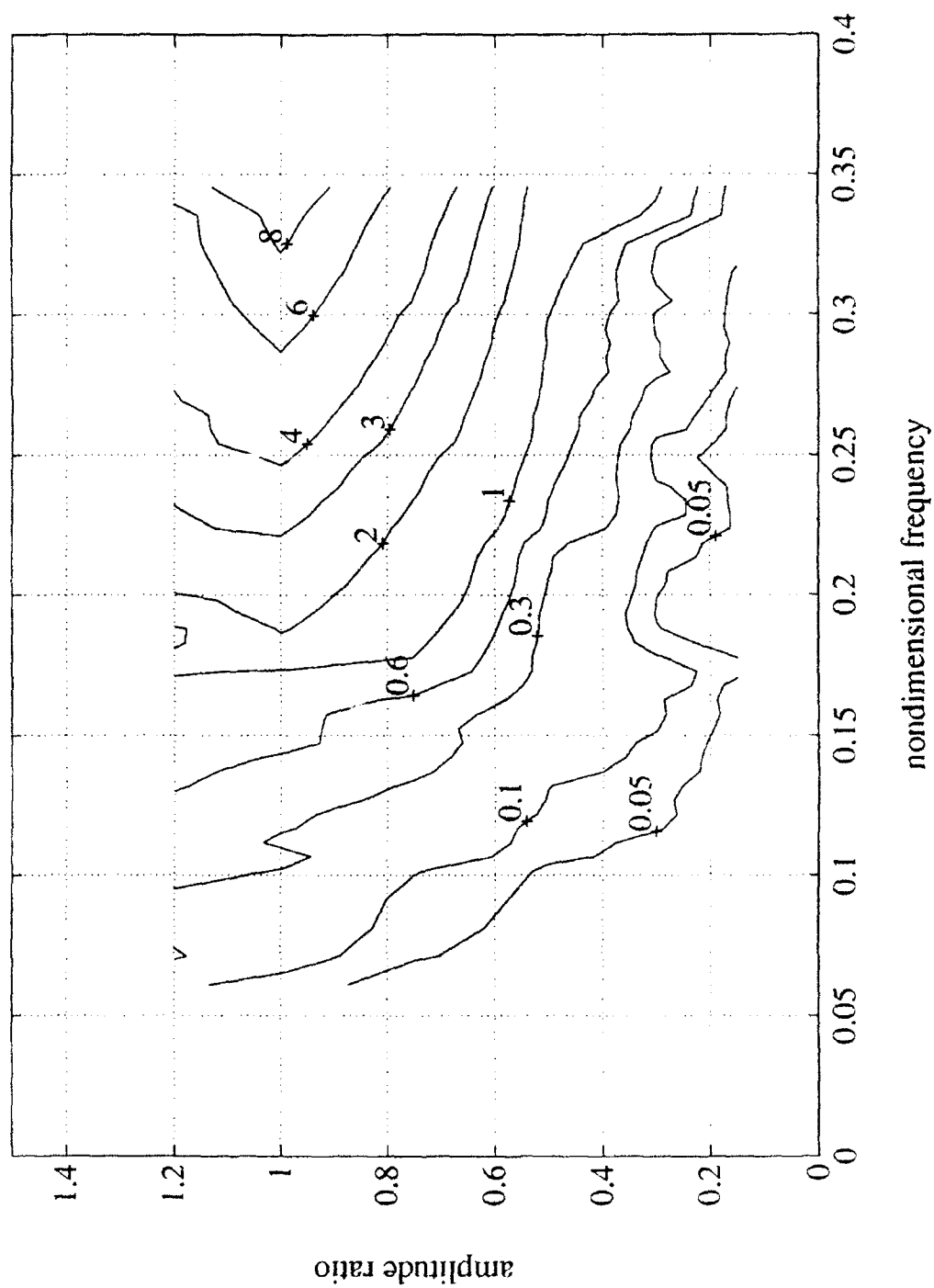


Figure 3-14: Contours of the lift coefficient in phase with velocity; sinusoidal oscillations.

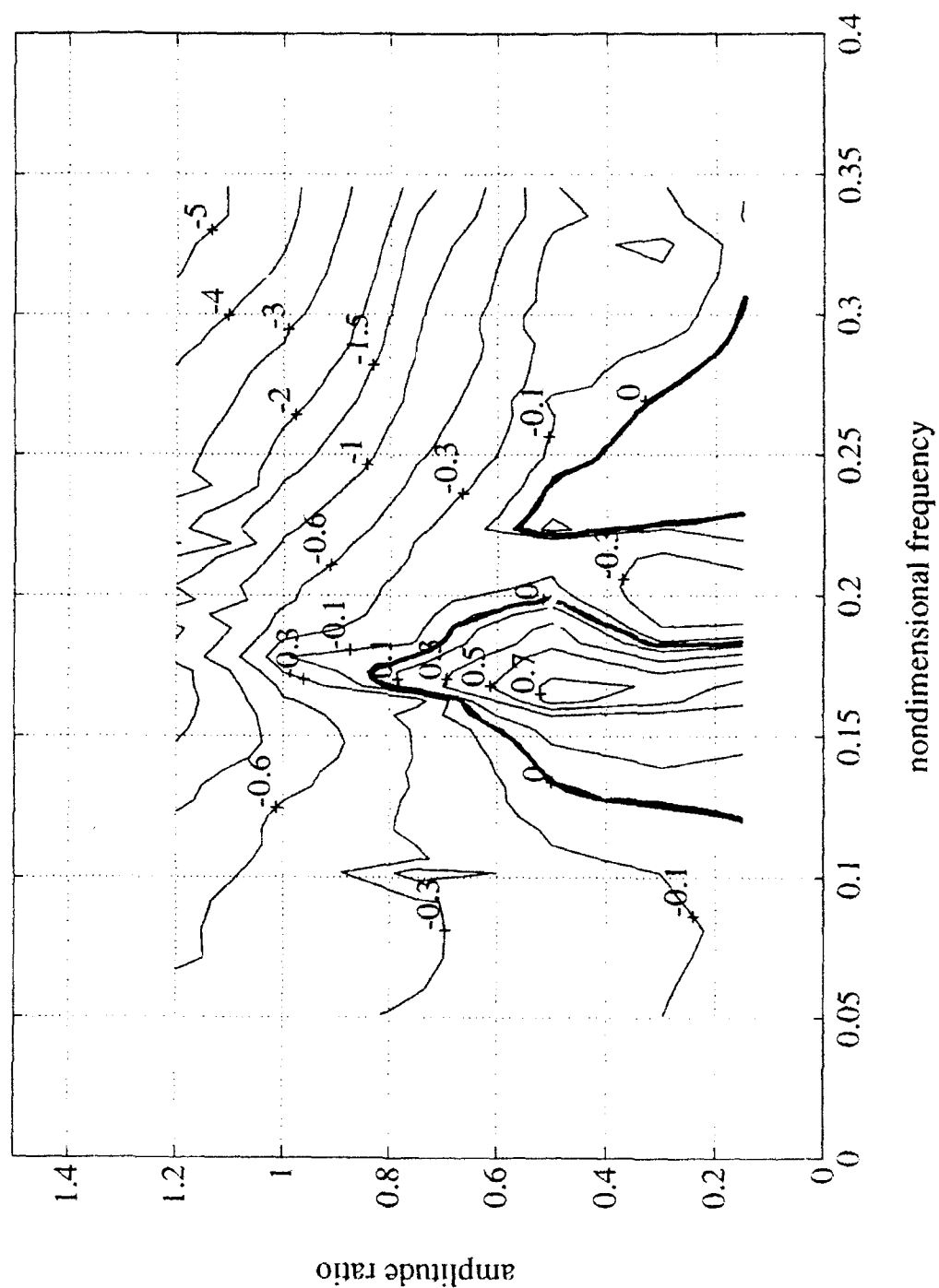


Figure 3-15: Contours of the lift coefficient in phase with acceleration: sinusoidal oscillations.

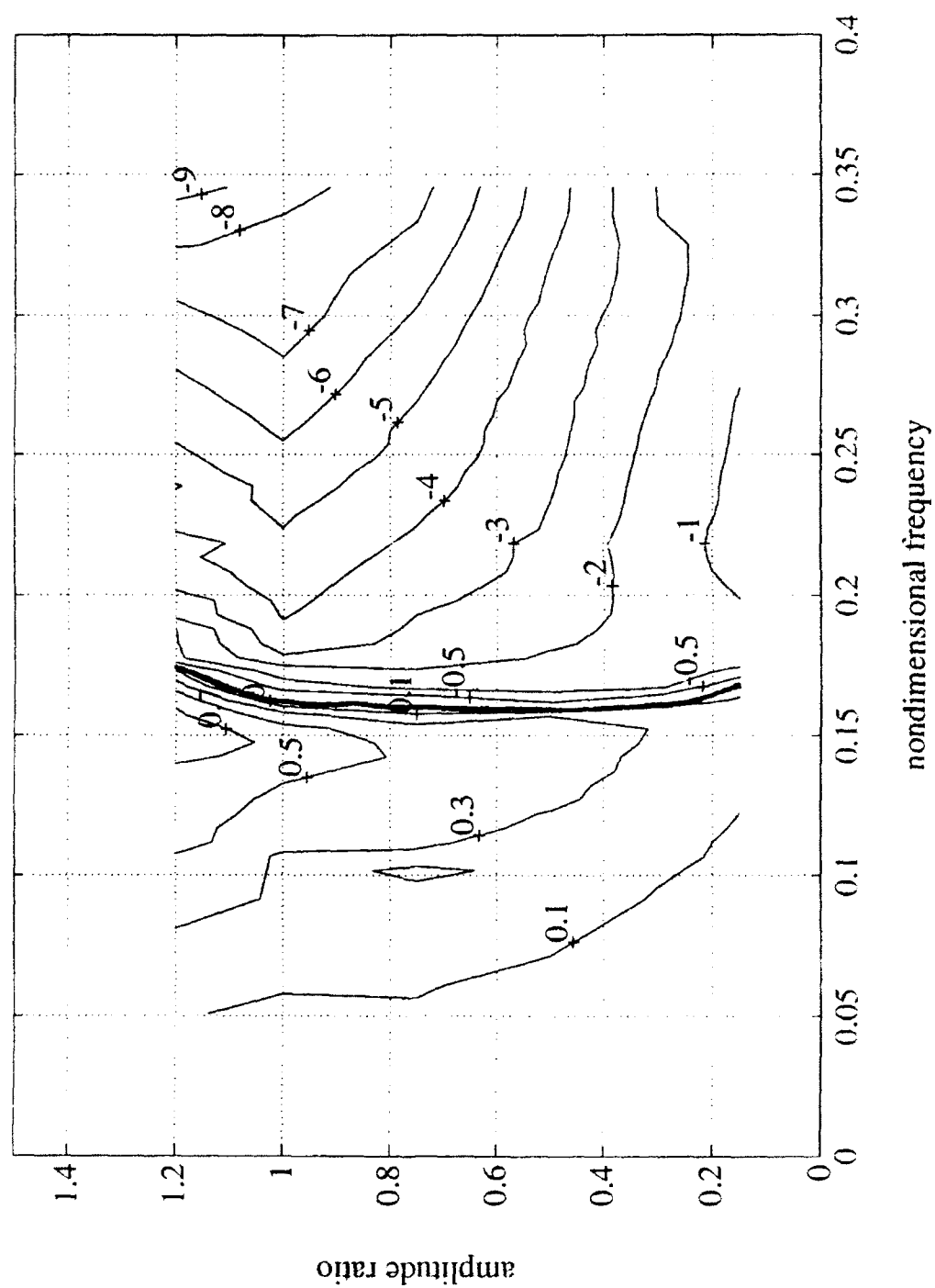
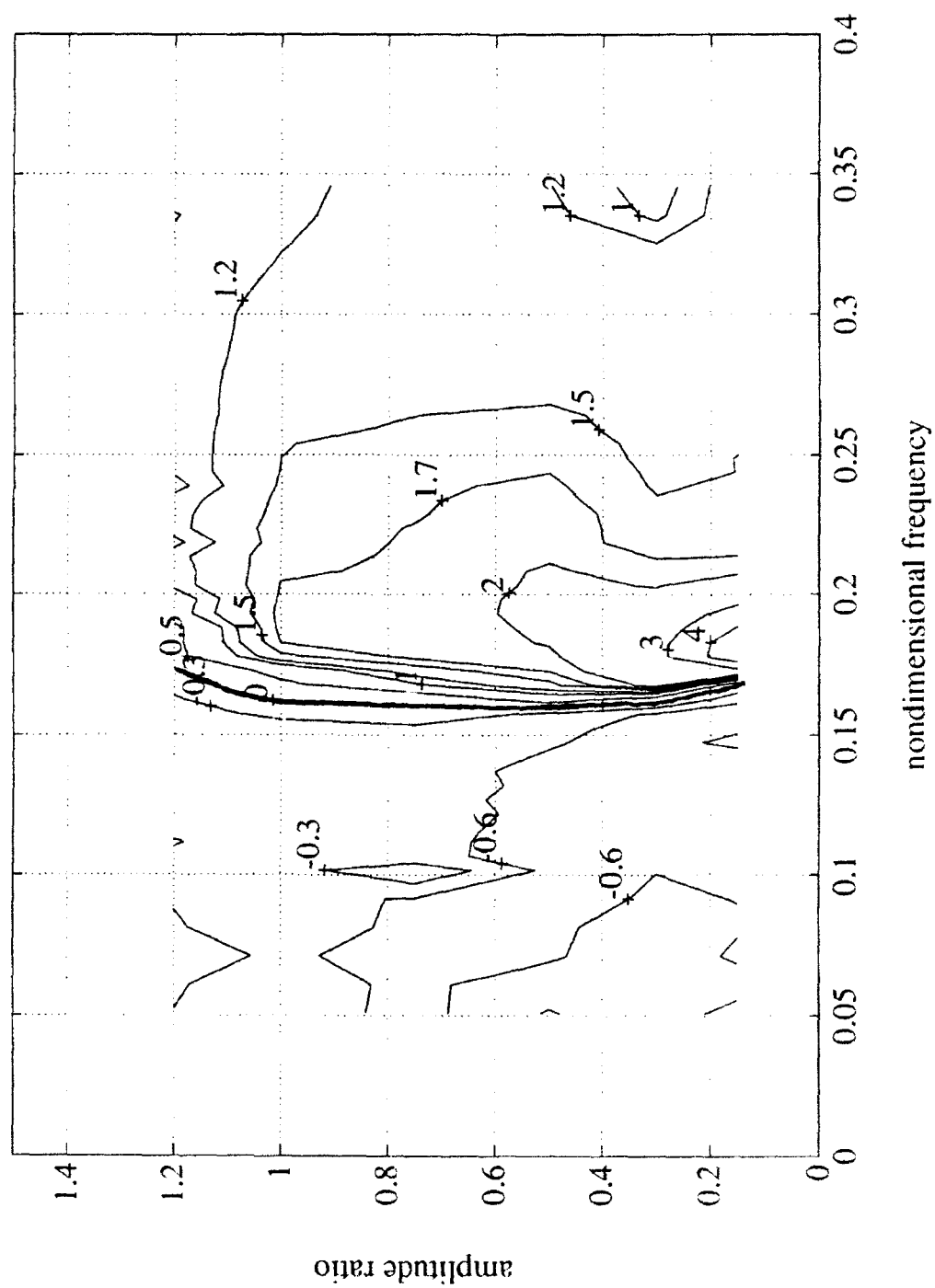


Figure 3-16: Contours of the added mass coefficient: sinusoidal oscillations.



the relevant coefficient along the specified lines. Each figure contains results for all of the sinusoidal tests conducted, i.e. each figure represents data collected at 50 discrete frequencies and 6 discrete amplitude ratios, for a total of 300 data points. No attempt has been made to smooth the data in any way, and simple linear interpolation has been used between data points in order to generate the contour plots. A brief description of each contour plot follows.

Mean drag coefficient. Contours of the mean drag coefficient C_{D_m} are presented in Figure 3-12. The amplification of the mean drag in the primary resonant region ($0.15 < \hat{f}_0 < 0.18$) is clearly seen, with a C_{D_m} value of about 2.60 for an amplitude ratio of 1.00. A secondary amplification peak can be discerned (at frequencies near 0.32) for moderate oscillation amplitudes, but fades away for very small or very large motions. Drag coefficient values for other combinations of oscillation frequency and amplitude are easily obtained from the figure. It should be noted that while these contour maps have not been presented in the past, our underlying mean drag results are similar to those of Sarpkaya [67] and Mercier [47].

Oscillating drag coefficient. Results for the oscillating drag coefficient C_{D_o} are presented in Figure 3-13. At low oscillation amplitudes and/or frequencies, the magnitude of C_{D_o} is very small, agreeing with the conventional view that the oscillating drag force is about 10% (or less) of the mean drag force [65, 37, 7]. *This is not always true!* At high oscillation amplitudes and frequencies, the oscillating drag coefficient was found to be as large as 8.0, i.e. several times the magnitude of the mean drag coefficient. A more detailed look at these remarkable results, as well as other facets of the oscillating drag force, is presented in a later section of this chapter.

Lift coefficient in phase with velocity. Figure 3-14 shows contours of the lift coefficient in phase with oscillation velocity, $C_{L_{A_0}}$. The thick black line marked on the figure corresponds to the zero contour, i.e. the separation between positive (exciting) and negative (damping) values of the coefficient. The primary and secondary excitation (resonant) regions are clearly seen, with the primary excitation region centered around a nondimensional frequency of about 0.17 and extending to a maximum amplitude ratio of about 0.85.

With increasing amplitude (in the resonant region), C_{L/A_0} decreases and finally becomes negative. The significance of Figure 3-14 is that it contains practically all of the fluid force information required to make an accurate prediction of the vortex-induced response amplitude in a typical VIV problem. The use of such contours in making response predictions will be explained in Chapter 4.

Lift coefficient in phase with acceleration. Figure 3-15 shows contours of the lift coefficient in phase with oscillation acceleration, C_{L/A_0} , and Figure 3-16 shows contours of the related added mass coefficient, C_{M_0} . As before, the thick black line marked on the figures corresponds to the zero contour, showing the transition from positive to negative values of the coefficients. A remarkable result is that although the zero transition occurs very rapidly, the frequency at which this transition takes place is only very weakly dependent on amplitude.

It will be noticed that results for the lift coefficient magnitude and phase angle were not presented in the form of contour maps. The lift force phase angle was found to behave in an unexpected manner not amenable to presentation via a contour plot, and the lift force magnitude information is not useful without the accompanying phase information. Instead of magnitude and phase plots, the lift force coefficients in phase with velocity and in phase with acceleration were computed directly and presented here. A detailed discussion of the behavior of the lift phase angle is contained in the next section of this chapter.

3.4 The behavior of the lift force phase angle

We have seen in earlier sections that the phase angle between the lift force and the cylinder motion is very important in determining the precise action of the lift force. In particular, if the motion is expressed as $y(t) = Y_0 \sin(2\pi f_0 t)$, the lift force can be written as $L(t) = L_0 \sin(2\pi f_0 t + \phi_0)$, where ϕ_0 is defined as the angle by which the lift force vector leads the motion vector; this angle then determines whether the lift force is *exciting* or *damping*.

Figure 3-17 shows this concept in a graphical manner. In this figure, the cylinder oscillation and lift force are represented by vectors that rotate (in an anticlockwise direction) around the origin at an angular velocity of $2\pi f_0 t$. (In electrical engineering parlance, such

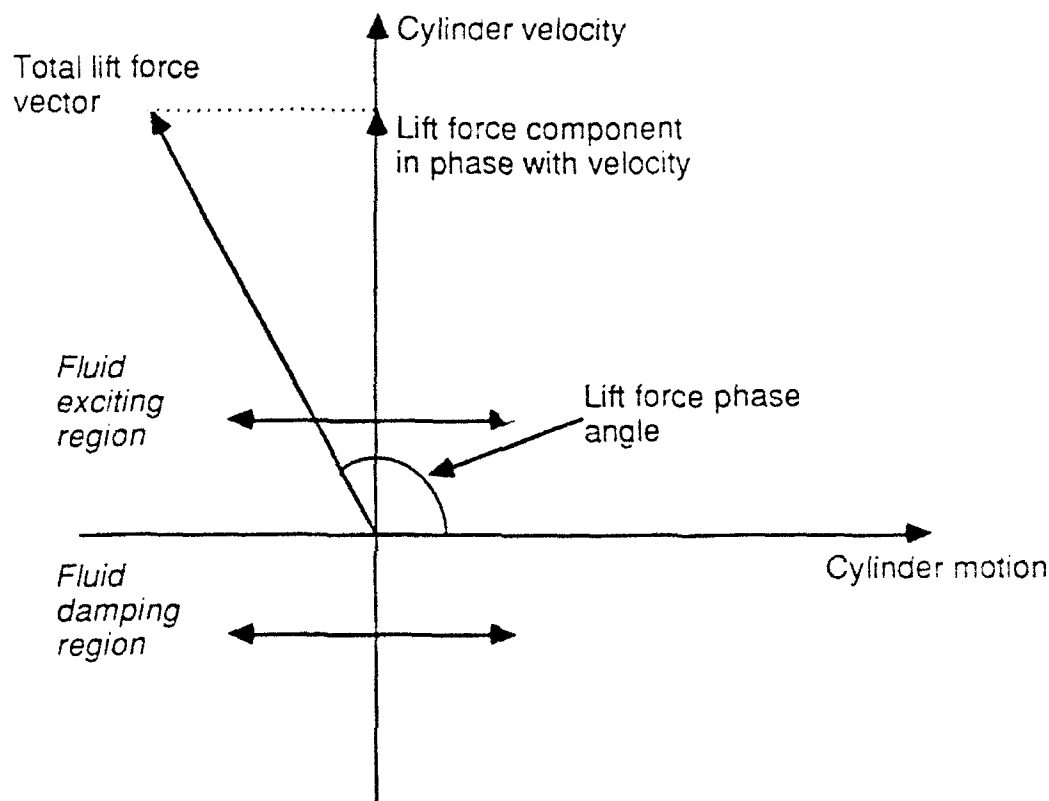


Figure 3-17: Vector diagram of the cylinder oscillation, velocity and acceleration; and vortex-induced lift force.

vectors are called *phasors*.) If we choose (arbitrarily) the motion vector to lie along the positive X axis, then the oscillation velocity vector (being the derivative of the motion) lies along the positive Y axis, and the oscillation acceleration vector (being the derivative of the velocity) lies along the negative X axis. The lift force is some arbitrary vector with a phase angle measured in an anticlockwise direction from the positive X axis.

From Figure 3-17, the importance of the phase angle is clear. If the phase angle lies in the range $0 < \phi_0 < +\pi$, the component of the lift force in phase with cylinder velocity is positive. Thus there is positive power transfer from the fluid to the cylinder, and vortex-shedding acts to *excite* the cylinder vibrations. On the other hand, if the phase angle lies in the range $+\pi < \phi_0 < +2\pi$ (or alternatively $-\pi < \phi_0 < 0$), the component of the lift force in phase with cylinder velocity is negative: there is negative power transfer from the fluid

to the cylinder, and vortex-shedding acts to *damp* the cylinder vibrations.

For each of our sinusoidal tests, the phase angle ϕ_0 was calculated as the difference between the phase angle of the lift force (with respect to our reference sinusoid) and the phase angle of the cylinder motion (with respect to the same reference sinusoid). Figures 3-18 and 3-19 illustrate the phase angle data for "small" and "large" oscillation amplitudes (with the classification based on the observed behavior).

For the amplitude ratios of 0.15, 0.30 and 0.50, (the "small" amplitudes) the variation of phase angle is shown in Figure 3-18. While there are differences in the behavior for the different amplitudes, there is strong similarity as well. At low frequencies of oscillation,

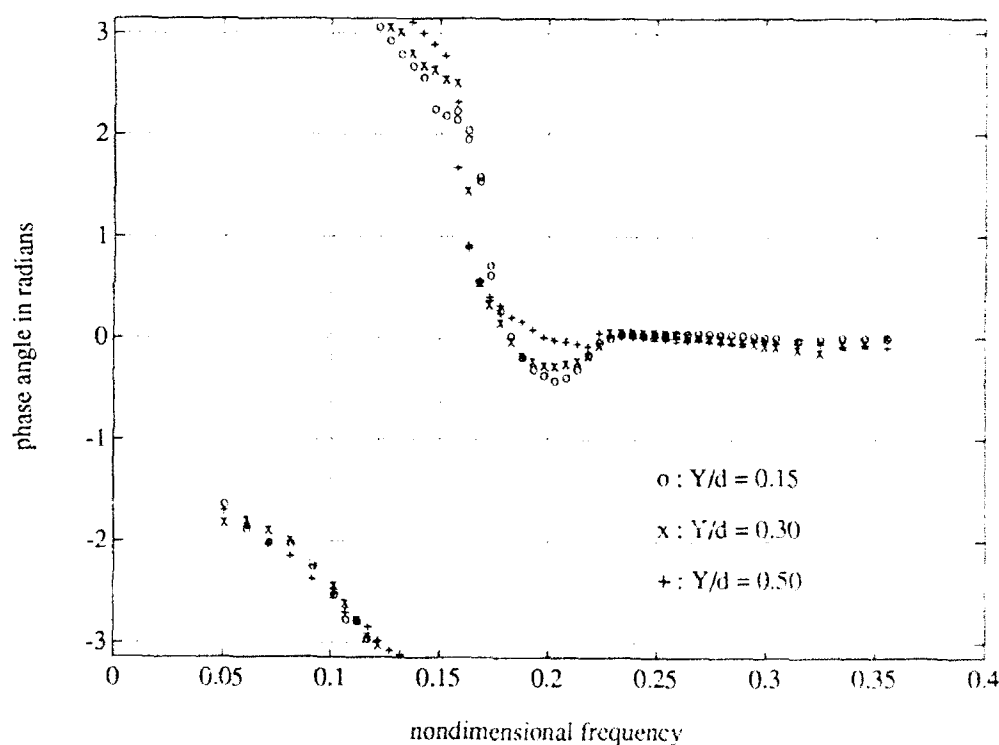


Figure 3-18: Variation of phase angle with nondimensional frequency for "small" amplitude ratios 0.15, 0.30 and 0.50.

the phase angle in all three cases is about $-\frac{3\pi}{2}$. As the frequency is increased, the phase becomes more negative, until it reaches $-\pi$ and "wraps-around" to $+\pi$, i.e. from *lagging* one cycle of oscillation, the lift force vector can be considered as *leading* the next successive cycle. With further increase in the frequency (near the natural Strouhal shedding value), the phase angle transits rapidly from $+\pi$ to 0 through the exciting region; this range of

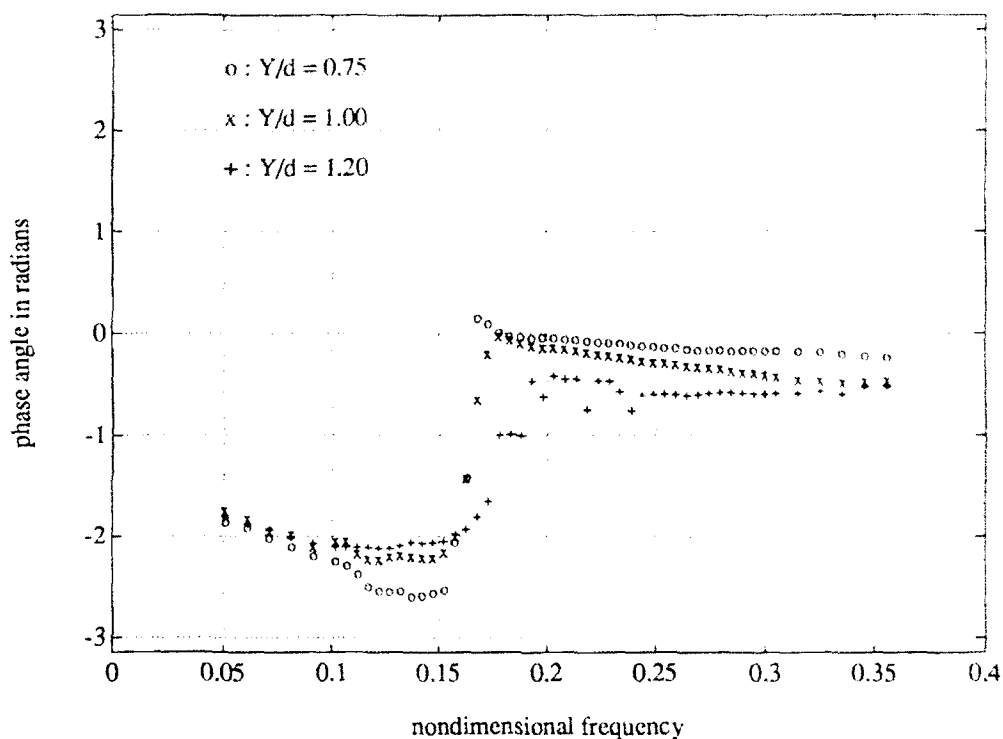


Figure 3-19: Variation of phase angle with nondimensional frequency for "large" amplitude ratios 0.75, 1.00 and 1.20.

frequency then defines the excitation or resonant region. At high oscillation frequencies the phase stabilizes at a little less than 0 radians.

For the "large" amplitude ratios of 0.75, 1.00, and 1.20, the variation of phase angle is shown in Figure 3-19. While the results for the individual amplitudes in this figure are comparable with each other, the behavior for these large amplitudes is quite different from the small amplitude behavior of the previous paragraph. At low oscillation frequencies, the phase angle is once again about $-\frac{3\pi}{2}$ radians, and at high oscillation frequencies too, the phase angle is once again a little less than 0. However, the rapid transition of phase (near the Strouhal frequency) is in the opposite direction. Instead of reaching $-\pi$ and then wrapping around, the phase moves towards zero by becoming less negative with increasing frequency.

The difference between the "small" and the "large" amplitude behavior of phase angle is easily visualized in Figure 3-20. Like Figure 3-17, Figure 3-20 is a vector diagram of the lift force relative to the cylinder oscillation, velocity, and acceleration vectors. At low

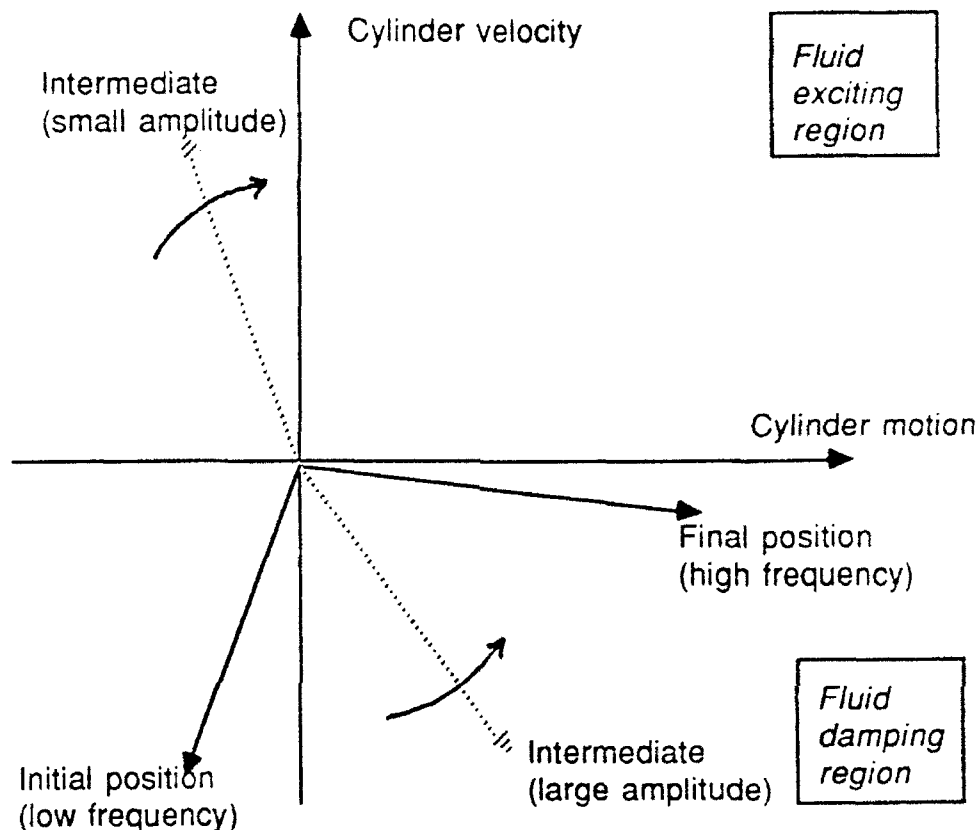


Figure 3-20: Vector diagram showing "small" and "large" amplitude phase transition behavior.

frequencies, the lift force vector is in the third quadrant, and at high frequencies, the lift force vector is in the fourth quadrant. In either case, the lift force has a damping effect. For "small" amplitudes, the lift vector transits from the initial (low frequency) state to the final (high frequency) state in a *clockwise* fashion, i.e. it transits through the exciting region. For "large" amplitudes, the lift vector transits from the initial to the final state in an *anticlockwise* fashion, i.e. it remains everywhere in the damping region. (This is not strictly true for all amplitudes, since for the amplitude ratio of 0.75, a small excursion of the phase angle into the exciting region is seen at the end of the rapid transition range: see Figure 3-19.)

Needless to say, we found these results for the phase angle very interesting, in part due to their novelty. Prior to our data, the most complete results for the lift force phase angle

were due to Staubli [74, 75], illustrated in the three-dimensional view of Figure 1-4. That figure shows that the variation of phase is in one direction for all amplitudes of oscillation, in direct contradiction to Figures 3-18 and 3-19. Staubli does say, however, that

“The measured area is displayed with full lines ... additional points (interrupted lines) have been estimated in order to complete the picture over the whole area.” [74]

Close examination of Figure 1-4 reveals that Staubli's full lines (actual data) are only for relatively low oscillation amplitudes, and the observed behavior has been extrapolated to higher amplitudes. Our data suggests that this extrapolation may have been incorrect.

In order to check that our results were in fact correct and not due to some obscure artifact of the Fourier-component data processing method, we devised a time-domain scheme to calculate the lift force phase angle. This algorithm found the time points of upcrossing of the lift force time trace and calculated the time difference, and hence the phase angle, relative to the nearest upcrossing of the corresponding LVDT motion time trace. All of the sinusoidal test data were processed with this time-domain scheme, which verified that the phase angles from the harmonic analysis were indeed correct. For example, Figures 3-21 and 3-22 show the phase angle variation calculated by both the frequency-domain as well as the time-domain algorithms for the amplitude ratios $Y_0/d = 0.50$ and $Y_0/d = 0.75$ respectively. Good agreement is seen between the two methods, and such agreement was observed for all of the amplitude ratios tested. In addition, it may be noted that later sinusoidal oscillation experiments with very fine frequency resolution (conducted in our laboratory as part of an oil-industry sponsored Joint Industry Project [84]) also revealed very similar phase angle variations.

The physical significance of the different phase angle trends for the “large” versus the “small” oscillation amplitudes (the “phase flipping” behavior) is that it provides an explanation for the self-limiting nature of vortex-induced vibrations. It is well known that the exciting lift coefficient (the lift coefficient in phase with velocity, C_{L-V_0}) decreases as amplitude increases, and finally becomes negative at a limiting amplitude of about one diameter (Griffin and Ramberg [26], Sarpkaya [65], and our results of Figure 3-14). This observed cessation of the exciting force has been explained as being due to a breakdown of the Kármán vortex street at large amplitudes (Blevins [7]). Meanwhile, the low Reynolds

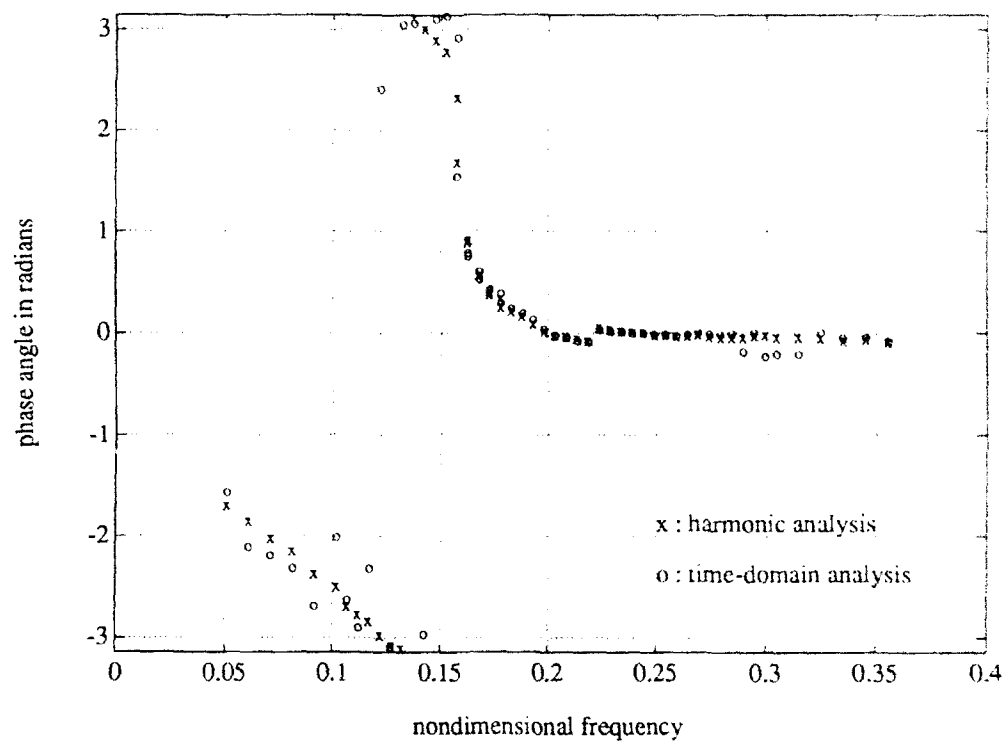


Figure 3-21: Variation of ϕ_0 for $Y_0/d = 0.50$ by both frequency-domain and time-domain methods.

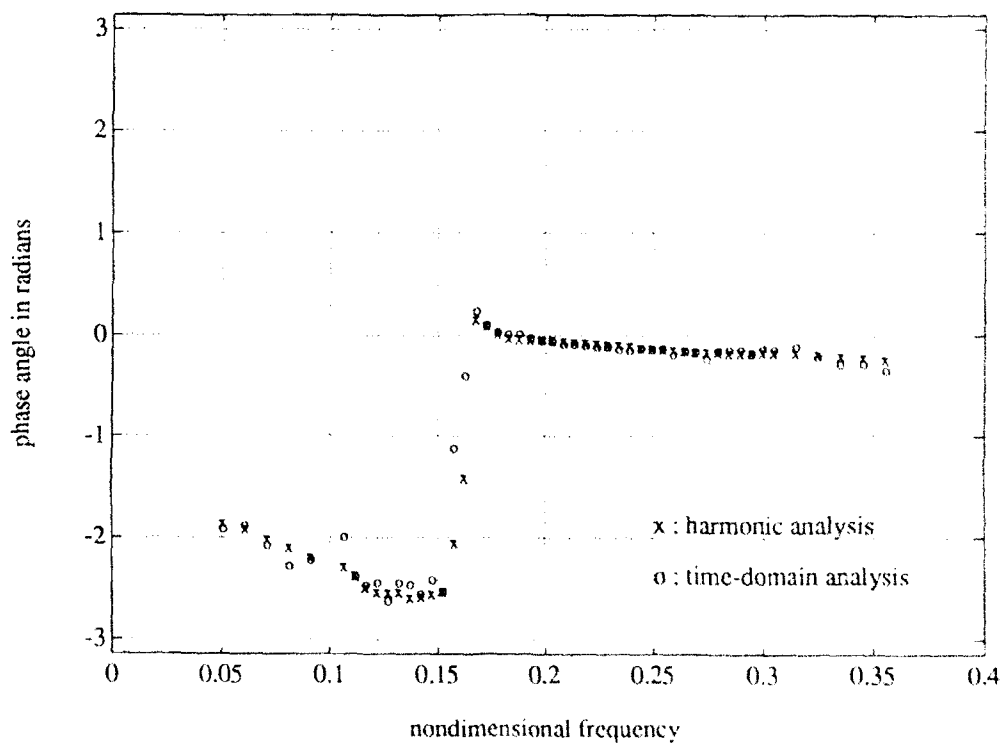


Figure 3-22: Variation of ϕ_0 for $Y_0/d = 0.75$ by both frequency-domain and time-domain methods.

number flow visualization results of Ongoren and Rockwell [53], as well as Williamson and Roshko [95], indicate that the sharp variation in phase angle near the Strouhal frequency is brought about by a change in the phasing of the vortex shedding process relative to the motion of the cylinder. It is reasonable to suppose, therefore, that our observed "phase-flipping" behavior is due to a similar change in the phasing of the vortex shedding process due to a change in oscillation amplitude. Thus the vanishing of the exciting lift coefficient (leading to limit-cycle behavior of the oscillations) might well be due to a simple change in phasing of the vortices rather than a complete breakdown of the vortex street.

An argument based on the observed limit-cycle behavior of the exciting lift coefficient can also be used to demonstrate that Staubli's extrapolation of the phase angle variation (Figure 1-4) must be incorrect. If in fact the phase angle traverses through the exciting region ($0 < \phi_0 < +\pi$) for *all* amplitudes of oscillation, then there must exist a range of frequencies, however small, within which the exciting lift coefficient remains positive, and the cylinder oscillation amplitude grows indefinitely. Since this is not the case with VIV, one must conclude that the phase angle variation depicted by Staubli is in error.

3.5 The behavior of the oscillating drag force

3.5.1 Large amplification at high oscillation frequencies

In Figure 3-13 we saw that the oscillating drag coefficient C_{D_0} was found to attain very large values at high oscillation frequencies and amplitudes. While this amplification is not significant in the primary resonant region and is unlikely to play a role in most VIV situations, it is important to be able to predict the oscillating drag should the need arise (as it would, for example, if high frequency structural oscillations are caused by some other mechanism). A particularly interesting way of illustrating the C_{D_0} amplification phenomenon is by plotting together both the mean and oscillating drag coefficients for a typical large amplitude of motion, say $Y_0/d = 0.75$. Figure 3-23 shows both C_{D_m} and C_{D_0} for this amplitude. From the figure, the sharp increase of the oscillating drag (for frequencies above the resonant range) is clearly seen. For frequencies above about 0.21, the amplitude of the oscillating drag force *exceeds* the mean drag level, at the highest frequencies tested the oscillating drag was found to be more than twice the mean drag.

This huge increase of the oscillating drag force is no less dramatic when visualized in

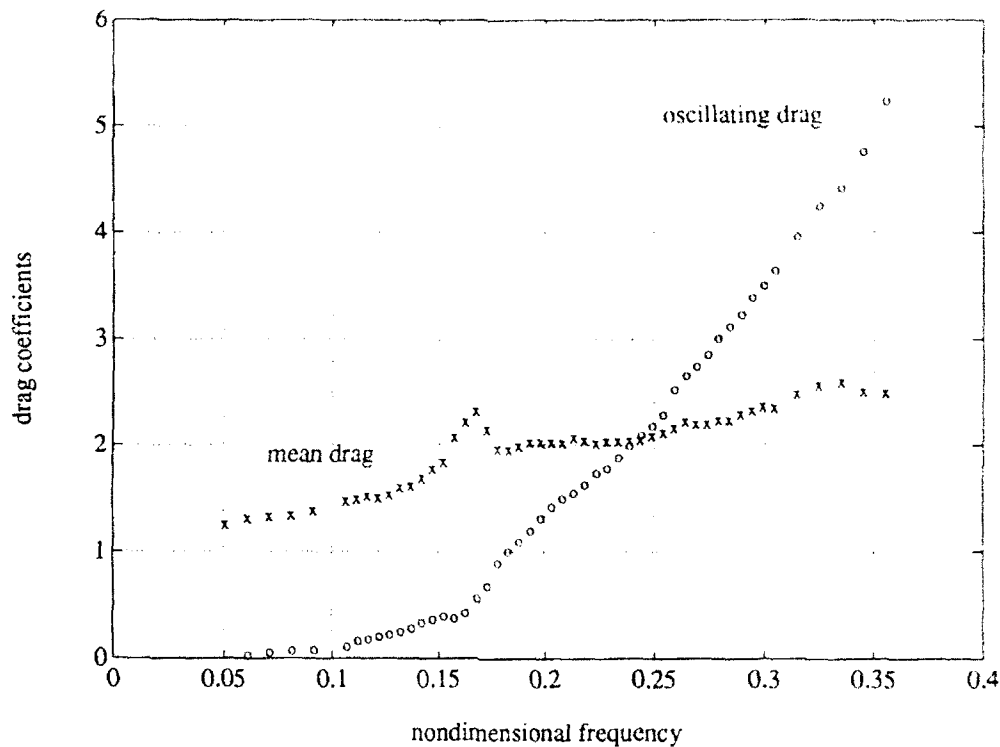


Figure 3-23: Mean and oscillating drag coefficients for amplitude ratio 0.75.

the time domain. Figures 3-24 and 3-25 show time segments of two different drag force data traces, purposely chosen to include a few seconds of run time and a few seconds of the final zero period. Figure 3-24 shows the drag force measured for sinusoidal oscillations at an amplitude ratio of 0.75 and a nondimensional frequency of 0.132; i.e. at a frequency *below* the resonant frequency. The oscillating drag force appears as relatively small fluctuations about the mean drag value; one could use the figure to directly estimate $D_m \approx 2.0$ N and $D_0 \approx 0.3$ N. As an example of a case *above* the resonant frequency, Figure 3-25 illustrates the drag force at the same amplitude ratio and a nondimensional frequency of 0.285. The tremendous increase of the oscillating drag dominates the figure. The mean drag could be estimated as $D_m \approx 3.0$ N, a slight increase over the previous value, but the oscillating drag is now $D_0 \approx 4.0$ N (compared to 0.3 N previously), an approximately 13-fold increase !

References can be found in the literature to unexpectedly large observed values of the oscillating drag coefficient, but very little quantitative data exists. For example, Sarpkaya [65] (who does not provide any numbers for the oscillating drag coefficient) reports that:

“[For constant amplitude ratio and flow velocity] the frequency of the oscilla-

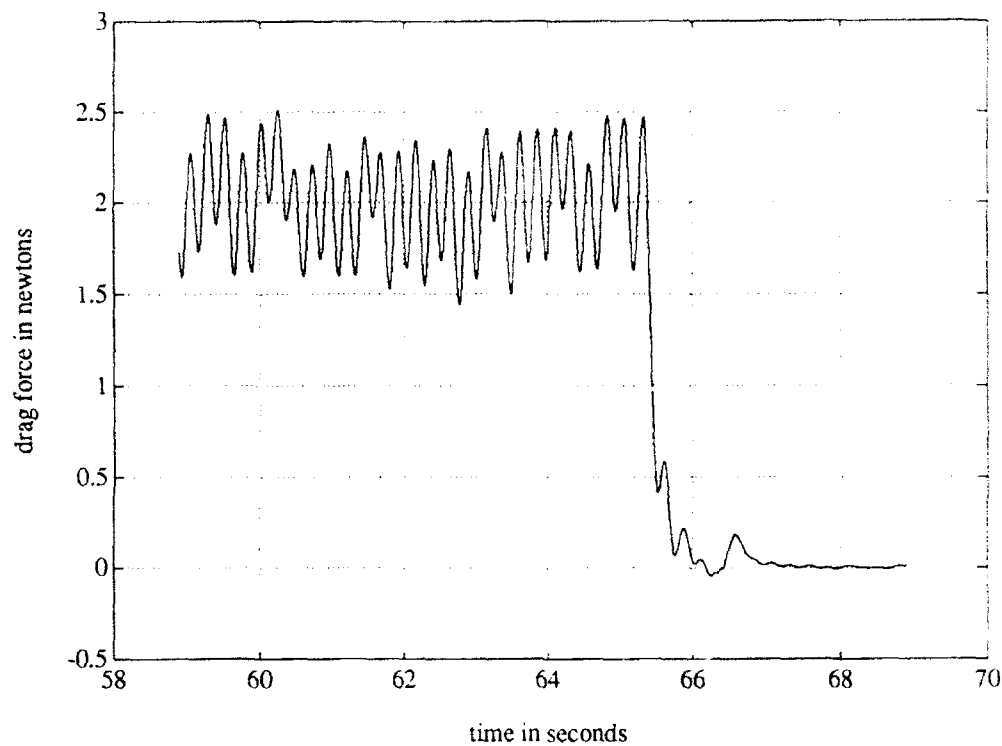


Figure 3-24: Time segment of the drag force; $Y_0/d = 0.75$; $\hat{f}_0 = 0.132$.

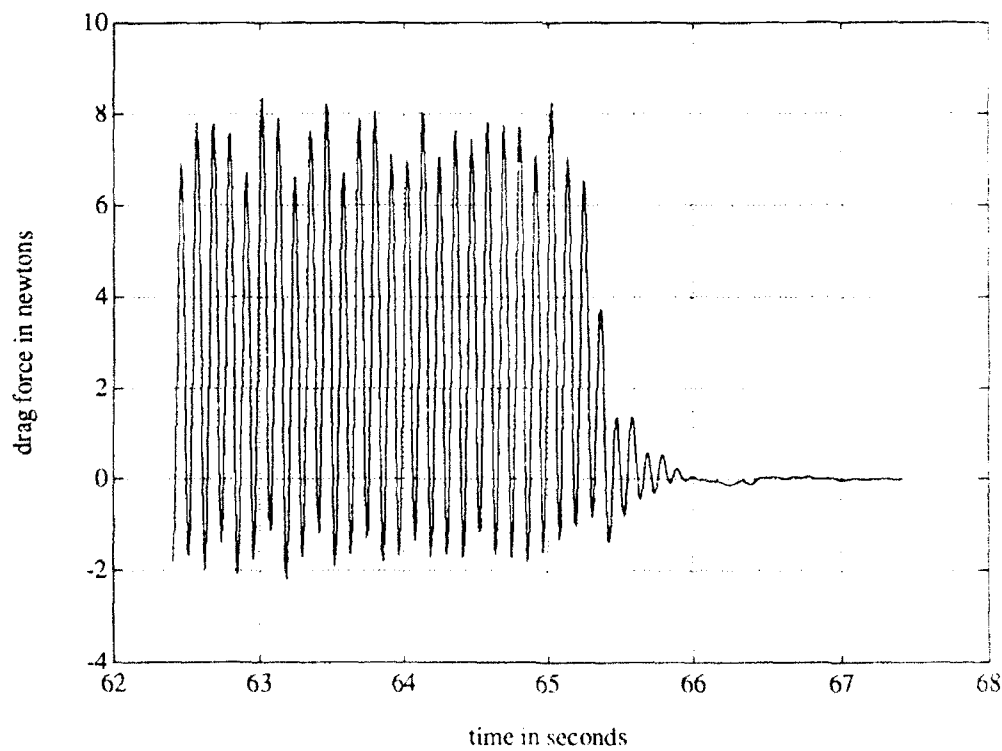


Figure 3-25: Time segment of the drag force; $Y_0/d = 0.75$; $\hat{f}_0 = 0.285$.

tions was gradually increased ... and the resulting in-line force was continuously recorded ... the in-line force increases rapidly but with very little oscillations superimposed on it. As soon as the frequency of oscillations nears the Strouhal frequency, the amplitude as well as the frequency of the force oscillations increases."

The most complete data for C_{D_0} prior to our results were from Mercier [47]. He reports that:

"The magnitudes of [oscillating drag] forces become unanticipatedly large, especially for large amplitudes of oscillation and values of reduced velocity, $[V_R]$, below that corresponding to the critical frequency."

Mercier presents a plot of C_{D_0} versus V_R for several amplitude ratios of oscillation, but the highest value of C_{D_0} he measured was about 2.50, well below the maximum values that we recorded. On the basis of the above references, it is reasonable to view our results (particularly Figure 3-13) as an important set of quantitative data verifying and extending previous reports on the amplification of the oscillating drag coefficient.

While this amplification behavior of the oscillating drag is an interesting result, the origin of the phenomenon is less obvious. From dimensional considerations, it is reasonable to expect the oscillating drag (and lift) forces to be proportional to the square of the tangential velocity of the separating boundary layer, which in turn scales approximately as the frequency of oscillations (for constant amplitude). Thus it is reasonable to expect large force magnitudes at large oscillation frequencies, although the precise cause (in terms of the vortex shedding process) is as yet undetermined. Instantaneous measurements of the velocity field in the near wake are required to resolve this issue. It is also important to note that in-line (drag direction) oscillations of the test cylinder might well serve to change the measured drag forces appreciably. Such in-line oscillations are not currently feasible with our apparatus, but they have been done elsewhere in different contexts (Moe and Wu [49], Alexander [1]). It is suggested that an investigation into the causes of very large oscillating drag forces would prove to be a worthwhile future research endeavor.

3.5.2 Higher harmonics of the oscillating drag

During manual data processing of some of the experimental runs (carried out as part of the initial system verification process), it was noticed that a few of the drag force traces (particularly those corresponding to large amplitude motions) contained appreciable higher harmonic components. For example, Figure 3-26 shows time segments of the motion (LVDT) and the drag force traces for the sinusoidal oscillation case of amplitude ratio $Y_0/d = 0.75$, and frequency $\hat{f}_0 = 0.157$ (in the resonant region). Harmonic components higher than

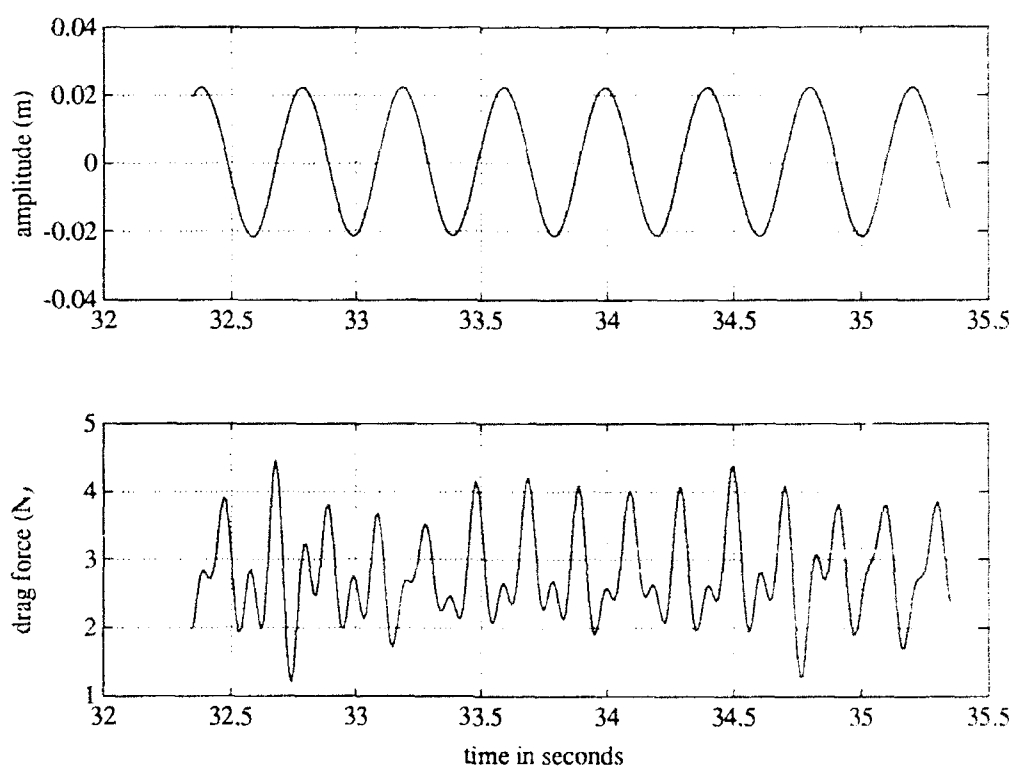


Figure 3-26: Time segments of the motion (LVDT) and the drag force; $Y_0/d = 0.75$; $\hat{f}_0 = 0.157$.

the expected second-harmonic are clearly seen in the drag force. Mercier [47] had briefly mentioned a similar observation but had not investigated the matter further. We decided to pursue the phenomenon and computed the first four harmonics of the oscillating drag force for each of the three highest amplitudes of oscillation.

To carry out this analysis, the sinusoidal oscillation runs for amplitude ratios 0.75, 1.00 and 1.20 were reprocessed from the raw data. A modified filter program was used so as to lowpass filter the data at a cutoff frequency of 4.4 multiplied by the oscillation frequency

(i.e. to preserve information up to and including the fourth harmonic). The total drag coefficient (nondimensional drag force) was now modeled as

$$C_{D_{total}} = C_{D_m} + C_{D_{0-1}} \sin(2\pi(f_0)t + \psi_{0-1}) + C_{D_{0-2}} \sin(2\pi(2f_0)t + \psi_{0-2}) + C_{D_{0-3}} \sin(2\pi(3f_0)t + \psi_{0-3}) + C_{D_{0-4}} \sin(2\pi(4f_0)t + \psi_{0-4}) \quad (3.9)$$

where C_{D_m} is the mean drag coefficient (as before), $C_{D_{0-1 \dots 4}}$ are the oscillating drag coefficient magnitudes at the first four harmonics of the oscillation frequency (f_0 , $2f_0$, $3f_0$ and $4f_0$) respectively, and $\psi_{0-1 \dots 4}$ are arbitrary phase angles. Note that by our previous definition of the oscillating drag coefficient (Equation 2.9), we have

$$C_{D_0} \equiv C_{D_{0-2}} \quad (3.10)$$

The coefficients $C_{D_{0-1 \dots 4}}$ were computed using a modified version of the previously described MATLAB routine. The variation of $C_{D_{0-2}}$, $C_{D_{0-3}}$, and $C_{D_{0-4}}$ with oscillation frequency for amplitude ratios 0.75 and 1.20 are plotted in Figures 3-27 and 3-28. (The first harmonic $C_{D_{0-1}}$ was found to be of small magnitude everywhere and so has been omitted.) From Figures 3-27 and 3-28, the following features can be clearly seen:

- The oscillating drag is dominated by the conventional second-harmonic component, $C_{D_{0-2}}$.
- The third-harmonic component $C_{D_{0-3}}$ is amplified at high oscillation frequencies.
- The fourth-harmonic component $C_{D_{0-4}}$ is amplified in a region near the resonant frequency range, but is reduced at high frequencies.

The importance of these features of the behavior of the oscillating drag force is that they can be directly related to the vortical patterns in the wake. Recall that the conventional vortex street is formed with two vortices shed per cycle of cylinder oscillation. Each vortex causes one cycle of variation of the in-line velocity in the near wake of the cylinder, which then translates directly to one cycle of variation of the in-line drag force. Thus, two vortices (or one vortex pair) per cycle of cylinder oscillation corresponds to an oscillating drag force at twice the frequency of oscillation. By the converse argument, a drag force found to be

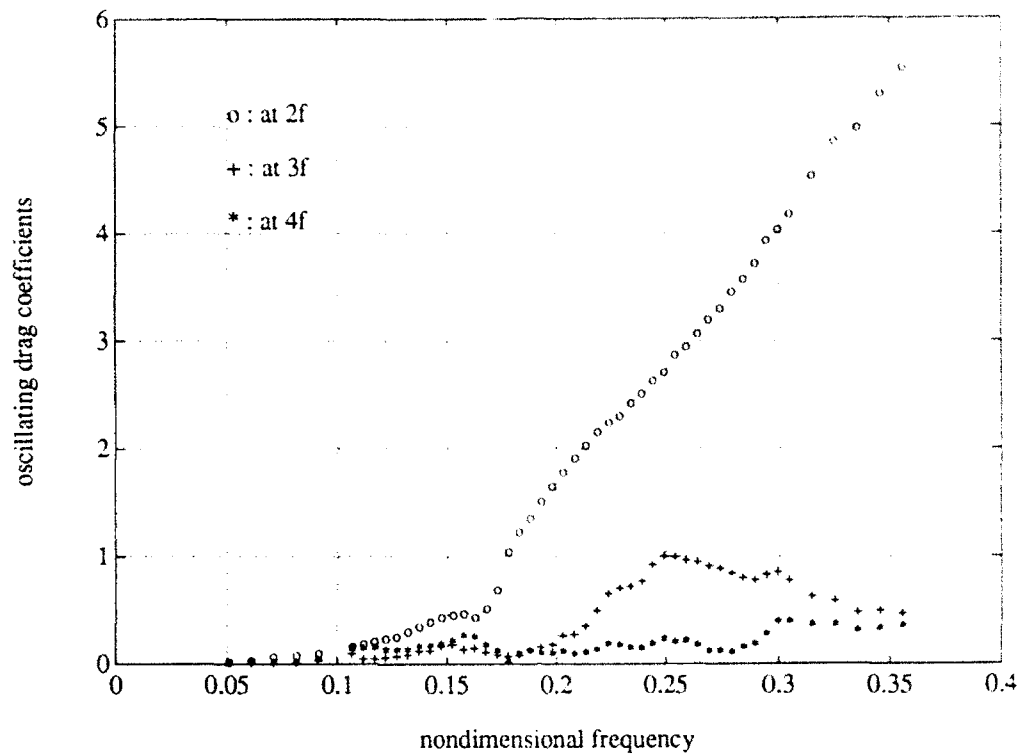


Figure 3-27: Higher harmonic oscillating drag coefficients; $Y_0/d = 0.75$.

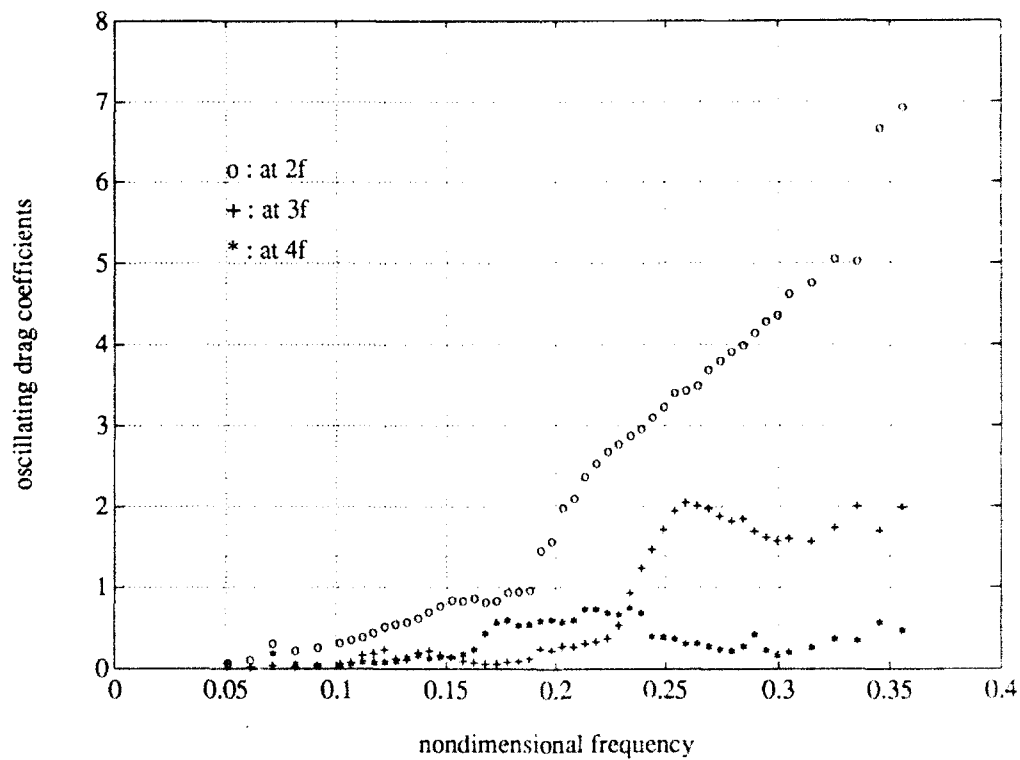


Figure 3-28: Higher harmonic oscillating drag coefficients; $Y_0/d = 1.20$.

oscillating at the N th-harmonic of the oscillation frequency implies that N vortices are formed in the wake per cycle of motion.

Based on the preceding explanation, Figures 3-27 and 3-28 are in agreement with the findings of Williamson and Roshko [95] regarding vortex synchronization patterns in a circular cylinder wake. As we saw in Chapter 1 (Figure 1-5), the authors observed different vortex patterns in the wake depending on the cylinder oscillation amplitude and frequency. These patterns were classified variously as 2S, 2P, P+S, etc., with S denoting a single vortex and P denoting a vortex pair. At amplitudes of oscillation of about one cylinder diameter and low frequencies (high wavelength), Williamson and Roshko were unable to detect any definite vortex pattern, consistent with the low values of oscillating drag that we measured in that range. For frequencies near the natural Strouhal frequency, they observed the 2P mode of vortex formation (four vortices per cycle), consistent with the amplification of the fourth-harmonic that we detected. For high oscillation frequencies, they observed an asymmetric P+S mode (three vortices per cycle), corresponding to our measured amplification of the third-harmonic of the oscillating drag.

An important fact in all of this is that while Williamson and Roshko conducted their experiments at Reynolds numbers between 300 and 1000, our Reynolds number was constant at about 10,000. While the previous authors did not study the possible effect of Reynolds number on their visualized vortex formation patterns, we believe from our results that those patterns are indeed representative of the wake modes to be found over a large Reynolds number range.

3.6 Lock-in behavior and excitation

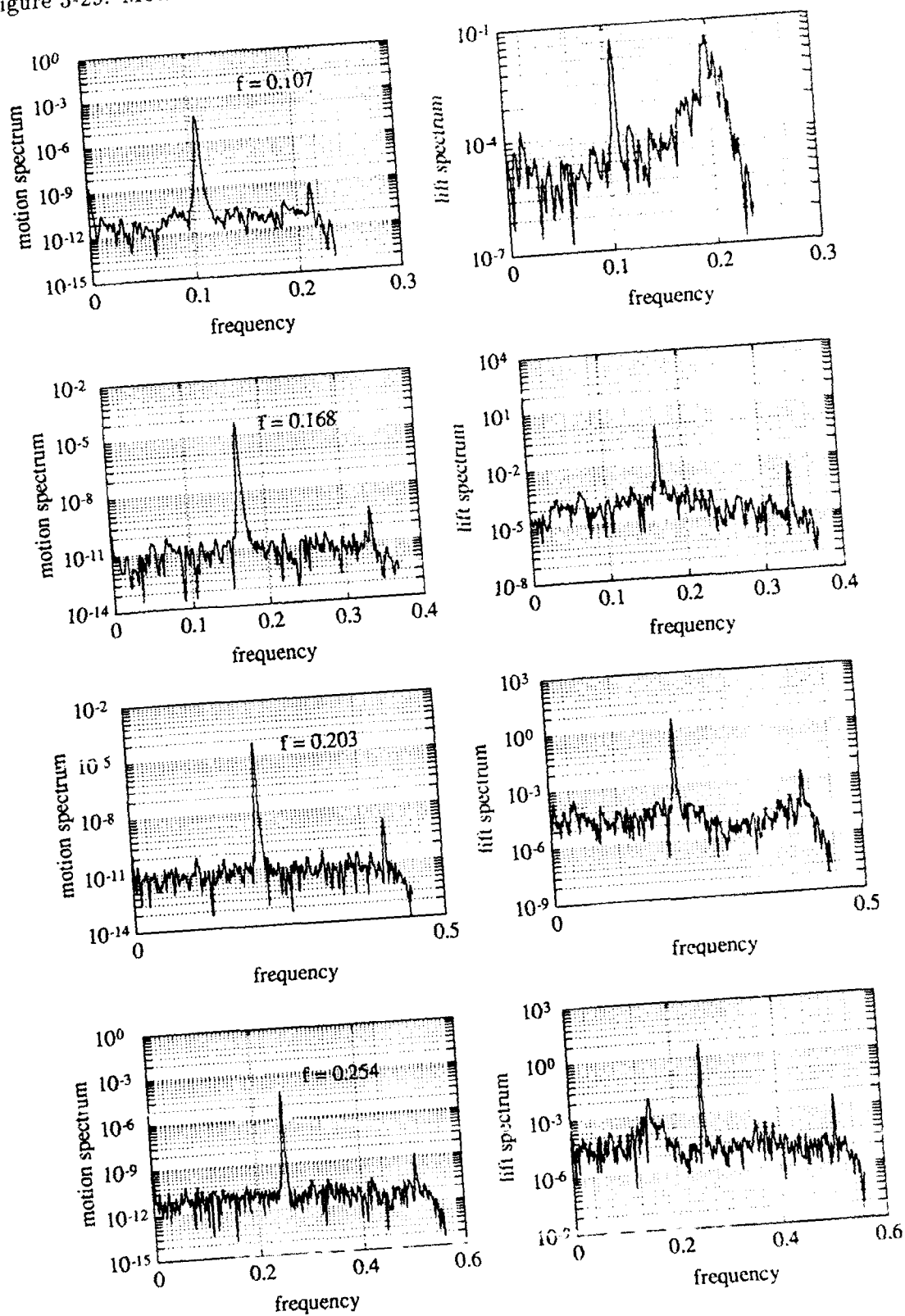
A phenomenon that researchers have extensively studied in the past is that of "lock-in", sometimes called "wake-capture". When the externally imposed cylinder oscillation frequency (or structural natural frequency, in the case of free oscillations) comes within a certain range of the Strouhal shedding frequency, there is an apparent breakdown of the Strouhal relation (Equation 1.1). The shedding process then collapses onto the cylinder vibration frequency, and this is commonly accompanied by increased vortex strength, increased correlation length, and a reduction of random irregularities in the vortex-induced forces. Information on experimentally determined lock-in ranges is widely available, for

example see Bishop and Hassan [6] or Stansby [73]. Recent numerical investigations into the phenomenon (Karniadakis and Triantafyllou [35]) have revealed that the transition from the nonlock-in state to the lock-in state or *vice versa* takes place in a continuous but rapid manner, and that a chaotic response of the vortex wake can develop at the lock-in boundaries.

For purposes of comparison and in order to establish the lock-in boundaries for our cylinder model, we conducted a spectral analysis of each lift force data trace. A MATLAB routine was written that performed the computations and sent the results in a graphical form directly to a printer; these hardcopy results were then scanned visually to determine under what conditions the natural shedding frequency disappeared in favor of the imposed cylinder frequency. For example, Figure 3-29 illustrates the calculated motion (LVDT) and lift force spectra for four tests at amplitude ratio $Y_0/d = 0.50$ and different oscillation frequencies. In this figure, the subplot columns are organized into motion spectra (left column) and lift force spectra (right column), while the rows correspond to different frequencies. The top row contains the spectra for the test conducted at a nondimensional frequency $\hat{f}_0 = 0.107$; the lift force clearly contains components at both the oscillation frequency as well as the Strouhal shedding frequency: this is an example of nonlock-in. The two intermediate rows represent data collected at nondimensional frequencies of 0.168 and 0.203; the lift force spectra contain components only at the respective oscillation frequencies, and hence these plots illustrate lock-in. The fact that lock-in occurs over a finite range of frequencies is demonstrated by the two different realizations. Finally, the last row represents data collected at a frequency of 0.254. In this case, the natural Strouhal shedding component has reappeared in the lift force spectrum, showing that the oscillation frequency is now above the lock-in range; here again is an example of nonlock-in.

By repeating the data analysis steps associated with Figure 3-29 for a large number of frequency and amplitude combinations, we constructed a picture of the overall lock-in region, shown in Figure 3-30. For each of the amplitude ratios considered, the asterisk marks the observed lock-in boundary, i.e. the transition from lock-in to nonlock-in or *vice versa*. A dashed line has been drawn through the asterisks as a visual aid. For frequency and amplitude combinations within the lock-in boundaries (the region marked "lock-in"), vortex shedding occurs only at the oscillation frequency. Outside the lock-in boundaries (the regions marked "nonlock-in"), both the oscillation frequency and the natural Strouhal

Figure 3-29: Motion and lift spectra for $Y_0/d = 0.50$ and four oscillation frequencies.



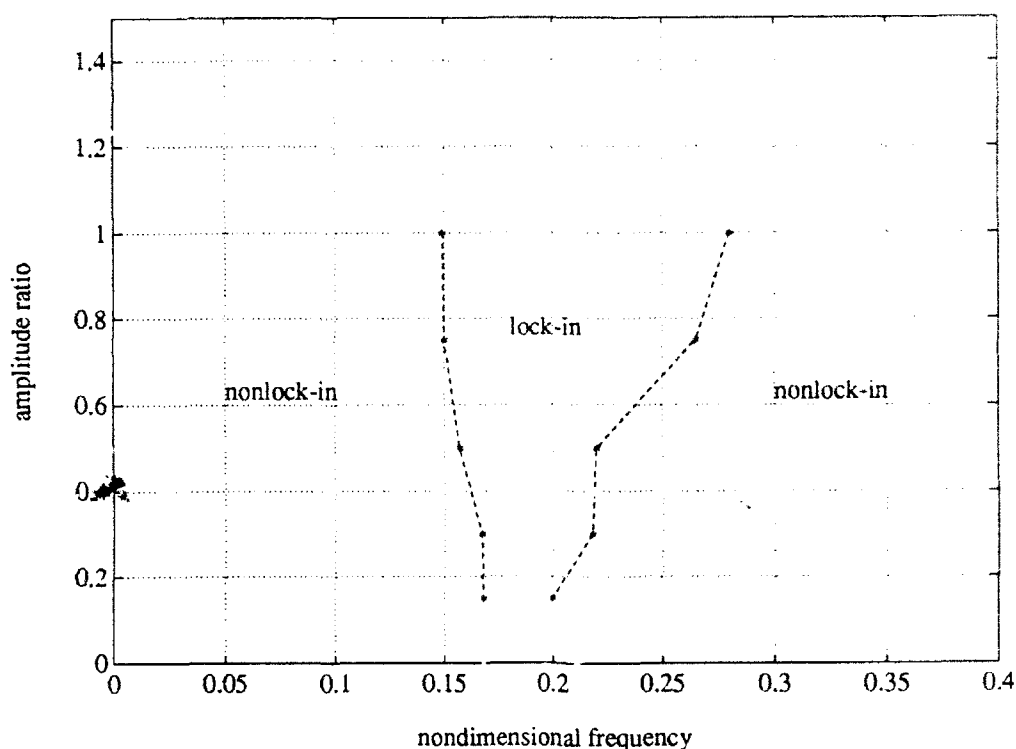


Figure 3-30: Experimentally determined lock-in region for sinusoidal oscillations.

frequency can be detected in the wake. It should be noted that the determination of the lock-in boundaries became increasingly difficult at higher oscillation amplitudes.

Our experimentally determined lock-in region of Figure 3-30 is not dissimilar from widely available published results [6, 7, 47, 50, 73], but it is very important to distinguish this lock-in region from the *excitation region*. The latter refers to the range of frequency and amplitude combinations over which self-excited oscillations are possible, and is obtained directly from the zero contour of Figure 3-14. The excitation regions (primary and secondary) are illustrated in Figure 3-31, where the notations "power +" and "power -" are used to denote the regions of positive power transfer (excitation) and negative power transfer (damping) respectively. Also marked on Figure 3-31 are the asterisks denoting the lock-in boundaries seen earlier. It is readily apparent that lock-in, which is determined by frequency considerations, is not at all the same thing as excitation, which is determined by phase considerations. Depending on the values of parameters such as the structural natural frequency, ambient flow velocity, etc., it is entirely possible for a cylinder to exhibit vortex-induced vibrations without the wake being synchronized to the structural oscillations. Such behavior has been

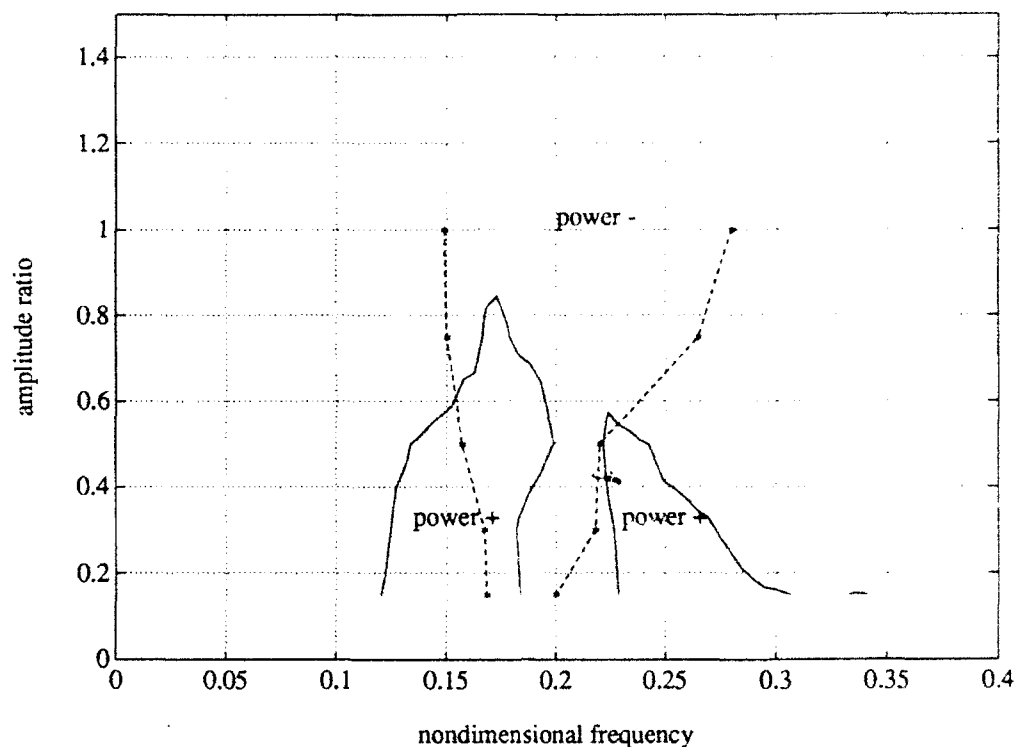


Figure 3-31: Excitation and lock-in regions for sinusoidal oscillations.

suggested by the laboratory work of Moeller [50], and Van Atta and Gharib [86], and has recently been confirmed by experiments on lightly damped cylinders conducted by Vandiver *et al.* [87].

While the lock-in phenomenon is a fascinating feature of the vortex shedding problem, knowledge or estimates of the lock-in boundaries do not provide any information on the exciting or damping effect of the lift force. The excitation phenomenon is far more useful from the point of making engineering response predictions. We believe that the two concepts of lock-in and excitation have been confused in the literature.

3.7 Time-domain analysis of the wake response

In Section 3.4 we mentioned that a time-domain upcrossing analysis was used to verify the behavior of the lift force phase angle. This time-domain method was extensively modified, refined and used in the analysis of beating records, to be presented in Chapter 5. In the process of verifying the analysis method, we found it useful to process our sinusoidal runs in the same manner. We discovered that the time-domain method was often better than

the frequency-domain method (presented in the previous section, as in Figure 3-29) for the detection and classification of the response modes of the cylinder wake.

From their numerical study of a vortex wake subjected to external forcing, Karniadakis and Triantafyllou [35] concluded that three typical wake response modes could be detected. These were:

1. *Periodic nonlock-in*, which is identical to the unforced natural shedding process. The external forcing (cylinder oscillations) is such that the wake does not "feel" this forcing.
2. *Quasiperiodic nonlock-in*, which is due to interaction between the natural shedding frequency and the forcing frequency. For certain values of the forcing, this could lead to a chaotic state of the response.
3. *Periodic lock-in*, which is the classical "wake-capture" mode. The external forcing controls the vortex shedding process and the natural shedding frequency disappears.

Karniadakis and Triantafyllou termed the boundary between the first two modes the "receptivity boundary" (i.e. outside this boundary the wake is not receptive to the external forcing) and the boundary between the second and third modes the "lock-in boundary". As we saw in the earlier section, an analysis of spectra was sufficient to distinguish between nonlock-in and lock-in, but not sensitive enough to further discriminate between types of nonlock-in, i.e. to capture the receptivity boundary.

Figures 3-32, 3-33, and 3-34 illustrate some results of our time-domain processing; we have purposely chosen two of the same cases of Figure 3-29. Each of these figures consists of several subplots. The first two subplots (from the top) are time traces of the motion amplitude ratio and normalized lift coefficient magnitude respectively. The time points corresponding to each upcrossing of each of the time traces were determined, and then used to calculate the "instantaneous" periods (and hence "instantaneous frequencies") of lift and motion and the "instantaneous" phase angle between the lift and the motion. (The term "instantaneous" is used within quotes to denote the values of frequency or phase angle calculated from one upcrossing to the next, i.e. over one cycle of oscillation.) The third subplot shows the variation of the "instantaneous" phase angle with time. Finally, the fourth and fifth subplots (at the bottom) depict histograms of the calculated motion and

Figure 3-32: Time-domain processing applied to $Y_0/d = 0.50$, $\hat{f}_0 = 0.107$.

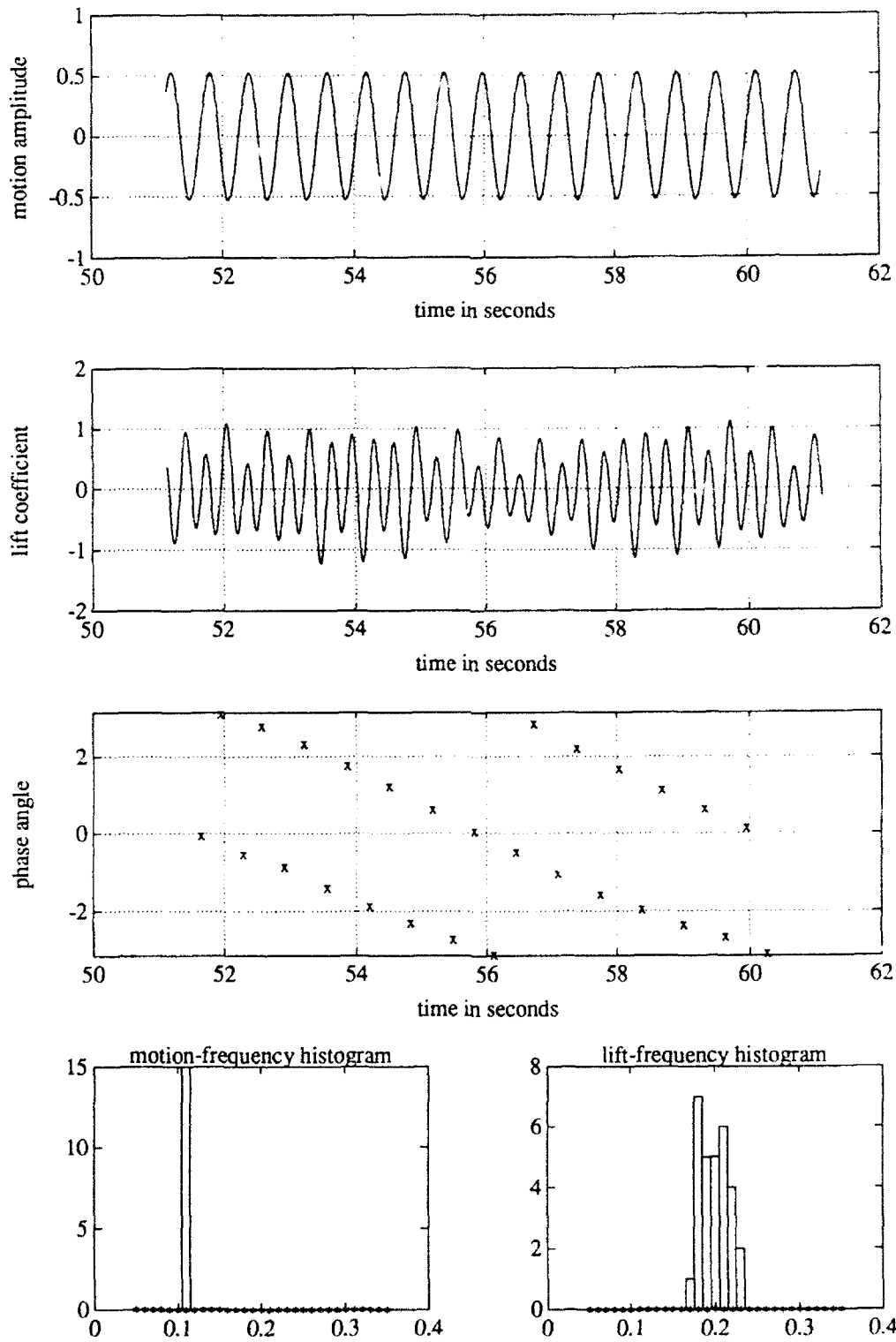


Figure 3-33: Time-domain processing applied to $Y_0/d = 0.50$, $\hat{f}_0 = 0.152$.

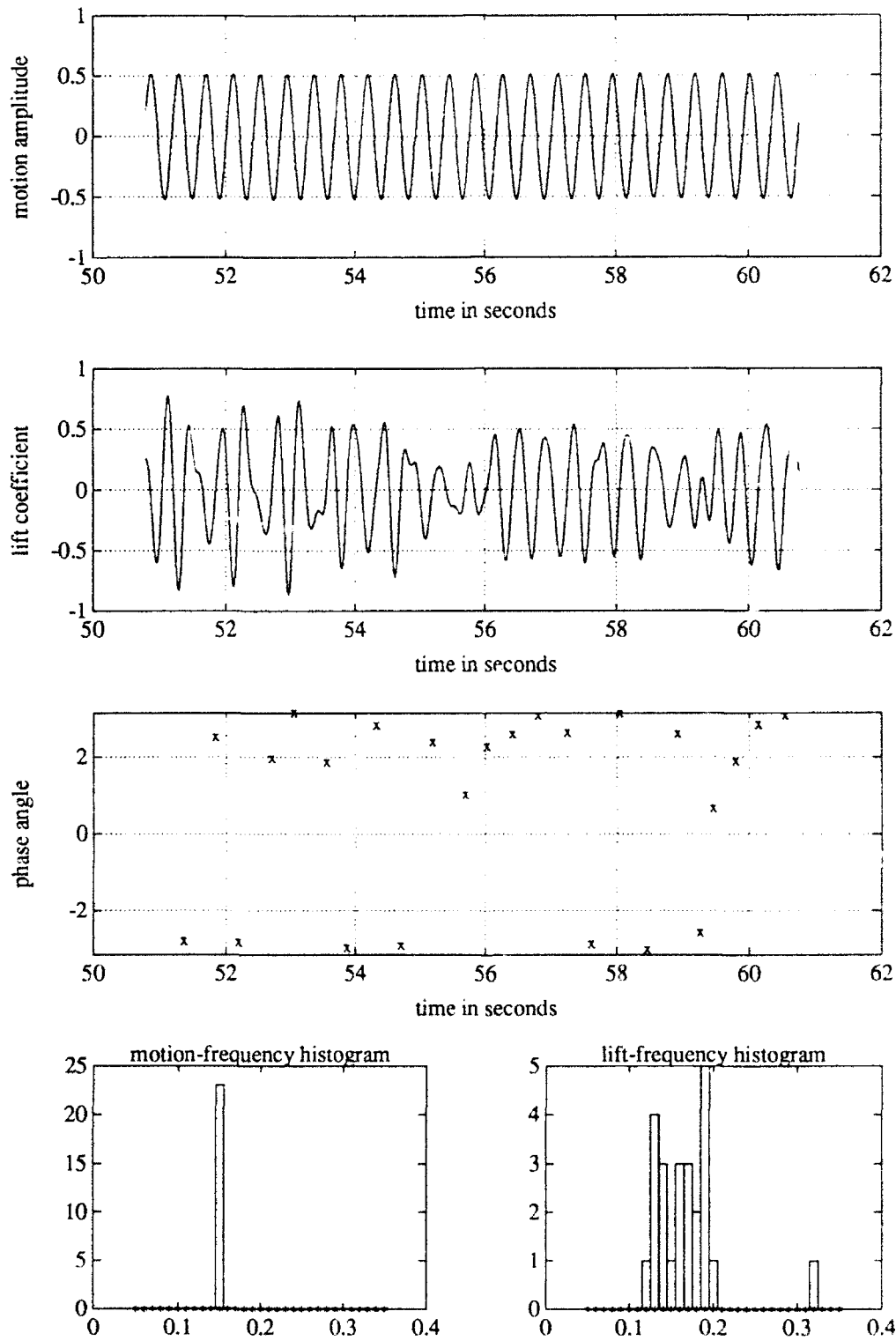
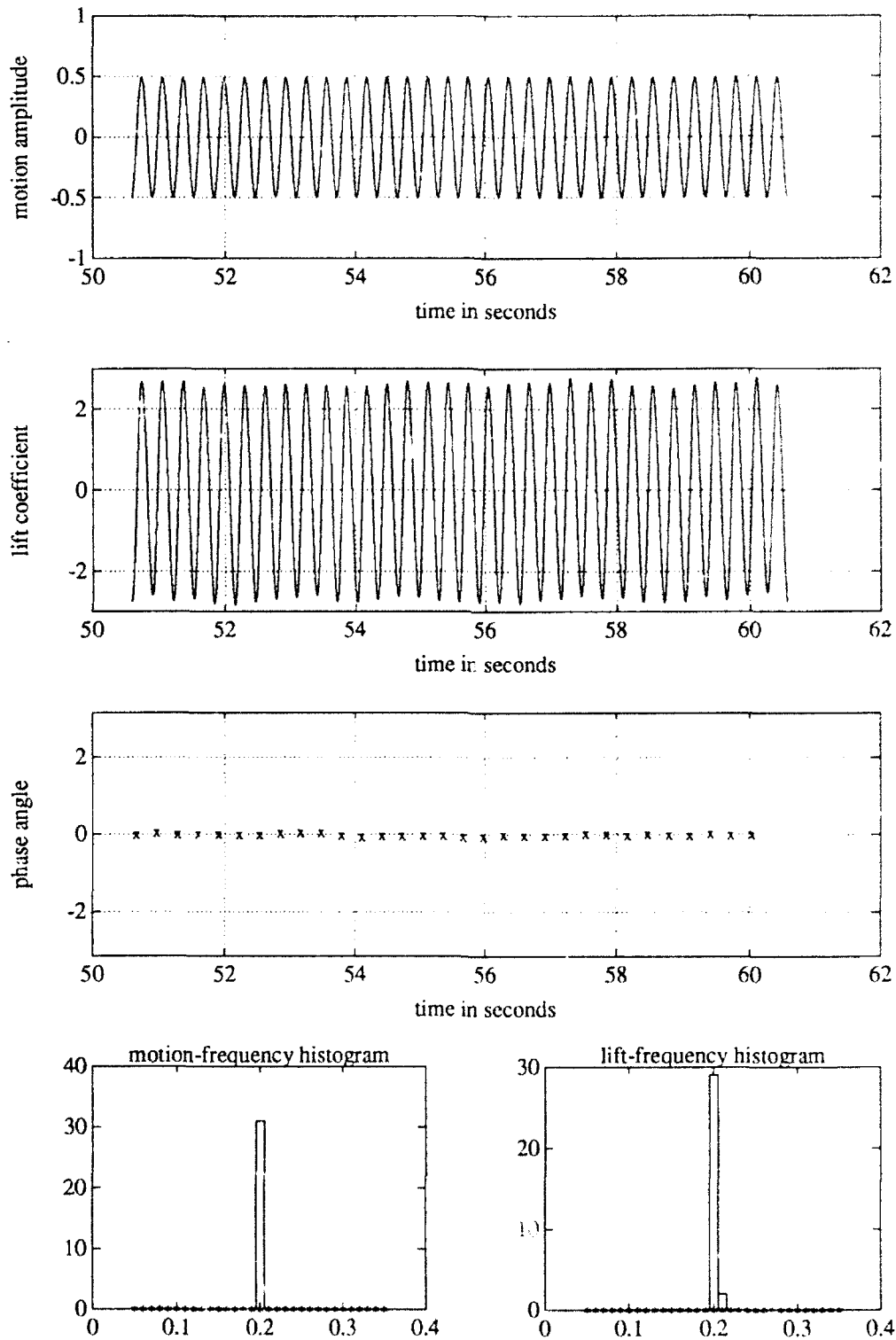


Figure 3-34: Time-domain processing applied to $Y_0/d = 0.50$, $\hat{f}_0 = 0.203$.



lift frequencies, plotted using 30 bins between $\hat{f}_0 = 0.05$ and $\hat{f}_0 = 0.35$.

Figure 3-32 shows the case of sinusoidal oscillations at an amplitude ratio $Y_0/d = 0.50$ and a nondimensional oscillation frequency $\hat{f}_0 = 0.107$. From the time traces of the motion and the lift coefficient, it is clear that the wake vortex shedding frequency (lift) is not the same as the external forcing frequency (motion). Some amplitude-modulation of the lift force trace is seen, but this is not dissimilar to the purely stationary (unforced) case, as in Figure 3-5. The plot of phase angle against time shows the variation characteristic of a phase calculation between waveforms of different (constant) frequencies. The frequency histograms reveal that while the motion has a constant frequency near 0.10, the lift force has "instantaneous" frequencies in a band around the natural Strouhal shedding value of 0.20. One concludes that the wake does not feel the effect of the cylinder oscillations, and hence this is an example of *periodic nonlock-in*.

At the same amplitude ratio and a slightly higher oscillation frequency, Figure 3-33 illustrates the results for $\hat{f}_0 = 0.152$. In this case, the lift force trace is clearly irregular in nature, and the phase angle is widely scattered. One is tempted to use the word "chaotic", although a convincing demonstration of chaos in a mathematical sense requires far longer time traces than are shown here. The frequency histograms show that while the motion is a single-frequency oscillation at $\hat{f}_0 \approx 0.15$, the lift force fluctuates randomly between the cylinder oscillation frequency and the natural Strouhal frequency. Because of competition between these two components, the resulting wake response is irregular: this is an example of *quasiperiodic nonlock-in*.

The third situation of *periodic lock-in* is depicted by Figure 3-34. There is a dramatic change in the nature of the lift force trace, which now appears as almost a pure sinusoidal waveform at the same frequency as that of the motion. The phase angle assumes a constant value with little variation, and the histograms show negligible scatter of the "instantaneous" frequencies of either the motion or the lift.

A large number of cases at different oscillation amplitudes and frequencies were analyzed as above by the time-domain method. The lower receptivity and lock-in boundaries (at frequencies below the Strouhal number) were easy to identify. The upper boundaries (at frequencies above the Strouhal number) were less clearly distinguishable, owing to the increasing "saturation effect" of the inertial component of the lift force. Figure 3-35 is a wake response state diagram, and illustrates the regions of amplitude and frequency

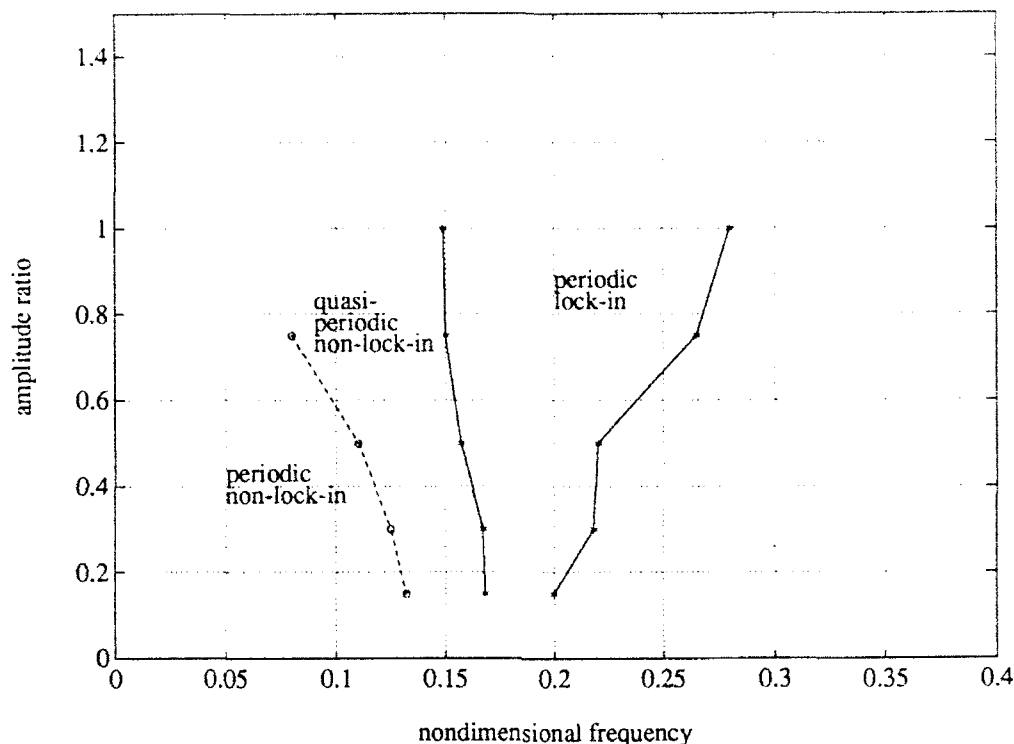


Figure 3-35: Wake response state diagrams from time-domain processing.

corresponding to periodic nonlock-in, quasiperiodic nonlock-in, and periodic lock-in. The lock-in boundaries (shown by asterisks connected by solid lines) were almost identical to those found earlier (Figure 3-30). Only the lower receptivity boundary could be determined (shown by circles connected by a dashed line). Although Karniadakis and Triantafyllou [35] do not provide any quantitative information on the locations of the lock-in and receptivity boundaries, Figure 3-35 confirms their findings in a qualitative sense. The wake response states depicted here are typical of the situation below an oscillation amplitude of about one diameter; above this range, more complex periodic states are likely (Williamson and Roshko [95], and Section 3.5.2).

It should be noted that transition from one wake state to another across the lock-in or receptivity boundaries can occur by a change in the oscillation amplitude at constant frequency. Early in our experimental schedule, we conducted a few tests of sinusoidal cylinder motion with slow linear variation of the amplitude; the object being to accumulate a large quantity of data in a short time. These tests were later abandoned due to difficulties with data processing; however some of the runs illustrate the different wake modes clearly.

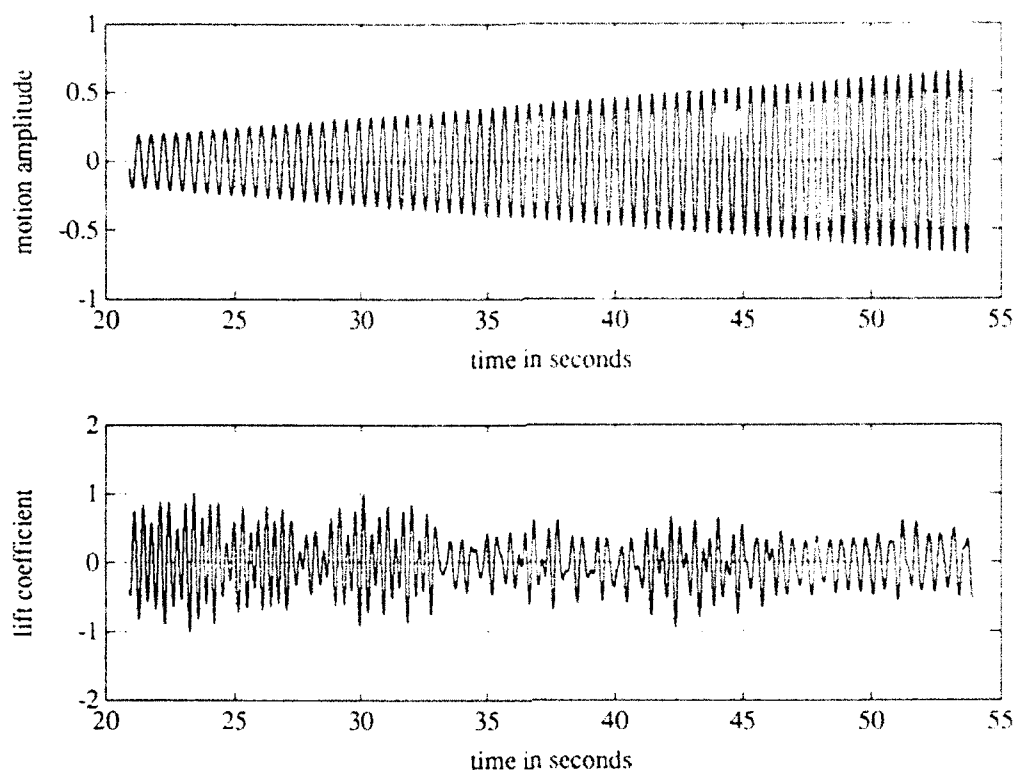


Figure 3-36: Motion and lift for increasing linear amplitude. $\hat{f}_0 = 0.132$.

Figure 3-36 is a typical example, showing the normalized motion and lift force time traces for oscillations at frequency 0.132 and amplitude increasing from approximately 0.20 to 0.70 in a duration of about 25 seconds. Initially, up to a time of about 33 seconds, the lift responds at a frequency higher than the imposed oscillation frequency; this is periodic nonlock-in. From about 33 seconds until about 47 seconds, the lift trace has a very irregular form corresponding to quasiperiodic nonlock-in. Finally, from a time of about 47 seconds until the end of the record, the lift shows signs of stabilizing at the oscillation frequency; this range corresponds to the beginning of periodic lock-in. We do note that the transition amplitudes (the amplitudes at times 33 and 47 seconds) correspond only roughly with the state diagram of Figure 3-35; we attribute this to the possible “memory” effect of the amplitude variation, as well as the difficulty of accurately classifying the wake response at high oscillation amplitudes.

Chapter 4

Error Analysis and Application to VIV Predictions

4.1 Preliminary remarks

In this chapter we shall survey some of the important considerations regarding the applicability of our experimental data to both scientific and engineering situations. The most important consideration is, of course, an error analysis, which studies the extent to which our data truly represents the variable or phenomenon being measured. In addition, while it is not the purpose of this thesis to develop a comprehensive VIV prediction algorithm, we shall present some general principles involved in the application of our data to such predictive calculations. We shall also study cross-sectional effects, i.e. we shall investigate the vortex-induced forces on a variety of “real-world” structural cross-sections that are often represented as smooth circular cylinders, but in fact may not be so.

4.2 Error analysis

4.2.1 Introduction

In experimental studies such as ours, the risk of system errors is always present. In general, there are two types of errors that could arise from flaws or limitations of the experimental method: *systematic errors*, which affect the overall *accuracy* and cause a consistent deviation of the measured data from the true values; and *random errors*, which affect the overall

precision and set a limit to the repeatability of the experimental realizations. Systematic errors are not easy to detect, since one requires an *a priori* knowledge of the true value of the variable in consideration. Random errors can be identified by a statistical analysis of a number of measurements, but in general are impossible to separate from the underlying properties of the random distribution of the physical quantity being measured. In this section we shall use a variety of techniques in an attempt to quantify both the systematic and random errors introduced by our experimental system.

In Chapter 2, we saw that great care was taken in the selection and operation of each component of the experimental apparatus; but an overall system accuracy was impossible to obtain from a knowledge of the individual component specifications. During the data processing stage, several methods were used to minimize the introduction of additional error. For example:

- The majority of the processing took place via the use of large batch programs set up to execute automatically, with a minimum of subjective decision making.
- In the process of initial setup and verification of the experimental apparatus, the accuracy of the lead-screw and motor system in reproducing desired oscillation amplitudes and frequencies was investigated. It was found that the oscillation frequency was extremely accurate to 0.01%, but the oscillation amplitude was accurate only to about 5%. As a result, the actual realized oscillation amplitude was calculated for each data set, and based on the ratio of this value to the desired amplitude, a small linear correction was applied to the calculated force coefficient magnitudes. The calculations were flagged for manual investigation if the amplitude error exceeded 5%, and were abandoned entirely (and the run repeated) if the error exceeded 10%.
- In order to avoid the accumulation of errors due to frequency, a "time-gating" procedure was developed so that the oscillating force coefficients were calculated over successive gates of length 20 cycles each, and the values obtained for the different gates averaged.
- In the case of the mean drag force, the final zero period was chosen to provide the baseline value since it was found that large force transients on carriage start-up interfered with the accurate recording of the initial zero period. Care was taken to ensure

that the mean value of the drag force during the run period was calculated over an integer number of oscillation cycles.

As we shall see, the combined effect of all of the above error control procedures was that we can rightfully claim a high degree of confidence in our data.

4.2.2 Wet calibrations and long-term stability

In Chapter 3, we presented results for several runs conducted with the model cylinder held stationary, in what we termed "wet calibrations". Figures 3-2 and 3-3 of that chapter showed histograms of the mean drag coefficient and oscillating lift coefficient respectively for the stationary runs; we saw that these data formed well-defined normal distributions with standard deviations of the order on 3% of the mean in the case of the mean drag, and 23% of the mean in the case of the oscillating lift.

Figures 4-1 and 4-2 illustrate the same data plotted against sequential event indices along the X axis. The realizations of the mean drag coefficient (Figure 4-1) appear randomly distributed about a value between 1.10 and 1.20, while the realizations of the lift coefficient (Figure 4-2) are scattered primarily between 0.30 and 0.50. The important point to be made from these figures is the excellent long-term stability of our experimental system. The 122 realizations shown here spanned a period of about 16 months, during which time the apparatus was dismantled, stored, reassembled, and re-calibrated on at least four occasions. There is no evidence that these operations caused any significant drifts and/or "DC-offsets" in the measured data. Least-squares straight line curve-fits through the data points revealed long-term variations of only 0.34% in the mean drag data and 1.24% in the lift data, providing indirect evidence of the lack of systematic errors in our method.

4.2.3 Statistical properties of the sinusoidal data

We investigated the statistical distribution properties of our sinusoidal data in two ways: we calculated the data spread *within* each experimental run, and we conducted a number of runs at constant oscillation amplitude and frequency in order to find the data spread *across* several runs of the same type.

Earlier in this chapter, as well as in Chapter 2, we saw that all of our experimental data traces were divided into "gates" of 20 oscillation cycles each, and the various results calcu-

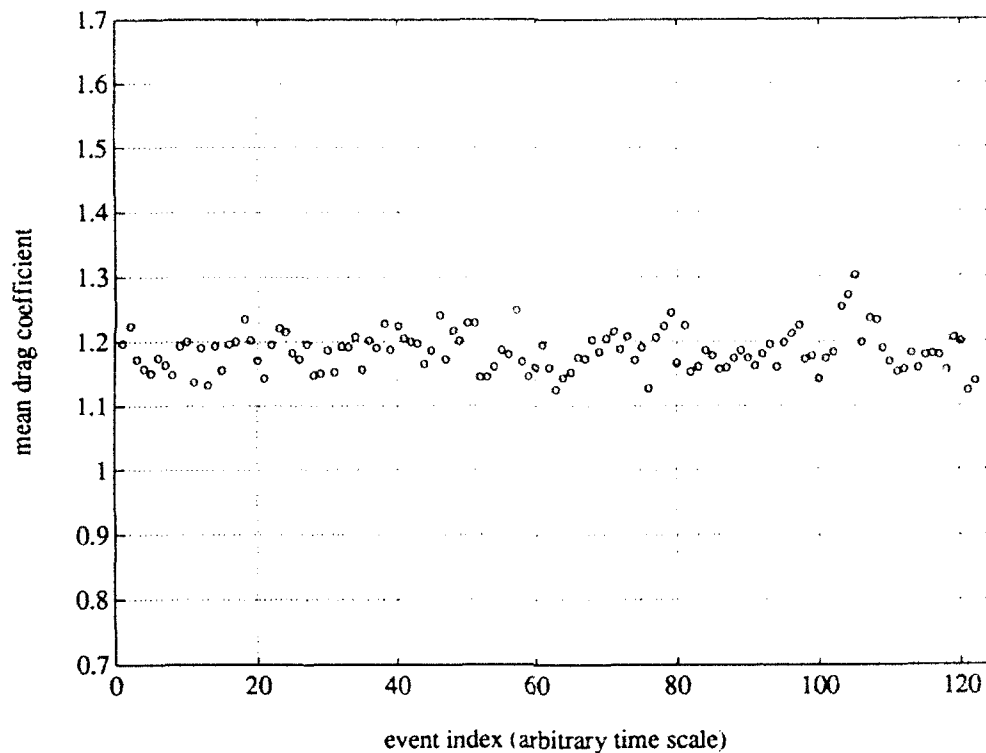


Figure 4-1: Realizations of the mean drag coefficient; stationary runs.

lated for each gate and finally averaged. For the purposes of error analysis, our MATLAB processing routine was modified so as to record the maximum and minimum values of the force coefficients calculated for the different gates within each run. These maximum and minimum values were then taken to represent the data spread of the corresponding coefficient for that particular run. For example, Figures 4-3 and 4-4 show the results for the lift coefficient magnitude (amplitude ratio 0.15) and the lift coefficient phase angle (amplitude ratio 0.50) respectively, together with the corresponding maximum and minimum values plotted in the form of error bars. It is clear from these figures that the data spread across the different gates for each of the values remained consistently small, except in regions of rapid variation of coefficient magnitude or phase angle. Similar results were obtained for the various lift and drag force coefficients for these and other amplitude ratios. It should be noted that while this spread analysis is not rigorous in a statistical sense (since the number of gates within a particular run was not constant but varied from 2 at the lowest oscillation frequencies to 13 at the highest oscillation frequencies), it does provide some idea of the variability of the data.

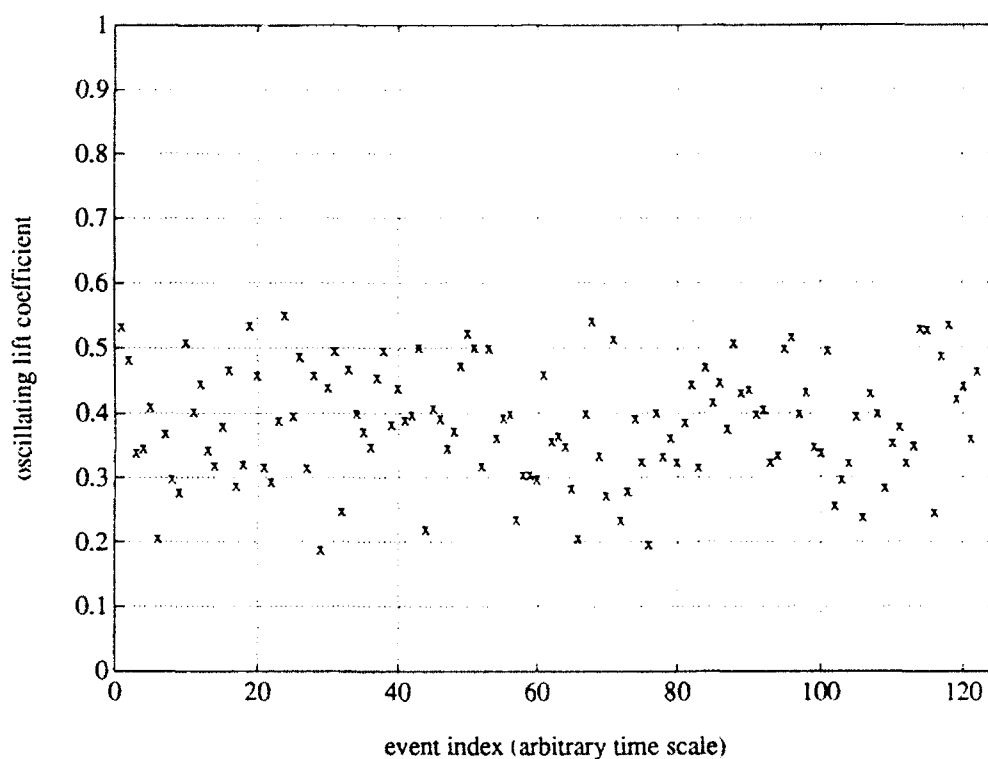


Figure 4-2: Realizations of the oscillating lift coefficient; stationary runs.

In addition to the spread of the data within each run, we selected (arbitrarily) one particular oscillation amplitude and frequency combination for further analysis. Thus 36 complete sinusoidal oscillation tests were conducted at a nondimensional frequency $\hat{f}_0 = 0.203$ and an amplitude ratio $Y_0/d = 0.75$. Values of the mean and oscillating drag coefficients and the lift coefficient magnitude and phase angle were calculated and histograms constructed from the results. Figure 4-5 shows the histogram of the mean drag coefficient results: it can be approximated by a normal distribution, with a mean of 1.961 and a standard deviation of the order of 1.6% of the mean. Figure 4-6 illustrates the histogram of the lift coefficient magnitude for the same runs: this appears as a skewed normal distribution with a mean of 3.095 and a standard deviation of the order of 1.8% of the mean. While the asymmetry of Figure 4-6 could point to an insufficient number of realizations (or could possibly reflect the underlying characteristics of the lift force distribution), the important fact is that the total data spread across the 36 individual realizations is remarkably small. Results for the oscillating drag coefficient and lift force phase angle data were similar to Figures 4-5 and 4-6; the net conclusion was that the *precision* of our experimental process was excellent.

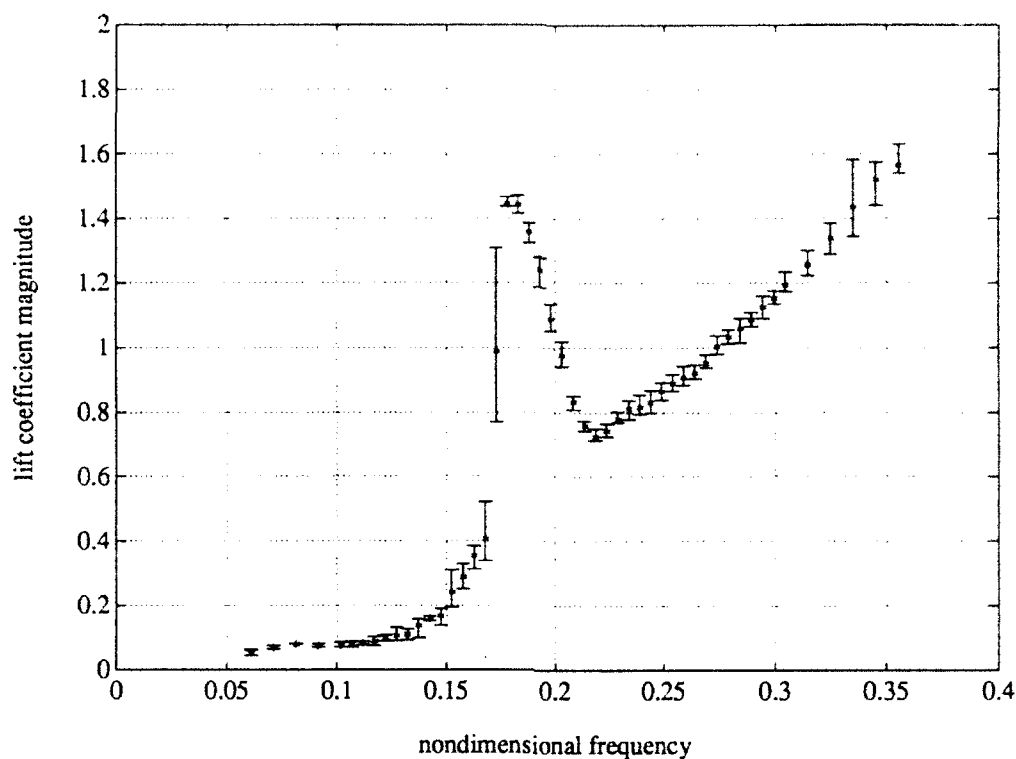


Figure 4-3: Lift coefficient magnitude for $Y_0/d = 0.15$, with error bars.

4.2.4 Comparisons with published results

The previous paragraphs demonstrate that our experimental apparatus and analysis methods produced highly reproducible data (i.e. low random errors), but they do not conclusively show that our results accurately reflected the actual physical phenomena (i.e. low systematic errors). Fortunately, a great deal of data has been accumulated over the years on the vortex-induced forces acting on sinusoidally oscillating cylinders, and this data provides a convenient standard for the results from our apparatus. (As we mentioned in Chapter 3, the original *rationale* for our sinusoidal oscillation tests was that we could use these as a means of relating the beating oscillation data to standard sinusoidal results available in the literature.)

In the case of the mean drag force, the variation of the *resonant* mean drag as a function of oscillation amplitude is commonly available. This is the maximum value of the drag coefficient (at a given amplitude) over all oscillation frequencies in the vicinity of the resonant Strouhal number, and is commonly given in terms of the ratio of the resonant drag coefficient (with oscillations) to the stationary drag coefficient, i.e. $C_{D_{m_{\text{oscillations}}}}/C_{D_{m_{\text{stationary}}}}$.

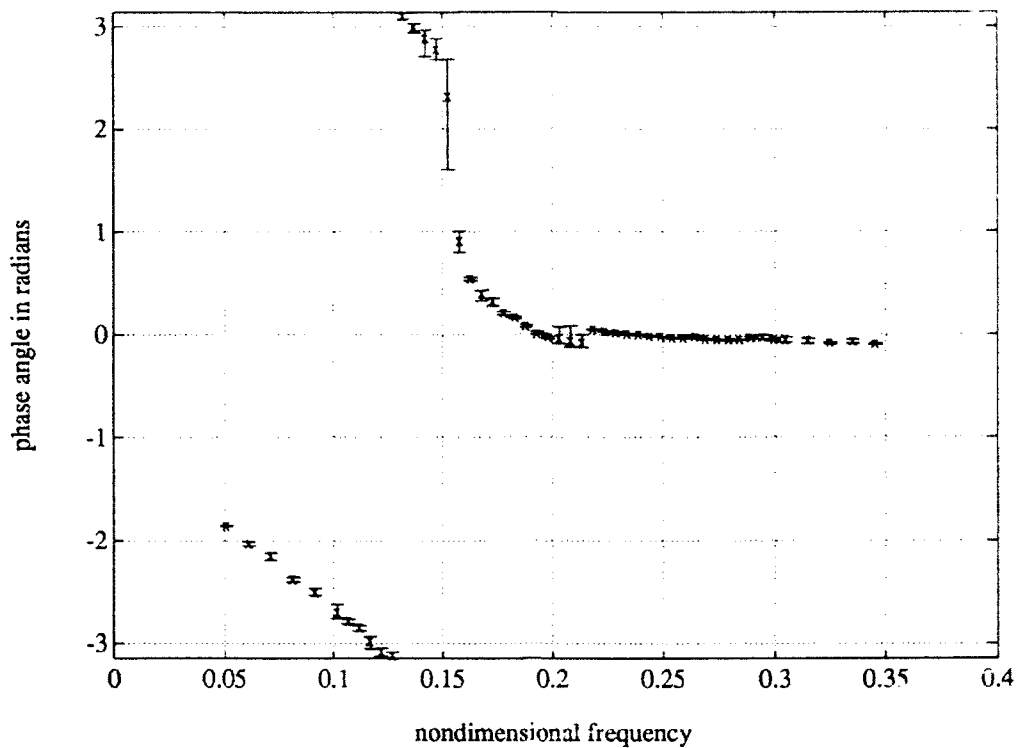


Figure 4-4: Lift coefficient phase angle for $Y_0/d = 0.50$, with error bars.

Figure 4-7 illustrates this drag amplification ratio as a function of oscillation amplitude ratio for sinusoidal oscillations, with data from various sources (Reynolds numbers in the range $5,000 < Re < 60,000$). Individual data points are marked with numerals “1”, “2”, etc. identifying their origin; the dashed line shows a curve-fit through data from various sources, including field experiments on marine cables (Vandiver [89], Kim [36]). A large scatter in the data is seen, illustrating the strong influence of different experimental conditions. Our present data, identified by “MIT”, are clearly in the middle of all the scatter, and the maximum deviation from Vandiver’s curve-fit is only of the order of 10%.

In the case of the oscillating lift coefficient, fewer sources are available, and the data are not always comparable. For instance, many researchers quote only the measured lift coefficient magnitude (or RMS value), which conveys very little useful information without knowledge of the associated phase angle. Even those sources that do include both lift magnitude and phase information often use different sign and angle conventions, and direct comparisons are difficult. We shall compare our lift coefficient results to those of Sarpkaya [65] and Staubli [75].

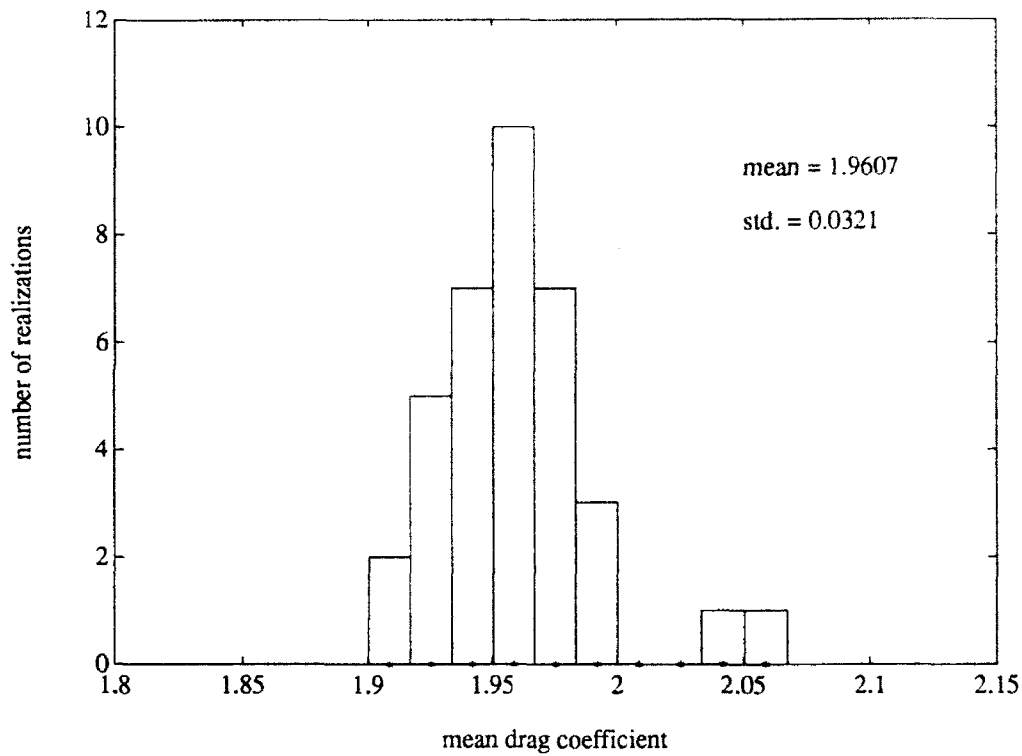


Figure 4-5: Histogram of C_{D_m} ; sinusoidal oscillations at $Y_0/d = 0.75$ and $\hat{f}_0 = 0.203$

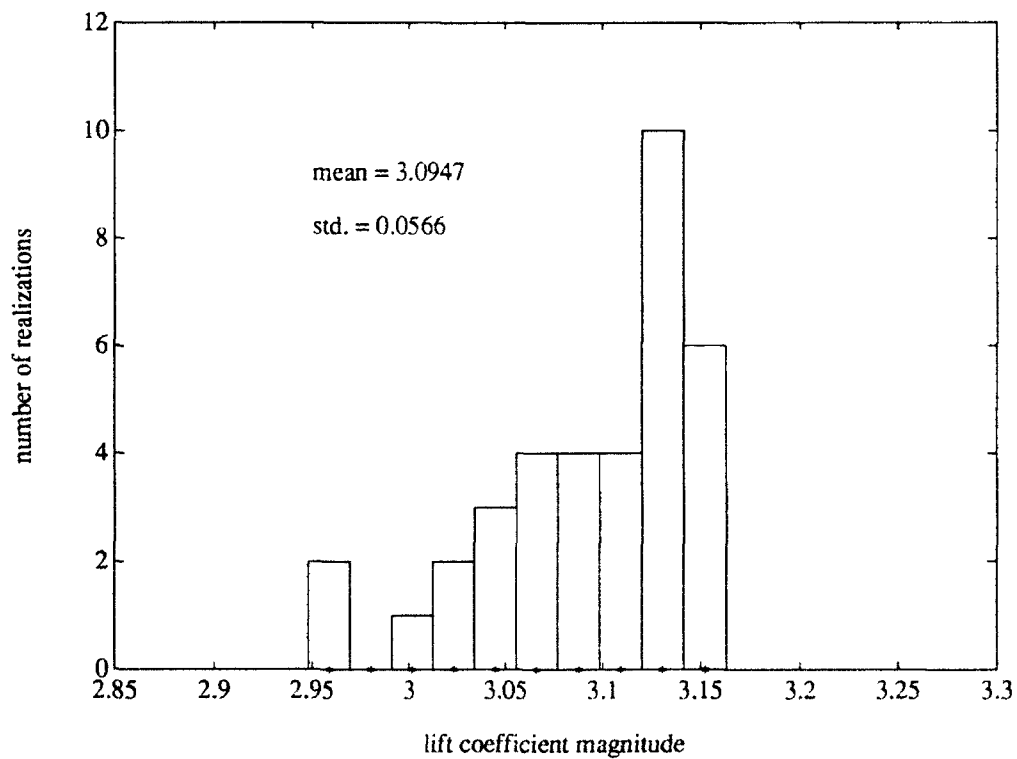
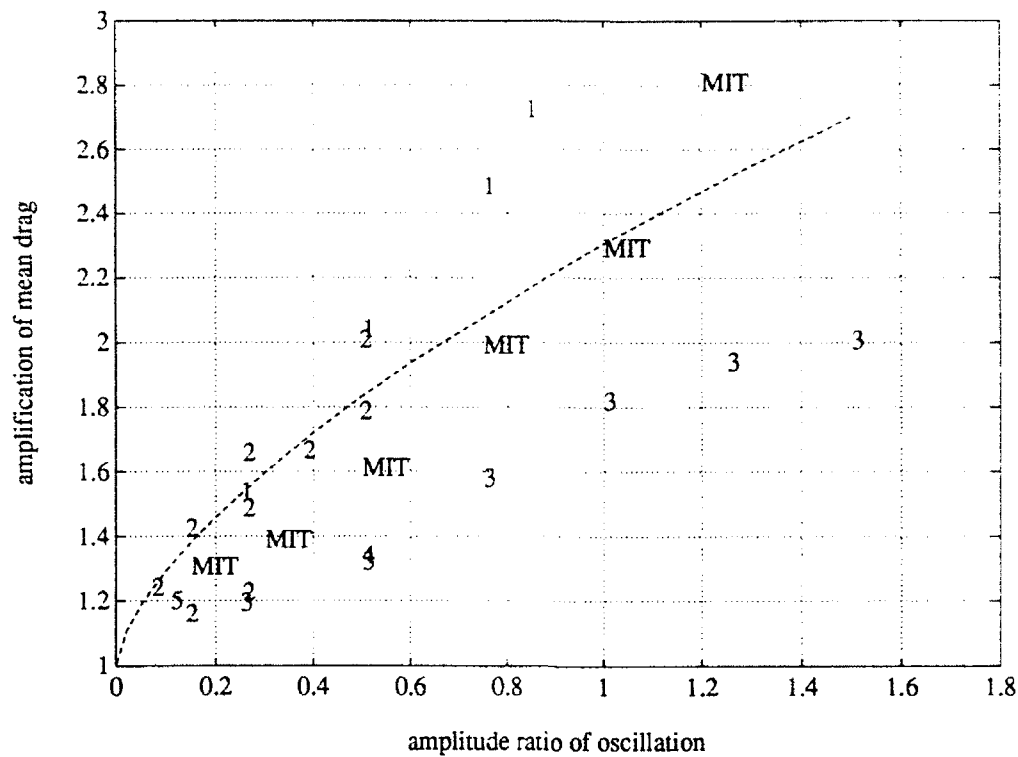


Figure 4-6: Histogram of C_{L_0} ; sinusoidal oscillations at $Y_0/d = 0.75$ and $\hat{f}_0 = 0.203$



| Legend | |
|--------|---------------------------------|
| - - - | curve fit from Vandiver [89] |
| 1 | data from Sarpkaya [65] |
| 2 | data from Schargel [68] |
| 3 | data from Mercier [47] |
| 4 | data from Bishop and Hassan [6] |
| 5 | data from Staubli [75] |
| MIT | present results |

Figure 4-7: Drag amplification ratio as a function of amplitude ratio, various data sources.

Figures 4-8 and 4-9 show plots of our lift coefficient components in phase with (negative) acceleration and (positive) velocity respectively for the constant amplitude ratio of 0.15, compared to Staubli's coefficients \hat{C}_{LOC} and \hat{C}_{LOS} for the amplitude ratio 0.11 [75]. The X axes in all the plots represent nondimensional frequency. Staubli's sign convention is such that his \hat{C}_{LOC} is equal to the *negative* of our C_{L-A_0} , while his \hat{C}_{LOS} is identical to our C_{L-V_0} . In addition, he uses the notation S_0 for the nondimensional frequency and $\hat{\xi}$ for the nondimensional amplitude ratio. From the figures, it is clear that the variations of $-C_{L-A_0}$ and C_{L-V_0} with frequency compare very well to the variations of \hat{C}_{LOC} and \hat{C}_{LOS} respectively. The small differences that do exist could well be due to the differences in

Figure 4-8: Comparing our $-C_{L-A_0}$ results with those from Staubli (1983)

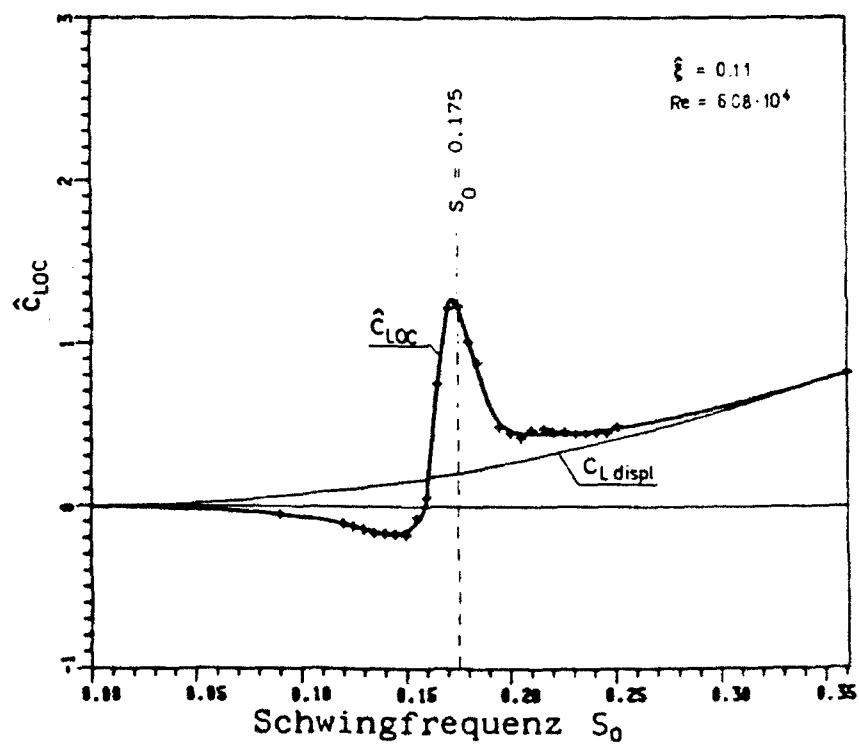
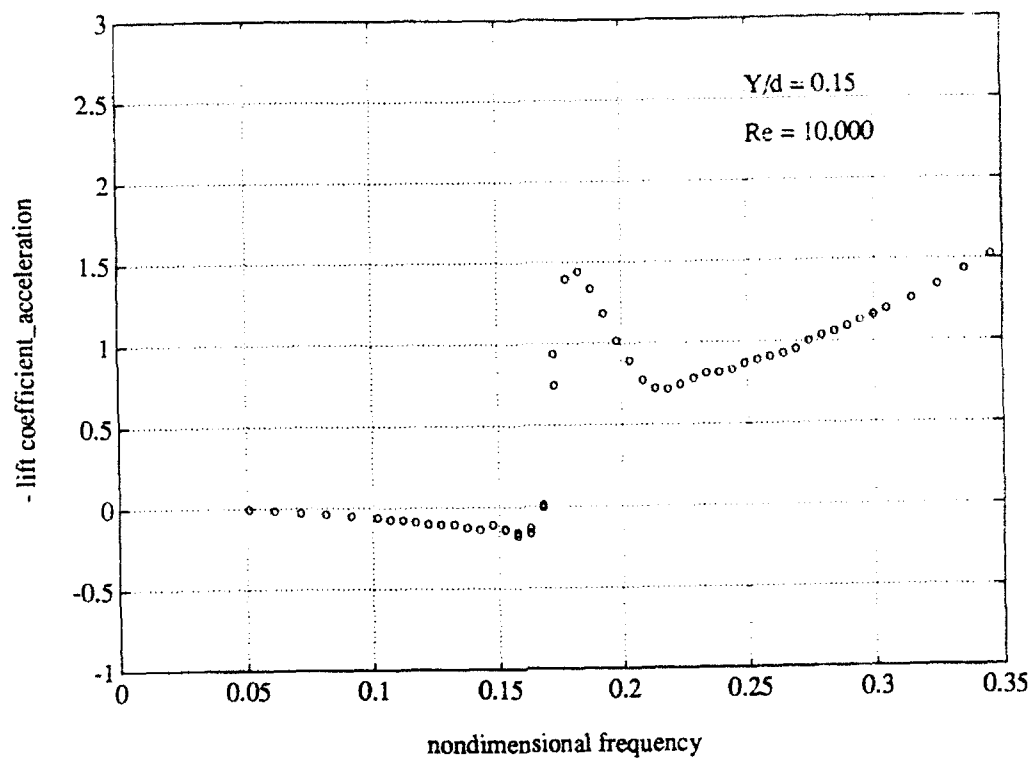
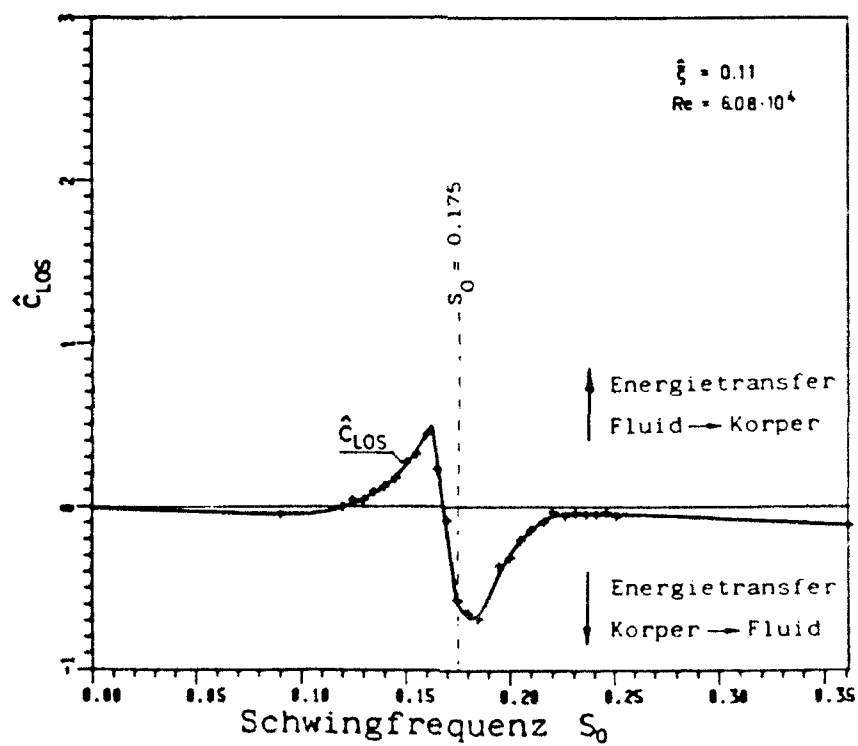
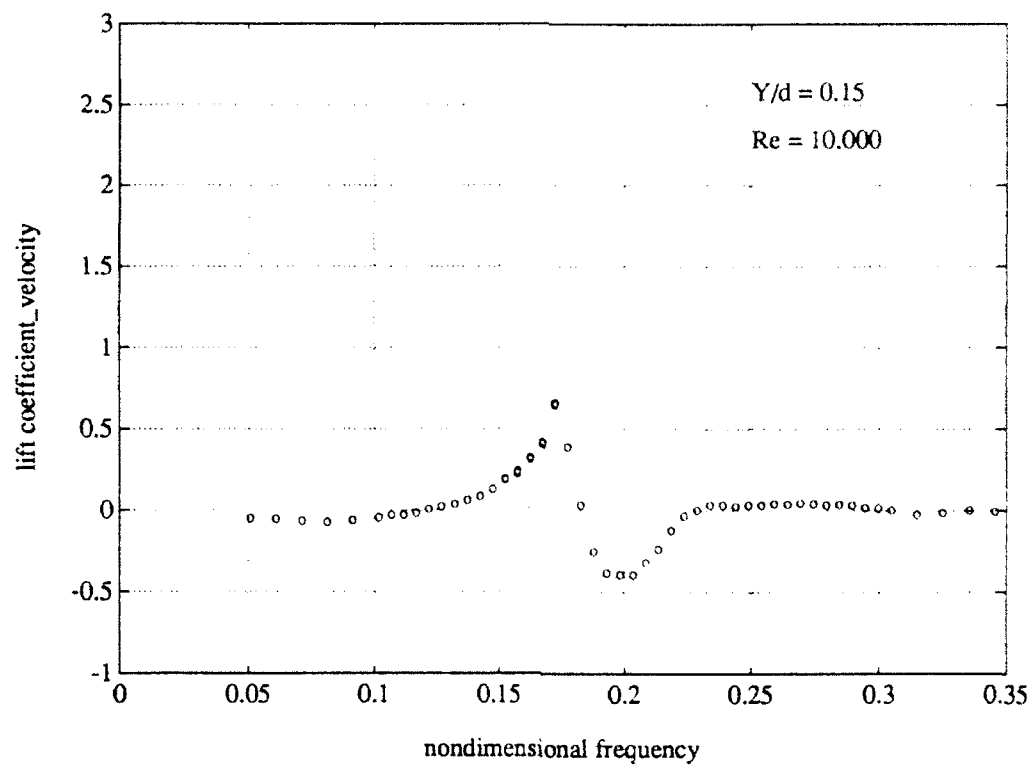


Figure 4-9: Comparing our C_{L-V_0} results with those from Staubli (1983)



Reynolds number or oscillation amplitude.

Figures 4-10 and 4-11 show plots of our results for $-C_{L_{A_0}}$ and $-C_{L_{V_0}}$, compared to Sarpkaya's coefficients C_{mh} and C_{dh} respectively [65]. All the data were collected at the amplitude ratio 0.50, and are displayed against the nondimensional reduced velocity $V_R (= 1/\hat{f}_0)$. Sarpkaya's angle convention is such that his coefficients are precisely the negative of ours, i.e. $C_{mh} = -C_{L_{A_0}}$ and $C_{dh} = -C_{L_{V_0}}$, and he favors reduced velocity rather than nondimensional frequency as the independent variable. From Figure 4-10, the variation of $-C_{L_{A_0}}$ compares very well with the variation of C_{mh} , except for a shift of the X axis. A careful look at Figure 4-11 shows that while the data for $-C_{L_{V_0}}$ and C_{dh} look quite different, the main features of the excitation/damping trends are preserved, with the exception again of a shift in the reduced velocity axis. The differences between our lift coefficient data and Sarpkaya's are likely due to the large difference in the aspect ratios (and hence end conditions) of the models tested: we had an aspect ratio of 24 versus Sarpkaya's aspect ratios of between 3 and 11 (different models). The Reynolds numbers of the different experiments were all in the range $7,000 < Re < 11,000$.

4.2.5 The "bottom line"

Our analysis of the errors in the results obtained with our experimental apparatus and methods, as developed in the preceding paragraphs, eventually led us to the following summary conclusions (the "bottom line"):

- The experimental system and analysis procedures were capable of producing high precision, highly repeatable data. Conservative estimates of the random errors obtained would be of the order of 3-5% for the mean drag data and 5-8% for the oscillating drag and lift data.
- The data obtained compared favorably with other established results, indicating that systematic errors were also low. A precise estimate of the absolute accuracy is difficult to obtain, but our best indications are that this does not exceed 10-15%. Given the strong sensitivity of the vortex-shedding phenomenon to the prevalent physical conditions, we believe that few researchers can rightfully claim a higher accuracy for their experimental data.

Figure 4-10: Comparing our $-C_{L\alpha}$ results with those from Saipkaya (1977)

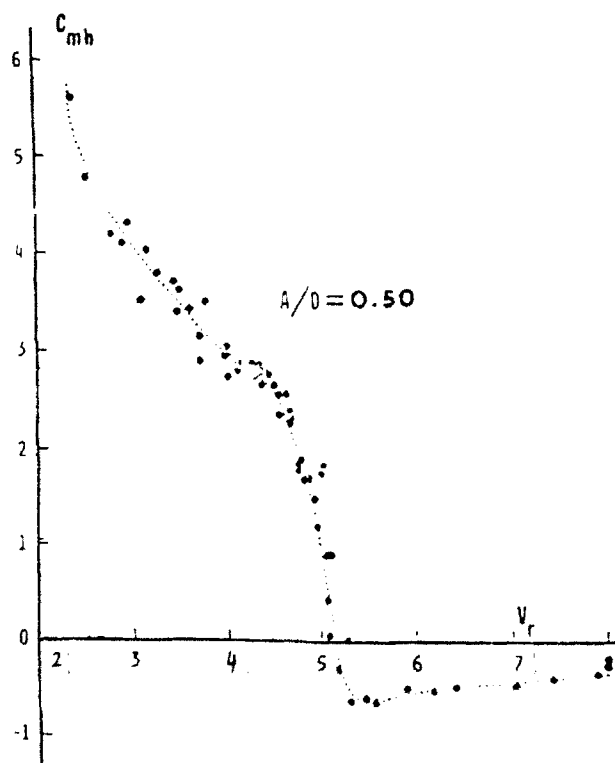
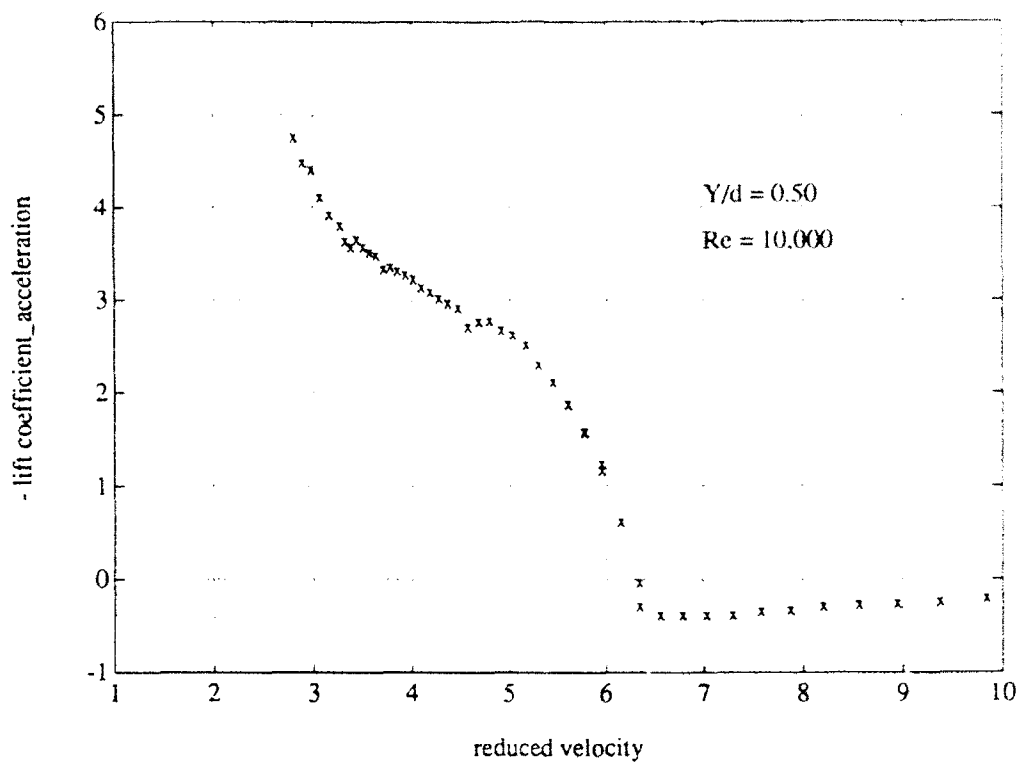
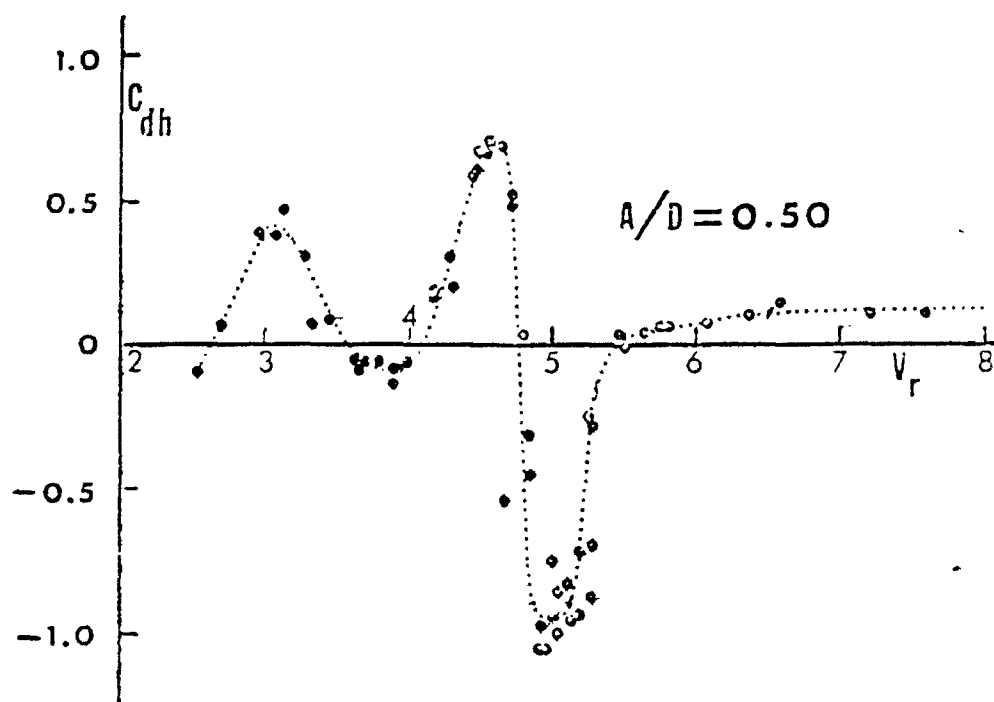
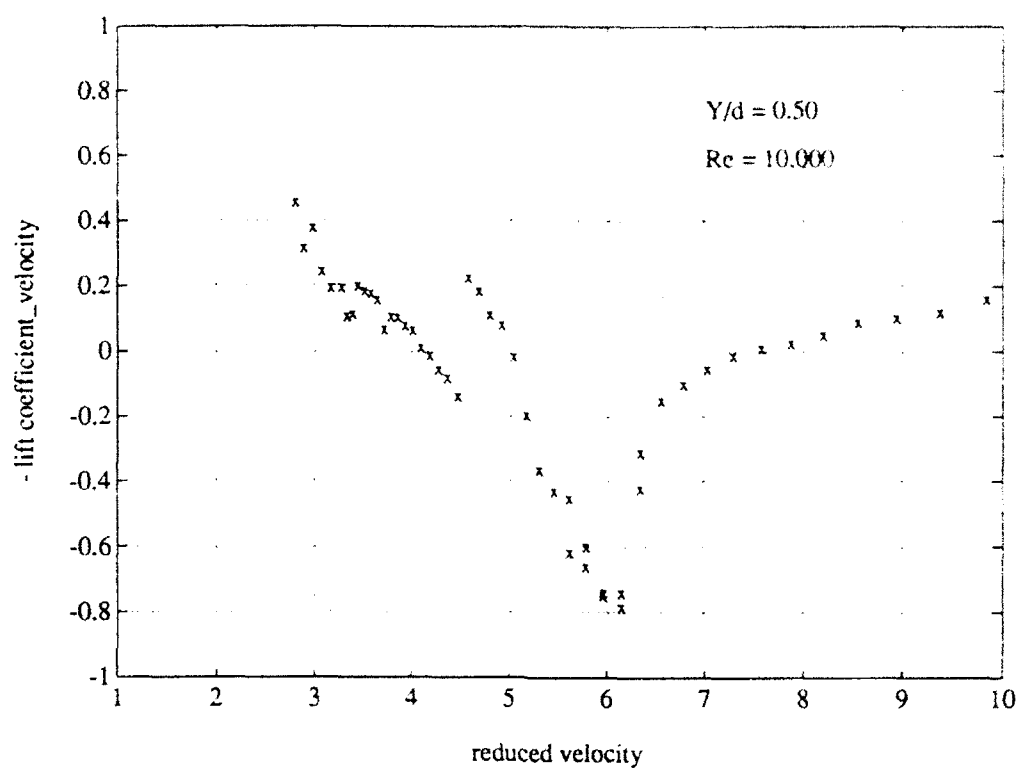


Figure 4-11: Comparing our $-C_{L\alpha}$ results with those from Sarpkaya (1977)



4.3 Applying our data to VIV predictions

4.3.1 General principles

From an engineering perspective, the primary purpose of conducting laboratory-scale experiments such as ours is to be able to predict the full-scale VIV response of structures in the ocean. The variable of interest changes with the circumstances. For example, in the case of an oil production or exploration riser exposed to current or wave action, one would be interested in predicting the frequency and magnitude of the induced oscillations so as to estimate the fatigue life of the riser, and also the mean drag force so as to estimate the static stress levels. In the case of an oceanographic towing (or mooring) cable, the VIV-amplified mean drag force determines the static configuration and the expected towing (or mooring) tension in the cable. In the case of a mooring line connecting to an acoustic transponder or array, knowledge of the amplitude and frequency of the vortex-induced cable strumming could be critical, as the vibrations could affect the acoustic measurements. In all of these cases, one would like to use the existing database, combined with some suitable mathematical model, to estimate the expected motions and forces.

In most situations, VIV response predictions involve two stages:

1. Estimating the oscillation frequencies and amplitudes from a knowledge of the flow configuration, using available lift coefficient data.
2. Estimating the static mean drag coefficient as a result of the oscillations found in the first step.

In general, the process could be iterative, since the mean drag force could act to change the static configuration and hence the flow around the structure. A VIV predictive algorithm has three essential components: a structural model, a fluid model (that interacts in some way with the structural model), and a solution technique. For the fluid model, one would ideally like to solve the time-dependent Navier-Stokes equations in the presence of the body motion; out of this analysis should emerge the frequency and magnitude of the fluid forcing. Unfortunately, theoretical and/or numerical solutions of the Navier-Stokes equations are available only for simplified cases or very low Reynolds numbers, and one has to resort to physical experiments to obtain the required data. In between direct Navier-Stokes solutions and physical experiments is a class of "wake-oscillator" models (Hartlen and Currie [30],

Skop and Griffin [71], Iwan and Blevins [32, 7]), that purport to depict the behavior of the vortex wake as a nonlinear Van der Pol or Rayleigh oscillator. Most of these models, however, are phenomenological constructs that do not stem from the underlying physics (Sarpkaya [66]), and hence need to be calibrated against experimental data themselves. Thus, forced-oscillation results such as ours could be used directly as the hydrodynamic input to a general VIV prediction scheme, or indirectly through a phenomenological model.

A question that commonly arises is how one might justify the use of externally forced experimental data to predictions of vortex-induced vibrations, since the latter are self-excited (free) oscillations. In principle, forced-excitation tests on nonlinear systems cannot be used to infer any general conclusions about the corresponding free-oscillation behavior. In the specific case of vortex-shedding, Sarpkaya [66] and Bearman [4] have pointed out that forced-oscillation tests tend to obscure the intricate effects of the flow history on the development of VIV, and can be used only if and when a stable, steady-state oscillation is reached. Notwithstanding the above difficulties, practical experience shows that useful results may be achieved (perhaps surprisingly so!) with the use of forced-oscillation data. For example, Staubli [74] has shown that the hysteresis effects seen in some free-oscillation tests can be replicated by simulations using forced-oscillation data, and Moe and Wu [49] have shown that the lock-in regions predicted by free- and forced-oscillation tests are very similar if the variation of added mass is taken into account. In the next subsection we shall show that our forced-oscillation data, used in a highly idealized model, can be used to make VIV predictions that are reasonably accurate.

4.3.2 A simple method of estimating response

Consider a very basic structural model consisting of a spring-mounted rigid cylinder with viscous damping, as shown in Figure 4-12. The cylinder is exposed to a uniform flow of velocity U and is constrained to move perpendicular to the flow. From elementary vibration theory (Rao [61], Blevins [7]), the equation of motion of the cylinder is

$$m \frac{d^2 y}{dt^2} + 2m\zeta\omega_n \frac{dy}{dt} + ky = F_0(t) \quad (4.1)$$

where y is the dynamic displacement of the cylinder, m is the cylinder mass per unit length, ζ is the structural damping factor, k is the spring constant, and F_0 is the fluid forcing

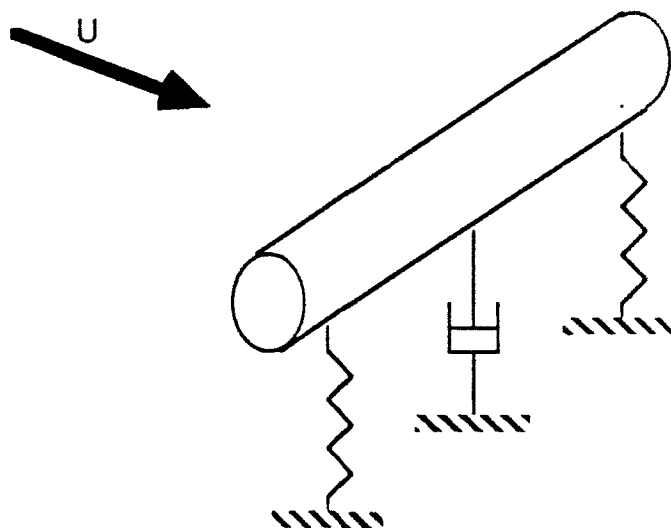


Figure 4-12: Simple structural model of a rigid cylinder.

term. Oscillations of the cylinder take place due to the constant interchange of kinetic energy (governed by the mass) and potential energy (governed by the spring constant); the frequency of these oscillations being the natural frequency $\omega_n = \sqrt{k/m}$. The overall level of energy in the system oscillations is determined by a balance between the damping term and the fluid forcing term (more correctly, the component of the fluid forcing in phase with the oscillation velocity). If the work done due to fluid forcing exceeds the work done due to damping, the amplitude of oscillations tends to increase, and *vice versa*. The amplitude is a constant when the forcing exactly balances the damping.

Let us suppose that we are interested in the worst possible case, i.e. the situation wherein the maximum fluid excitation occurs at the same frequency as the structural natural frequency. If the oscillations of the cylinder at its natural frequency are given by

$$y = Y_n \sin(2\pi f_n t) \quad (4.2)$$

where $f_n = \omega_n/2\pi$ is the natural frequency in Hertz, and Y_n is the amplitude of oscillation, then from our forced oscillation tests, we know that the fluid forcing term (per unit length)

will be given by

$$F_0 = \frac{1}{2} \rho d U^2 \{C_{L-V_0}|_n \cos(2\pi f_n t) - C_{L-A_0}|_n \sin(2\pi f_n t)\} \quad (4.3)$$

where the lift coefficients $C_{L-V_0}|_n$ and $C_{L-A_0}|_n$ (at resonance) are functions of the nondimensional natural frequency \hat{f}_n and the nondimensional amplitude ratio Y_n/d , and other terms have their usual meanings. For the worst case scenario noted above, we will assume that the fluid resonant frequency, equal to \hat{f}_n , is that value of nondimensional oscillation frequency \hat{f}_0 at which there is a peak in the value of C_{L-V_0} . The appropriate values of \hat{f}_n , $C_{L-V_0}|_n$, and $C_{L-A_0}|_n$ can be read off from the contour maps of Figures 3-14 and 3-15; Figure 4-13 shows the variation of these quantities with the nondimensional resonant amplitude ratio Y_n/d .

In order to predict the value of the oscillation amplitude Y_n , we need to consider the action of the forcing terms of Equation 4.3. We notice that the term $-C_{L-A_0}|_n \sin(2\pi f_n t)$ is in phase with the acceleration term $m \frac{d^2 y}{dt^2}$ in Equation 4.1, for $y = Y_n \sin(2\pi f_n t)$. Hence (as expected), the action of the coefficient C_{L-A_0} is to cause an *added mass* effect and modify the natural frequency $2\pi f_n = \sqrt{k/\bar{m}}$. If we are still interested in the worst case situation, we can assume that the flow velocity is tuned in such a manner so as to counteract any detuning effect of the added mass, i.e. the flow resonant frequency is still identical to the structural natural frequency, including added mass. In that case the oscillation amplitude is a result of a balance between the damping term of Equation 4.1 and the C_{L-V_0} term of Equation 4.3, i.e.

$$2\bar{m}\zeta(2\pi f_n) \frac{dy}{dt} \iff \frac{1}{2} \rho d U^2 C_{L-V_0}|_n \cos(2\pi f_n t) \quad (4.4)$$

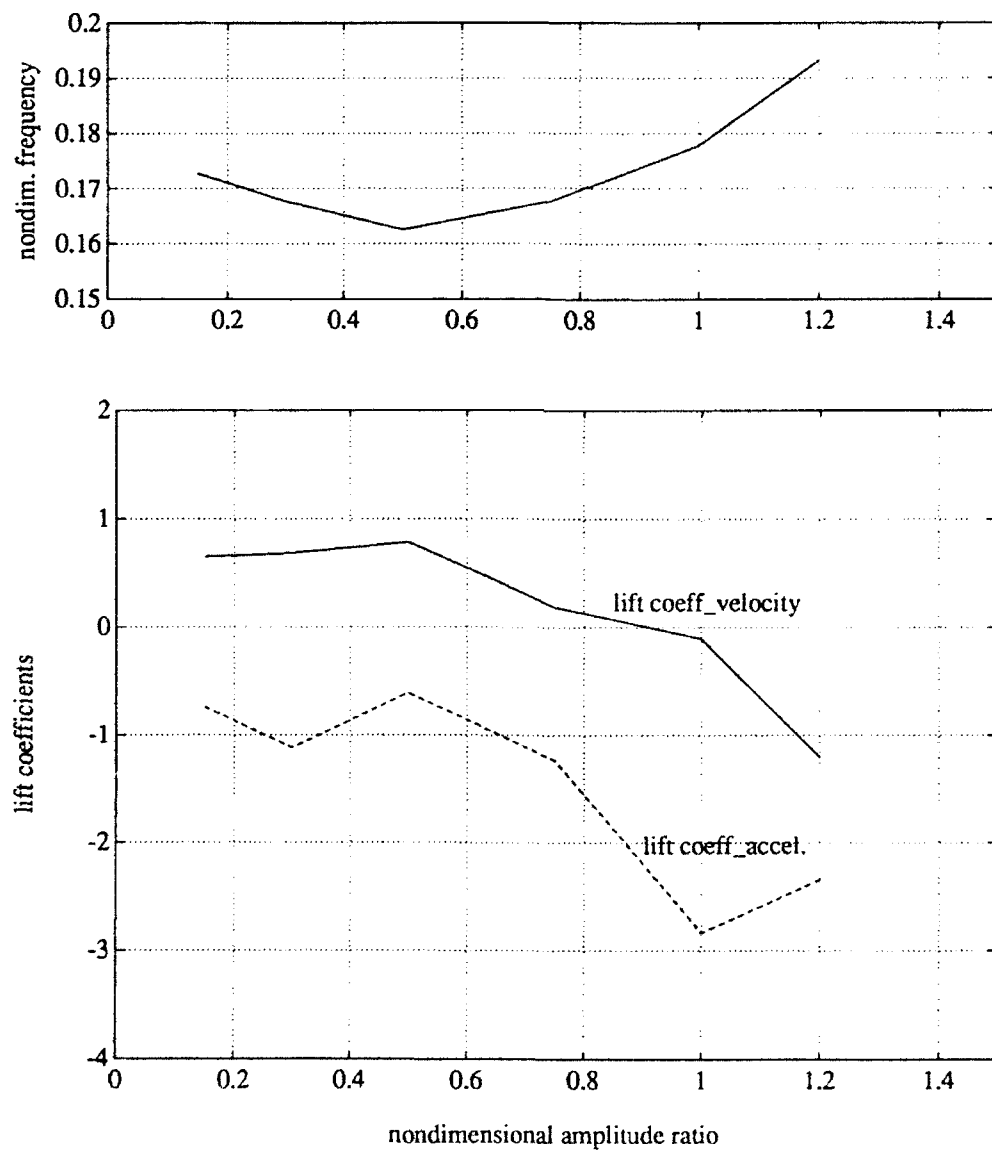
where the symbol \iff has been used to denote "in balance with", and the term \bar{m} on the LHS now includes added mass. Substituting $y = Y_n \sin(2\pi f_n t)$ and $U = f_n d / \hat{f}_n$, we get

$$2\bar{m}\zeta(2\pi f_n) Y_n(2\pi f_n) \cos(2\pi f_n t) \iff \frac{1}{2} \rho d \frac{f_n^2 d^2}{\hat{f}_n^2} C_{L-V_0}|_n \cos(2\pi f_n t) \quad (4.5)$$

Canceling common terms and rearranging others, we have

$$2 \left\{ 2\pi \hat{f}_n^2 \left(\frac{2\bar{m}(2\pi\zeta)}{\rho d^2} \right) \right\} \frac{Y_n}{d} \iff C_{L-V_0}|_n \quad (4.6)$$

Figure 4-13: Resonant nondimensional frequency \hat{f}_n and lift coefficients $C_{L-V_0}|_n$ and $C_{L-A_0}|_n$ against resonant amplitude ratio Y_n/d ; smooth circular cylinder.



The term within the curly braces {...} on the LHS of Equation 4.6 is referred to as the "response parameter" S_G [65, 88] or the "reduced damping" $2\pi S^2 k$, [7, 26], and is commonly used as a parameter governing the VIV response of structures. (It is essentially a product of the mass ratio (including added mass) and the structural damping ratio of the model.) Although the indiscriminate use of S_G in such calculations has been recently criticized (Vandiver [88], Zdravkovich [101]), its use in our simple model (under complete synchronization) is valid. We are thus left with the very simple relation

$$2 S_G \frac{Y_n}{d} \iff C_{L-V_0}|_n \quad (4.7)$$

where, for any given value of S_G , the resonant oscillation amplitude occurs when the quantity on the LHS of Equation 4.7 (the damping) equals the quantity on the RHS (the excitation).

Figure 4-14 demonstrates Equation 4.7 in a graphical manner. Shown here is the variation of $C_{L-V_0}|_n$ against Y_n/d (from Figure 4-13), together with several lines of $2S_G Y_n/d$ for different values of S_G . The mean value of the lift coefficient for the stationary runs has been taken as the zero value of $C_{L-V_0}|_n$. For each value of the response parameter S_G , the resulting oscillation amplitude is given by the intersection of the corresponding straight line with the curve for $C_{L-V_0}|_n$. The performance of this simple predictive scheme is shown on Figure 4-15, from Griffin [24], which illustrates the variation of $2Y_n/d$ against S_G for a wide range of *free-oscillation* results from various field and laboratory experiments on circular cylinders. The legend for the various data points is available in references [24] and [26]. Our results for $2Y_n/d$ for the different values of S_G from Figure 4-14 are illustrated on Figure 4-15 by intersecting horizontal and vertical arrows; the arrowheads point at the obtained results. Clearly, our simple predictive scheme gives results that lie within the experimental scatter.

Several points must be made about this prediction method and its results.

Firstly, it will be noticed from Figure 4-14 that *the success of this scheme depends on the amplitude-limited nature of the exciting lift coefficient C_{L-V_0}* ; this fact ensures that a balance is obtained between the exciting force and the damping force for *all* values of the response parameter. The negative slope of the lift coefficient curve corresponds to *hydrodynamic damping*, which in this case has been taken into account automatically in the exciting (RHS) term. It is clear that even if the structural damping term is zero, the

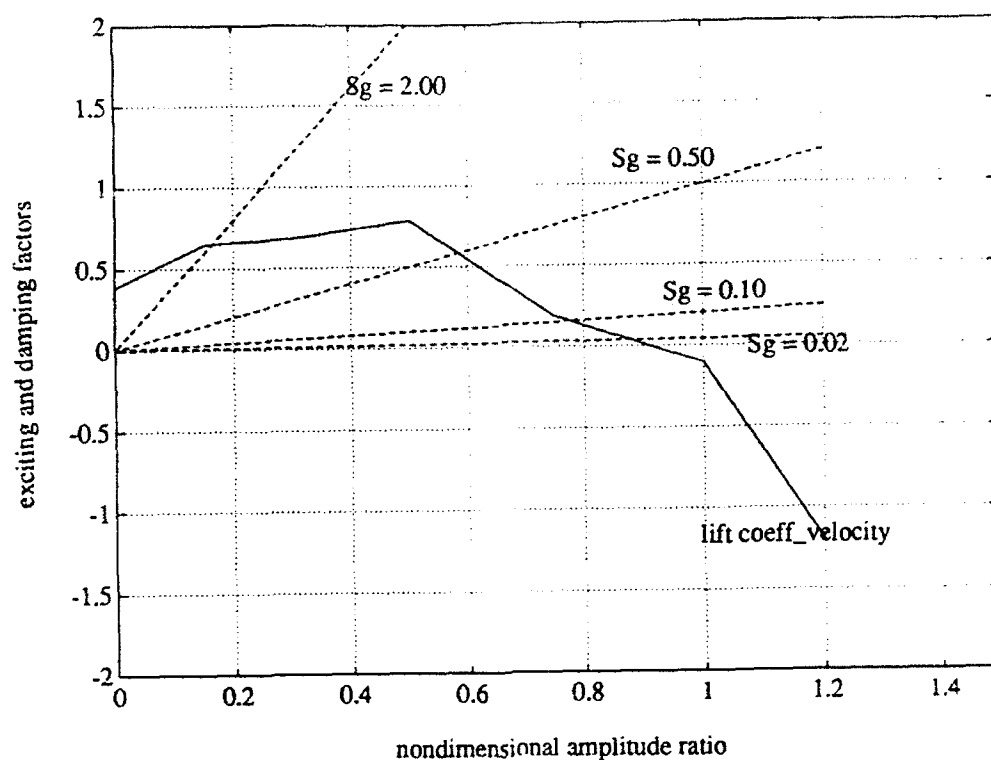


Figure 4-14: Graphical illustration of the simple predictive scheme $2S_G Y_n/d \Leftrightarrow C_{L-V_0}|_n$

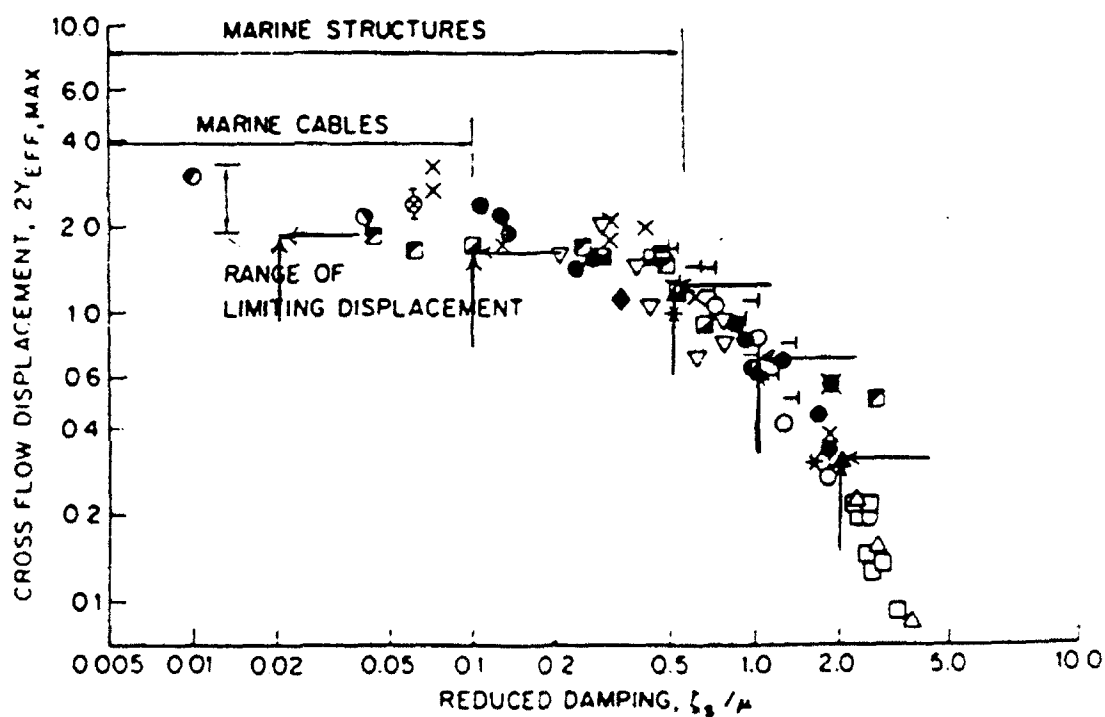


Figure 4-15: Performance of the predictive scheme compared to various experimental data from Griffin (1985).

oscillation amplitude does not increase indefinitely, but is limited to about one diameter.

Secondly, a glance at Figure 4-15 leads inevitably to the following question: since the results from field and laboratory experiments follow such a clear trend, why not use a curve-fit through these data to make VIV predictions instead of using our scheme? In fact such curve-fits have been proposed for just this purpose; for example, Griffin and Ramberg [26] have

$$\frac{Y_n}{d} = \frac{1.29}{[1 + 0.43S_G]^{3.35}} \quad (4.8)$$

Other similar expressions can be found in Blevins [7]. The important point is that the data in Figure 4-15 (and leading to Equation 4.8) are for *smooth circular cylinders* only. The method we have illustrated, using a few relatively straightforward forced-oscillation experiments, is applicable to any cross-section (square, triangular, or circular with a vortex suppression device) for which free-oscillation test data are not readily available, or would be difficult to obtain.

Thirdly, a note regarding the novelty of our scheme. The principle of the oscillation amplitude being determined by a balance between excitation and damping is well known, and has been used by several researchers (Moeller [50], Vandiver [90, 88], Every *et al.* [15], and others). The phenomenon of the amplitude-limited lift coefficient (in phase with velocity) has also been widely published (Blevins [7], Griffin and Ramberg [26], Sarpkaya [65]). It is therefore surprising that to the best of our knowledge, the combination of these two concepts has not appeared in the literature thus far (in the simple form outlined here).

4.3.3 Long tubulars in shear flow

In the previous section, we illustrated a very basic prediction scheme utilizing a rigid cylinder, obeying a simple harmonic equation of motion with linear damping, performing pure sinusoidal transverse oscillations in perfect synchronization with the two-dimensional vortex shedding due to a uniform flow. In the real world, such ideal conditions rarely exist. A problem of particular concern to offshore and oceanographic engineers is that of a long, flexible cylinder in sheared flow. From a structural standpoint, the simplest equation of motion for such a problem is that of a string under tension, and involves both a time and space dependence. Other considerations such as bending stiffness, elasticity, spatially varying properties, and large-amplitude nonlinearities may or may not be taken into account.

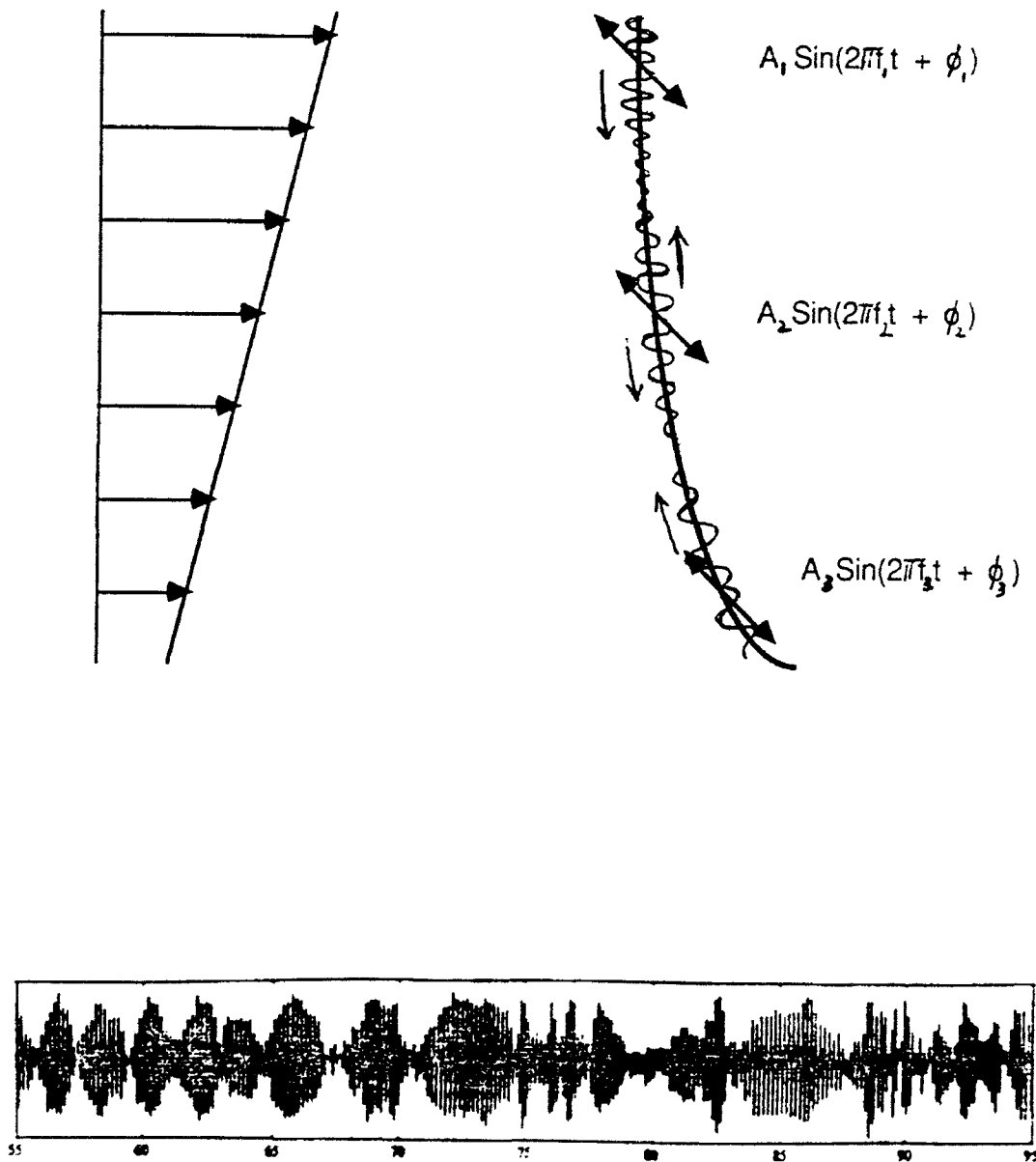
From a hydrodynamics standpoint, the difficulty is that the vortex-induced excitation varies in magnitude and frequency along the length of the structure. Depending on the length of the cylinder and the degree of shear in the flow, the structure may undergo relatively broadband, multimode, beating oscillations. Such behavior has been observed in the field by Alexander [1], Vandiver [90, 88], Kim [36], Grosenbaugh [28, 27], and others.

Figure 4-16 illustrates the hydrodynamic difficulties noted in the previous paragraph. Shown here is a long cylinder (e.g. a tow cable), with a curved static configuration, in a linearly varying shear current. Due to the length of the cable, structural perturbations could be damped out before they reach the end points, and hence the cable could respond as one of infinite length. Each point on the cable responds primarily to the local vortex-induced forcing. Traveling waves of the corresponding local frequency are radiated out from each point in both directions along the cable. These waves are damped out within a few wavelengths, but are sufficient to affect the oscillation at neighboring points. As a result, the net oscillation at any given point along the cable consists of the local forcing frequency as well as contributions due to different frequencies from adjacent sections of the cable. At the bottom of Figure 4-16 is a time trace of the displacement at a point on a long vertical tow cable in a sheared flow, from reference [27]. It is clear that the cable oscillations are not purely sinusoidal, but rather resemble an amplitude-modulated, or beating, waveform.

Several attempts have been made in the last decade to develop algorithms for VIV predictions in sheared flows. Various modal superposition techniques have been developed with varying degrees of sophistication and success, for example see Whitney and Nikkel [93], Patrikalakis and Chryssostomidis [58], and Vandiver's group at MIT (Vandiver [90], Kim [36], Chung [10], Capozucca [8]). The algorithms developed by the latter group have achieved widespread industry acceptance. Examples of simulations attempted in the time domain include the work of Nordgren [52], Howell [31], Dong and Lou [12], and Hansen *et al.* [29] (this latter effort being unusual in that a numerical random vortex method has been integrated into the algorithm to provide the hydrodynamic loading). In addition to the above simulation techniques, a recent closed-form quasi-theoretical solution, assuming infinite cable behavior, has been developed by Triantafyllou [83, 84].

All of the algorithms listed above utilize different solution techniques, and the details and assumptions surrounding the structural and hydrodynamic models differ as well. In essence, however, the hydrodynamic calculations in most of the cases are based on the

Figure 4-16: Illustrating a long flexible cylinder in sheared flow.



same principles. Required as inputs are models (in general nonlinear) for three fluid force coefficients in the transverse direction: an exciting or “lift” coefficient, a damping or “drag” coefficient, and an added mass coefficient. (Care must be taken to distinguish this “drag” coefficient, which provides damping in the lift direction, from the mean drag coefficient C_{D_m} which expresses the mean force in the drag direction.) All of these inputs can be estimated from our forced-oscillation data. The added mass coefficient as a function of oscillation frequency and amplitude is given directly by Figure 3-16. Both the “lift” and “drag” coefficients act in phase with oscillation velocity, and hence are contained in our contours of C_{L-V_0} , Figure 3-14. The net effect is either exciting or damping depending on the sign of C_{L-V_0} . If separate exciting and damping coefficients are desired (e.g. to satisfy the solution method), it is possible to fit a particular model for one of the coefficients to the data and to consider the residual as the variation of the other coefficient. Once the predicted oscillation amplitude is obtained from the algorithm, our contours of C_{D_m} (Figure 3-12) can be used directly to estimate the mean drag force.

The significant issue that remains is the effect of the multifrequency beating oscillations on the hydrodynamic force coefficients. Since vortex shedding is a highly nonlinear process, there is no reason to suppose that the force coefficients from sinusoidal tests can be applied to beating simulations in a linear superposition sense. In fact, Triantafyllou and Karniadakis [79] have shown via numerical simulations that beating oscillations cause the force coefficients to be modified in unforeseen, nonlinear ways. It is an important part of this thesis to determine the force coefficients on typical beating oscillations, and we shall address this issue in the next chapter.

4.4 Cross-sectional effects

4.4.1 Preliminary remarks

It is well known that the cross-sectional geometry of a prismatic cylinder plays an important role in determining the nature of the vortex shedding and the vortex-induced forces acting on the cylinder. Stationary Strouhal numbers for a wide variety of noncircular cross-sections (as well as references to more information) can be found in Blevins [7]. Typical research on noncircular sections has focused on geometries such as flat, rectangular, triangular, half-circular, etc. Much less is known about the vortex-induced forces on sections that are

nominally circular but in fact may not be so, such as a typical braided wire-rope section, or a conventional bare riser section with satellite kill- and choke- lines. Most of the results of tests conducted on such sections are confidential information that have not been published in the open literature.

In the following subsections, we shall present results of forced oscillation tests conducted on four noncircular models: a wire-rope, a chain, a typical production riser, and a haired-fairing, all at Reynolds numbers of approximately 10,000. It should be stressed that the intention is *not* to produce a catalog of commercially useful data, but rather to illustrate some of the important techniques and pitfalls in the application of our experimental data to real-life situations. Most of the results presented shall be of the lift coefficient in phase with velocity, C_{L-V_0} , since it is this coefficient that most accurately signals the presence or absence of VIV.

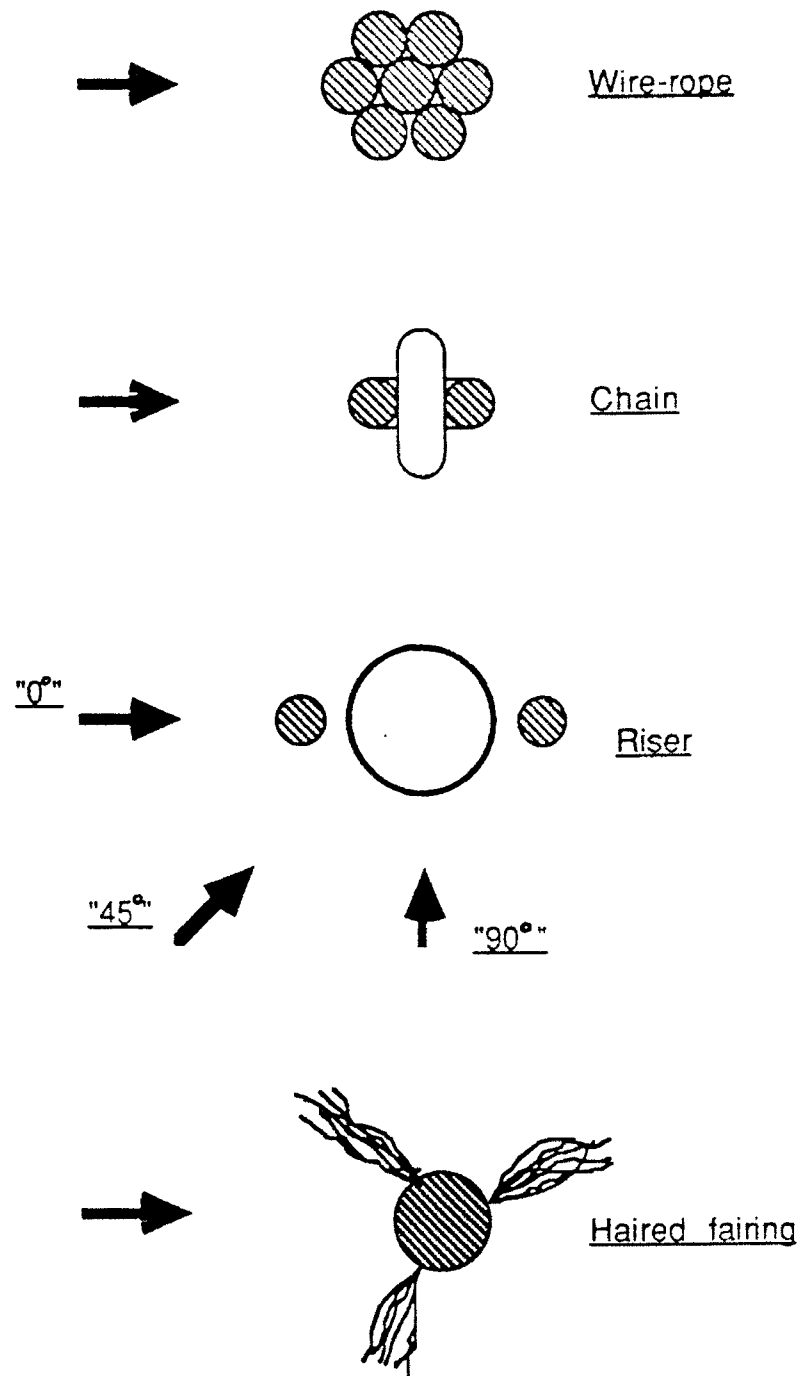
Figure 4-17 illustrates the cross-sectional and flow geometries of the models tested. Table 2.1 of Chapter 2 summarized the construction details of these models.

4.4.2 Defining an "effective diameter"

One of the most common structural components in oceanographic or offshore engineering situations is the stranded or braided wire-rope. Such a wire-rope is commonly regarded as a circular cylinder for the purposes of VIV computations, with little effort given to establishing the validity of this assumption. In this subsection we shall show that a typical wire-rope section can in fact be treated with circular cylinder data, as long as a proper "effective diameter" is chosen in the computations.

Sinusoidal oscillation tests with a 2.70 cm diameter 7-strand wire-rope specimen (Figure 4-17) were carried out at a constant amplitude ratio $Y_0/d = 0.30$ and a range of oscillation frequencies. Figure 4-18 illustrates the behavior of the mean drag coefficient C_{D_n} and the exciting lift coefficient C_{L-V_0} for the wire-rope section (open circles), together with the corresponding data for the smooth circular cylinder (solid lines). In a qualitative sense, the behavior of the vortex-induced forces in the case of the wire-rope are similar to the behavior in the case of the cylinder. Quantitatively, it is clear that the resonant vortex peak for the wire rope occurs at a higher oscillation frequency, and the magnitude of the peak forces are lower.

Figure 4-17: Cross-sectional and flow geometries of the models tested.



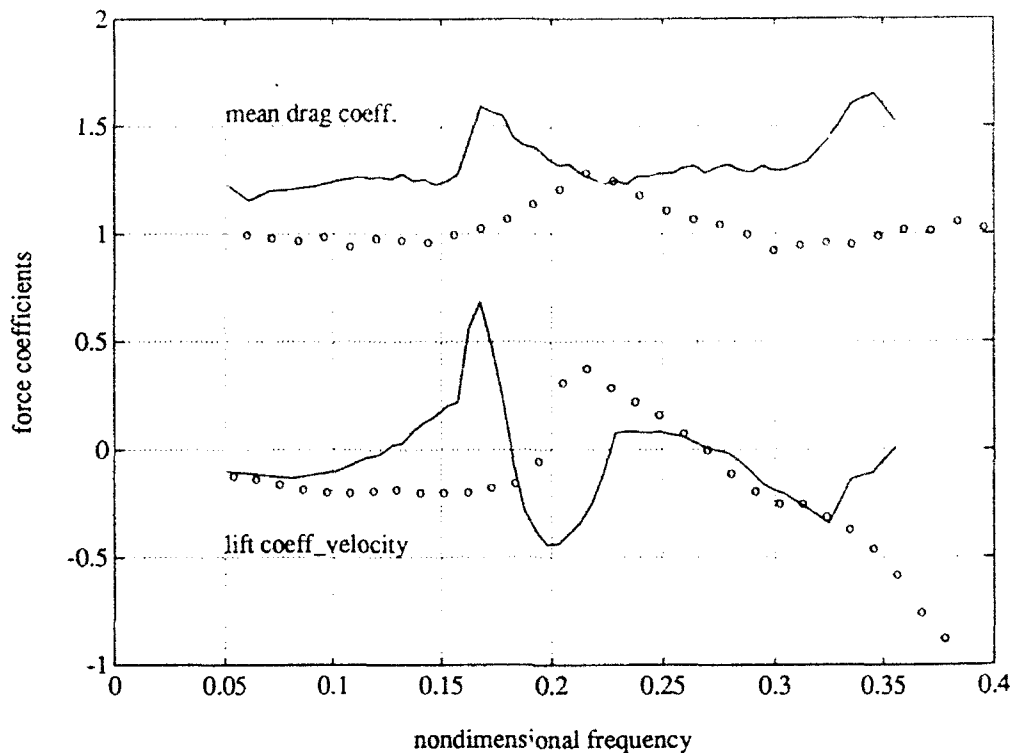


Figure 4-18: C_{D_m} and C_{L-V_0} for the wire-rope, $Y_0/d = 0.30$, and circular cylinder data.

The occurrence of a higher resonant frequency and lower peak forces both lead to the same conclusion: if the wire-rope is to be modeled as a circular cylinder, then the length scale (here the outer diameter) used in the normalization (in the numerator for the nondimensional frequency, and in the denominator for the force coefficients) was probably too high. Figure 4-19 illustrates the same data as Figure 4-18, now nondimensionalized with an effective diameter 77% of the outer diameter, or 2.08 cm. It is clear that the wire-rope data in this case (crosses) more closely track the circular cylinder data (solid lines). While certain differences remain (e.g. the wire-rope data show no sign of a second harmonic resonance), it can be argued that VIV predictions for this particular section can be made using circular cylinder data, as long as the wire-rope is treated as having an effective diameter of the order of three-quarters of its outer diameter.

It is important to point out that the concept of an effective diameter can only be applied to certain cross-sections that behave qualitatively like a circular cylinder. Tests were conducted with a chain model (Figure 4-17) of outer (link) diameter 2.30 cm, at the same amplitude ratio of 0.30. Figure 4-20 shows the behavior of C_{D_m} and C_{L-V_0} for the

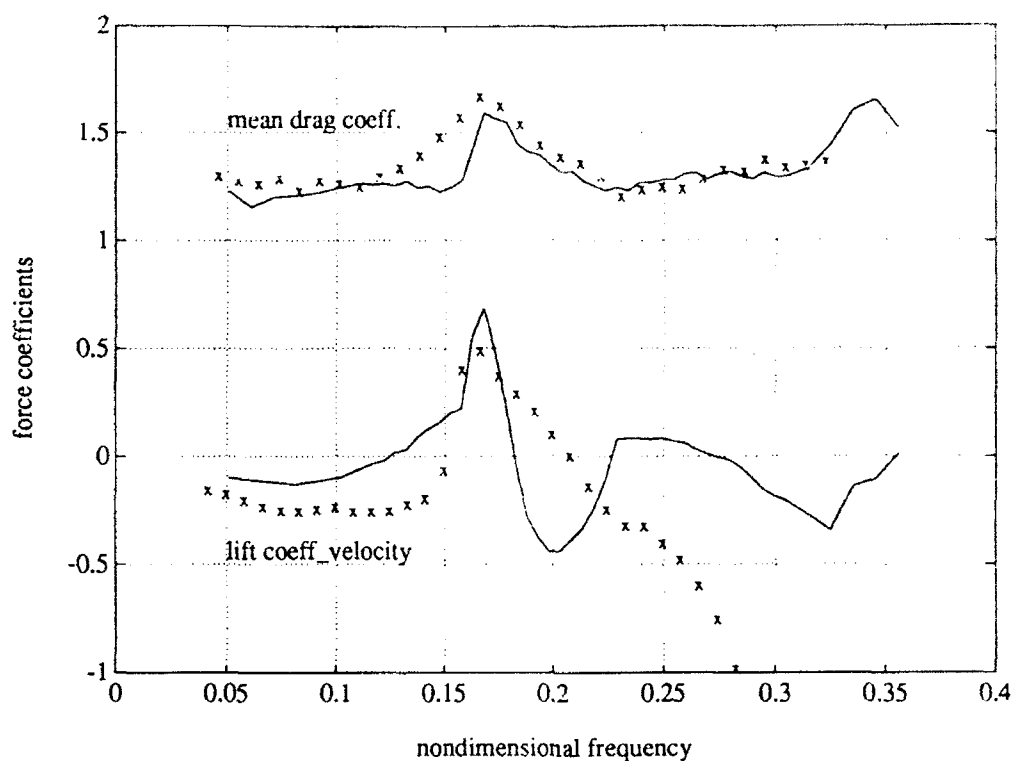


Figure 4-19: C_{D_m} and $C_{L_{V_0}}$ for the wire-rope, effective diameter 77%, and circular cylinder data.

chain section (open circles), compared to the circular cylinder results (solid lines). No vortex-induced resonance of any form can be detected. Due to the open geometry of the chain, vortex-shedding does not take place in the same manner as for the circular cylinder or wire-rope, and the chain “lies dead in the water”. The concept of effective diameter is not applicable.

4.4.3 Multiple cylinder interference effects

In the previous subsection we showed that for certain cross-sections, an “effective diameter” can be defined for the purpose of VIV computations. In the case of a multiple cylinder bundle such as a typical production riser, care must be taken to account for possible interference and shielding effects, which can be quite dramatic. It has been well known for a number of years that complex vibratory phenomena can occur in banks of multiple cylinders, such as those used in heat exchangers. Recently, Zdravkovich [100] has reviewed the similarities and differences between heat exchanger banks and offshore riser configurations,

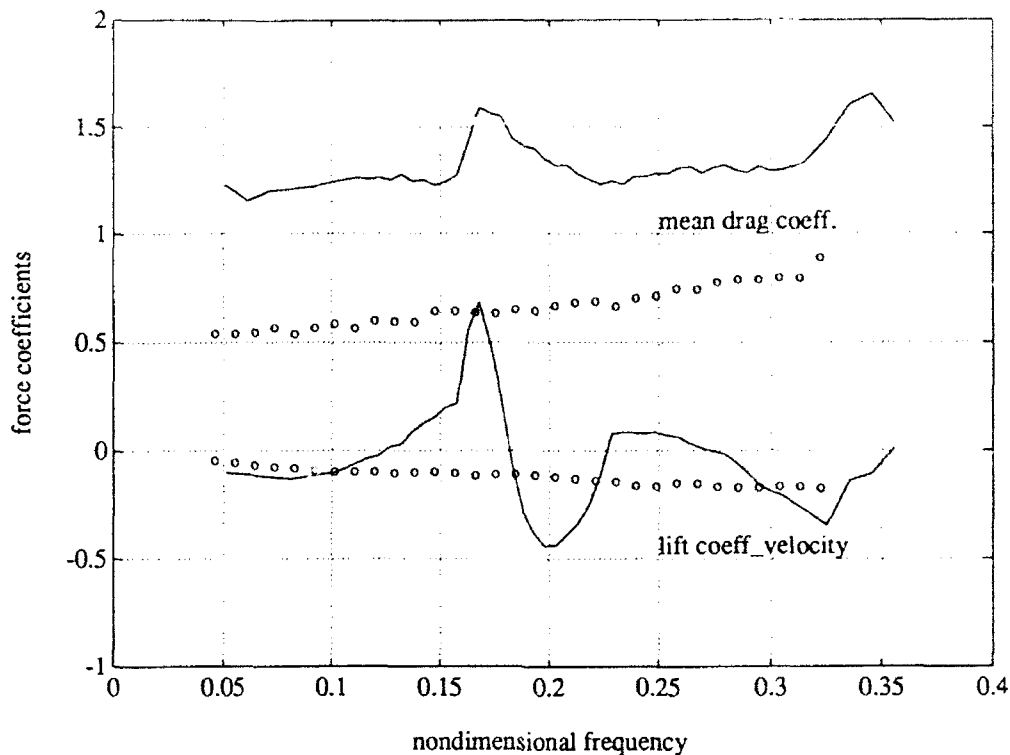


Figure 4-20: C_{D_m} and $C_{L_{V_0}}$ for the chain, $Y_0/d = 0.30$, and circular cylinder data.

with a view towards compiling the relevant heat exchanger data which are applicable in the marine situation. A type of multiple cylinder arrangement that does not occur in heat exchangers is the “satellite” production riser configuration, where a large central tube is surrounded by smaller cylinders (e.g. kill- and choke- lines). Usually, such satellite bundles are held together by flange plates [48] and hence the riser section can be considered as a single structure for the purposes of response computations.

In this subsection, we investigate the behavior of a typical production riser section, where for simplicity (and to illustrate the effects of flow angle) we have modeled a central cylinder with two smaller cylinders arranged diametrically opposite each other (Figure 4-17); we call this arrangement our “typical riser”. Experimental data (from free-oscillation tests) on more complex multiple tube arrangements have been presented by Moe and Overvik [48], Overvik and Moe [56], and Price *et al.* [59], among others.

Sinusoidal oscillation experiments were conducted with our riser model at a number of nondimensional frequencies and a single amplitude ratio of 0.30. The diameter of the central cylinder was used in the nondimensionalization of the oscillation frequencies and measured

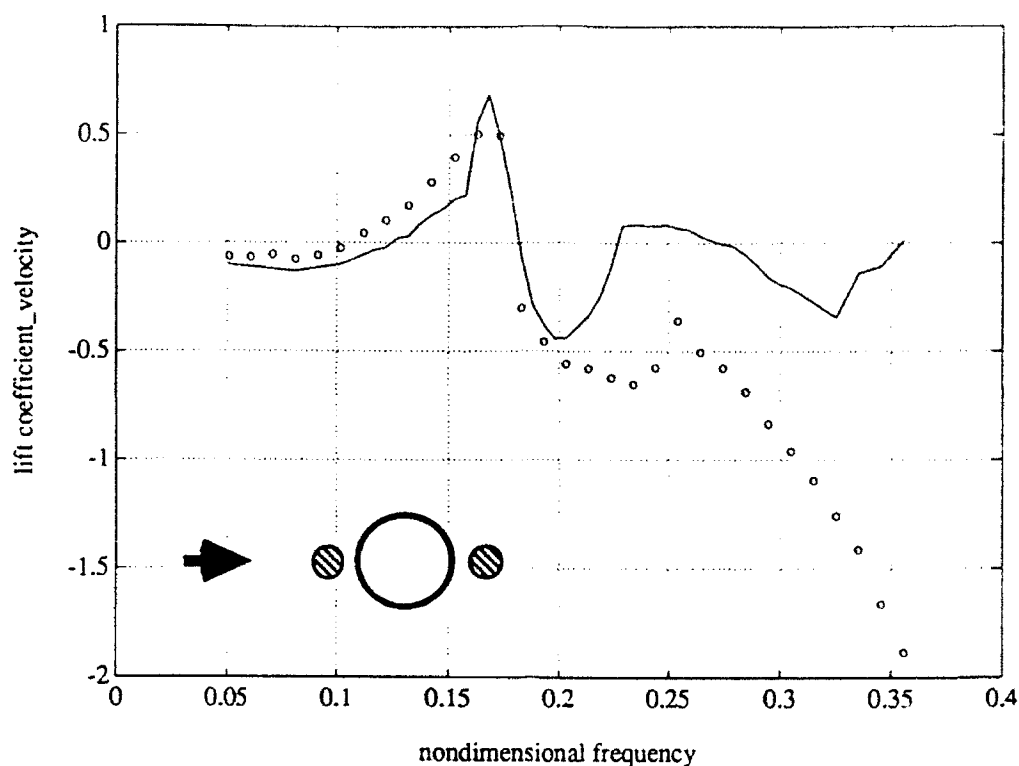


Figure 4-21: $C_{L_{V_0}}$ for the riser at 0° , $Y_0/d = 0.30$, and circular cylinder data.

forces. Three different flow angles were tested, 0° (satellite cylinders in-line with the flow), 90° (satellite cylinders on a diameter transverse to the flow), and 45° (satellite cylinders on a diameter inclined to the flow).

Figure 4-21 shows the results for the lift coefficient in phase with velocity, $C_{L_{V_0}}$, for the 0° configuration: the riser data is marked with open circles and compared to the corresponding bare cylinder data marked by a solid line. Apart from the absence of a secondary excitation region, the values of the lift coefficient for the riser in this configuration is very similar to the cylinder data.

Figure 4-22 illustrates the variation of $C_{L_{V_0}}$ for the 90° configuration, also compared to the circular cylinder data. A dramatic increase is seen in the width of the excitation region, together with an increase in the peak magnitude of the exciting lift coefficient. These data appear to indicate that vortex-induced oscillations of the riser exposed to flow from this angle would be considerably more severe than for the bare cylinder.

Figure 4-23 shows the $C_{L_{V_0}}$ data for the intermediate flow angle of 45° . The results are quite unexpected: instead of being an intermediate solution between the data of Figure 4-21

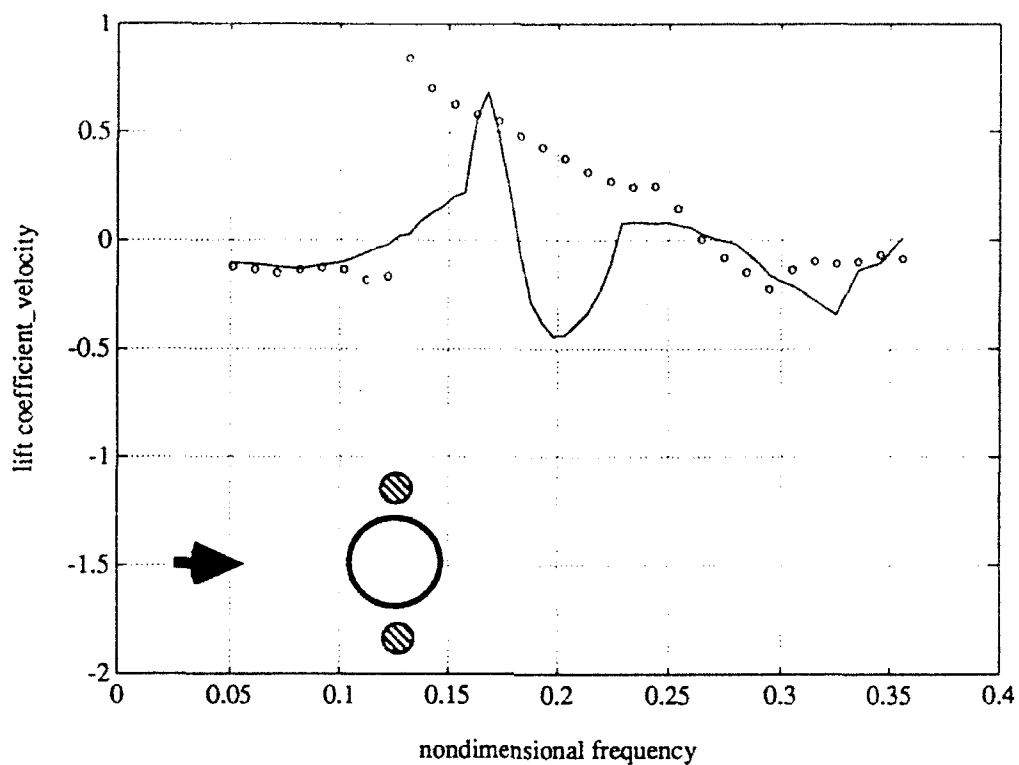


Figure 4-22: C_{L-V_0} for the riser at 90° , $Y_0/d = 0.30$, and circular cylinder data.

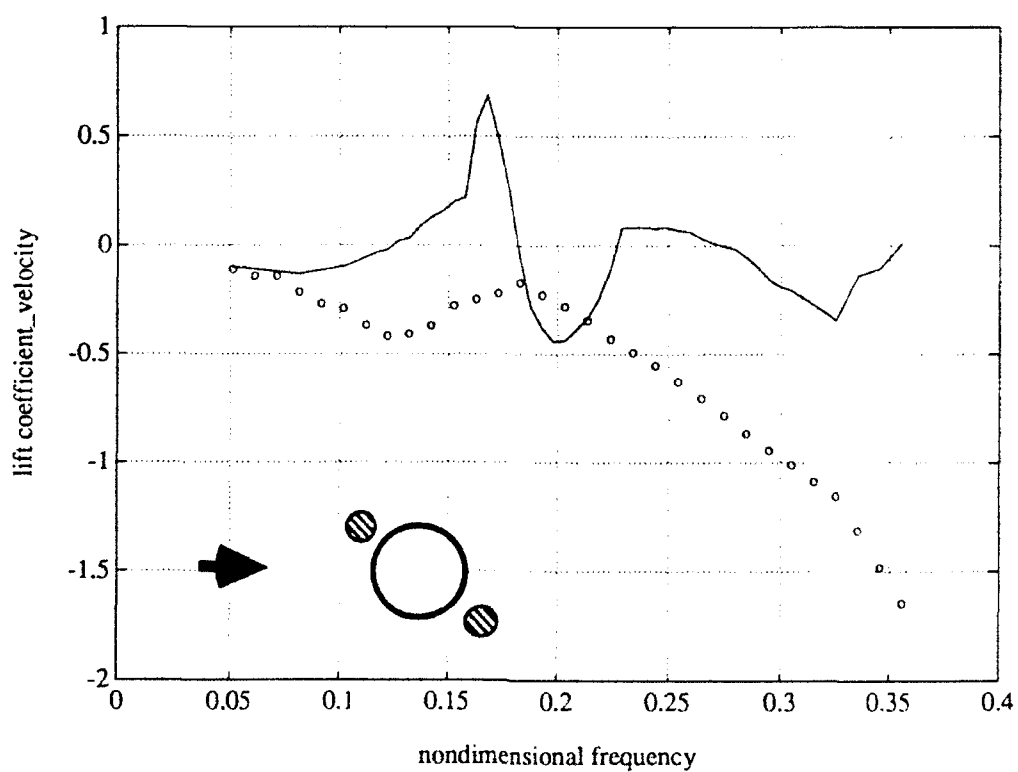


Figure 4-23: C_{L-V_0} for the riser at 45° , $Y_0/d = 0.30$, and circular cylinder data.

and the data of Figure 4-22, the present values show no sign whatsoever of vortex excitation. The lift coefficient in phase with velocity is negative for all values of oscillation frequency, indicating complete suppression of vortex-induced motions.

Further experimental tests were carried out as a check on the accuracy of the previous results. For each flow configuration, the value of the oscillation frequency corresponding to the resonant peak in the C_{L-V_0} data was determined. Tests were conducted at these (constant) frequencies and six amplitude ratios, in order to determine the amplitude dependence of the exciting lift coefficient in each case. Figure 4-24 shows the results of these tests compared to the circular cylinder data (from Figure 4-13). Stationary (nonoscillating)

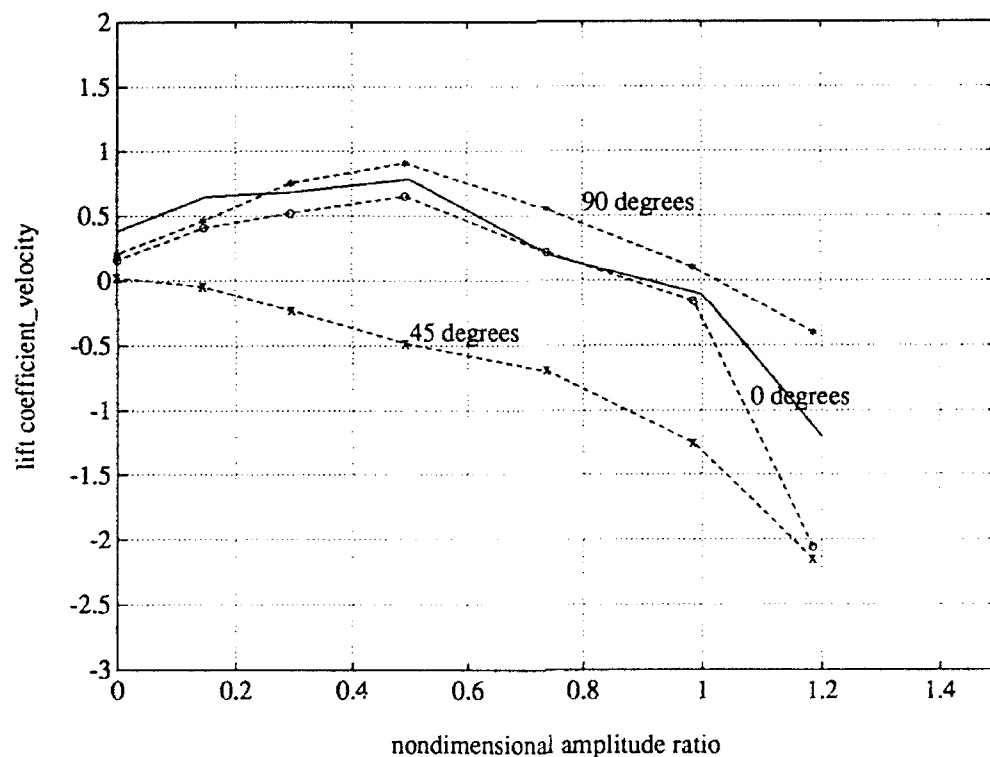


Figure 4-24: Variation of $C_{L-V_0}|_n$ against amplitude ratio for the riser at different angles, and circular cylinder data.

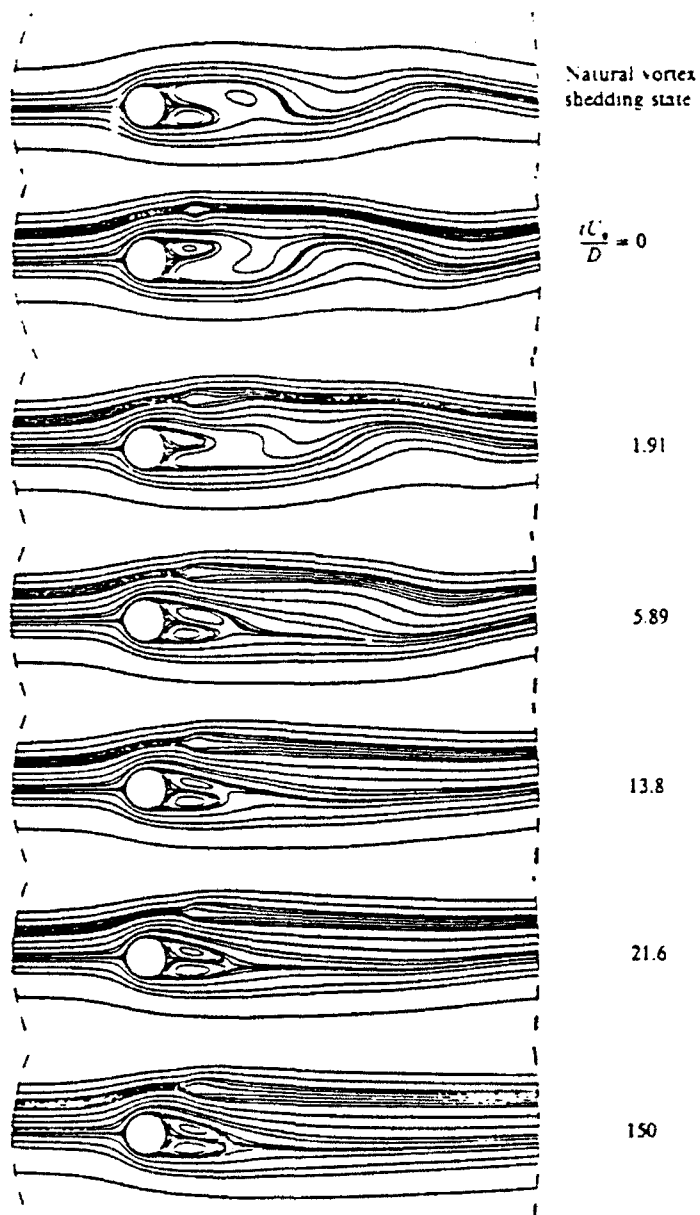
tests were conducted to provide the values at zero amplitude. These results are consistent with the previous data of Figures 4-21 ~ 4-23: the 0° data are similar to the bare cylinder, the 90° data predicts slightly larger amplitudes of oscillation, while the intermediate 45° configuration is almost completely damped.

The data from our riser tests, especially those corresponding to the 45° flow angle,

indicate a result of interest to scientists and practicing engineers alike: the vortex-induced oscillations of a cylinder can be controlled by the strategic placement of just one or two smaller cylinders in the near vicinity. Strykowski and Sreenivasan [76] have shown recently that for small Reynolds numbers, the vortex shedding behind circular cylinders can be suppressed entirely by positioning a second, much smaller, cylinder in the near wake of the main cylinder. Figure 4-25 illustrates a few instantaneous streamline patterns from their numerical computations. The top frame shows the natural vortex shedding state of the main cylinder. In the second frame, at a nondimensional time-step of zero, a "control" cylinder (having a diameter one-seventh the diameter of the main cylinder) is introduced slightly behind the main cylinder and to one side of the wake centerline. As the rest of the frames illustrate, vortex shedding is suppressed within a few time-steps and remains so for all time. Strykowski and Sreenivasan were able to achieve similar results from physical flow-visualization experiments as well, and argued that the observed results were due to a modification of the stability properties of the main cylinder wake due to the presence of the control cylinder. Given the similarity between the position of the control cylinder in the above results and the position of the aft satellite cylinder in our runs at the 45° flow angle, there is reason to believe that the absence of positive values of the exciting lift coefficient at that flow angle has a similar physical origin.

What, therefore, are the implications of our results on full-scale VIV predictions for riser bundles? Given the large qualitative differences between the riser data at certain flow angles and the circular cylinder data, it would appear that separate tests would be required for each riser configuration under study. Since the nature of currents in the ocean is omnidirectional, it is clearly impractical to collect and use data at well-defined flow angles. It may be necessary to conduct experiments for several flow angles and use the "worst" data in the computations to be assured of a conservative result. If the problem involves the design of a new riser bundle, experiments should ideally be conducted early in the design stage so as to achieve a configuration with optimum vortex-cancellation characteristics. Such an approach has been attempted by Johnson and Zdravkovich [33], who measured the stationary lift and drag coefficients on several riser models to determine the configuration having the smallest force coefficients. As we shall see in the next subsection, small stationary force coefficients do not necessarily imply correspondingly small dynamic force coefficients. The design of optimum riser bundles should include dynamic oscillation experiments as well.

Figure 4-25: Suppression of vortex shedding using a "control" cylinder, from Strykowski and Sreenivasan (1990).



4.4.4 Evaluating a vortex-suppression device

In the previous subsections, we focused on the applicability of our circular cylinder data to practical situations. In the following paragraphs, we shall consider an important application of our forced-oscillation experimental methods taken as a whole: the evaluation of vortex-suppression devices.

It is well known that prevention or reduction of vortex-induced oscillations can be attained through the use of add-on devices that suppress or disrupt the formation of the vortex street [7]. Commonly used are such devices as helical strakes, axial shrouds, and splitter plates. A very comprehensive review of vortex-suppression means has been published by Zdravkovich [102], who points out that most of these devices have been developed through ad-hoc tests conducted by different researchers; almost all of these tests have involved stationary or free-oscillation experiments. Reliable, quantitative comparisons of different devices are difficult to obtain because the vibratory response of each model depends very much on factors such as stiffness and damping of the supports, mass of the model, aspect ratio, free-stream turbulence, etc.. It is our belief that a program of forced-oscillation experiments using a well tested system (which also allows for interchangeable models) would be an excellent way to overcome several of these problems and to obtain comparative assessments of the effectiveness of various vortex-suppression devices.

To demonstrate the use of our system for such a purpose, we conducted tests on a model of a cable equipped with a "haired-fairing". The fairing consisted of three equally spaced rows of fine nylon thread (the "hairs"), woven into the kevlar surface sheath of a cable. When immersed in a flow, the hairs are designed to trail aft and apparently interfere with the formation of the vortex street. Figure 4-17 illustrates the geometry of the section; additional details were furnished in Chapter 2.

Several nonoscillating tests were conducted first to establish the values of the stationary force coefficients and Strouhal number. These results are summarized in Table 4.1. The forced-oscillation test program consisted of runs conducted at 16 discrete frequencies and 3

| | S | C_{D_m} | C_{L_0} | C_{D_0} |
|------|--------|-----------|-----------|-----------|
| Mean | 0.1406 | 1.5957 | 0.0344 | 0.0043 |

Table 4.1: Summary of results for the stationary haired-fairing model.

discrete amplitude ratios, for a total of 48 tests. The data collection and analysis procedures were identical to those followed for the circular cylinder, explained in Chapters 2 and 3. Contour maps were created of the lift and drag force coefficients, in analogy with Figures 3-12 – 3-16. The contours of the exciting lift coefficient C_{L-V_0} , and the mean drag coefficient C_{D_m} for the haired-fairing are presented in Figures 4-26 and 4-27 respectively. As before, the thick black line marked on Figure 4-26 corresponds to the zero contour, and marks the extent of the primary excitation region. No secondary excitation region is seen.

In analogy with the method developed for the circular cylinder in Section 4.3.2., the exciting lift coefficient data of Figure 4-26 can be used to estimate the VIV response of the haired-faired cable for different structural damping levels. Figure 4-28 shows the peak (resonant) values of the lift coefficient, $C_{L-V_0}|_n$, against the amplitude ratio of oscillation; also shown are the damping force lines $2S_G Y_n/d$ for various values of the response parameter S_G . The response amplitudes at these values of S_G correspond to the intersections between the damping lines and the curve for $C_{L-V_0}|_n$. Figure 4-29 illustrates the response amplitude predictions for the haired-fairing compared to the same experimental data of Figure 4-15; as before, our predictions are shown by intersecting horizontal and vertical arrows. It is clearly seen that the haired-fairing indeed succeeds in reducing the amplitude of the vortex-induced oscillations of the smooth cylinder; the reduction is about 60% at low values of the response parameter, and up to 85% at high values of the parameter. Although no free-oscillation test results for this particular haired-fairing were available for purposes of verification, the predicted percentage reduction of amplitude was of the same order as some of the good vortex-suppression devices reviewed by Zdravkovich [102].

In addition to demonstrating the use of our experimental system as described in the first paragraph of this section, our results for the haired-fairing also indicate the *importance of dynamic oscillation tests* in VIV predictions. Consider the stationary haired-fairing results of Table 4.1 compared to the stationary smooth cylinder results of Table 3.1 in Chapter 3. The stationary lift coefficient of the haired-fairing is about one-tenth that of the smooth cylinder, and the mean drag coefficient is slightly larger. One would be tempted to conclude that the addition of a haired-fairing would reduce vortex-induced oscillations of a smooth circular cylinder tenfold, at the expense of a 35% increase in the mean drag force. These conclusions would be quite wrong! Our dynamic tests (Figures 4-28 and 4-27) predict that for negligible structural damping, the haired-faired cable would respond at an amplitude

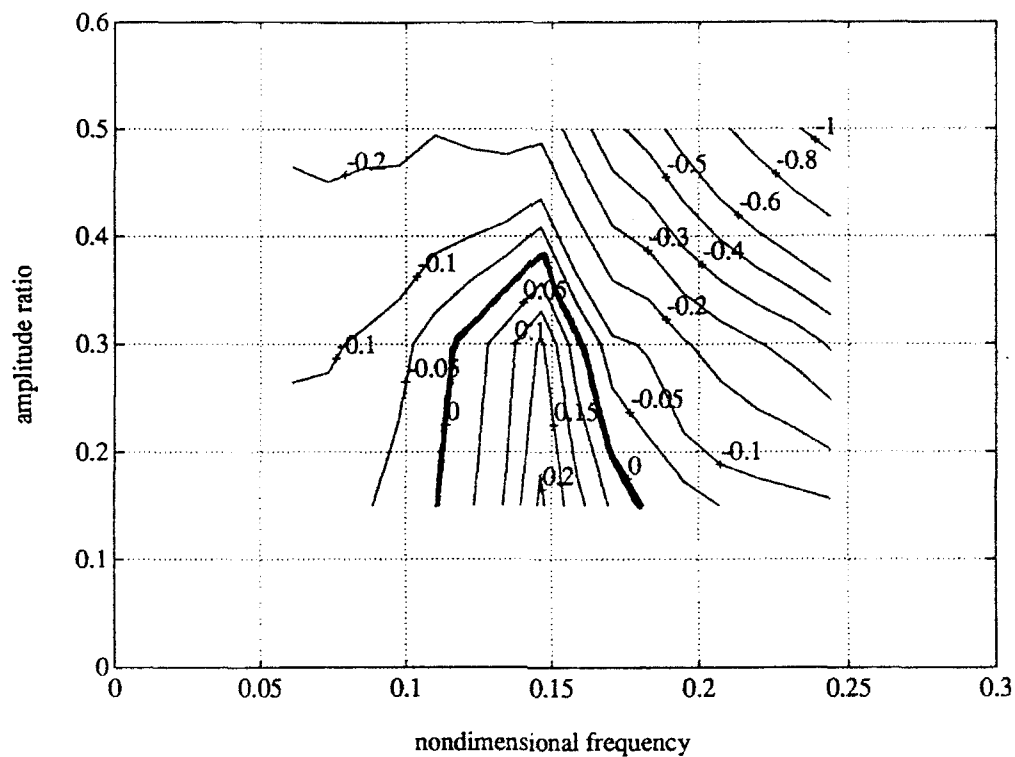


Figure 4-26: Contours of the lift coefficient in phase with velocity; haired-fairing.

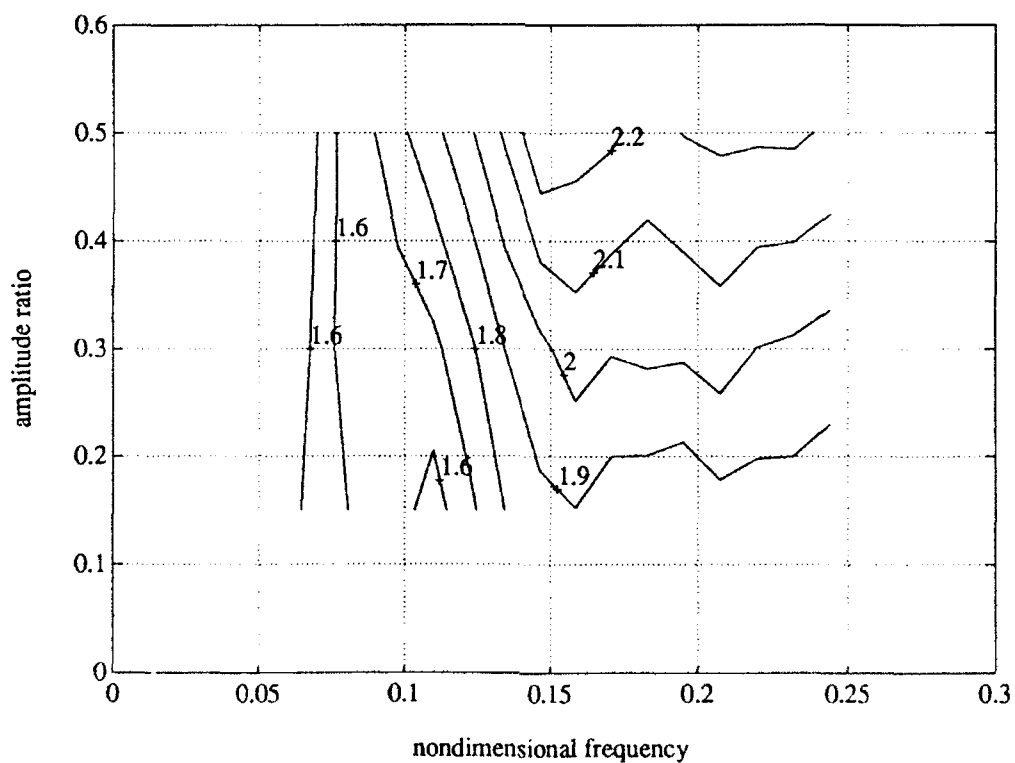


Figure 4-27: Contours of the mean drag coefficient; haired-fairing.

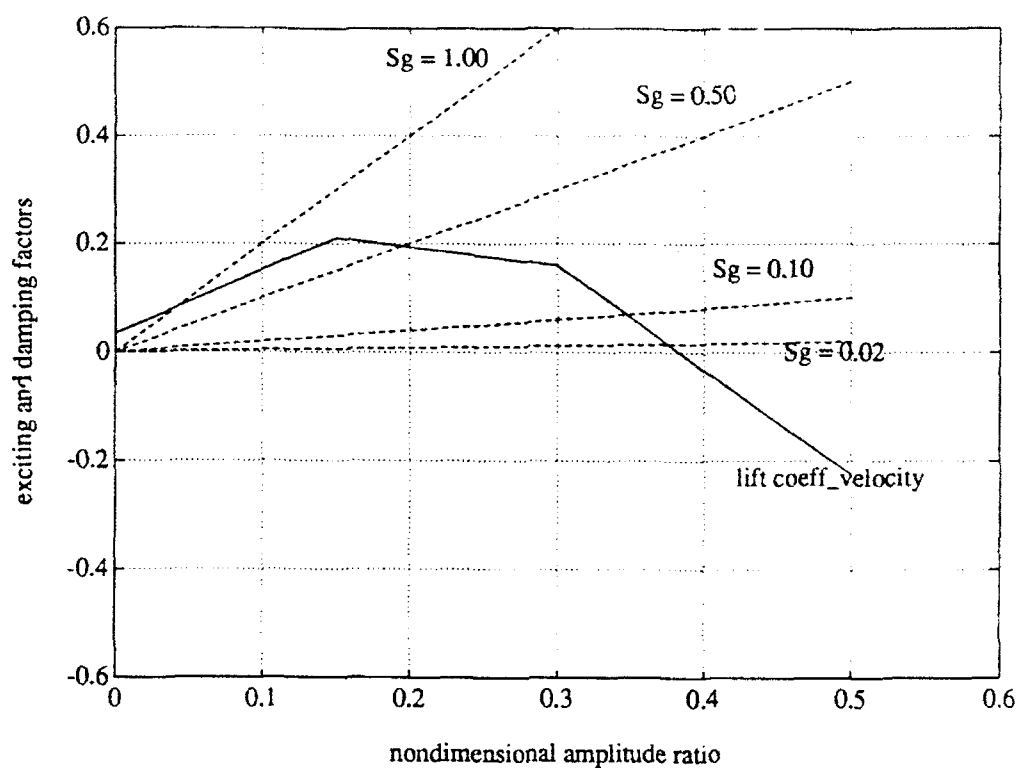


Figure 4-28: The predictive scheme $2S_G Y_n/d \Leftrightarrow C_{L-V_0}|_n$ applied to the haired-fairing.

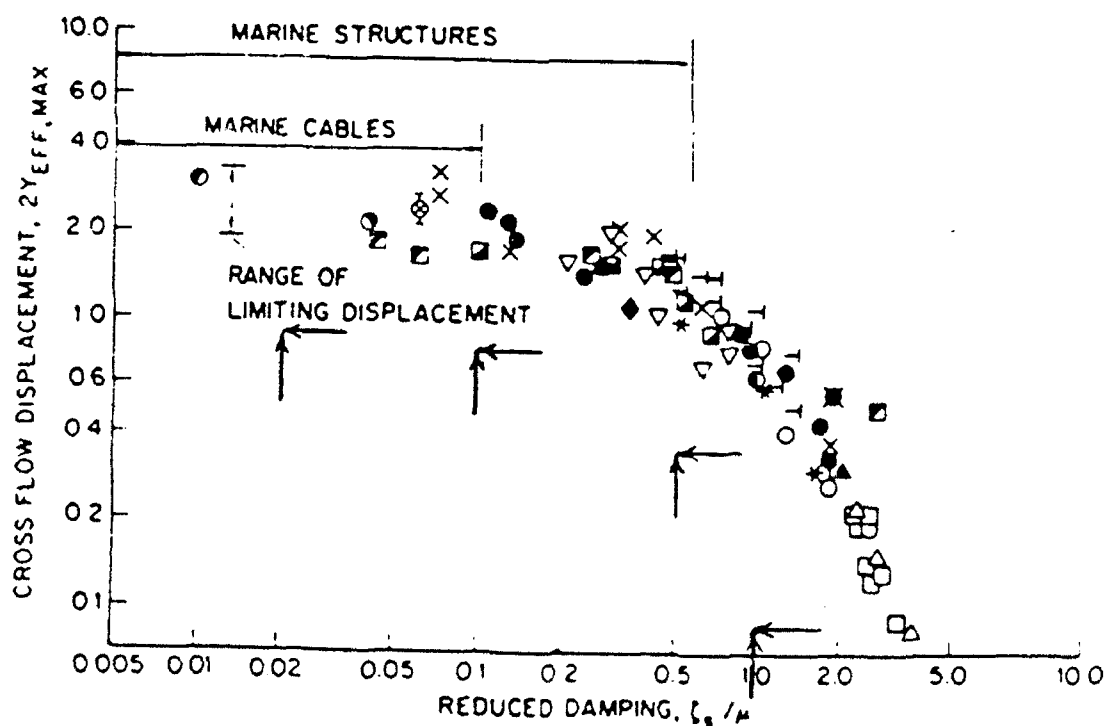


Figure 4-29: Performance of the predictive scheme applied to the haired-fairing.

ratio of about 0.40 and a nondimensional frequency of 0.147, causing an (amplified) mean drag coefficient of about 2.10. The corresponding results for the smooth cylinder (Figures 4-14 and 3-12) are an amplitude ratio of about 0.90 at a nondimensional frequency of about 0.175, causing an amplified mean drag coefficient of about 2.40. Thus the dynamic results for the haired-fairing predict a much smaller reduction of amplitude than do the stationary results, but with the added bonus that the effective mean drag force is slightly reduced as well. The importance of measuring dynamic force coefficients for the purposes of VIV predictions cannot be over-stressed.

Chapter 5

Beating Oscillation Tests

5.1 Introduction

5.1.1 Background

In previous chapters we have introduced the need for tests with amplitude-modulated oscillations. Section 4.3.3 and Figure 4-16 illustrated the situation with long tubulars in shear flow, and the resulting beating oscillations at any point along the cylinder. A segment of actual data from a field experiment [27] was included in Figure 4-16, showing the amplitude-modulation of the cylinder displacement. Such a time-varying nature of the response amplitude is a result of the participation of multiple frequencies at every spatial location along the tubular.

In the interest of simplicity of the experimental procedures and analysis methods, we decided to investigate the fundamental properties of the vortex-induced forces acting on cylinders undergoing amplitude-modulated oscillations by limiting the excitation to regular, dual-frequency beating. Thus, we do not claim to reproduce exactly the oscillations observed in the field; rather, we hope to extend our understanding of this complex phenomenon by making the transition from single-frequency pure sinusoidal motion to regular beating motion.

In Section 2.3.3, we introduced the essential mathematical definitions and formulations for beating motion. Dual-frequency beating can be expressed as the sum of two sinusoids

at different frequencies f_1 and f_2 as:

$$y(t) = Y_1 \sin(2\pi f_1 t) + Y_2 \sin(2\pi f_2 t) \quad (5.1)$$

If the frequencies f_1 and f_2 are held constant and the amplitudes Y_1 and Y_2 are varied, a number of waveforms of constant *modulation ratio* (relating to frequency) but varying *modulation depth* (relating to amplitude) are attained. For example, Figure 5-1 illustrates the waveforms obtained for the cases $f_1 = 1.0$, $f_2 = 1.2$, $Y_1 = 1.0$, and Y_2 varying as

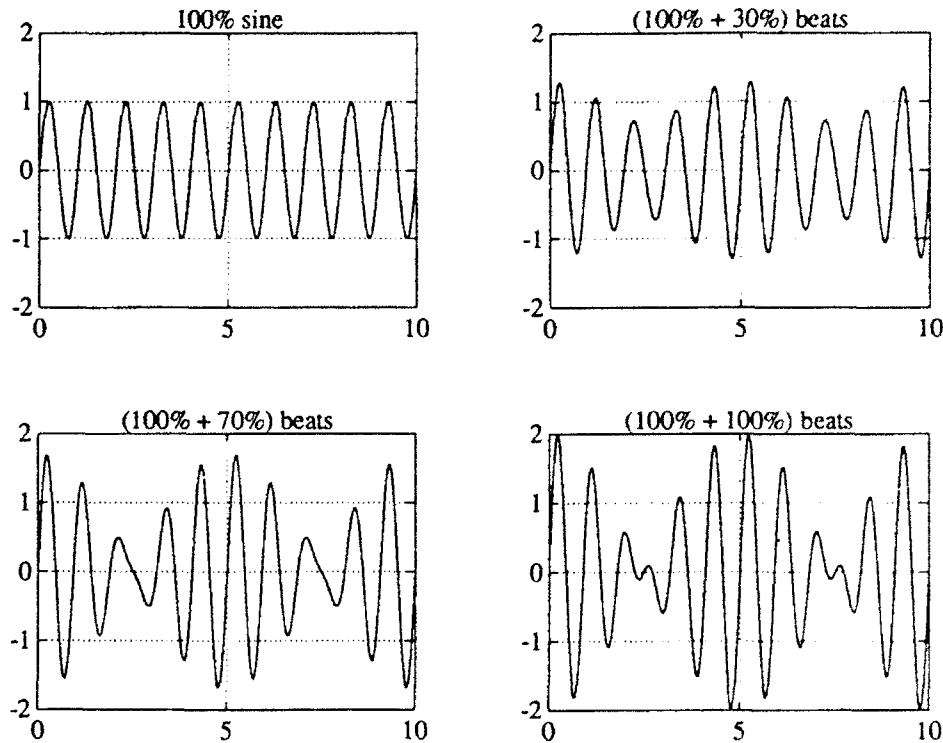


Figure 5-1: Waveforms at constant modulation ratio and varying modulation depth.

0%, 30%, 70%, and 100% of Y_1 . Notice that the modulation ratio, or the size of the beat "packet" in terms of the number of rapidly varying cycles, is a constant; on the other hand the modulation depth, or the amount of narrowing of the amplitude envelope, varies. Notice also that the total peak amplitude of the waveform is given by the sum $Y_1 + Y_2$. If we were now to hold the amplitudes Y_1 and Y_2 constant and vary the frequencies f_1 and f_2 , the result will be a number of waveforms of constant modulation depth (and peak amplitude), but varying modulation ratios. For example, Figure 5-2 illustrates the waveforms obtained for the cases $Y_1 = Y_2 = 0.50$, $f_1 = 1.00$, and $f_2 = 1.05$, 1.10, and finally 1.33. A pure

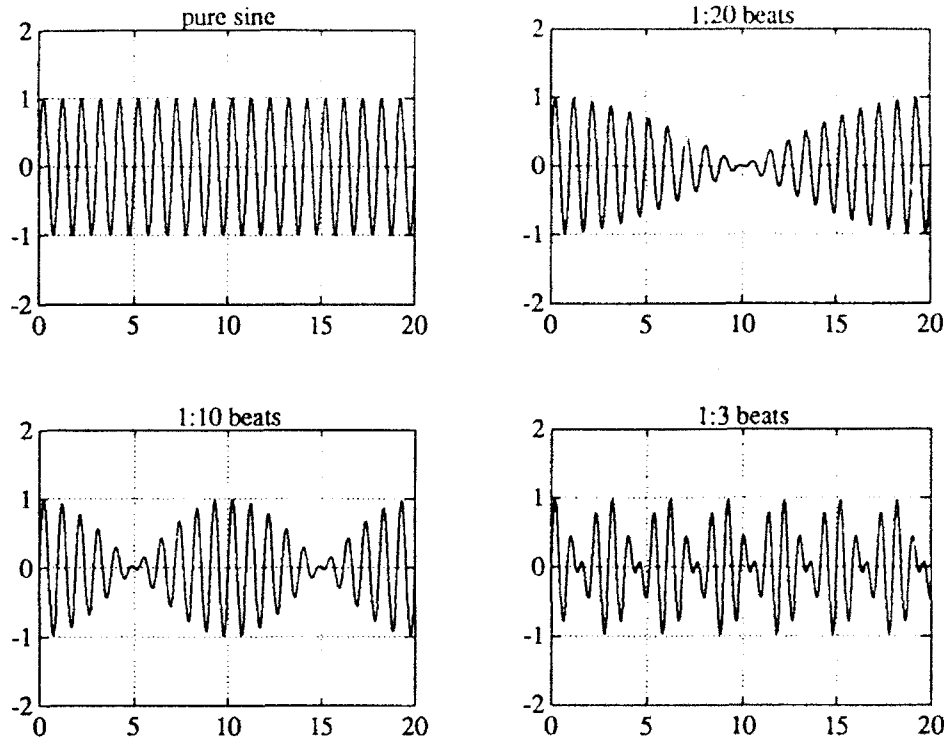


Figure 5-2: Waveforms at varying modulation ratio and constant modulation depth.

sinusoidal waveform is also illustrated for comparison.

If the amplitudes Y_1 and Y_2 are equal (as in Figure 5-2), then Equation 5.1 can be written as the product of two sinusoids at the “carrier frequency” f_c and the “modulation frequency” f_m as

$$y(t) = 2Y_1 \sin(2\pi f_c t) \cos(2\pi f_m t) \quad (5.2)$$

where the frequencies f_c , f_m , f_1 , and f_2 are related to each other by Equations 2.17 through 2.20 in Section 2.3.3. The modulation ratio, or the ratio of unity to “the number of oscillations at the carrier frequency contained in one beat packet”, is then given by

$$\text{Modulation ratio} = 1 : \left(\frac{f_c}{2f_m} \right) \quad (5.3)$$

The beating experiments reported in this thesis were all conducted at 100% modulation depth, i.e. with amplitudes $Y_1 = Y_2$. Six nondimensional peak amplitude ratios, $2Y_1/d$, were chosen between 0.15 and 1.50. Three modulation ratios of 1:20 (“slow” modulations), 1:10, and 1:3 (“fast” modulations) were tested. (More precisely, the values of f_2 were chosen

to be $(f_1 + f_1/20)$, $(f_1 + f_1/10)$, and $(f_1 + f_1/3)$, yielding actual modulation ratios 1:20.5, 1:10.5, and 1:3.5). The above tests were repeated for 36 sets of values $\{f_1, f_2\}$ such that the carrier frequency $f_c = (f_1 + f_2)/2$, when nondimensionalized as $\hat{f}_c = f_c d/U$, varied between 0.05 and 0.25.

Before proceeding further, it would be useful to discuss the questions that we seek to answer about beating motion. From an engineering standpoint, the primary issues concern the behavior of the vortex-induced lift and drag force coefficients in the presence of beating motion: how the force coefficients vary with amplitude, frequency, and modulation ratio; the implications for VIV calculations; and whether or not sinusoidal results can be extended to the beating case. From a scientific standpoint, one would be interested in exploring the response of the cylinder wake to beating excitation, or in other words the interaction between the natural (absolute) wake instability and the time-varying cylinder motion amplitude (the external forcing). A subtle but important question that presents itself concerns the amplitude to be used to characterize a beating waveform: whether this should be the peak amplitude $2Y_1$, the component amplitude Y_1 , or the RMS amplitude Y_{RMS} ($= Y_1$ for dual-frequency beats). We shall attempt to resolve these and other related issues in the sections that follow.

5.1.2 A summary of related research

Prior to our work, very little general attention has focused on the vortex-induced forces on cylinders undergoing beating motion. In this subsection we shall summarize the existing literature on the subject.

Triantafyllou and Karniadakis. Simulations of the flow around cylinders undergoing beating oscillations have been conducted by Triantafyllou and Karniadakis [79] and Triantafyllou [78], using a numerical spectral element method. The prescribed cylinder motion was a regular dual-frequency waveform given by

$$\eta(t) = Y \sin(2\pi f_e t) \sin(2\pi f_m t) \quad (5.4)$$

where $\eta(t)$ was the instantaneous displacement, Y the peak amplitude of motion, and f_e and f_m the frequencies of the “fast” and “slow” motions respectively. (The notation of

Equation 5.4 is identical to that of Triantafyllou and Karniadakis [79]. In terms of our notation in this thesis, $\eta(t) \equiv y(t)$, $Y \equiv 2Y_1$, and $f_e \equiv f_c$.) The frequency f_e was chosen to be the natural Strouhal frequency of the vortex shedding, the modulation ratio was fixed at 1:2.5, and two amplitude ratios were tested: 0.63 and 1.26. The Reynolds number of the simulations was 100. Time trace segments of the lift and drag forces calculated in each of the cases were presented, and compared to results obtained for the cylinder undergoing harmonic (pure sinusoidal) oscillations. The principal findings reported by the authors were:

1. The frequency content of the vortex-induced forces was considerably richer during the beating motion as compared to the sinusoidal motion.
2. In the y-direction (lift) the amplitude of the vortex-induced force was about the same in the modulated as in the harmonic case.
3. In the x-direction (drag), the modulated motion caused a significant decrease of the average drag force and a significant increase of the fluctuating drag force.

Owing to the above findings, Triantafyllou and Karniadakis eventually concluded that classical harmonic results could not be used in situations where beating was present, and that measurements from physical tests with amplitude-modulated cylinder vibrations were required.

Nakano and Rockwell. Low Reynolds number flow visualization studies of the wake behind a circular cylinder undergoing amplitude-modulated oscillations have been conducted by Nakano and Rockwell [51] at Lehigh University. These tests were carried out from the point of view of "active wake control", with the aim of altering the various forcing parameters (frequency, amplitude, modulation ratio, etc.) and classifying the different possible states of response of the wake. The authors used a hydrogen bubble flow visualization technique in a free-surface water channel, with a cylinder Reynolds number of 136. The cylinder was forced by a computer-controlled traverse table system, similar in concept to our own lead-screw oscillation mechanism. The cylinder motion had the form

$$y(t) = -\left(\frac{Y_e}{2}\right) [1 - \cos(2\pi f_m t)] \sin(2\pi f_e t) \quad (5.5)$$

where f_m and f_e were the modulation and excitation (carrier) frequencies respectively, and Y_e was the peak amplitude of motion. (In this case, the notation of Equation 5.5 cannot be expressed directly in terms of our notation; see the discussion later in this section. Y_e is similar to our $2Y_1$, and f_e and f_m are similar to our f_c and $2f_m$ respectively.) The frequency f_e for most of the runs was fixed at 95% of the natural Strouhal frequency so as to provide for slight detuning, and a range of values of f_m/f_e and Y_e/d were considered. Images of the cylinder wake were recorded on a high-speed video system, and then classified into a number of categories of deterministic vortex patterns. Four basic patterns were found for amplitude-modulated excitation, consisting of the following:

1. *f_m periodic with f_e lock-in:* In this pattern, the vortices are formed at essentially the same instantaneous phase (relative to the cylinder displacement) from one f_e cycle to the next. Further, this pattern of vortex formation is periodic at frequency f_m (i.e. it repeats in every beat packet).
2. *f_m periodic with f_e nonlock-in:* Here, the near-wake vortical structure is periodic with each f_m beat packet but is not locked-in to each f_e cycle; i.e. the vortices are not formed at the same instantaneous phase. Indeed, the observed patterns suggest a time-varying phase modulation of the vortex shedding process relative to the cylinder displacement, periodic at frequency f_m .
3. *$2f_m$ periodic with f_e nonlock-in:* This is essentially a period-doubled version of the previous pattern. The vortices do not exhibit lock-in during each f_e cycle, and the pattern does not repeat from one f_m cycle to the next. However, essentially identical patterns are formed between times $0 < t < 2/f_m$ and times $2/f_m < t < 4/f_m$ (and so on for every two f_m cycles), indicating a period-doubling effect.
4. *f_m periodic with f_e nonlock-in; mode $(n + 1)$:* Similar to Pattern 2 above, an f_m -periodic phase modulation of the near wake structure is observed, with the difference that an extra pair of vortices is observed during each f_m beat packet (compared to the number of cylinder oscillations at f_e during the beat packet).

Nakano and Rockwell conducted a number of such experimental runs to determine the ranges of the parameters f_m/f_e and Y_e/d corresponding to each of the observed wake patterns; Figure 5-3, from their paper [51], illustrates these response state ranges.

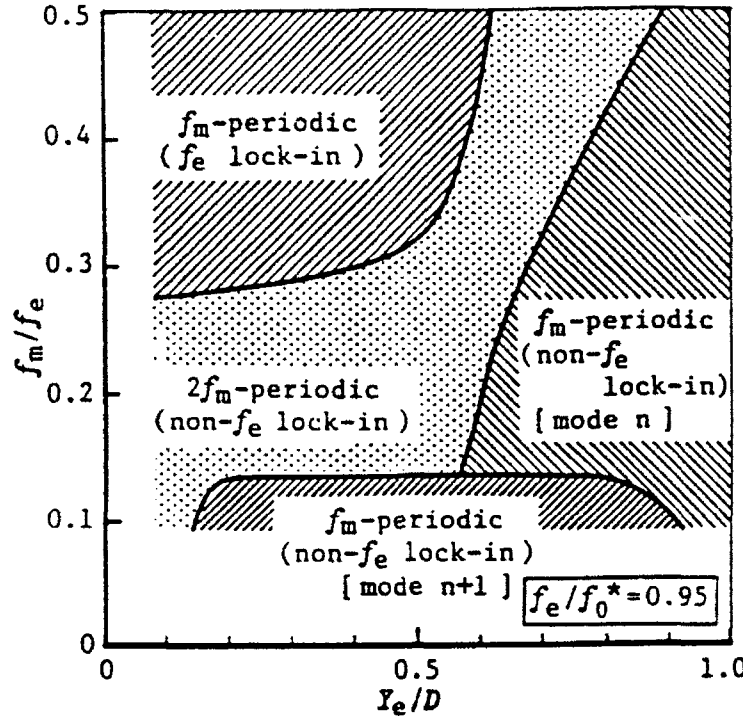


Figure 5-3: States of response of near-wake as a function of dimensionless modulation frequency f_m/f_e and amplitude Y_e/d at $f_e/f_s = 0.95$; from Nakano and Rockwell (1991).

It should be noted that the amplitude-modulated cylinder excitation used by Nakano and Rockwell differed from the type of waveform used by us and by Triantafyllou and Karniadakis [79, 78]. Equation 5.5 can be written in the alternative form

$$y(t) = \frac{Y_e}{4} \sin(2\pi(f_e - f_m)t) - \frac{Y_e}{2} \sin(2\pi f_e t) + \frac{Y_e}{4} \sin(2\pi(f_e + f_m)t) \quad (5.6)$$

We notice that this corresponds to the superposition of *three* sinusoids at frequencies f_e , $(f_e - f_m)$, and $(f_e + f_m)$. This difference in the imposed waveforms implies that comparisons between the results of Nakano and Rockwell and our own research should be made in a qualitative sense only. In passing, it may be noted that the ratio of unity to the number of carrier frequency oscillations contained in one beat packet, previously defined as the modulation ratio, is in this case given by

$$\text{Modulation ratio} = 1 : \left(\frac{f_e}{f_m} \right) \quad (5.7)$$

(Nakano and Rockwell have used the reciprocal quantity f_m/f_e to characterize their experiments.)

Gopalkrishnan et al. As we mentioned in Chapter 1, results from a preliminary set of our beating oscillation experiments were published in Gopalkrishnan et al. [21, 20]. Rather than describe those experiments in detail, we shall summarize the key findings.

Experiments were conducted using procedures very similar to those reported in this thesis, using an excitation of the form given by Equation 5.1. The amplitude ratio Y_1/d was maintained at 0.15, while the amplitude ratio Y_2/d was increased from 0% of Y_1 to 100% of Y_1 . The modulation ratio was fixed at 1:5, and 10 sets of frequencies $\{f_1, f_2\}$ were tested. Thus these were experiments to determine the effect of *varying modulation depth at constant modulation ratio*.

Owing to the relative sparsity of the testing grid, definite distributions of the beating force coefficients could not be determined. However, the following general conclusions were reached from an analysis of the data:

1. The presence of a second frequency component (beating) caused the lift force coefficients to be smaller than the pure sinusoidal values. The influence of the beating motion clearly increased with increasing modulation depth.
2. Beating caused a reduction of the mean drag coefficient and an increase of the RMS oscillation drag coefficient.

From these results, we were encouraged to pursue the matter further and conduct the experiments that are reported in this chapter. We decided to investigate the influence of varying amplitude and modulation ratio. Since the effects of beating seemed to be maximum at maximum (100%) modulation depth, this parameter was not varied during the present experiments. Owing to improvements and automation of the experimental and analysis procedures, a far denser testing grid was successfully completed.

5.2 Force coefficient measurements

5.2.1 Mean drag coefficient

The mean drag coefficient C_{D_m} for the beating oscillation data was calculated in a manner similar to the stationary and sinusoidal oscillation tests, as the (nondimensionalized) difference between the mean value of the drag force trace during the run period and the value during the final zero period. Not unexpectedly, (given the conclusions of Triantafyllou and Karniadakis [79, 78] and our own previous experiments [21, 20]), the principal result was that the presence of beating reduced the peak amplification of the mean drag. For example, Figure 5-4 shows the variation of C_{D_m} with nondimensional frequency for sinu-

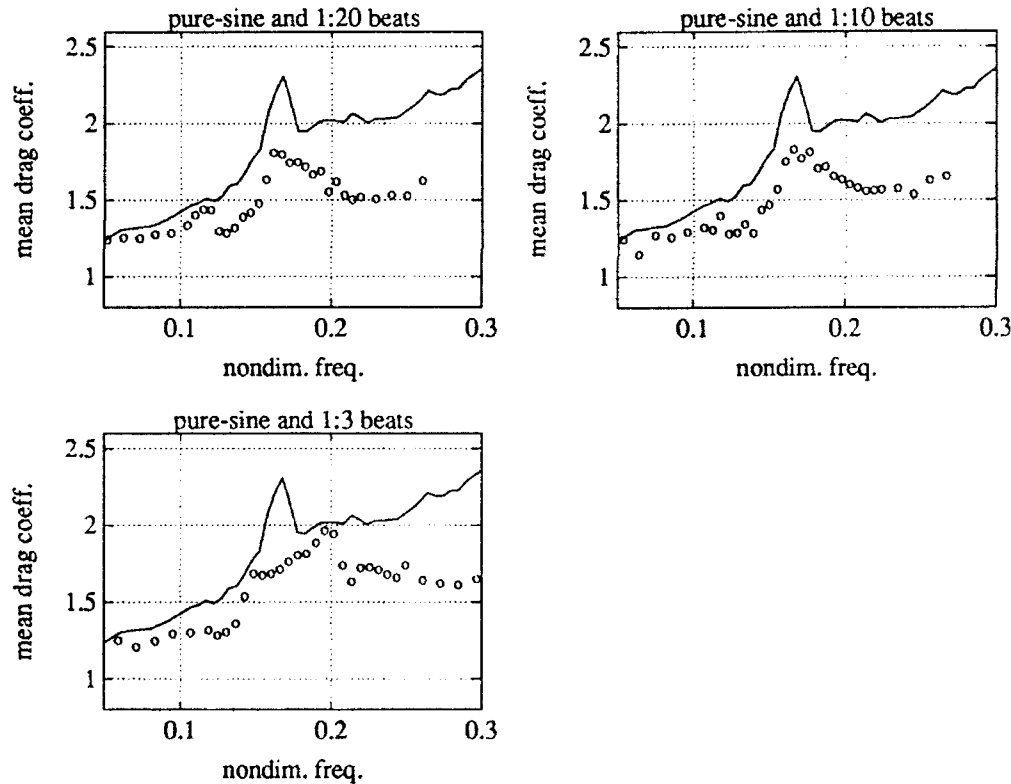


Figure 5-4: C_{D_m} for beating motion with $2Y_1/d = 0.75$ (open circles), and for peak-matched sinusoidal motion (solid lines).

sinoidal oscillations (solid lines) and beating oscillations (open circles) of amplitude ratio 0.75. Note that for the sinusoidal data, the amplitude ratio $Y_0/d = 0.75$ and the nondimensional oscillation frequency \hat{f}_0 are well defined; for the beating oscillations, the data correspond to the *peak* amplitude ratio $2Y_1/d = 0.75$ and the nondimensional *carrier* frequency \hat{f}_c .

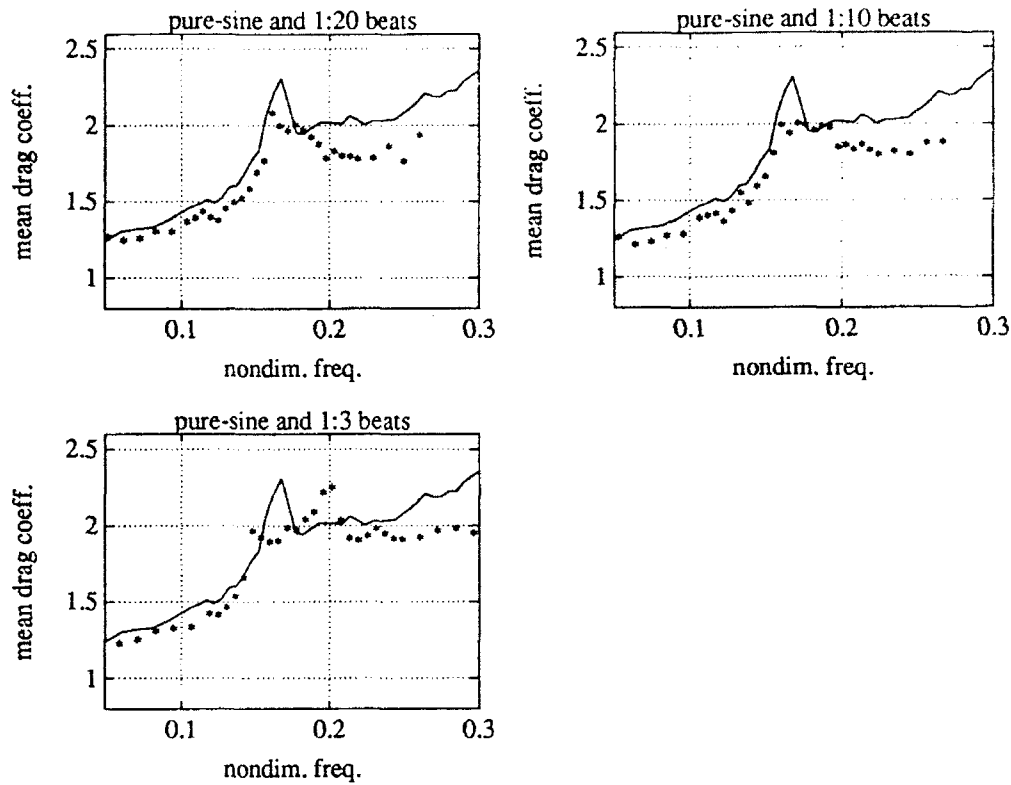


Figure 5-5: C_{D_m} for beating motion of RMS amplitude ratio $Y_{RMS}/d = 0.53$ (asterisks), and for RMS-matched sinusoidal motion (solid lines).

From Figure 5-4, it is clear that the presence of beating significantly reduces the mean drag force. The data for the 1:20 and 1:10 beats (relatively slow modulation) are similar and show a reduction and associated widening of the C_{D_m} amplification peak. The data for the 1:3 beats (relatively fast modulation) shows a “plateau” or “double peak” behavior of the mean drag, consistent with the observations of Schargel [68, 69] in his analysis of (relatively broadband, hence rapidly modulated) random cylinder oscillations.

The reduction of the mean drag as illustrated in Figure 5-4 could perhaps be explained as being due merely to the fact that the beating input oscillations have the same peak amplitude as the sinusoidal oscillations (“peak-matched”), and hence have a smaller RMS amplitude and lower input *power*. In fact, it would appear that the presence of beating causes a reduction of the peak mean drag coefficient even if the RMS of the input motions are the same. (See also Gopalkrishnan *et al.* [21, 20]). This phenomenon is illustrated in Figure 5-5, which depicts the same sinusoidal C_{D_m} data as the previous figure (peak amplitude ratio = 0.75, RMS amplitude ratio = 0.53) (solid lines), compared here to the

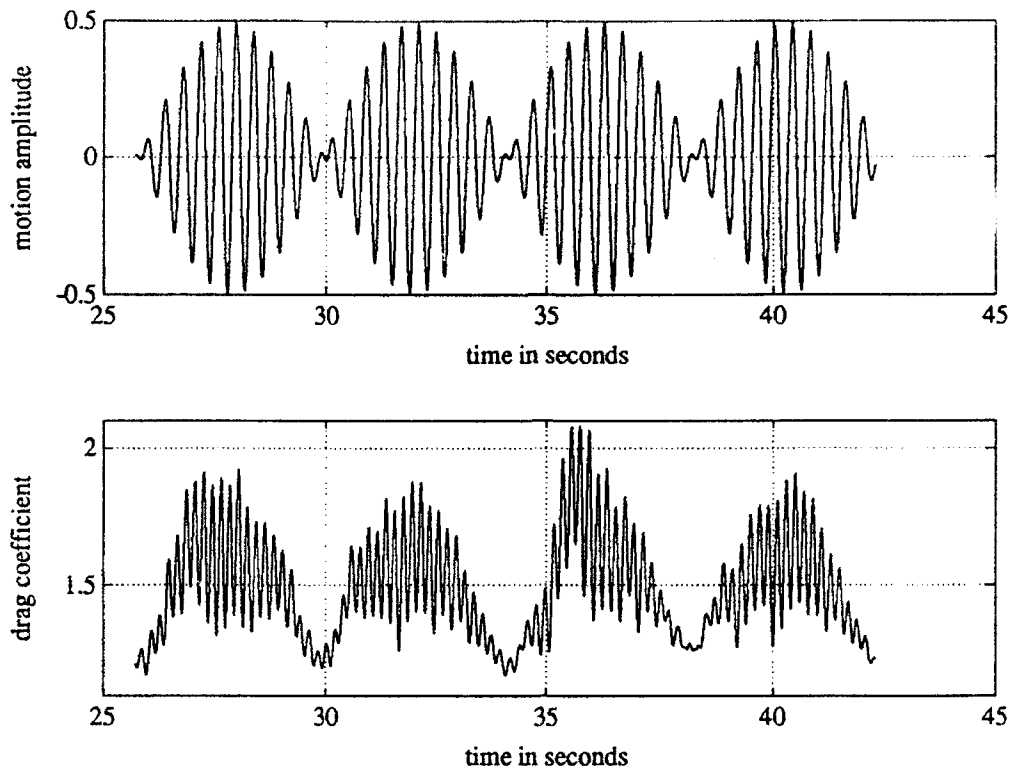


Figure 5-6: Motion and drag for a typical 1:10 beating case; $\hat{f}_c = 0.160$, $2Y_1/d = 0.50$.

results obtained for beating motions having the same RMS oscillation amplitude (“RMS-matched”) (asterisks). While in an overall sense the beating mean drag coefficients are now much closer to the sinusoidal data, it is seen once again that the peak values predicted from the sinusoidal results are not observed. The fast modulation data (1:3 beats) again exhibit a double-peaked behavior, but the locations of the C_{D_m} peaks are quite different from the sinusoidal case.

From the preceding observations, it would seem that the values of the beating mean drag coefficient cannot be obtained directly from sinusoidal data, and that one must seek other models to achieve such predictions. An attempt along these lines (first suggested by Triantafyllou [78]) is to consider the “instantaneous mean drag coefficient” of a beating oscillation waveform as being a quasistatic, nonlinear process dependent on the instantaneous oscillation amplitude. For example, Figure 5-6 illustrates a typical set of amplitude-modulated data, showing time-trace segments of the cylinder motion and corresponding (normalized) drag coefficient for a waveform of 1:10 modulation ratio, peak amplitude ratio $2Y_1/d = 0.50$, and nondimensional carrier frequency $\hat{f}_c = 0.16$. If we define the “instanta-

neous mean drag coefficient" $C_{D_m}^{inst}$ as the average value of the drag coefficient calculated over one carrier frequency cycle, Figure 5-6 suggests that this instantaneous drag rises and falls with the *envelope* of the beating motion, taking on the appearance of a rectified sinusoid. To arrive at the model, we assume that the value of this instantaneous mean drag coefficient is equal at all times to the value of the mean drag coefficient for a *pure sinusoidal* oscillation having the same *instantaneous* oscillation amplitude. The resultant beating mean drag coefficient is then the "average instantaneous mean drag coefficient", and is given by

$$C_{D_m} = \overline{C_{D_m}^{inst}} = C_{D_{m-0}} + (\overline{C_{D_{m-S}} - C_{D_{m-0}}}) \quad (5.8)$$

where $C_{D_{m-0}}$ has been used to denote the stationary mean drag coefficient (a constant), $C_{D_{m-S}}$ to denote the sinusoidal mean drag coefficient (a function of oscillation amplitude and frequency), and the overline symbol denotes an average taken over all the instantaneous amplitudes of the beating input. If now the sinusoidal mean drag is considered to be a linear function of oscillation amplitude (a reasonable approximation, see Figure 4-7), Equation 5.8 can be simplified to depend only on $C_{D_{m-0}}$ and the *maximum* value of $C_{D_{m-S}}$, i.e. the value of $C_{D_{m-S}}$ at the peak amplitude of motion. The expression for the beating mean drag then is

$$C_{D_m} = \overline{C_{D_m}^{inst}} = C_{D_{m-0}} + \frac{2}{\pi}(C_{D_{m-S}}^{peak} - C_{D_{m-0}}) \quad (5.9)$$

where the factor $2/\pi$ appears as the average value of a rectified sinusoid.

Values of the beating mean drag coefficient C_{D_m} were computed according to Equation 5.9 for all of the amplitude-modulated cases and compared to the actual measured values. It was found that the quasistatic model gave excellent results for the slow modulation cases, but was inaccurate for the fast modulations. Figure 5-7 shows the measured mean drag coefficient for beating oscillations with $2Y_1/d = 0.50$ (open circles), compared to the results calculated according to the above model (dashed lines); the validity of the model for slow modulations is clearly seen.

For the fast beating cases (1:3 ratio), it was found necessary to develop an alternative model not based on a quasistatic analysis. The characteristic double-peaked C_{D_m} results obtained for the 1:3 ratio beats suggested a linear addition behavior. Hence, a model was devised that consisted of the linear superposition of the sinusoidal drag amplification

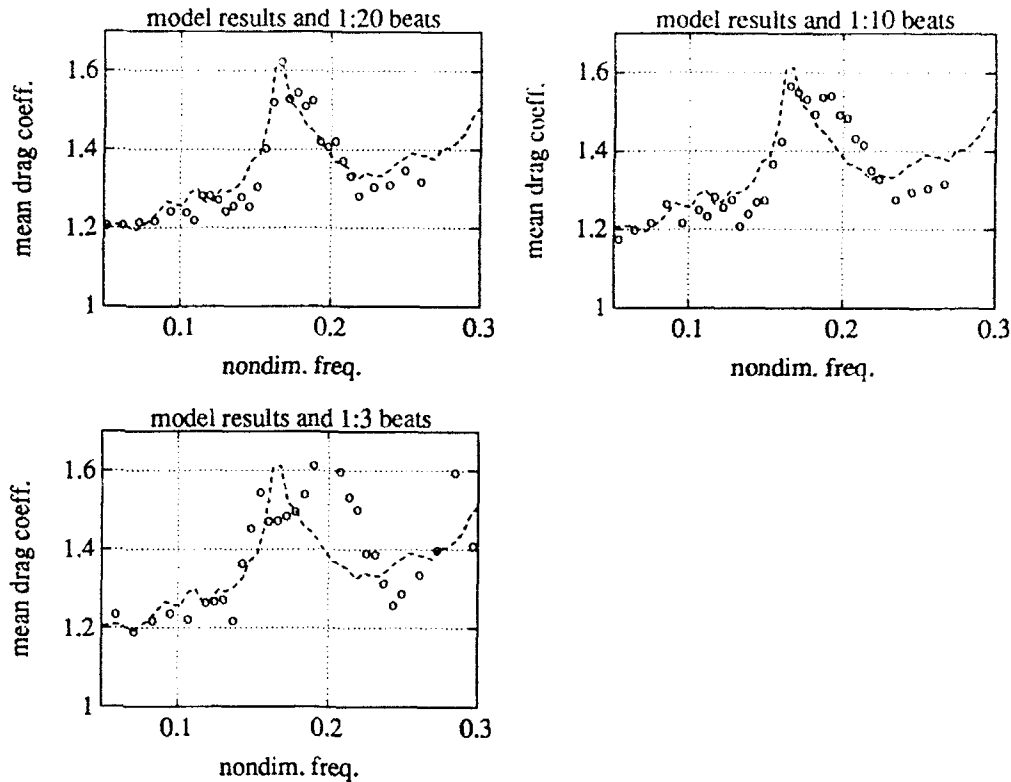


Figure 5-7: Results from the quasistatic C_{Dm} model (dashed lines) and measured data (open circles); beating motion with $2Y_1/d = 0.50$.

results for each of the two spectral components comprising the beating waveform. Thus, for a particular beating input consisting of components at amplitudes and frequencies $\{Y_1, f_1\}$ and $\{Y_2, f_2\}$, the corresponding sinusoidal mean drag coefficients C_{Dm-s_1} and C_{Dm-s_2} were found (from, for example, Figure 3-12) and added to give the beating mean drag coefficient according to

$$C_{Dm} = C_{Dm-0} + (C_{Dm-s_1} - C_{Dm-0}) + (C_{Dm-s_2} - C_{Dm-0}) \quad (5.10)$$

Values of C_{Dm} by this alternative method were calculated and found to give good results for fast beats of moderate amplitude ratio. Figure 5-8 shows the measured mean drag coefficient for beating oscillations of peak amplitude ratio $2Y_1/d = 0.30$ (asterisks), compared to the results calculated according to the linear superposition model of Equation 5.10 (dashed lines); the 1:3 ratio beating results show fairly good agreement.

The primary purpose in devising the models discussed above was to evaluate the behavior

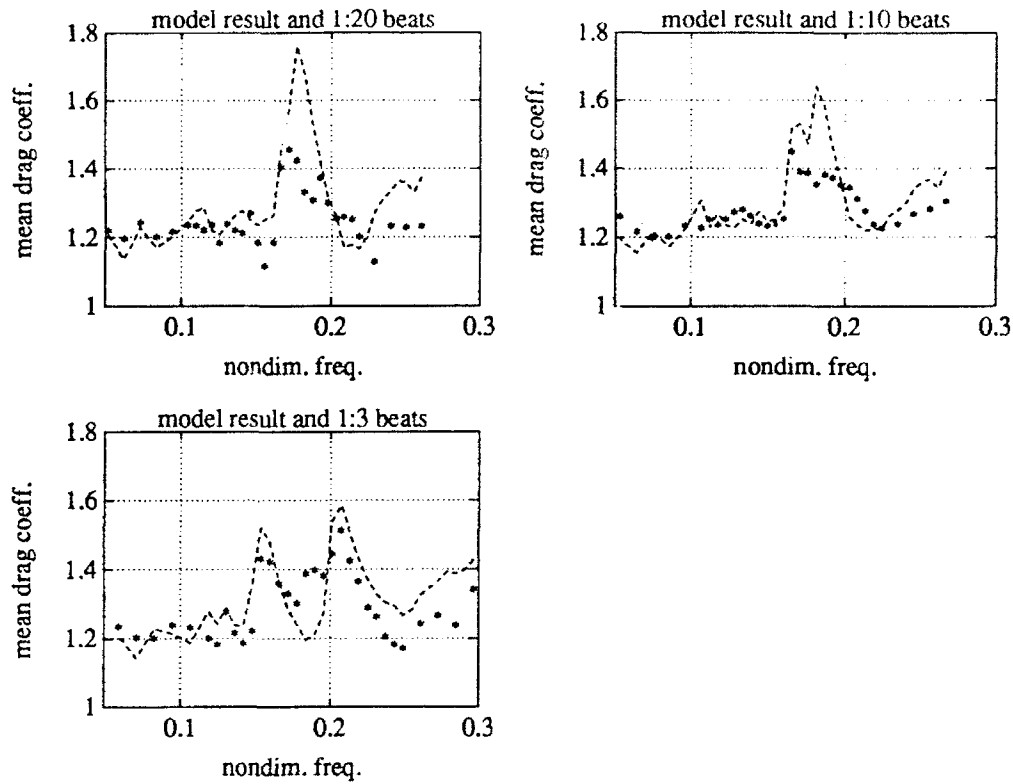


Figure 5-8: Results from the linear C_{D_m} model (dashed lines) and measured data (asterisks): beating motion with $2Y_1/d = 0.30$.

of the beating mean drag coefficient for different modulation ratios. In situations with fairly regular beating motions, the measured data could be used directly to estimate the mean drag force. Figures 5-9 , 5-10, and 5-11 are contour maps of the measured values of C_{D_m} for modulation ratios 1:20, 1:10, and 1:3 respectively. As before, the frequency axis refers to the nondimensional carrier frequency \hat{f}_c , while the amplitude axis refers to the peak amplitude ratio $2Y_1/d$. It can be seen from Figures 5-9 and 5-10 that the drag coefficient results for the 1:20 and 1:10 beats are rather similar. The contour map for the 1:3 ratio beats (Figure 5-11) shows a double-peak behavior that may be discerned at low amplitudes, while a flatter “plateau” behavior is seen at higher amplitudes.

5.2.2 Oscillating drag coefficients

Analysis of the oscillating drag coefficients proved to be less straightforward than that of the mean drag coefficient, as presented in the preceding paragraphs. Two problems had to be considered: first, preparing (and verifying) a model to represent the beating oscillating

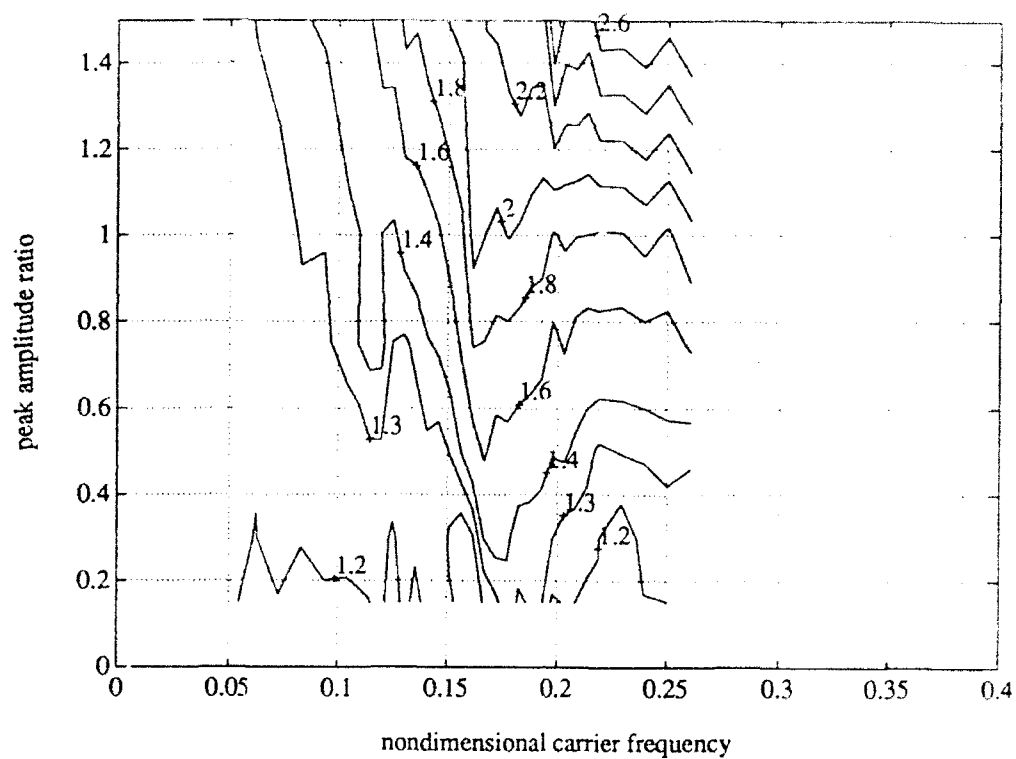


Figure 5-9: Contours of C_{D_m} ; 1:20 beating motion.

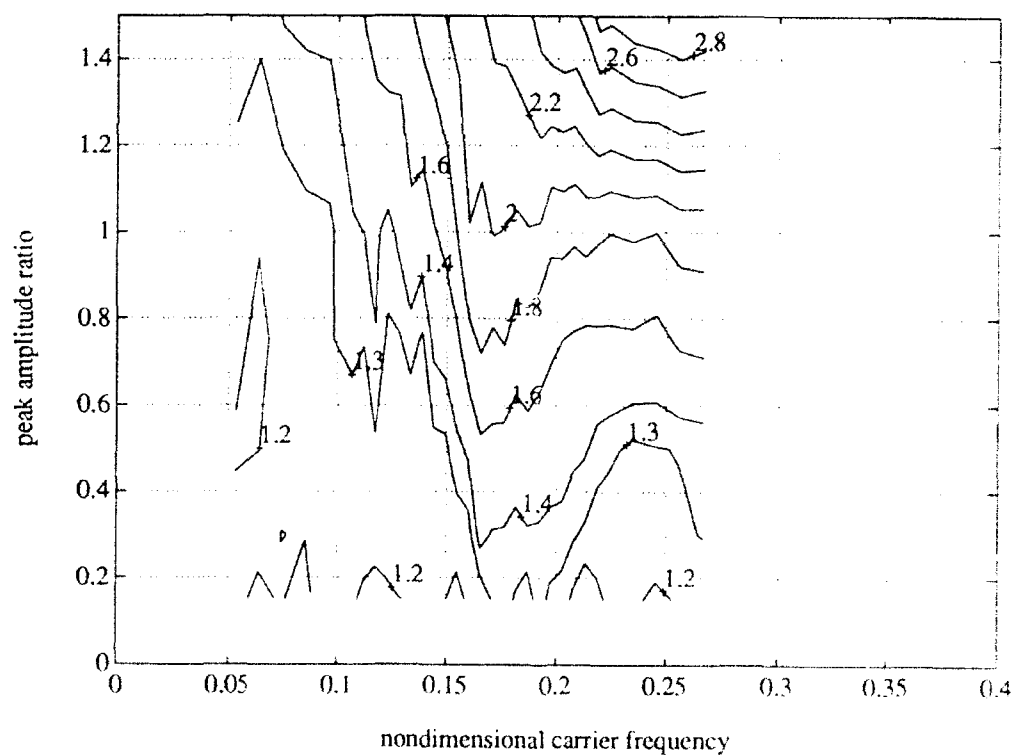


Figure 5-10: Contours of C_{D_m} ; 1:10 beating motion.

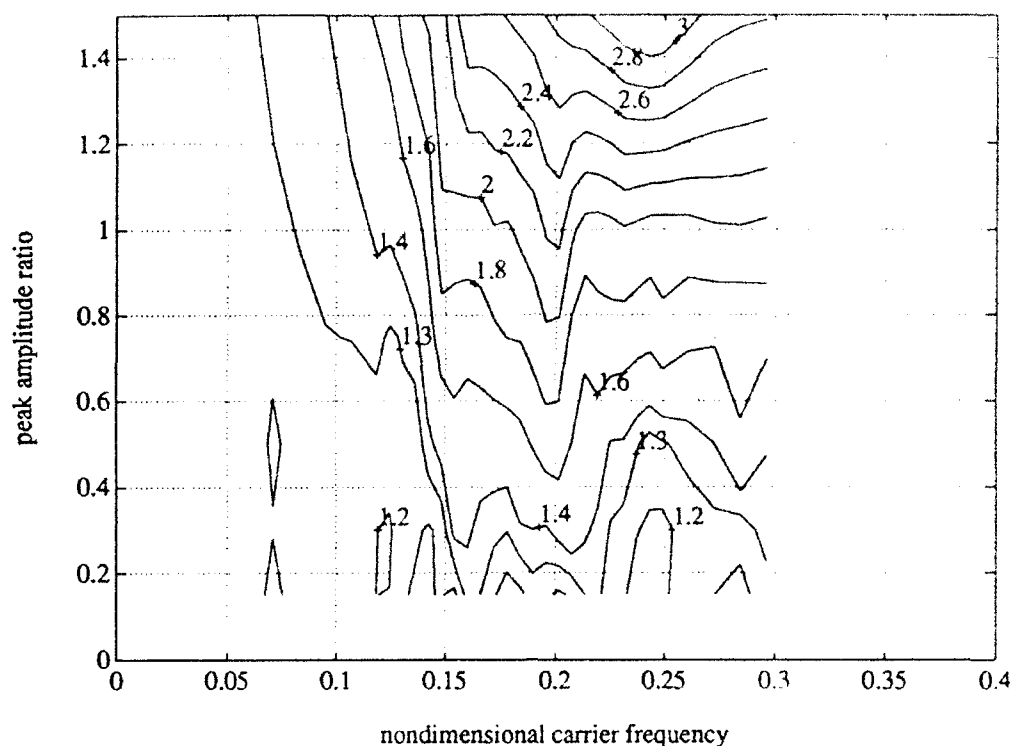


Figure 5-11: Contours of C_{Dm} ; 1:3 beating motion.

drag force; and second, evaluating the coefficients required in the model.

In the case of a pure-sinusoidal oscillation at frequency f_0 , the oscillating component $\overline{C_D}$ of the total drag coefficient C_D was given by

$$\overline{C_D} = C_{D_0} \sin(2\pi(2f_0)t + \psi_0) \quad (5.11)$$

where C_{D_0} was termed the oscillating drag coefficient, and represented the magnitude of a sinusoid at twice the frequency of the input oscillations. (The natural Strouhal component at frequency $2f_s$ has not been included.) By a direct extrapolation of Equation 5.11, one would expect the oscillating drag in the case of a beating input waveform containing components at frequencies f_1 and f_2 to be given by

$$\overline{C_D} = C_{D_1} \sin(2\pi(2f_1)t + \psi_1) + C_{D_2} \sin(2\pi(2f_2)t + \psi_2) \quad (5.12)$$

Values of the coefficients C_{D_1} and C_{D_2} were extracted from the beating data using a method analogous to that used in the sinusoidal case: the known frequencies $2f_1$ and $2f_2$ were used

to generate reference sine and cosine waveforms which were then used to estimate the appropriate Fourier coefficients of the drag force traces, using a 20-cycle time-gating procedure. For example, Figure 5-12 shows the coefficients C_{D_1} and C_{D_2} (circles and crosses, respectively) for beats of individual component amplitude $Y_1/d = 0.50$ (peak amplitude ratio $2Y_1/d = 1.00$), compared to the coefficient C_{D_0} (solid lines) for sinusoidal oscillations

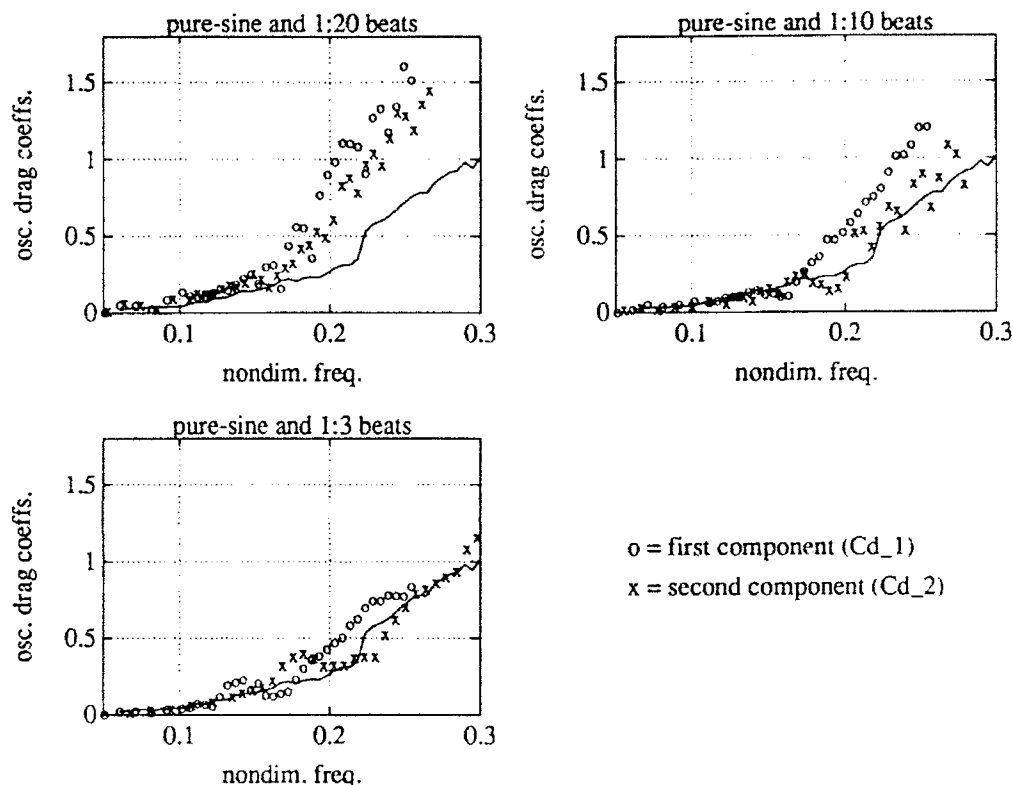


Figure 5-12: C_{D_1} and C_{D_2} for beating motion with $Y_1/d = 0.50$, and C_{D_0} for component-matched sinusoidal motion.

of comparable amplitude $Y_0/d = 0.50$ ("component-matched"). The frequency axis refers to the individual (nondimensional) frequency components \hat{f}_1 and \hat{f}_2 for the beating oscillations and \hat{f}_0 for the sinusoidal case. For fast modulations (1:3) ratio, the beating coefficients closely follow the sinusoidal result; considerable deviation occurs at slower modulation ratios.

To check whether the model of Equation 5.12 adequately represents the beating oscillating drag, we calculated the RMS oscillating drag coefficient from the coefficients C_{D_1} and C_{D_2} and from the actual data traces as well. If Equation 5.12 were accurate, then by

algebraic manipulation

$$C_{DRMS}^{calc.} = \sqrt{\langle \overline{C_D^2} \rangle} = \sqrt{\frac{C_{D1}^2}{2} + \frac{C_{D2}^2}{2}} \quad (5.13)$$

Values of $C_{DRMS}^{calc.}$ calculated from Equation 5.13 were compared to values of C_{DRMS} computed from the time traces of the drag force: Figure 5-13 illustrates the comparison for beating oscillations of peak amplitude ratio $2Y_1/d = 0.75$. The calculated values are a good

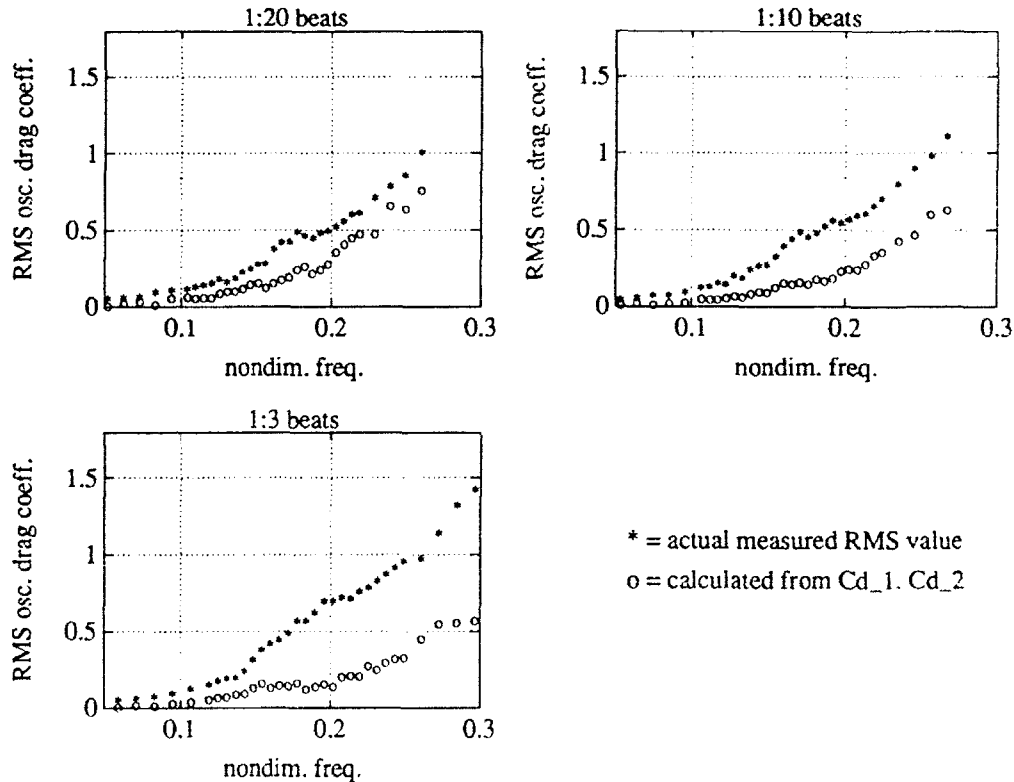


Figure 5-13: C_{DRMS} calculated from actual data, as well as $C_{DRMS}^{calc.}$ from C_{D1} and C_{D2} ; beating motion with $2Y_1/d = 0.75$.

deal lower than the measured values, with the difference increasing with the rapidity of the beating oscillations. Clearly, the beating oscillating drag force contains spectral components in addition to those of Equation 5.13.

A look at the time traces of Figure 5-6 of the previous subsection points to an obvious additional source of oscillating drag: the rise and fall of the drag force trace with the envelope of the beating motion. As a first step, this fluctuation can be modeled as a sinusoid at twice the modulation frequency, i.e. at a frequency $f_2 - f_1$ (see Equation 2.18). This gives for

the total oscillating drag coefficient

$$\begin{aligned} \widetilde{C_D} = & C_{D_{mod}} \sin(2\pi(f_2 - f_1)t + \psi_{mod}) + \\ & C_{D_1} \sin(2\pi(2f_1)t + \psi_1) + C_{D_2} \sin(2\pi(2f_2)t + \psi_2) \end{aligned} \quad (5.14)$$

where the coefficient $C_{D_{mod}}$ expresses the magnitude of the low-frequency oscillatory drag. Values of $C_{D_{mod}}$ were extracted from the beating drag traces, and in addition, were calculated via a simple quasistatic model derived from the same assumptions as the quasistatic model for the beating mean drag coefficient discussed in the previous subsection, i.e. the drag coefficient is assumed to fluctuate between the stationary mean drag coefficient and the sinusoidal mean drag coefficient at the peak amplitude of motion. Thus

$$C_{D_{mod}}^{calc.} = \frac{1}{2}(C_{D_{m-s}}^{peak} - C_{D_{m-0}}) \quad (5.15)$$

where the notation is as used previously. Figure 5-14 compares the experimentally deter-

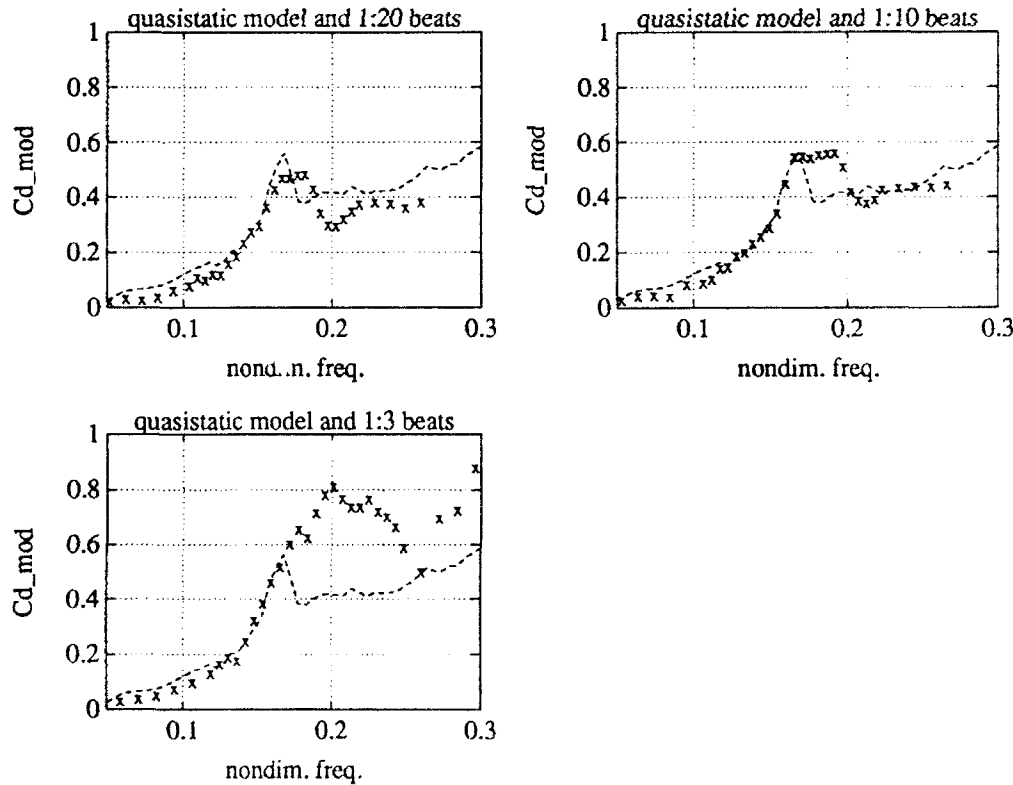


Figure 5-14: Measured values of $C_{D_{mod}}$ (crosses) and results from quasistatic model (dashed lines); beating motion with $2Y_1/d = 0.75$.

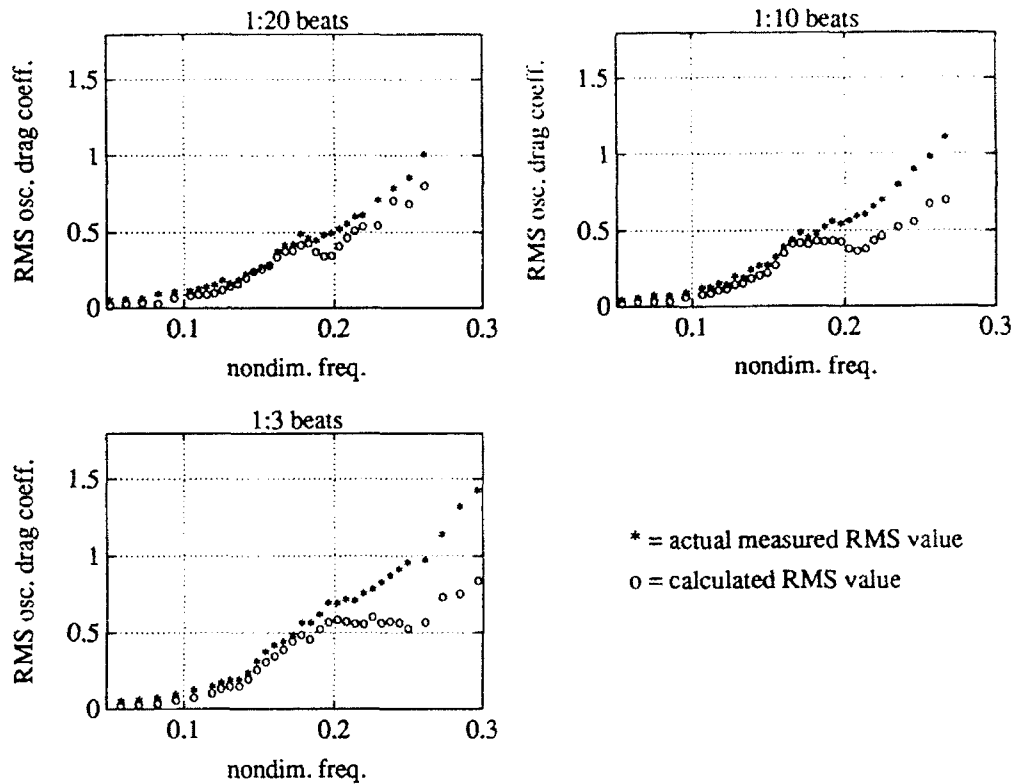


Figure 5-15: $C_{D_{RMS}}$ calculated from actual data, as well as $C_{D_{RMS}}^{calc.}$ from C_{D_1} , C_{D_2} and $C_{D_{mod}}$; beating motion with $2Y_1/d = 0.75$.

mined values of $C_{D_{mod}}$ (crosses) to the results from the quasistatic model (dashed lines) for beating oscillations of peak amplitude ratio $2Y_1/d = 0.75$. We see that the magnitudes of $C_{D_{mod}}$ are, in fact, very substantial; the quasistatic model proves to be adequate for slow modulations, but fails to predict $C_{D_{mod}}$ accurately for fast modulations.

To check the validity of Equation 5.14, we once again calculated the RMS oscillating drag coefficient from the individual oscillating drag coefficient magnitudes. By manipulation of Equation 5.14, $C_{D_{RMS}}$ is now given by

$$C_{D_{RMS}}^{calc.} = \sqrt{\langle \widetilde{C_D}^2 \rangle} = \sqrt{\frac{C_{D_{mod}}^2}{2} + \frac{C_{D_1}^2}{2} + \frac{C_{D_2}^2}{2}} \quad (5.16)$$

Figure 5-15 compares values of the RMS oscillating drag coefficient calculated according to Equation 5.16 with the corresponding values extracted from the actual data traces, for beating oscillations with $2Y_1/d = 0.75$. This time, we see that the calculated values $C_{D_{RMS}}^{calc.}$ closely follow the actual values at low frequencies, but fall off in magnitude at higher

frequencies. The difference between the actual $C_{D_{RMS}}$ and the calculated values increases with the rapidity of the modulations, and indicates that while we have now accounted for the bulk of the oscillating drag, yet additional frequency components are present as well. Figure 5-16 shows the power spectrum of the drag force for a typical high frequency 1:3 beating oscillation, in this case with amplitude ratio $2Y_1/d = 1.00$, nondimensional carrier frequency $\hat{f}_c = 0.279$, and actual component frequencies $f_1 = 3.760$ Hz and $f_2 = 5.013$ Hz. The oscillating drag components C_{D_1} at frequency $2f_1$, C_{D_2} at frequency $2f_2$, and $C_{D_{mod}}$ at frequency $f_2 - f_1$ are clearly visible, but additional sum-and-difference frequency components are present as well.

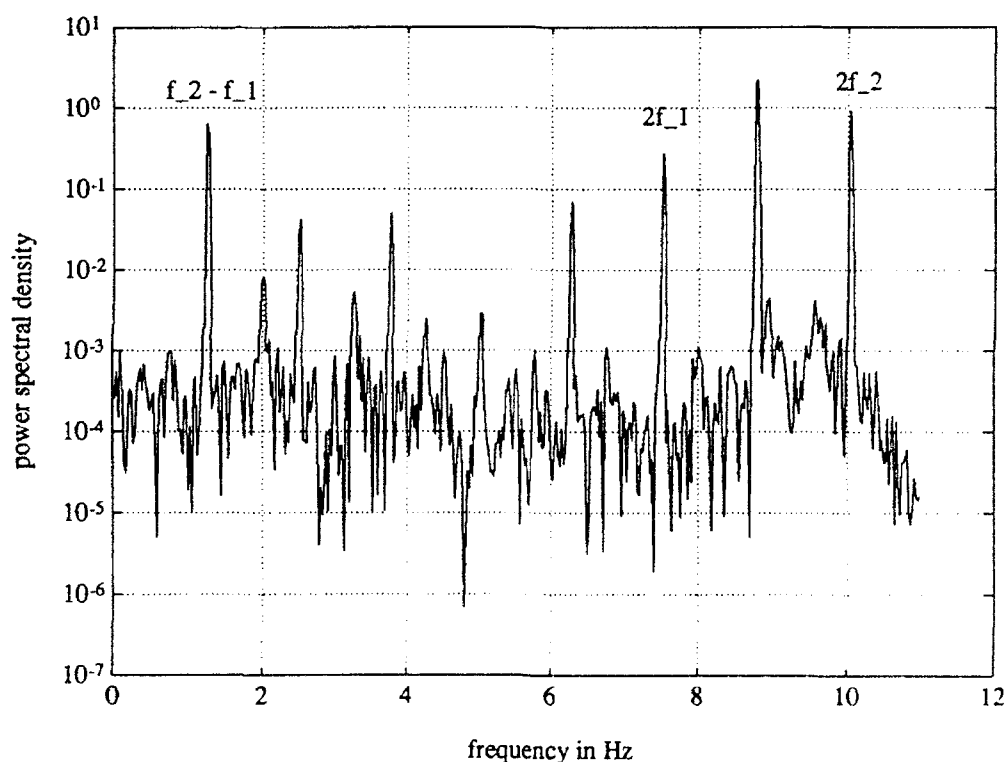


Figure 5-16: Power spectrum of a high frequency, 1:3 ratio, beating drag force trace.

To summarize the analysis thus far: the beating oscillating drag force contains significant spectral components at frequencies $2f_1$, $2f_2$, and $f_2 - f_1$, where f_1 and f_2 are the frequencies of the input components. The oscillating drag coefficients at the above frequencies, C_{D_1} , C_{D_2} , and $C_{D_{mod}}$ respectively, are difficult to estimate (all at once) from sinusoidal data. The coefficients C_{D_1} and C_{D_2} are similar to the sinusoidal results for *fast* modulations (Figure 5-12), while the coefficient $C_{D_{mod}}$ can be obtained via a quasistatic model for *slow*

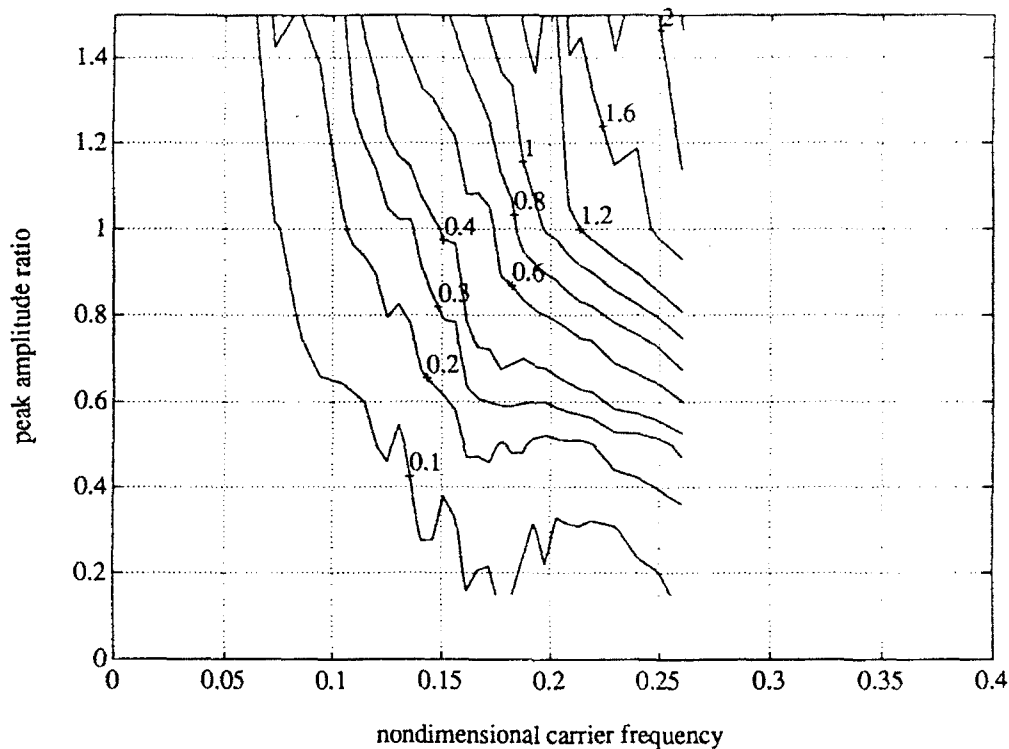


Figure 5-17: Contours of $C_{D_{RMS}}$; 1:20 beating motion.

modulations (Figure 5-14).

From the foregoing discussion, one is led to the conclusion that the simplest way of quantifying the beating oscillating drag would be use the RMS drag coefficient $C_{D_{RMS}}$ directly. An interesting fact that we notice is that the magnitude and variation of $C_{D_{RMS}}$ appear almost independent of the modulation ratio. Figures 5-17, 5-18, and 5-19 show the contours of the measured RMS oscillating drag coefficient for 1:20, 1:10, and 1:3 beating oscillations respectively. If the experimental data scatter is ignored (these contours have not been smoothed), we see that $C_{D_{RMS}}$ depends only very weakly on the rapidity of the beats. It is left to a future investigation to determine whether or not this is merely a fortuitous coincidence.

Before closing this subsection, it should be noted that the RMS oscillating drag coefficient for beating motions is, in general, higher than the corresponding RMS coefficient for sinusoidal oscillations. For example, Figure 5-20 depicts the measured values of $C_{D_{RMS}}$ for beating oscillations of peak amplitude ratio $2Y_1/d = 0.75$ (open circles), compared to the $C_{D_{RMS}}$ data obtained for pure sinusoidal oscillations of equal RMS input amplitude

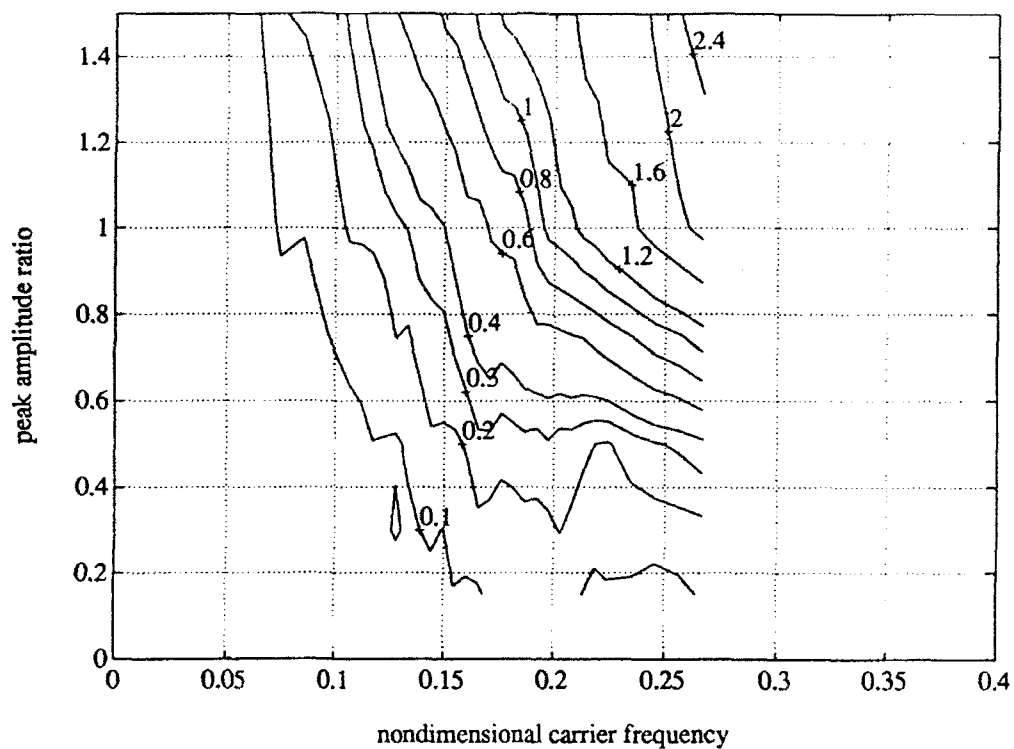


Figure 5-18: Contours of $C_{D_{RMS}}$; 1:10 beating motion.

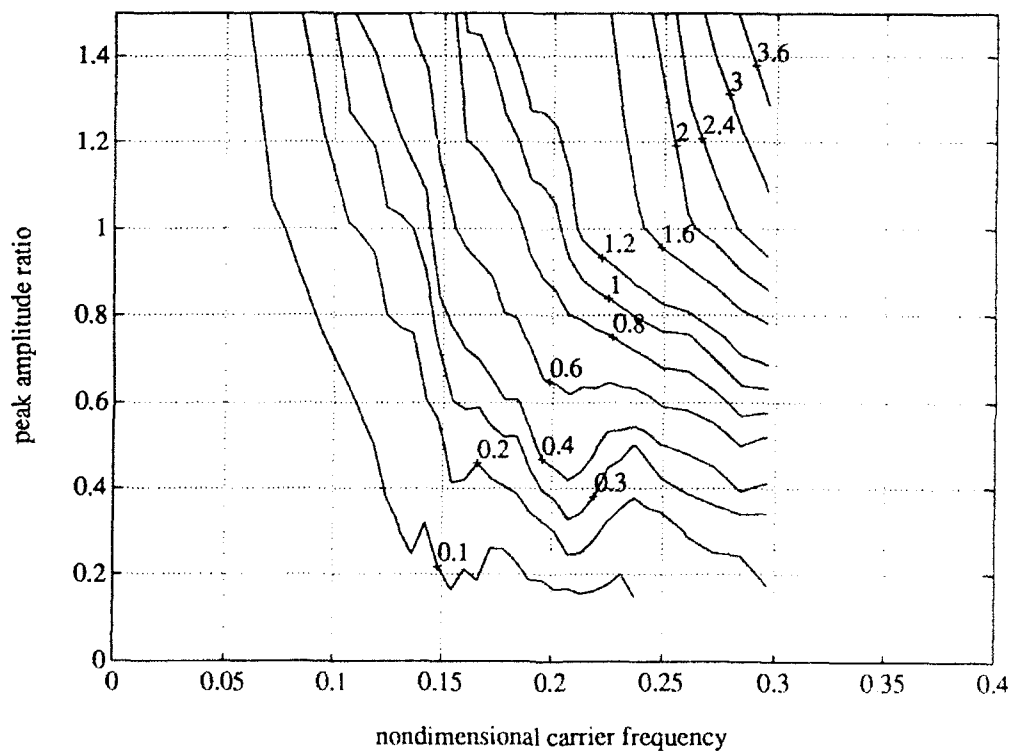


Figure 5-19: Contours of $C_{D_{RMS}}$; 1:3 beating motion.

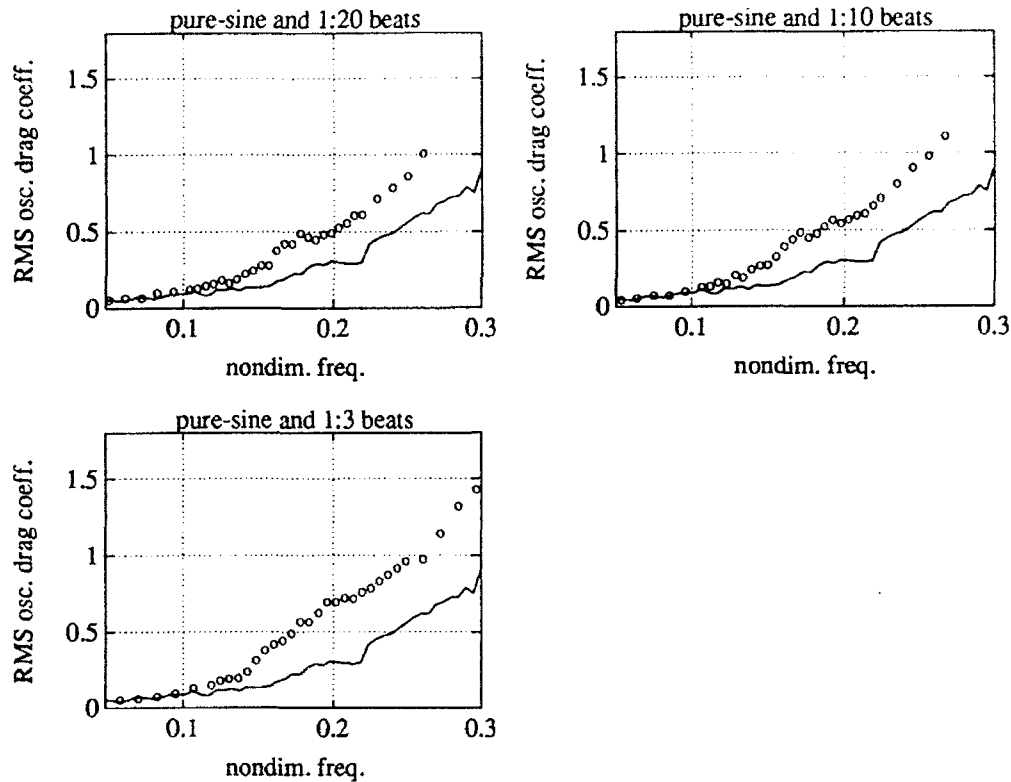


Figure 5-20: $C_{D_{RMS}}$ for beating motion with $2Y_1/d = 0.75$ (open circles), and for RMS-matched sinusoidal oscillations (solid lines).

(“RMS-matched”) (solid lines); the increase due to the beating motion is evident. Our drag data therefore confirm the numerical findings of Triantafyllou and Karniadakis [79, 78] mentioned earlier, i.e. the presence of beating causes a simultaneous *decrease* of the mean drag force and an *increase* of the oscillating drag force.

5.2.3 Oscillating lift coefficients

As in the previous subsection on the oscillating drag coefficients, our first attempt at the analysis of the beating lift forces involved a direct extension of the classical sinusoidal formulation. From Chapter 2 (Equation 2.22), we see that this approach gives, for a beating excitation of the form of Equation 5.1, a lift coefficient according to:

$$C_L = C_{L_1} \sin(2\pi f_1 t + \phi_1) + C_{L_2} \sin(2\pi f_2 t + \phi_2) \quad (5.17)$$

where C_{L1} and C_{L2} are the magnitudes of the lift coefficient components at the input frequencies f_1 and f_2 respectively, and the angles ϕ_1 and ϕ_2 represent the phase differences between the lift components and the corresponding motion (input) components. The coefficients C_{L1} and C_{L2} and the phase angles ϕ_1 and ϕ_2 were extracted from the beating data using the Fourier techniques outlined in Chapter 2. For example, Figure 5-21 illustrates the values of C_{L1} and C_{L2} (circles and crosses respectively) obtained for a beating waveform of relatively small individual component amplitude $Y_1/d = 0.15$, compared to the sinusoidal

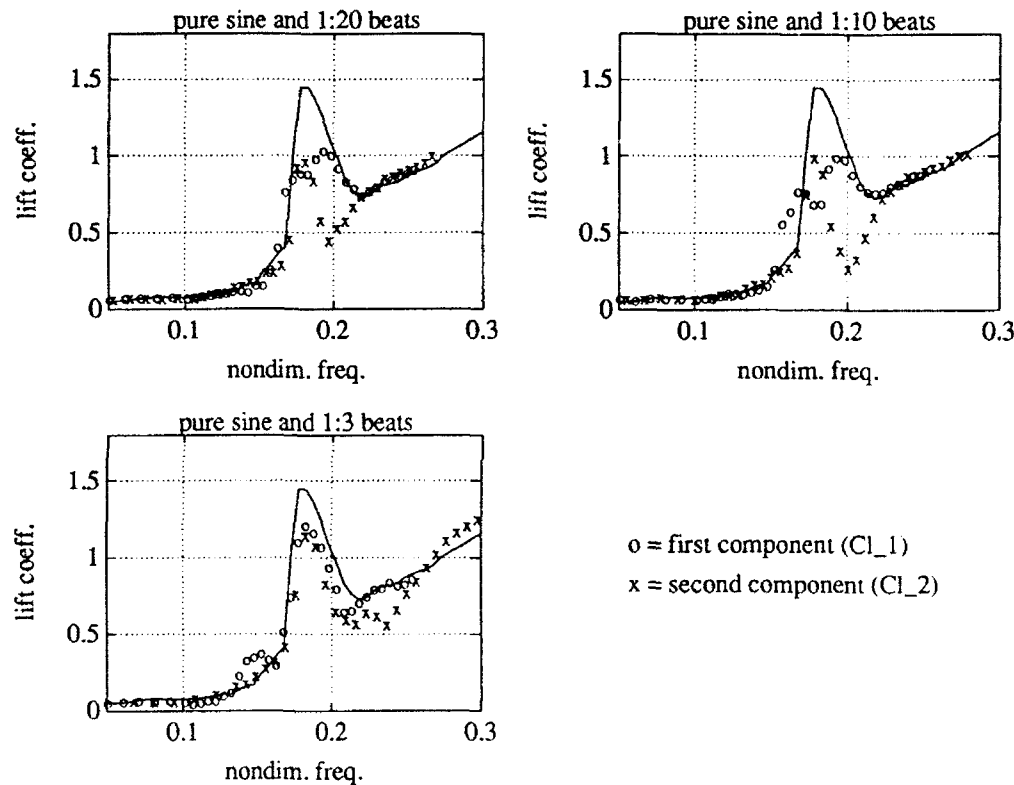


Figure 5-21: C_{L1} and C_{L2} for beating motion with $Y_1/d = 0.15$, and C_{L0} for component-matched sinusoidal motion.

coefficient C_{L0} (solid lines) for oscillations of component-matched amplitude $Y_0/d = 0.15$.

To show that the beating lift force does indeed consist primarily of the two components of Equation 5.17, we calculated the RMS oscillating lift coefficient from the expression

$$C_{L_{RMS}}^{calc.} = \sqrt{\langle C_L^2 \rangle} = \sqrt{\frac{C_{L1}^2}{2} + \frac{C_{L2}^2}{2}} \quad (5.18)$$

as well as directly from the beating lift force data traces. Figure 5-22 shows the $C_{L_{RMS}}^{calc.}$ values calculated from the individual components (open circles) compared to the $C_{L_{RMS}}$

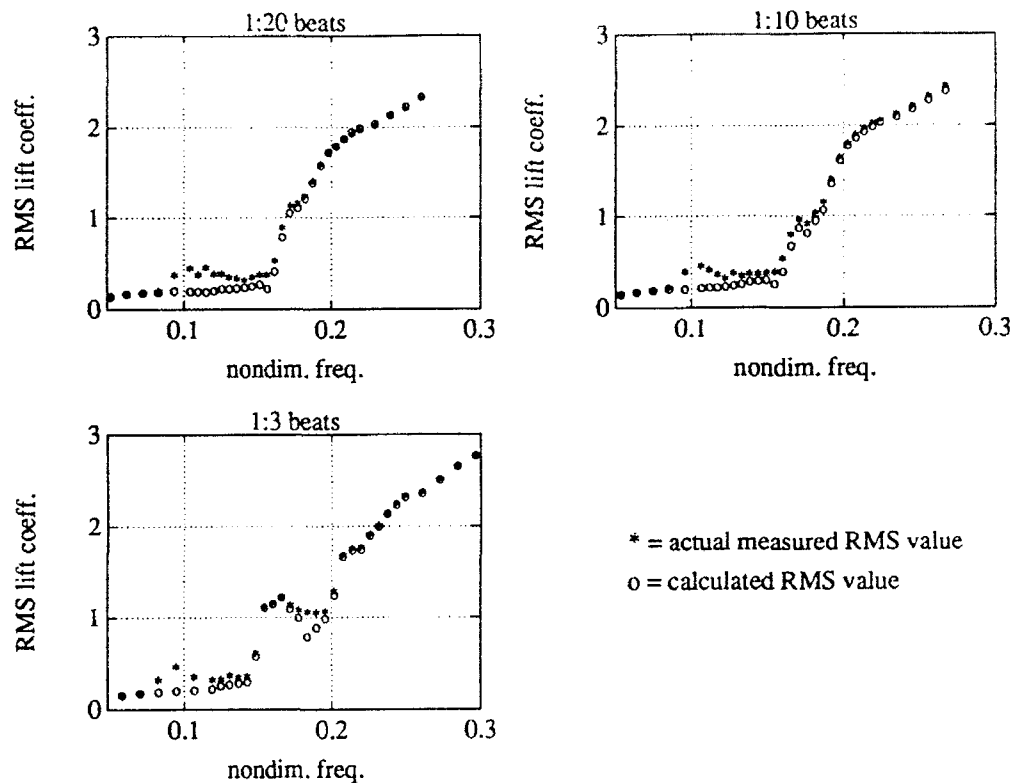


Figure 5-22: $C_{L_{RMS}}$ calculated from actual data, as well as $C_{L_{RMS}}^{calc.}$ from C_{L_1} and C_{L_2} ; beating motion with $2Y_1/d = 0.75$.

values computed directly from the data (asterisks), for beating oscillations of peak amplitude $2Y_1/d = 0.75$. We see that there are only small differences between the two sets of data, except for a small peak of unknown origin, near a nondimensional frequency of 0.10, in each of the actual $C_{L_{RMS}}$ data-sets. Nonetheless, the dual-frequency beating model of Equation 5.17 would appear to be a good one, independent of the modulation ratio. To make the point further, Figure 5-23 shows the lift force power spectrum for the same experimental run related earlier to Figure 5-16: a beating motion with modulation ratio 1:3, amplitude ratio $2Y_1/d = 1.00$, and component frequencies $f_1 = 3.760$ Hz and $f_2 = 5.013$ Hz. The lift force is dominated by the components at the input frequencies f_1 and f_2 . (Note the contrast to the drag force power spectrum (Figure 5-16)).

From the previous paragraph, we conclude that a cylinder undergoing dual-frequency beating motion sustains a vortex-induced lift force which may also be approximated as a dual-frequency beating oscillation, of the form given by Equation 5.17. (We shall investigate the limitations to this model in a later section.) The problem that arises, however, is that

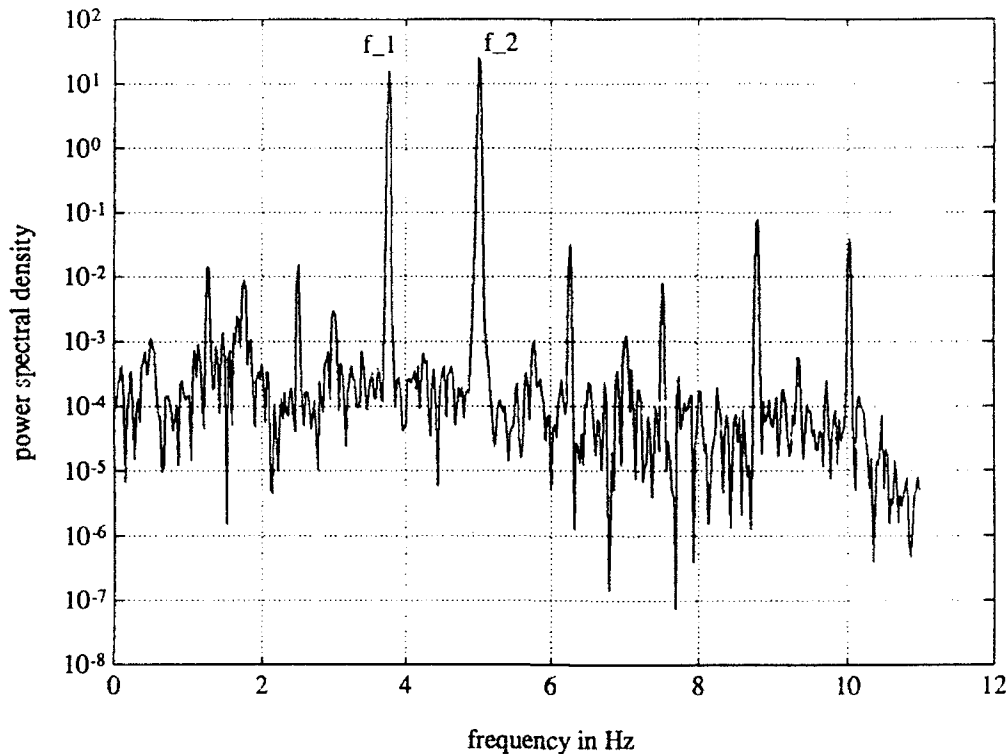


Figure 5-23: Power spectrum of a high frequency, 1:3 ratio, beating lift force trace.

the coefficients that characterize the lift force oscillation, C_{L1} , C_{L2} , ϕ_1 , and ϕ_2 , are not easy to estimate from available sinusoidal data. From Figure 5-21, we see that the presence of a second frequency component in the input motion alters the value of the lift coefficient at *both* frequency components. Figure 5-24 illustrates the variation of the phase angles ϕ_1 and ϕ_2 (circles and crosses, respectively) for beating oscillations of individual component amplitude $Y_1/d = 0.50$, compared to the component-matched sinusoidal results (solid lines). We see that the phase angles too are substantially modified from the sinusoidal data. We found that the effect of beating on the lift coefficient magnitudes and phase angles increased with oscillation amplitude, and at the higher amplitude ratios the beating data bore very little resemblance to sinusoidal results. A further drawback to the dual-frequency spectral model of Equation 5.17 is that the model cannot be related directly to the vortex dynamics in the wake of the cylinder, since there is no evidence to suggest that vortices are shed at two distinct frequencies.

From all of the above remarks, it would appear advantageous to simplify the position by reducing the number of variables involved, and to seek a single parameter that would

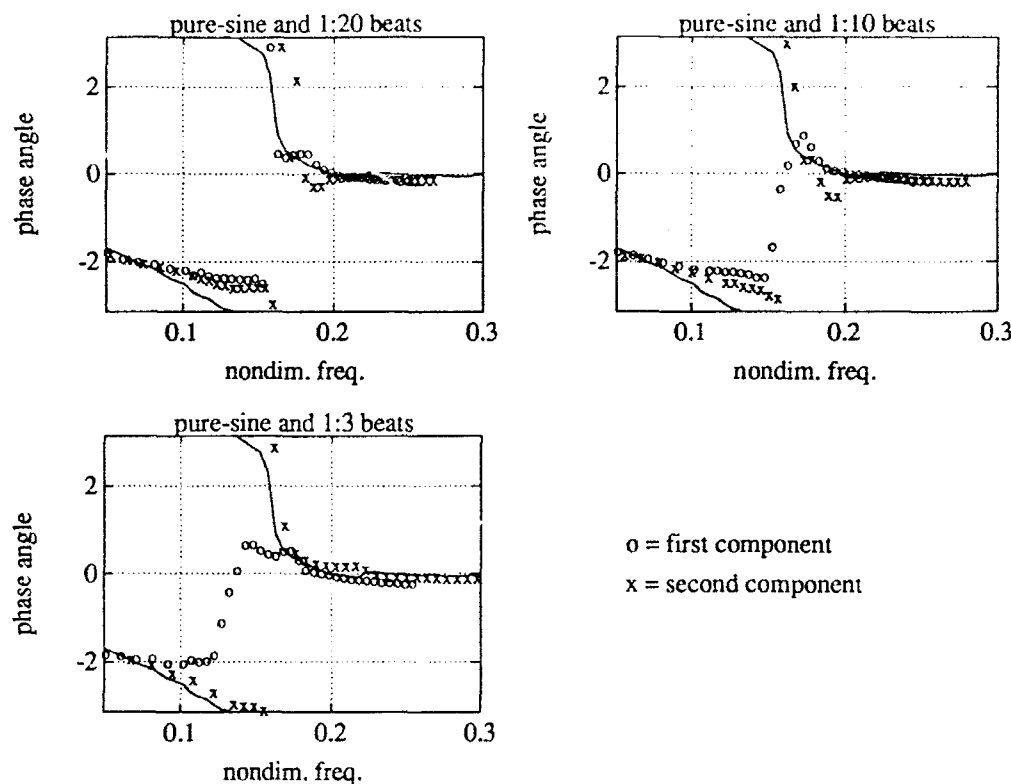


Figure 5-24: ϕ_1 and ϕ_2 for beating motion with $Y_1/d = 0.50$, and ϕ_0 for component-matched sinusoidal motion.

express the magnitude and effect of the lift force for the entire beating waveform. One candidate would be the RMS oscillating lift coefficient $C_{L_{RMS}}$, which has been widely used in the past, particularly in connection with field experiments [7]. In most cases however, the calculation of $C_{L_{RMS}}$ does not include any information about the phase angle, and so must be viewed with great caution. Without phase angle information, there is no way of knowing whether the action of the lift force is exciting or damping, and hence the utility of such data is enormously diminished.

In order to express both magnitude and phase angle information in a simplified manner, we proceeded to define two "equivalent lift coefficients" $C_{L_{V_c}}$ and $C_{L_{A_c}}$ at the carrier frequency f_c , to quantify the net magnitudes of the beating lift force in phase with cylinder velocity and in phase with cylinder acceleration respectively. These coefficients are defined by direct power transfer and inertial force calculations as:

$$C_{L_{V_c}} = 2 \frac{\langle C_L(t), \dot{y}(t) \rangle}{\sqrt{2 \langle \dot{y}(t), \dot{y}(t) \rangle}} \quad (5.19)$$

and

$$C_{L-A_c} = 2 \frac{\langle C_L(t), \ddot{y}(t) \rangle}{\sqrt{2} \langle \ddot{y}(t), \ddot{y}(t) \rangle} \quad (5.20)$$

where $C_L(t)$ is the total lift coefficient, $\dot{y}(t)$ is the cylinder velocity calculated directly from the cylinder motion, $\ddot{y}(t)$ is the cylinder acceleration calculated similarly, and $\langle \dots \rangle$ denotes the appropriate cross- or auto-correlation at zero lag. In the case of pure sinusoidal oscillations, Equations 5.19 and 5.20 revert to the original definitions of C_{L-V_0} and C_{L-A_0} as $C_{L_0} \sin(\phi_0)$ and $-C_{L_0} \cos(\phi_0)$ respectively (see Equations 3.3 and 3.5). For dual frequency beating oscillations, some algebraic manipulations of Equations 5.19 and 5.20 yield (keeping in mind that in our case $Y_1 = Y_2$)

$$C_{L-V_c} = \frac{2\pi f_1 Y_1 C_{L_1} \sin(\phi_1) + 2\pi f_2 Y_2 C_{L_2} \sin(\phi_2)}{2\pi f_c \sqrt{2} Y_1} \quad (5.21)$$

and

$$C_{L-A_c} = \frac{-4\pi^2 f_1^2 Y_1 C_{L_1} \cos(\phi_1) - 4\pi^2 f_2^2 Y_2 C_{L_2} \cos(\phi_2)}{4\pi^2 f_c^2 \sqrt{2} Y_1} \quad (5.22)$$

Stated in words, the equivalent lift coefficients C_{L-V_c} (and C_{L-A_c}) are those coefficients which, "when applied to a sinusoidal waveform at frequency f_c and of the same RMS input amplitude as the beating waveform, yield the same RMS output power (or inertial force)".

Values of the above equivalent coefficients were calculated for all of our beating experimental runs. Figures 5-25, 5-26, and 5-27 are contour maps of the equivalent lift coefficient in phase with velocity for beating oscillations of modulation ratio 1:20, 1:10, and 1:3 respectively. As in the case of the sinusoidal coefficient C_{L-V_0} (Figure 3-14), positive values of C_{L-V_c} denote an *exciting* effect of the lift force on the cylinder oscillations, while negative values denote a *damping* effect. The thick black lines marked on the figures correspond to the zero contours, defining the primary and secondary excitation regions. Compared to the sinusoidal contours of Figure 3-14, the primary excitation regions for the beating oscillations have grown in extent, essentially in the amplitude direction. For each of the modulation ratios, the secondary excitation region remains only in vestigial form. The extent of the excitation region along the frequency axis is seen to increase with the rapidity of the beats; a distinct double-peak effect is seen for the 1:3 ratio oscillations.

Contour maps of the equivalent lift coefficient in phase with acceleration are presented in Figures 5-28, 5-29 and 5-30 for beats of modulation ratio 1:20, 1:10 and 1:3 respectively.

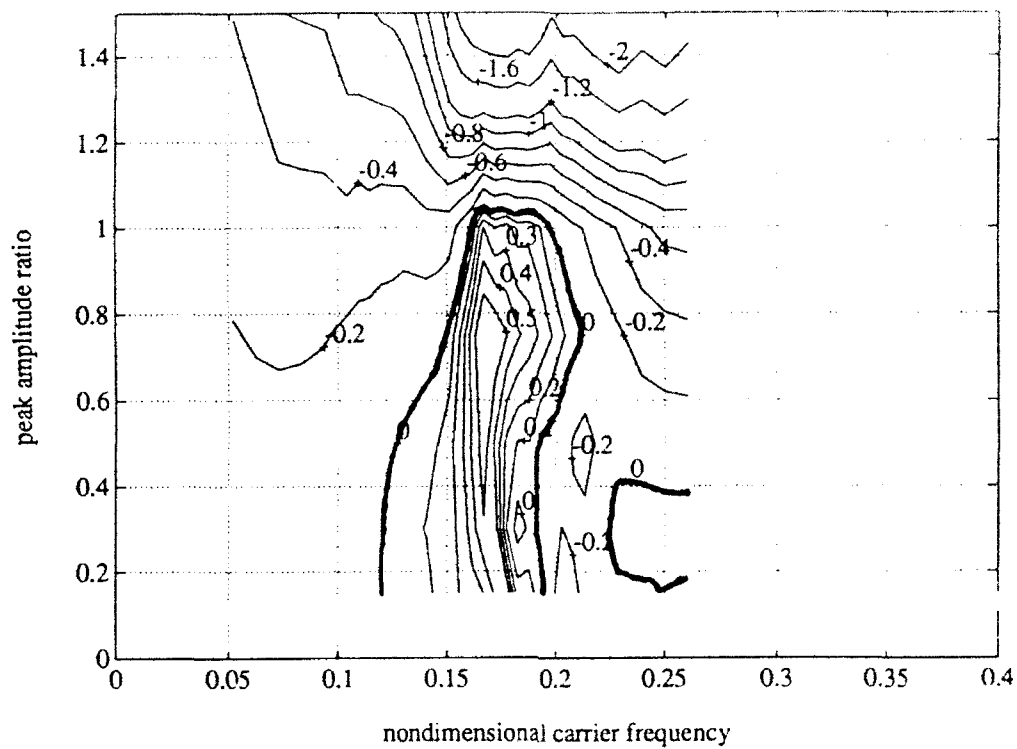


Figure 5-25: Contours of C_{L-V_c} ; 1:20 beating motion.

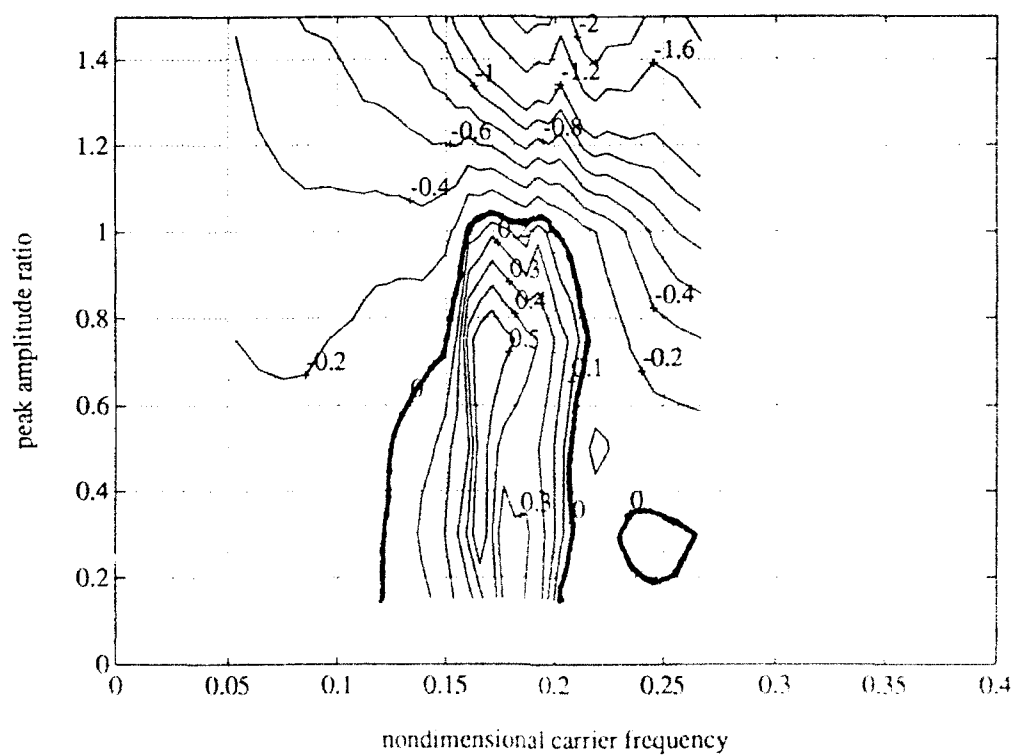


Figure 5-26: Contours of C_{L-V_c} ; 1:10 beating motion.

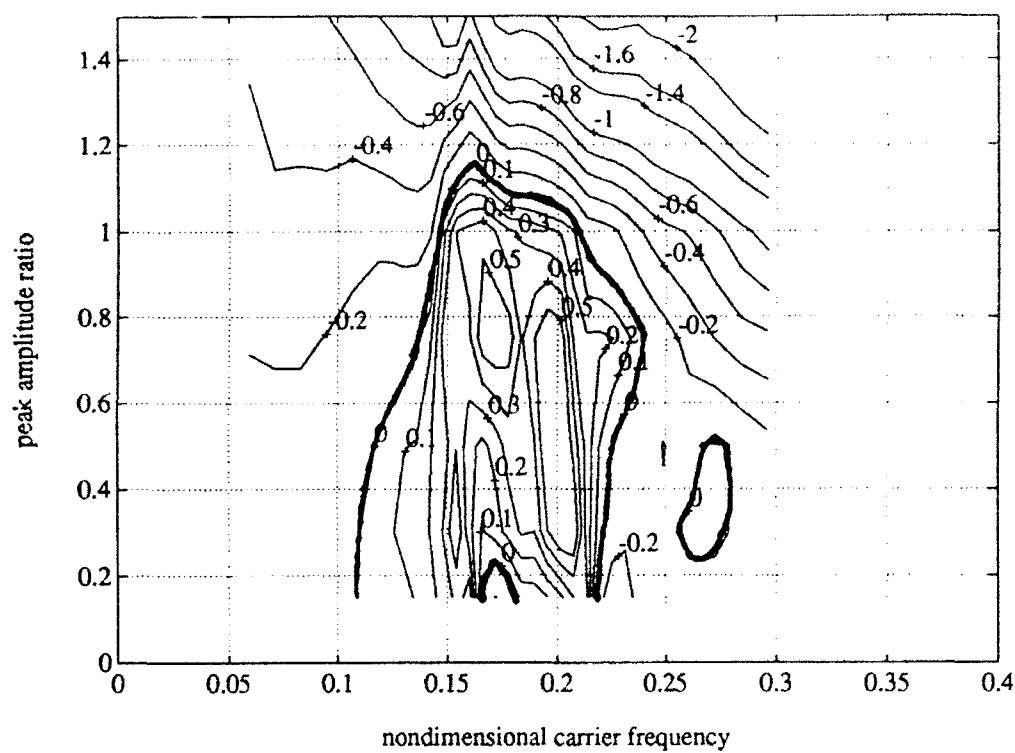


Figure 5-27: Contours of C_{L-V_c} ; 1:3 beating motion.

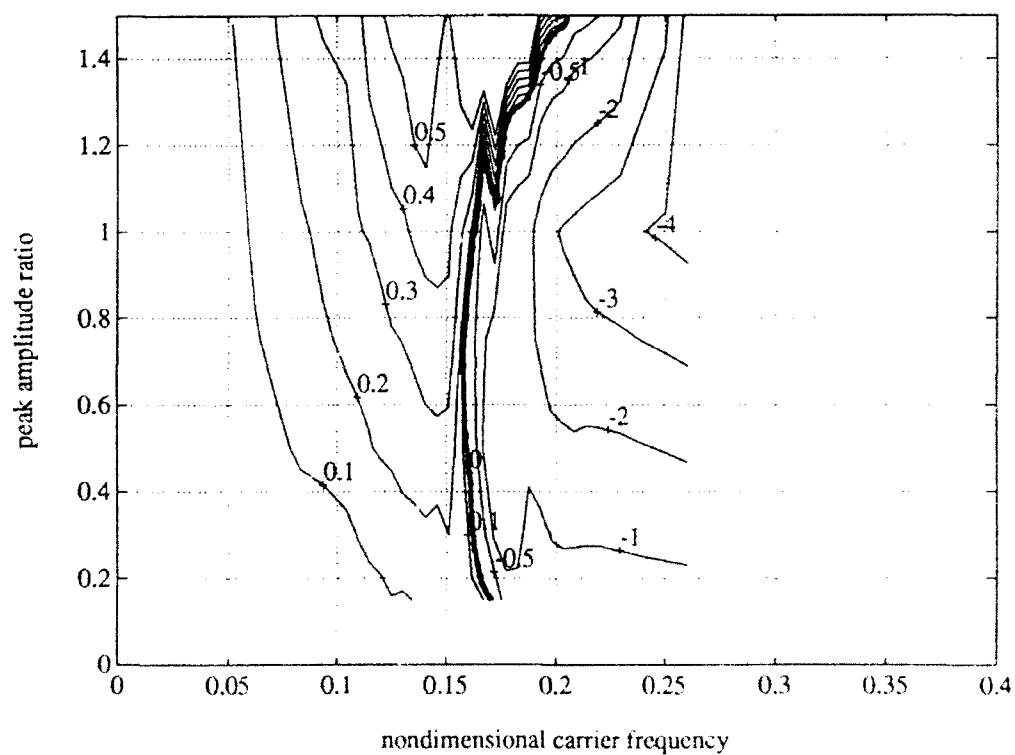


Figure 5-28: Contours of C_{L-A_c} ; 1:20 beating motion.

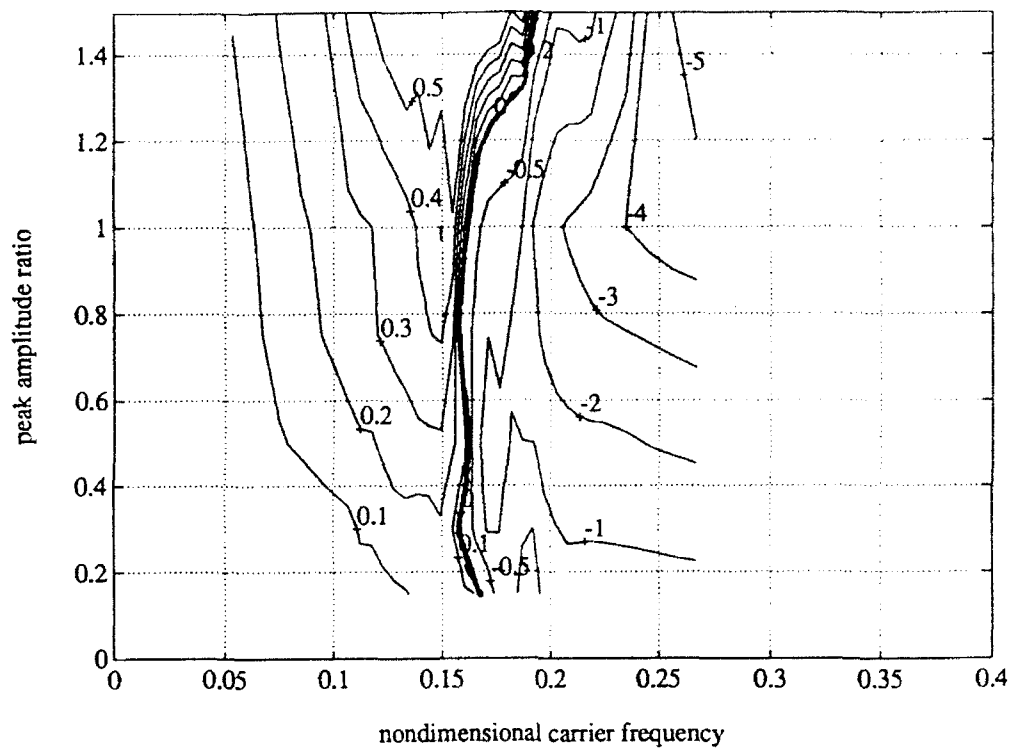


Figure 5-29: Contours of $C_{L_{Ac}}$; 1:10 beating motion.

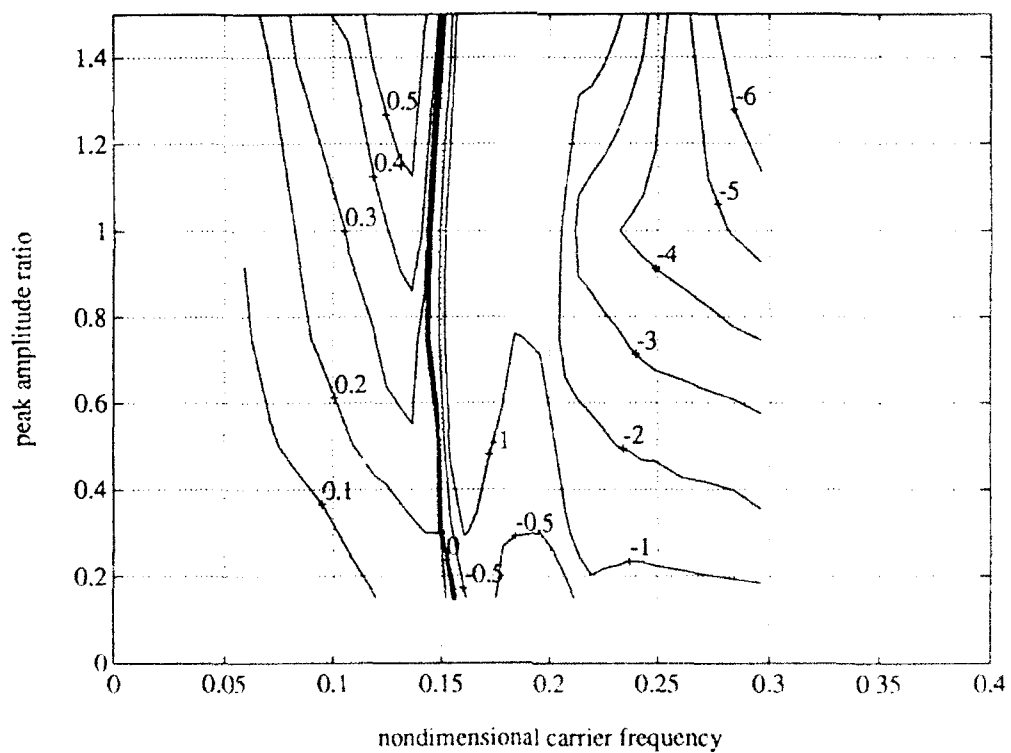


Figure 5-30: Contours of $C_{L_{Ac}}$; 1:3 beating motion.

As before, positive values of C_{L-A_c} denote negative values of inertial added mass, and *vice versa*. The thick black lines on the figures correspond to the zero contours. The beating results are remarkably similar to the sinusoidal C_{L-A_0} contours of Figure 3-15.

5.3 Analysis of the wake response

5.3.1 Preliminary remarks

In the previous few subsections, we discussed the results of cylinder force coefficient measurements for beating oscillations. Most of our presentation reflected a direct extension of the sinusoidal force coefficient formulations, and was not necessarily linked to the underlying wake dynamics for a beating cylinder. Some light has been shed on the beating wake dynamics from the low-Reynolds number flow visualization work of Nakano and Rockwell [51]. In our case, we found it useful to perform time-domain processing on our beating force records so as to detect and classify various types ("modes") of wake response.

The essential features of our time-domain analysis method have been introduced in Section 3.7 of Chapter 3. For every data set analyzed, the time points corresponding to each upcrossing of the motion and lift force time traces were determined, and then used to calculate "instantaneous" frequencies and phase angles. Results of this processing method were displayed and printed graphically, consisting of plots of the normalized motion and lift coefficient time traces, instantaneous phase angles, and histograms of the calculated motion and lift frequencies.

For the beating oscillations tested, several different wake modes were identified. In the following section, we shall discuss each of these wake modes, along with a typical example of each from the time domain processing.

5.3.2 Classification of wake response modes

The majority of the beating runs analyzed were found to fall into one of four response types: *periodic nonlock-in*, *frequency switching*, *random phase modulations*, or *periodic phase modulations*. The precise behavior in any single case depended on the carrier frequency, the amplitude ratio, and the modulation ratio.

Periodic nonlock-in. Figure 5-31 illustrates a typical example of periodic nonlock-in, in this case for a beating oscillation of peak amplitude ratio $2Y_1/d = 0.15$, nondimensional carrier frequency $\hat{f}_c = 0.144$, and modulation ratio 1:10. As in the case of sinusoidal oscillations (Figure 3-32 of Chapter 3), this mode corresponds to the unforced response of the wake, which does not "see" the external forcing. It is clear from the time traces that the vortex shedding frequency (lift) is not the same as the external forcing frequency (motion); the frequency histograms reveal that while the motion frequency is centered near 0.15, the lift force frequency is near the natural Strouhal value of 0.20.

Frequency switching. A very interesting mode observed in some of the time traces was that of frequency switching, illustrated in Figure 5-32. The specific data set in the figure refers to a 1:20 ratio beating motion with $2Y_1/d = 0.75$ and $\hat{f}_c = 0.1302$. The instantaneous frequency of the lift force time trace is not constant, but appears to fluctuate between two distinct values. The histograms reveal these two values to be the natural Strouhal shedding frequency, and the imposed external carrier frequency. The switching behavior convincingly demonstrates the nonlinear dependence of the vortex-induced force phenomena on the oscillation amplitude envelope: when the amplitude envelope is above some threshold value, the lift force frequency locks on to the externally applied frequency, while below the threshold value the wake responds in an unforced manner (with natural Strouhal oscillations).

Random phase modulations. Figure 5-33 illustrates the mode corresponding to random phase modulations, specifically beating oscillations with modulation ratio 1:10, amplitude ratio $2Y_1/d = 0.50$, and carrier frequency $\hat{f}_c = 0.1547$. In this case, the lift force time trace is very irregular, and bears no apparent relationship to the motion time trace. The motion histogram is tightly centered around the carrier frequency, while the lift force histogram shows a broadening effect. This mode is analogous to the case of *quasiperiodic nonlock-in* for sinusoidal oscillations (Figure 3-33).

Periodic phase modulations. The most ordered of the four common modes was that of periodic phase modulations, illustrated by Figure 5-34, pertaining to the specific case of 1:10 ratio beats with $2Y_1/d = 0.50$ and $\hat{f}_c = 0.208$. The lift force trace now resembles a

Figure 5-31: An example of periodic nonlock-in; 1:10 beats with $2Y_1/d = 0.15$, $\bar{f}_c = 0.144$.

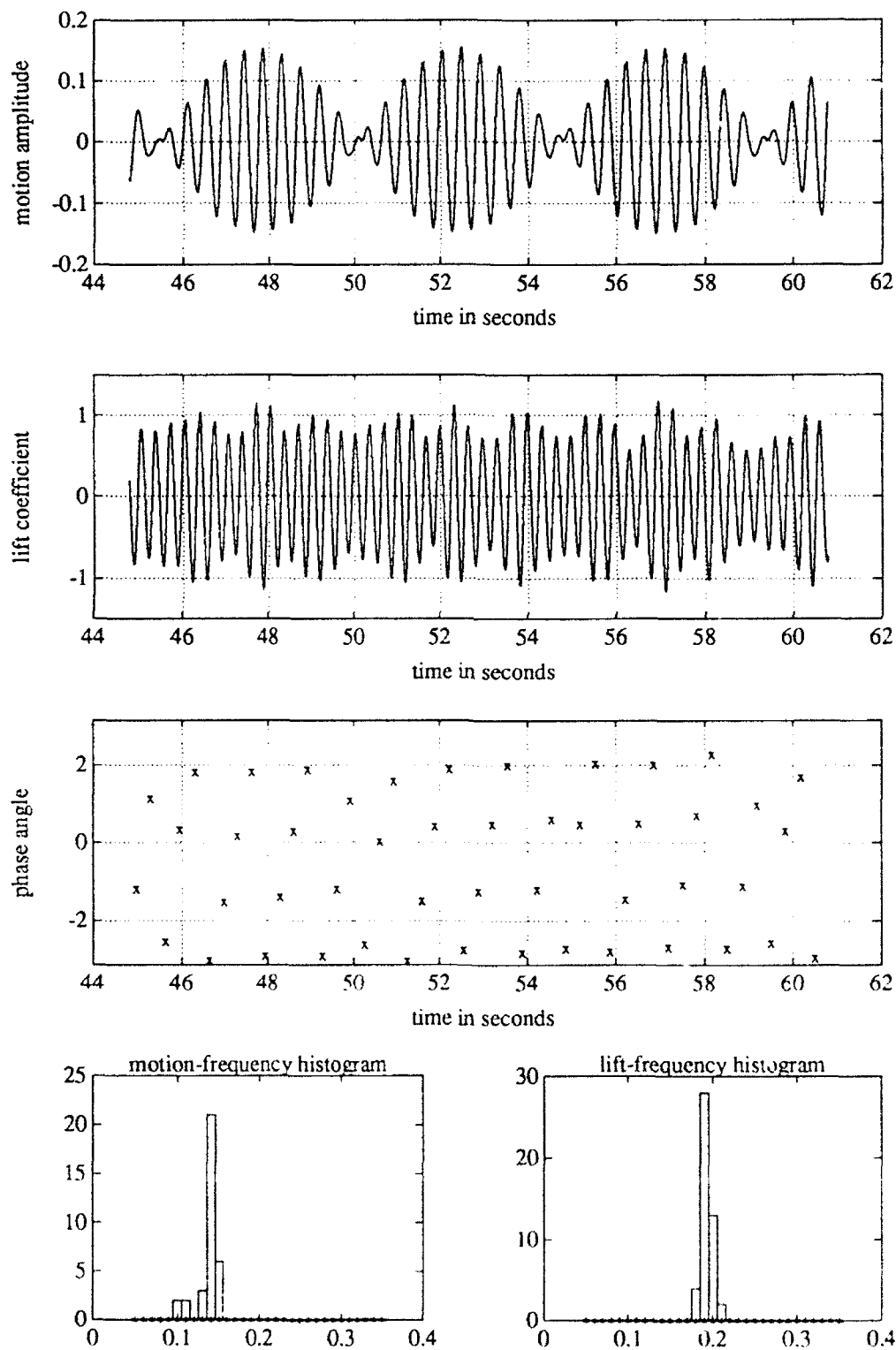


Figure 5-32: An example of frequency-switching; 1:20 beats with $2Y_1/d = 0.75$, $\hat{f}_c = 0.1302$.

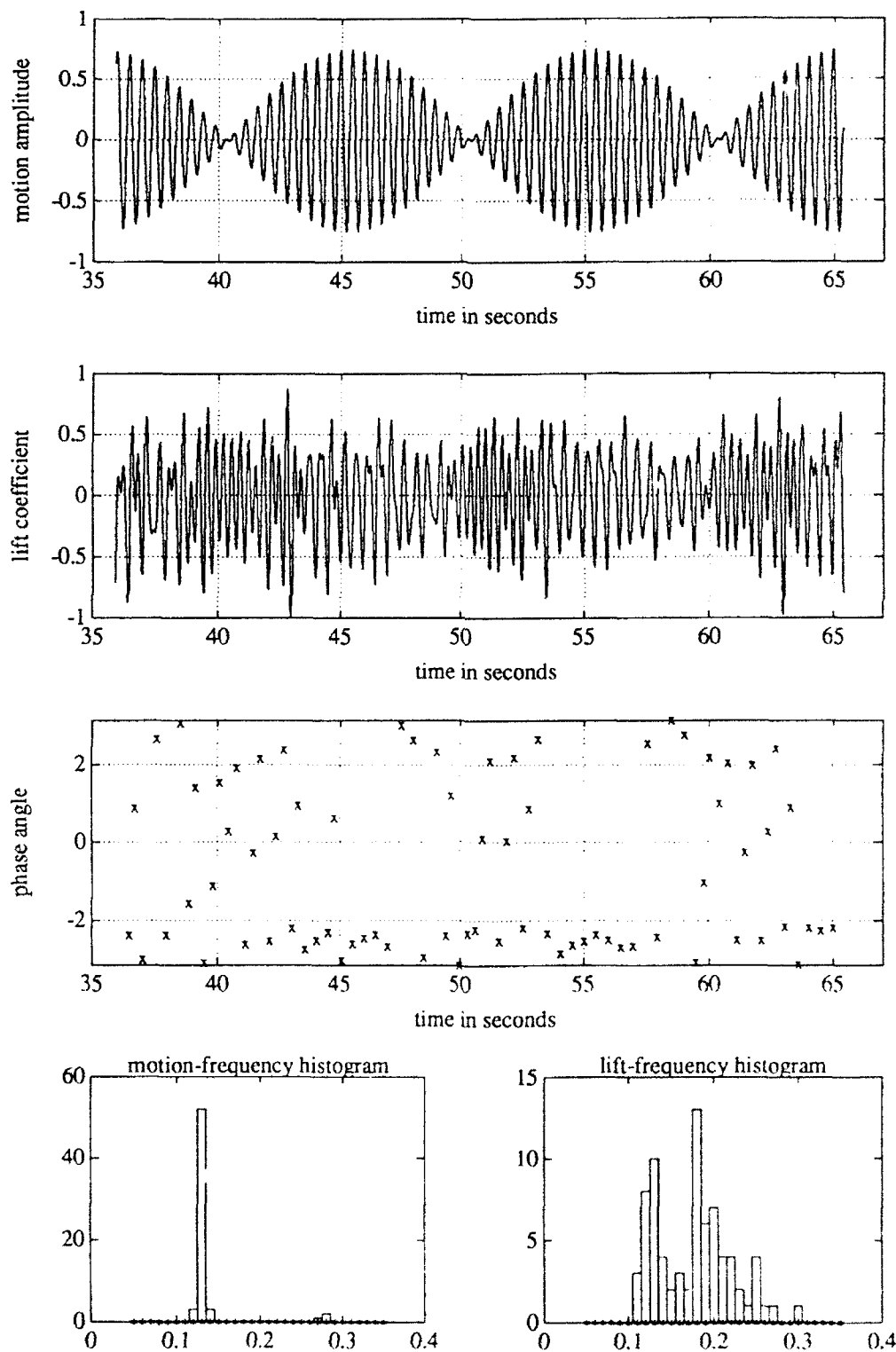


Figure 5-33: An example of random phase modulations; 1:10 beats with $2Y_1/d = 0.50$. $\hat{f}_c = 0.1547$.

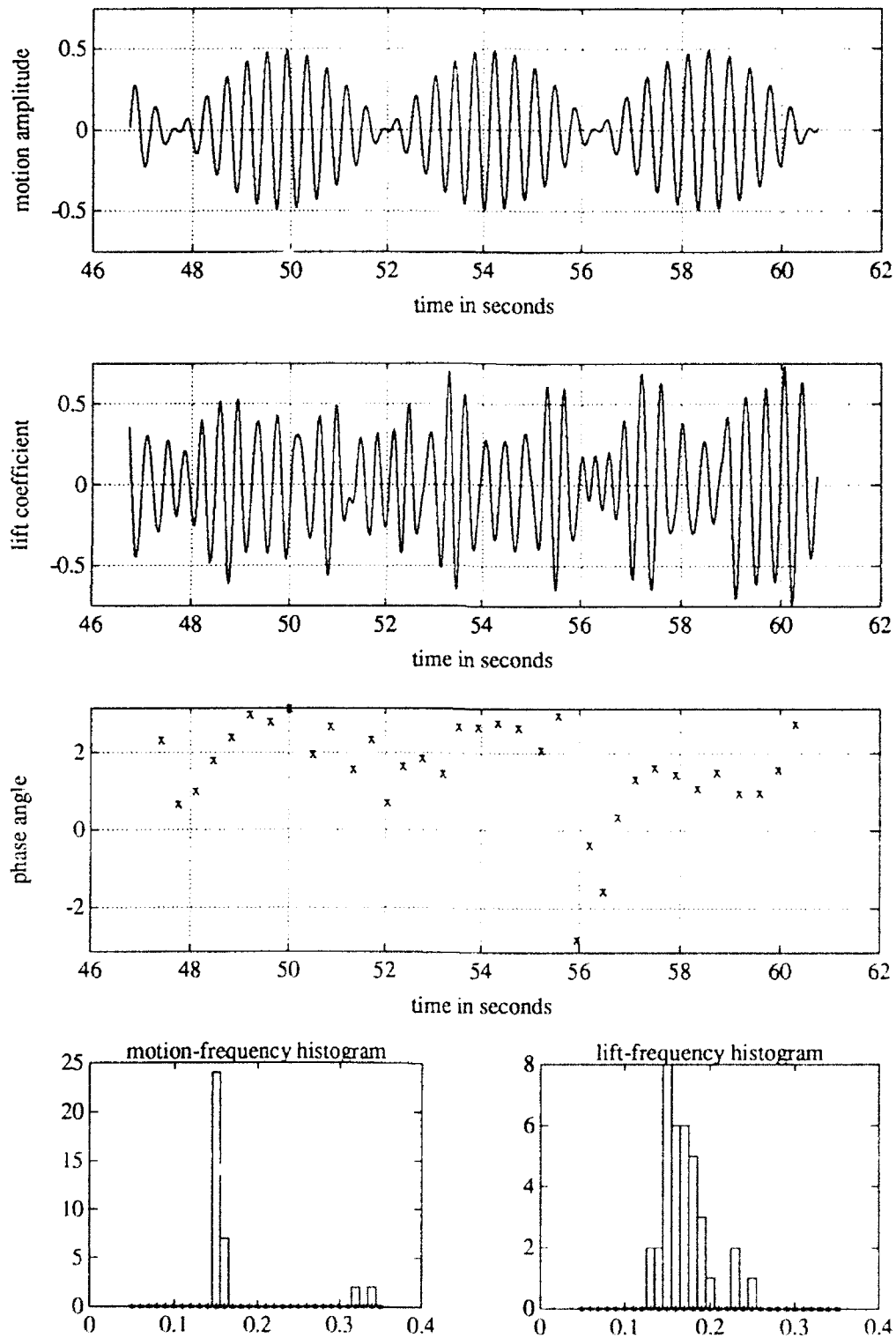
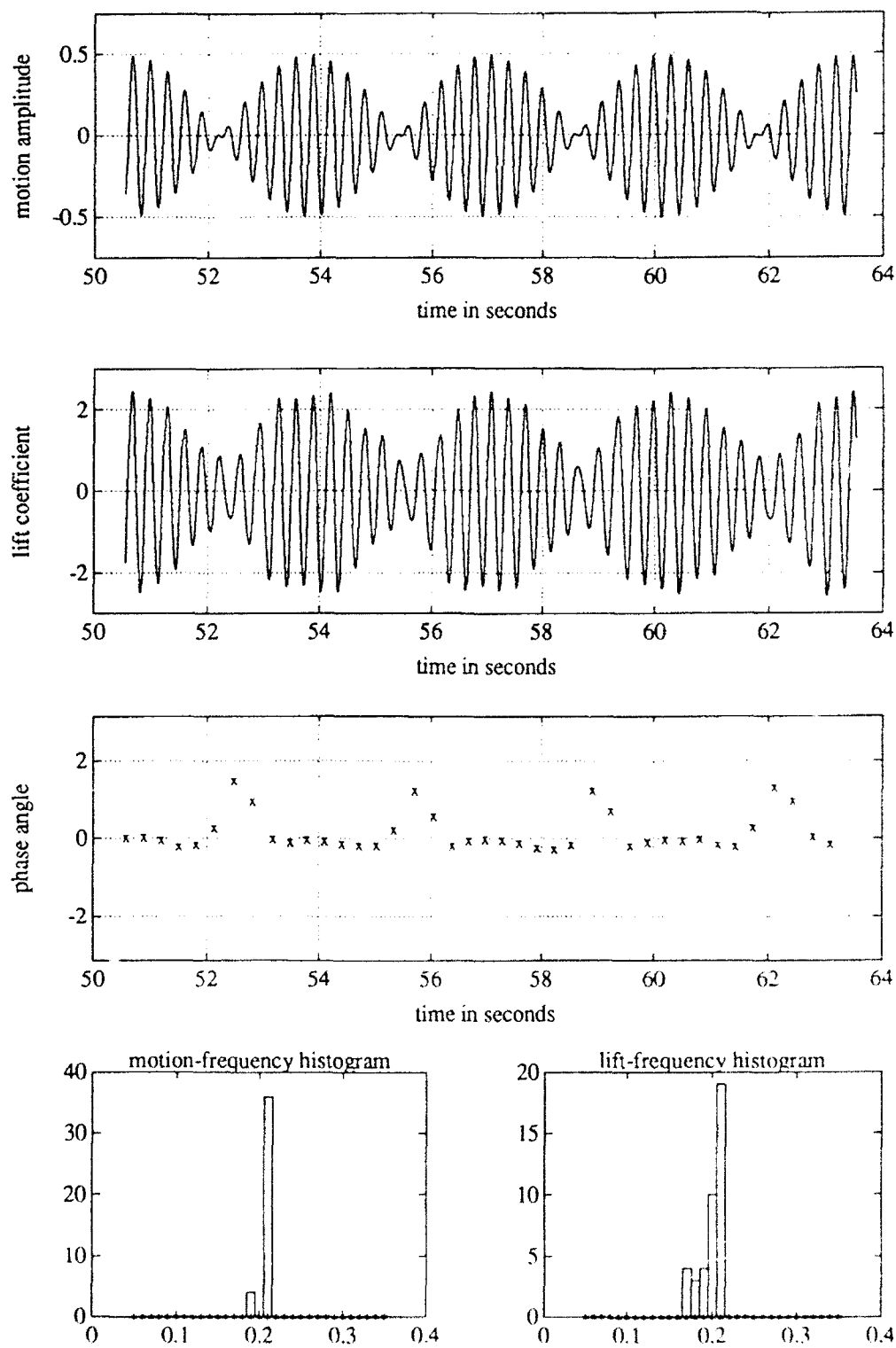


Figure 5-34: An example of periodic phase modulations; 1:10 beats with $2Y_1/d = 0.50$, $\hat{f}_c = 0.208$.



well-formed beating oscillation, and the instantaneous phase angles have taken on a periodic variation, with a pattern that repeats itself for every beat packet. Both the motion and lift frequency histograms are relatively tightly centered around the carrier frequency. As we shall see, for the most part, this mode takes the place of sinusoidal *lock-in*.

All of our beating data were processed by the time domain method, and the results were assembled into *wake response state diagrams*, as done in the case of sinusoidal oscillations. Due to limitations of the processing method, the modes were difficult to identify at nondimensional carrier frequencies \hat{f}_c below 0.10 and above 0.25, and peak amplitude ratios $2Y_1/d$ above 1.00. Within these constraints, however, the wake-response diagrams provide an excellent view of the behavior of the beating vortex-induced forces. Figures 5-35 and 5-36 are the response diagrams for 1:20 and 1:10 ratio beats respectively, and are seen to be quite similar. At very low (or high, presumably) frequencies, the wake does not feel the effect of the forcing and responds with periodic nonlock-in. As the frequency approaches the natural Strouhal value, the response mode changes to frequency switching, and then to random phase modulations. Within a certain range of frequencies bracketing the Strouhal number, periodic phase modulations are observed. The overall shapes of the wake-response diagrams are not dissimilar from the sinusoidal result, Figure 3-35.

For the fast 1:3 beats, a far richer distribution of wake responses was found, as illustrated in Figure 5-37. The most striking feature of Figure 5-37 is a distinct "dual" behavior, with two regions of periodic phase modulation surrounded by regions of random phase modulation and periodic nonlock-in. In addition, while no systematic frequency-switching was detected, a unique mode was found wherein the lift force exhibited beats at a modulation ratio of 1:7, or twice the externally imposed ratio. This "period-doubling" behavior is illustrated in Figure 5-38, which shows the time-domain processing results for the case of 1:3 beats with peak amplitude $2Y_1/d = 0.30$ and carrier frequency $\hat{f}_c = 0.184$. The beat packets of the lift force time trace are clearly twice as long as the beat packets of the motion time trace, and the doubling effect is reflected in the variation of the phase angle as well. It should be borne in mind, however, that the inherent mathematical modulation period of our beating input consists of two beat packets, not one. (From Equation 5.2, the first beat packet occurs during the first half-cycle of the modulation sinusoid $\cos(2\pi f_m t)$, and the second beat packet occurs during the second half-cycle.) The lift force waveform during

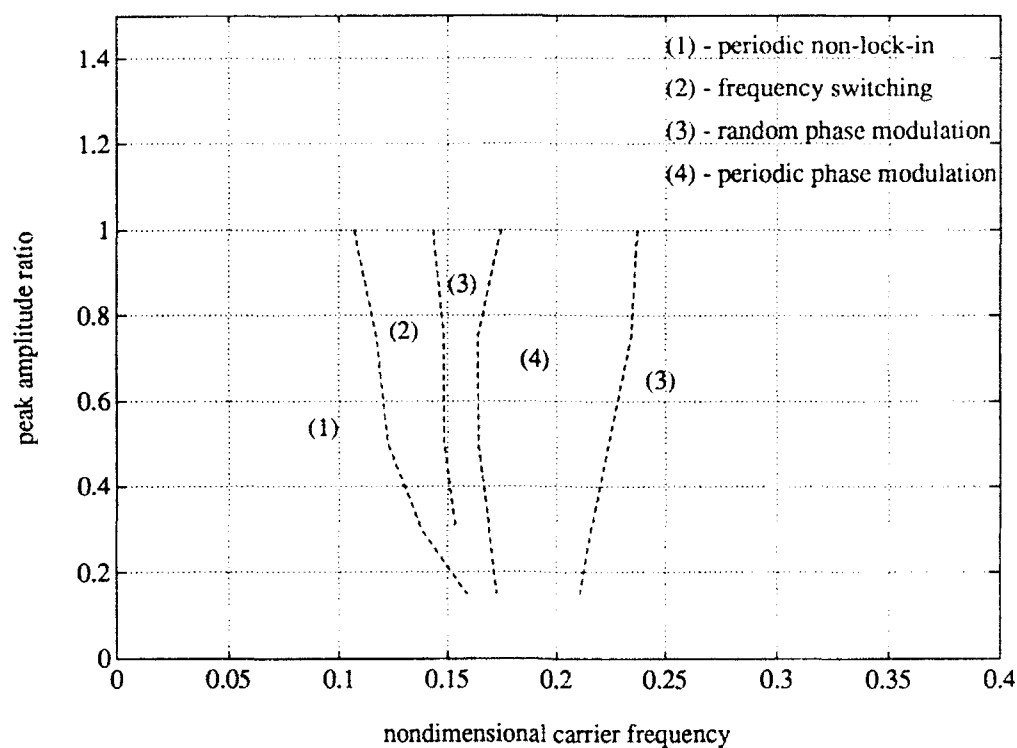


Figure 5-35: Wake response state diagram for 1:20 beats.

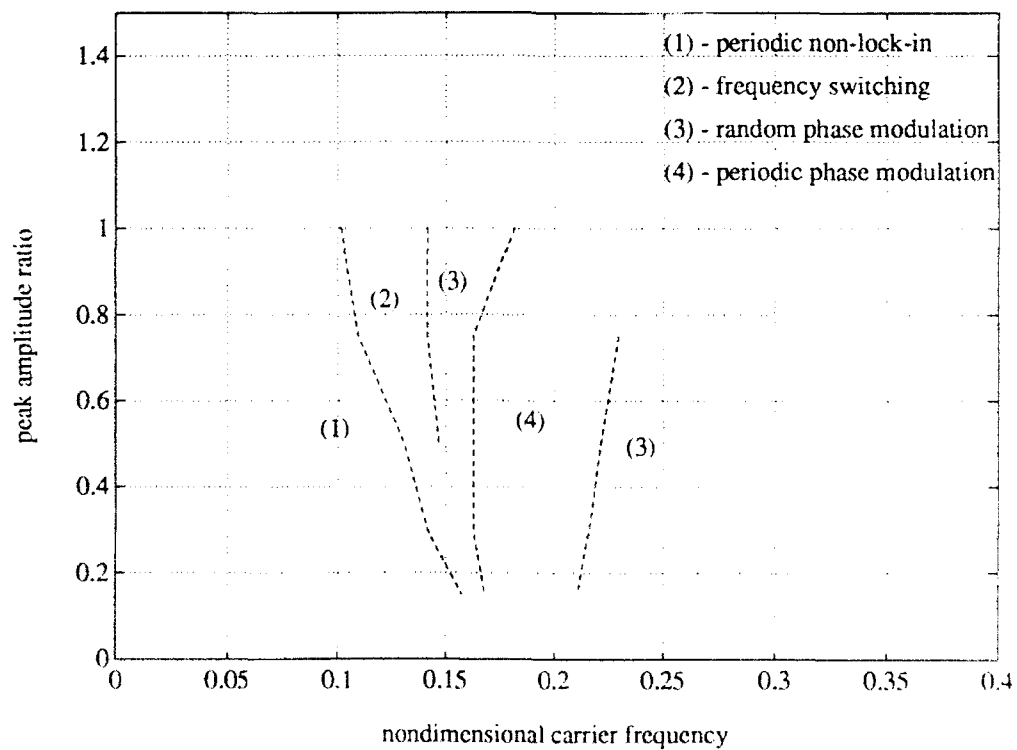


Figure 5-36: Wake response state diagram for 1:10 beats.

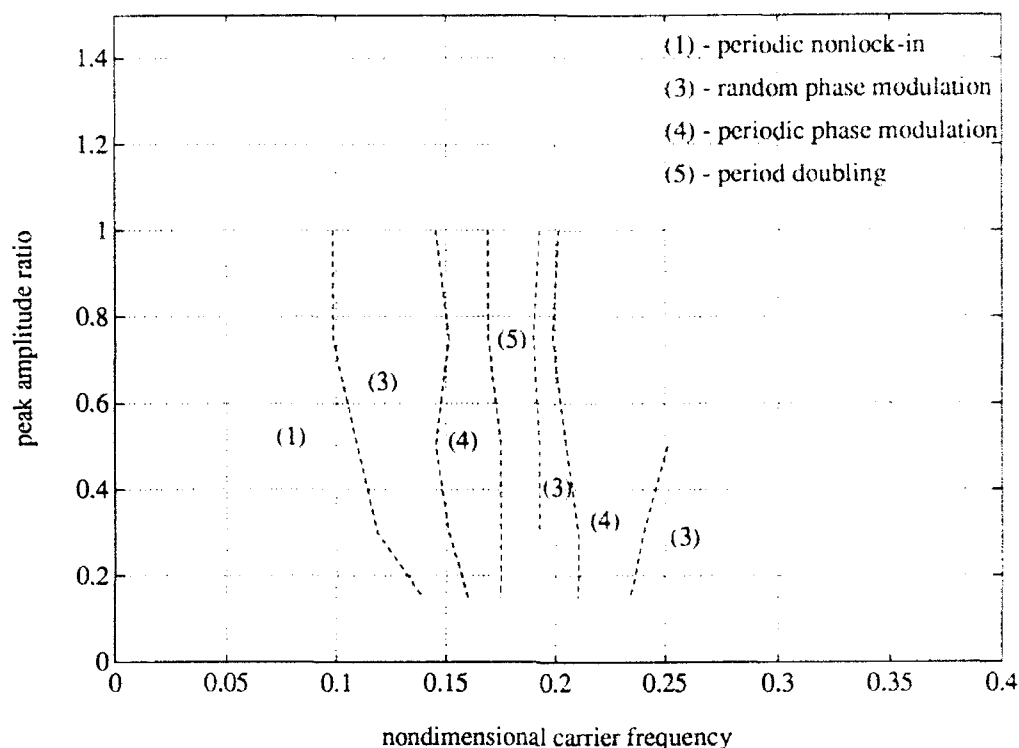


Figure 5-37: Wake response state diagram for 1:3 beats.

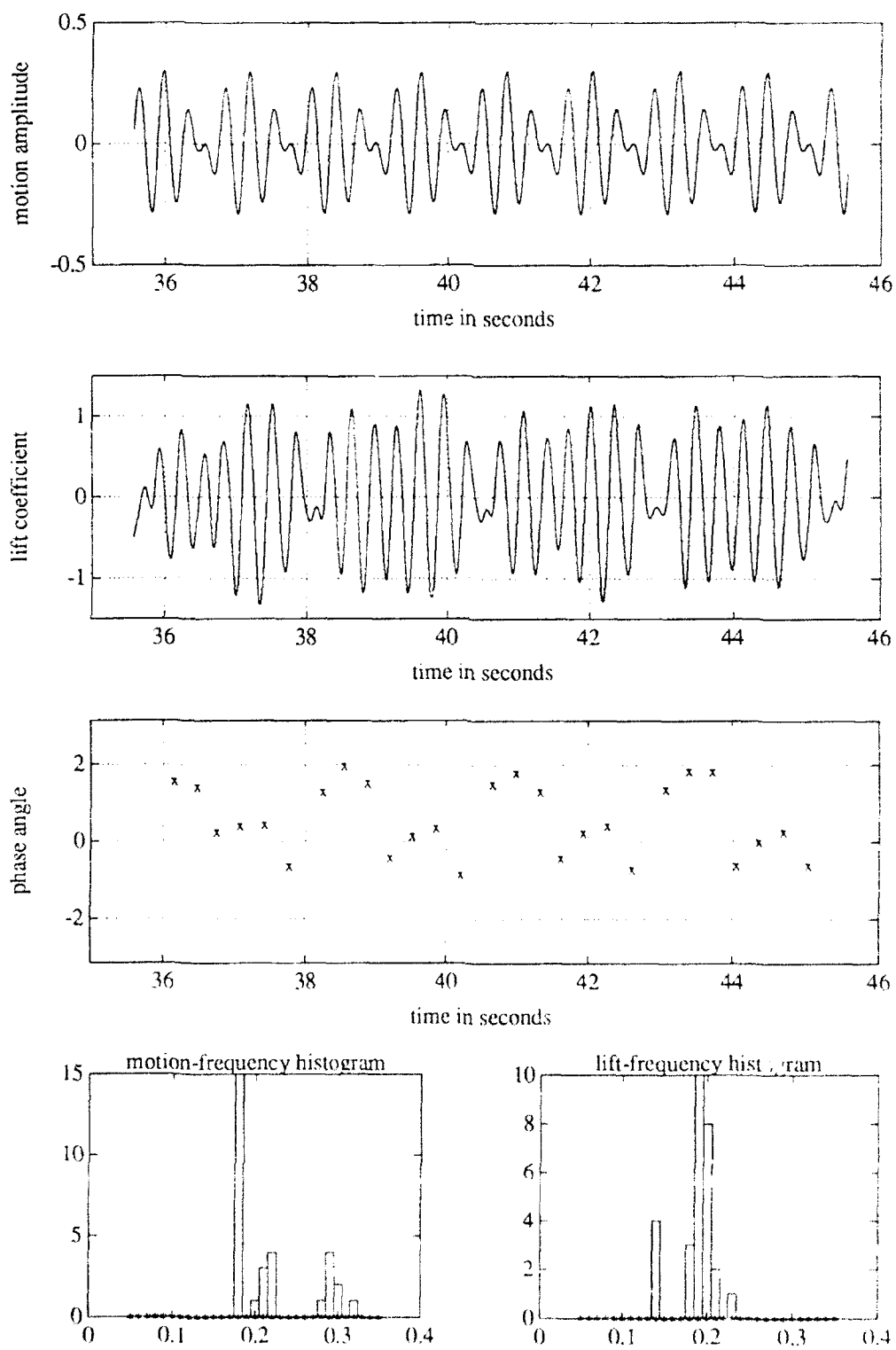
the “period-doubling” mode thus does not truly double the modulation period, but alters the shape of the lift force response within one modulation period.

5.3.3 Comparisons with published results.

In Section 5.1.2, we discussed the results of Nakano and Rockwell [51], who studied the states of response of the wake behind a beating cylinder at low Reynolds numbers. Although the methods and waveforms used by those authors differed from ours, it is useful to compare the wake response modes that we observed (from force measurement time traces) with their data (from vortex flow visualization).

Of the wake response modes observed by Nakano and Rockwell, none of our time traces exhibited the f_m periodic with f_c lock-in behavior. The instantaneous phase angles calculated in every one of our cases showed at least a slight periodic modulation, and not once assumed a constant value associated with pure lock-in. The lack of lock-in in our measurements could perhaps be related to the difference in Reynolds number regime and hence turbulence effects.

Figure 5-38: An example of "period-doubling"; 1:3 beats with $2Y_1/d = 0.30$, $\hat{f}_c = 0.184$.



Nakano and Rockwell's mode f_m periodic with f_e nonlock-in corresponds well with our "periodic phase modulation". Their words

"a time-varying phase modulation of the near-wake structure, relative to the cylinder displacement"

could be used to describe our data too. The authors do not make any mention of a "random phase modulation" mode, but perhaps they treated it as a special case of the same general type. Their mode f_m periodic with f_e nonlock-in, mode $(n + 1)$ could perhaps be a version of our "frequency-switching" — the extra pair of vortices they observed in the visualization being perhaps associated with shedding at the (higher) Strouhal frequency for a part of the modulation cycle.

As for the "period-doubling" mode for fast modulations, Nakano and Rockwell observed a similar pattern which they termed $2f_m$ periodic with f_e nonlock-in. They emphasized the importance of this mode, which they believed to represent a subharmonic bifurcation of the flow system revealing a route to turbulence in the wake. We have indicated earlier that the mode we observed is not truly a "period-doubling", since the fundamental modulation period of our waveform spans two beat packets, not one. We cannot say, therefore, whether our observations indicate an underlying feature of the beating wake (similar to Nakano and Rockwell's pattern), or stem merely from an artifact of our input forcing.

In conclusion, while obvious differences exist between our results and the previous data of Nakano and Rockwell, the basic observations are consistent. A variety of vortex patterns are seen to exist in the wake of a cylinder undergoing beating oscillations, depending on the oscillation amplitude, frequency, and modulation ratio. Some of these patterns (particularly the frequency-switching mode) illustrate the nonlinearity of the vortex shedding process, and indicate that great care must be exercised in the conduct and interpretation of traditional processing methods applied to the measured force signals.

5.4 Discussion and Summary

In this chapter, we have investigated the behavior of the vortex-induced lift and drag forces acting on cylinders undergoing simple, dual-frequency amplitude-modulated oscillations. Such amplitude-modulated, or beating oscillations occur in the VIV response of long flexible

cylinders in sheared flows, and we believe that our work is a useful addition to the limited literature on the subject.

In the case of the vortex-induced drag force, the presence of beating causes a reduction in the magnitude of the mean drag coefficient from established sinusoidal values. For slowly varying beating oscillations, the average mean drag varies with the instantaneous amplitude of the cylinder motion, and can be well predicted by a quasistatic application of sinusoidal data. For fast beating oscillations, this quasistatic analysis is not valid, and a linear superposition model gives reasonable results. The beating oscillating drag force consists of several linear and nonlinear spectral components, and is difficult to predict from sinusoidal data. An RMS description of the oscillating drag coefficient is useful.

In the case of the vortex-induced lift force, we defined "equivalent lift coefficients" C_{L-V_c} and C_{L-A_c} to express the net influence of the lift force in phase with cylinder velocity and acceleration respectively. On the C_{L-V_c} contour maps, the principal effect of beating is a "lengthening" of the primary excitation region from a limiting amplitude of about 0.85 (sinusoidal oscillations, Figure 3-14) to about 1.10 (beating oscillations, Figures 5-25 - 5-27). The C_{L-A_c} contour maps for beating motions remain rather similar to the corresponding sinusoidal data.

Time domain upcrossing analysis of the motion and lift force time traces reveal a number of different patterns, or modes, in the wake of a beating cylinder. Particularly interesting among these is a "frequency switching" behavior illustrating the dependence of the vortex-shedding process on the envelope of the oscillation amplitude. Pure lock-in behavior was never observed; at carrier frequencies close to the natural Strouhal number, the lift force sustains a regular phase modulation that repeats from one beat packet to the next. The absence of lock-in for beating oscillations, but the presence of very definite excitation regions in the C_{L-V_c} contour maps, once again emphasizes the difference between the "lock-in" and "excitation" concepts discussed in Chapter 3. The periodic phase modulation behavior provides an explanation for the lengthening of the excitation contours mentioned in the previous paragraph — from the phase variation of Figure 5-34, it is clear that the cylinder sustains a periodic alternating damping and excitation as the envelope of the motion rises and falls, with the net result being that the peak amplitude of motion could be higher than for the purely sinusoidal case. Given that the lift force time traces for only this periodic phase modulation behavior look like regular beating signals, it would appear that the dual-

frequency lift model of Equation 5.17 is strictly valid only for this range of oscillation parameters.

A general observation from all of our force coefficient measurements and time-domain analyses is that the slow (1:20 and 1:10) beating oscillations behave in a nonlinear quasistatic fashion, while the fast (1:3) beats behave more in a linear superposition fashion. A possible explanation for this could be that the rapid beats do not allow the wake enough time to adjust to the instantaneous envelope amplitude, thus giving a more linear appearance to the measured force coefficients. In any case, we found that the peak amplitude of motion $2Y_1/d$ was more descriptive than the component amplitude Y_1/d for the slowly varying modulations, and *vice versa* for the rapid modulations.

Numerous opportunities exist for the application of our beating data to engineering predictions of VIV in actual structures. In situations where regular beating motions are expected or known to occur, the lift coefficient contour maps of Figures 5-25 – 5-27 can be used with a simple “energy balance” model (as described in Chapter 4) to predict response amplitudes. The drag coefficient contour maps of Figures 5-9 – 5-11 and Figures 5-17 – 5-19 can be used directly (or with appropriate interpolation) to predict the mean and RMS oscillating drag forces. Application of the measured lift coefficient data in a more formal predictive model depends on the specific details of the model; for instance, the recently developed algorithm of Triantafyllou [83, 84] uses sinusoidal data in a time-domain calculation to simulate beating behavior, and does not use measured beating data for this purpose. On the other hand, efforts are under way at MIT (Tjavaras, [77]) to extend the sinusoidal wake oscillator concept (Hartlen and Currie [30], Skop and Griffin [71]) to beating oscillations, and it is expected that our data will provide a valuable means of calibrating such a model.



Chapter 6

A Paradigm of Vorticity Control: Cylinder-Foil Vortex Interaction

6.1 Introduction

6.1.1 Preliminary remarks

In previous chapters, we have studied the vortex-induced forces acting on cylinders forced with sinusoidal and amplitude-modulated oscillations under a variety of different forcing conditions. The focus thus far has been on studying the integrated forces acting on the cylinders (due to the engineering importance of these forces), rather than the detailed structure of the flow that causes the forces. We now turn to the study of the vortical structures behind a cylinder, with particular emphasis on ways to control these structures, and to reveal in the process the principal governing mechanisms. In order to focus our efforts, we shall study the interaction between the vorticity generated by a bluff cylinder and that generated by an oscillating hydrofoil operating in the wake of the cylinder. Two practical applications of this research are drag reduction through vortex repositioning, and signature reduction through vortex annihilation (or equivalently, flow enhancement through vortex reinforcement when, for example, vigorous mixing is desired). In order to investigate these ideas, we shall employ newly-developed flow visualization experiments as well as an extended form of our force measurements.

6.1.2 Background and motivation

It is well known that the characteristics of the Kármán vortex wake behind a stationary or oscillating bluff body are related to the drag force acting on that body. The Kármán vortices, through their arrangement and direction of rotation, are intrinsically connected with a wake velocity that is opposite in direction to the free-stream velocity. This leads to a time-averaged "velocity defect" profile, which from momentum considerations, is related to the drag force experienced by the body. Recent theoretical advances in the area of bluff body wake dynamics (Triantafyllou *et al.* [80]) show that the formation of the Kármán vortices is in fact due to an *absolute instability* of the time-averaged velocity profile in the wake, indicating that the vortex street and the velocity defect profile are intricately linked to each other.

From flow visualization experiments, we know that the cylinder wake can assume (or be transformed into) a variety of vortex patterns or "modes". In Chapter 1, we reviewed the work of Williamson and Roshko [95], and of Ongoren and Rockwell [53]. Both papers showed that the vortex patterns in the wake of a circular cylinder undergoing sinusoidal oscillations could vary widely, depending on the amplitude and frequency of the oscillation. In the preceding chapter, we have reviewed the results of Nakano and Rockwell [51], who studied the different vortex modes in the wake of a cylinder undergoing beating oscillations. In addition to the case of a single cylinder undergoing different types of oscillations, we know that interaction effects between multiple cylinders can cause a whole new range of vortex patterns — the work of Strykowski and Sreenivasan [76], and Johnson and Zdravkovich [33] can be cited as examples. Several of our own force measurements (Chapters 3, 4, and 5) support these flow visualization results.

A hydrofoil oscillating with some combination of linear translation (heave) and rotation (pitch) produces a vortex wake as well. (We employ the word *wake* in a liberal sense since the flow may in fact be a *jet*.) Under certain conditions of oscillation, the foil vortex wake closely resembles a bluff body Kármán street, but with reverse rotational direction of the vortices: this flow is associated with an average velocity profile in the form of a jet, causing a net *thrust* force on the foil. Figure 6-1 illustrates the (typical) vortex streets behind a bluff body (cylinder) and an oscillating foil, together with the associated mean velocity profiles.

A number of researchers have studied oscillating foil thrust generation. Experimental

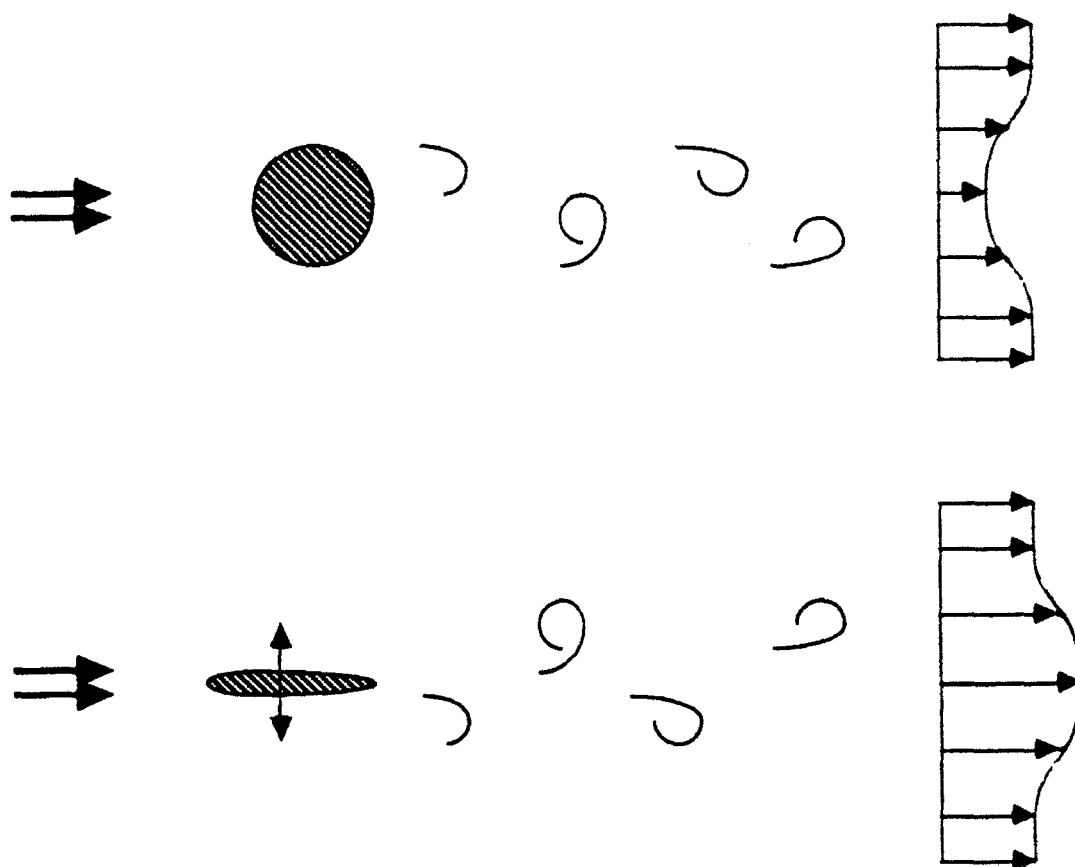


Figure 6-1: The vortex wakes of a bluff body and an oscillating foil.

investigations (primarily flow visualization) have been conducted by Oshima and Oshima [55], Oshima and Natsumi [54], Freymuth [17, 18], and Koochesfahani [38]. Linear and nonlinear inviscid theories have been presented by von Kármán and Burgess [92], Lighthill [40, 39, 41], Chopra [9], and Wu [96, 97, 98]. A basic limitation of inviscid theory is that the Kutta condition at the foil trailing edge, derived from steady-state foil operation, may become invalid in unsteady flow — for example, Freymuth [18] has shown that under certain conditions of large oscillation amplitude, dynamic stall occurs and the vortices generated at the leading edge may be used to advantage in producing large thrust forces. In a recent advance, Triantafyllou *et al.* [85] have demonstrated the importance of accounting for the vortex wake dynamics behind an oscillating foil. In analogy with the flow behind a

bluff body, the preferred frequency of vortex formation observed in the wake of a foil can be predicted by a linear stability analysis of the average velocity (jet) profile, and this frequency is also the frequency of optimal thrust generation. Triantafyllou *et al.* found that this preferred frequency f_F , when nondimensionalized by the average forward velocity U and the excursion of the foil trailing edge (double amplitude) h , led to a foil "Strouhal number" of about 0.30.

$$S_F = \frac{f_F h}{U} \approx 0.30 \quad (6.1)$$

Experimental results and data from fish observation confirmed that optimal foil efficiency is in fact achieved in the range $0.25 < S_F < 0.35$.

An interesting phenomenon that seems deserving of further investigation is the interaction between the vortex street generated by a bluff cylinder and the vortices generated by an oscillating foil operating in the wake of the cylinder. This idea owes a great deal of its motivation to the experimental work of Rosen [63], who visualized the flow around swimming fish. (Rosen studied small tropical fish, *Brachydanio albolineatus*, as well as dolphins.) Due to the poor reproduction quality of Rosen's pictures, we have chosen not to show any of them in this thesis; nonetheless the conclusions reached from the pictures and the accompanying text have no ambiguity. Rosen showed that the main forebody of a swimming fish generates drag vortices initially arranged in a staggered, Kármán-like fashion. The undulating motion of the fish afterbody and tail *positions* these upstream vortices so that they *all lie on a single line* in the wake of the fish. The vortices generated by the tail appear to *merge* with the upstream vortices, and do not disturb the straight-line configuration. Vortices positioned on a single line represent a flow intermediate between the drag and thrust flows of Figure 6-1, and are associated with a uniform average velocity profile causing neither thrust nor drag. The motion of the fish tail, therefore, brings about a *repositioning* of the drag vortices, and hence presumably a drag reduction. The *merging* of the cylinder and foil vortices could lead to a reduction (or enhancement) of the wake signature. The question then arises as to whether similar behavior can be detected in the case of a discrete cylinder / foil tandem arrangement.

Figure 6-2 illustrates and summarizes our experimental investigation. The upstream cylinder is used to generate a Kármán vortex street in the usual manner. The downstream oscillating foil and its vortex wake interact in some manner with the cylinder vortices. We

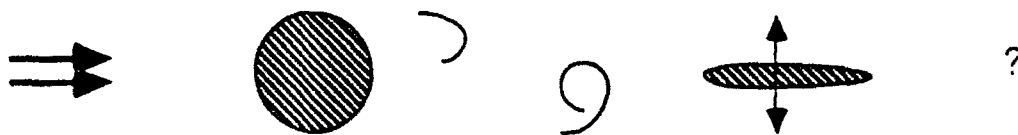


Figure 6-2: Illustrating the concept behind our experimental investigation.

wish to investigate the manner in which this interaction takes place, and whether or not the final vortex pattern produces a reduced in-line wake velocity (indicating a reduction in in-line drag force on the combined system).

The implications of our tandem bluff body / oscillating foil concept go beyond that of wake reduction. From a fluid mechanics standpoint, what we seek to achieve is an alteration of the mean flow properties via an alteration of the main vortical features, and thus our experiments have important flow control ramifications. And while this thesis is not concerned with biofluidmechanics, our experiments can be considered to be an abstraction of the fundamental mechanism of fish swimming, and hence may provide important insight to those who study aquatic animal propulsion.

6.1.3 The parameters of the problem

The complexity of the tandem cylinder/foil configuration is such that there are a great many independent parameters governing the physical apparatus and oscillation scheme. In this subsection, we shall consider these parameters and discuss our attempts to reduce their number to a manageable level.

Although a stationary bluff cylinder generates a Kármán vortex street, it is desirable to oscillate the cylinder so as to generate a stronger and more uniform vortex wake. Thus the

cylinder (of diameter d and length l) may be forced with a motion described by

$$y_C(t) = A_C \sin(2\pi f_C t) \quad (6.2)$$

where $y_C(t)$ is the instantaneous displacement, A_C is the oscillation amplitude, and f_C is the oscillation frequency. The foil, of chord length c , is placed a distance s behind the cylinder and subjected to a combined translation (heaving) and rotation (pitching) motion. The heave motion may be described by

$$y_F(t) = A_F \sin(2\pi f_F t + \psi) \quad (6.3)$$

where $y_F(t)$, A_F , and f_F are the displacement, heave amplitude, and frequency respectively of the foil oscillation, and ψ is the phase angle between the motion of the foil and that of the cylinder. The pitching motion of the foil, at the same frequency f_F and about a pivot point p from the leading edge, may be described by

$$\theta(t) = \theta_F \sin(2\pi f_F t + \psi + \phi) \quad (6.4)$$

where θ_F is the pitch angle amplitude and ϕ represents the phase angle between the pitching and heaving motions of the foil. The system operates in a flow of free-stream velocity U obtained in a fluid of kinematic viscosity ν .

Performing a dimensional analysis, we arrive at the following independent dimensionless parameters affecting the problem:

Reynolds number: Ud/ν .

Length parameters: Geometric ratio c/d , cylinder amplitude ratio A_C/d , foil amplitude ratio A_F/d , separation length s/d , model aspect ratios l/d and l/c , foil pivot point p/c .

Angle parameters: Pitch amplitude θ , phase angle between foil heave and cylinder heave ϕ , phase angle between foil pitch and foil heave ψ .

Frequency parameters: Cylinder Strouhal number $f_C d/U$, foil Strouhal number $f_F h/U$, where $h \approx 2\sqrt{A_F^2 + (c-p)^2\theta^2}$ is the double amplitude excursion of the trailing edge.

Note that other alternative nondimensional groupings may be formulated; we seek merely to illustrate the large number of variables (degrees of freedom) involved in the experimental setup.

In order to simplify the apparatus and proceed with the experiments in a timely fashion, we applied our judgment to select appropriate constant values (or limited ranges) for several of the above parameters and remove them as variables. Our reasoning is outlined in the paragraph below.

In the case of the Reynolds number, it is well known that a turbulent shear flow is only weakly dependent on variations in Re . For each of our experimental setups, we selected one value of Re in the turbulent subcritical regime: ≈ 550 for the flow visualization experiments and $\approx 20,000$ for the force measurement experiments.

Initially, one cylinder and two foil models were fabricated, giving us foil chord to cylinder diameter geometric ratios c/d of 1.00 and 2.00. Most of our tests were performed with the larger foil ($c/d = 2.00$), since preliminary visualization experiments showed that the smaller foil ($c/d = 1.00$) produced very weak vortex interactions.

Three values of cylinder oscillation amplitude ratio were selected to ensure strong lock-in vortex shedding, these were $A_C/d = 0.500$, 0.667 , and 0.833 . A major simplification of the experimental apparatus was obtained by using a single heaving mechanism to oscillate both the cylinder and the foil: this resulted in identical cylinder and foil oscillation amplitudes and frequencies, and a value of zero for the phase angle ψ . Since ψ was fixed, the separation length ratio s/d was made highly variable (21 discrete values between 1.5 and 8.0) so as to alter the phase of encounter between the foil oscillation and the upstream vortex street.

Fixed values were chosen for the model aspect ratios and foil pivot point, from the point of view of experimental convenience. The cylinder aspect ratios l/d were 5.33 for the flow visualization experiments and 12.00 for the force measurement experiments, while the foil aspect ratios l/c were 2.67 for the flow visualization experiments and 6.00 for the force measurement experiments. The foil pivot point ratio p/c was chosen to be 0.33 in all cases (from the leading edge).

The design of the foil pitching oscillator used in the flow visualization experiments was such that it allowed the following discrete values of pitch amplitude θ : 0° , 7° , 15° , 30° , 45° , and 60° . Of these allowable values, most of our runs were conducted with θ at 15° , 30° , or 45° .

Based on earlier experiments (Triantafyllou *et al.* [85]) and fish observation data (Rosen [63]), the phase angle ϕ between the foil pitching and heaving motions was fixed at 90° . As mentioned earlier, the phase angle ψ between the foil and cylinder heaving motions was fixed at 0° due to experimental considerations.

In order to ensure strong lock-in vortex generation, the experiments were conducted at cylinder Strouhal numbers in the range $0.17 < f_C d/U < 0.23$. As noted earlier, the foil oscillation frequency f_F was the same as the cylinder oscillation frequency f_C ; hence the selection of the cylinder Strouhal number determined the value of the foil Strouhal number.

Eventually, as a result of the simplifications noted in the above paragraphs, our experiments were conducted with different combinations of the following parameters: amplitude ratio A_C/d , Strouhal number f_C/d , pitch amplitude θ , and separation length s/d . As we shall see in the following sections, the separation length ratio s/d turned out to be a very important variable.

6.2 Flow visualization experiments

6.2.1 The Kalliroscope tank

In order to conduct flow visualization experiments with a minimum of dedicated equipment, we found it convenient to use a commercially available product called "Kalliroscope" fluid. This fluid (which we shall abbreviate to "K-fluid") is a very dilute colloidal suspension of organically derived guanine flakes in water. The guanine flakes have a typical dimension of $6 \times 30 \times 0.07 \mu\text{m}$ — thus they are very small and have a highly anisotropic shape. Although the specific gravity of guanine is about 1.62, the observed sedimentation velocity of Kalliroscope flakes in water is only about 0.1 cm/hour [44]. We added a blue-colored aqueous dye to the water to aid in the visualization; the overall effect of the flakes and the color being to make the K-fluid resemble several popular brands of detergent liquid. A number of experimenters have conducted flow visualization tests with K-fluid; we urge the reader to refer to the paper by Matisse and Gorman [44] for further details.

It is important to consider the action of the K-fluid suspension when subjected to a flow; i.e. the manner by which the flow visualization is obtained. Gorman and Swinney [22] used K-fluid to visualize the onset of turbulence in the Taylor-Couette system, and stated that the Kalliroscope platelets "align with the flow". The authors also reported that the

intensity of the scattered light measured with their K-fluid apparatus had the same features as velocity measurements using a laser Doppler velocimeter, and that the influence of the suspension on the properties of pure water was less than 0.1 %. Savaş [67] performed a general stochastic analysis of the motion of thin, ellipsoidal particles in a viscous fluid, with a view towards predicting the observed light field in flow visualization experiments. He concluded that in the presence of a shear flow, the flakes align themselves to be parallel to the stream surfaces, which are thus revealed in the visualization. Savaş showed that this technique of using small suspended particles is particularly unsuitable for visualizing flows involving small amplitude perturbations to backgrounds with high shear, e.g. Tollmien-Schlichting waves in a boundary layer. We infer from his analysis that the K-fluid is well suited for visualizing vortex flows, which are large-scale, high shear perturbations over uniform background flows.

In order to utilize the K-fluid, we constructed a separate, much smaller analog of the full-size towing tank. The original "K-tank" (as we shall refer to it) consisted of a rectangular Plexiglas structure of dimension 2.44 x 0.15 x 0.15 m; the tank was later replaced by a broader version of dimension 2.44 x 0.60 x 0.15 m. A small, belt-driven "carriage" was constructed to ride over the K-tank, supported rigidly by linear ball bearings on one side and a single cam follower on the other side. A DC motor was employed to provide the motive force to the towing belt, and allowed constant carriage velocities of up to 0.15 m/s. An ingenious oscillation mechanism, inspired by the experimental apparatus of Freymuth [18], was designed and implemented by Barrett [3]. Figure 6-3 is a schematic illustration of this mechanism, which allowed for both translation (heaving) and rotation (pitching) motions to be provided by a single DC motor. Independently adjustable settings provided for a heave amplitude of up to 3.81 cm, a pitch angle amplitude of up to 60°, and an oscillation frequency of up to 0.35 Hz. A number of values of phase angle ϕ could be set; we used only the setting of 90°. The oscillation mechanism was installed on the towing carriage such that the cylinder and foil models were suspended vertically into the K-fluid, via a mounting assembly that provided for close control of the separation length between the models. The K-tank was illuminated by diffuse lighting from overhead fluorescent sources. A high-resolution black-and-white video camera was mounted on a tripod bolted to the carriage, enabling video recordings of the wake patterns to be obtained from a frame of reference moving with the carriage. Still photographs of the wake could be obtained in two

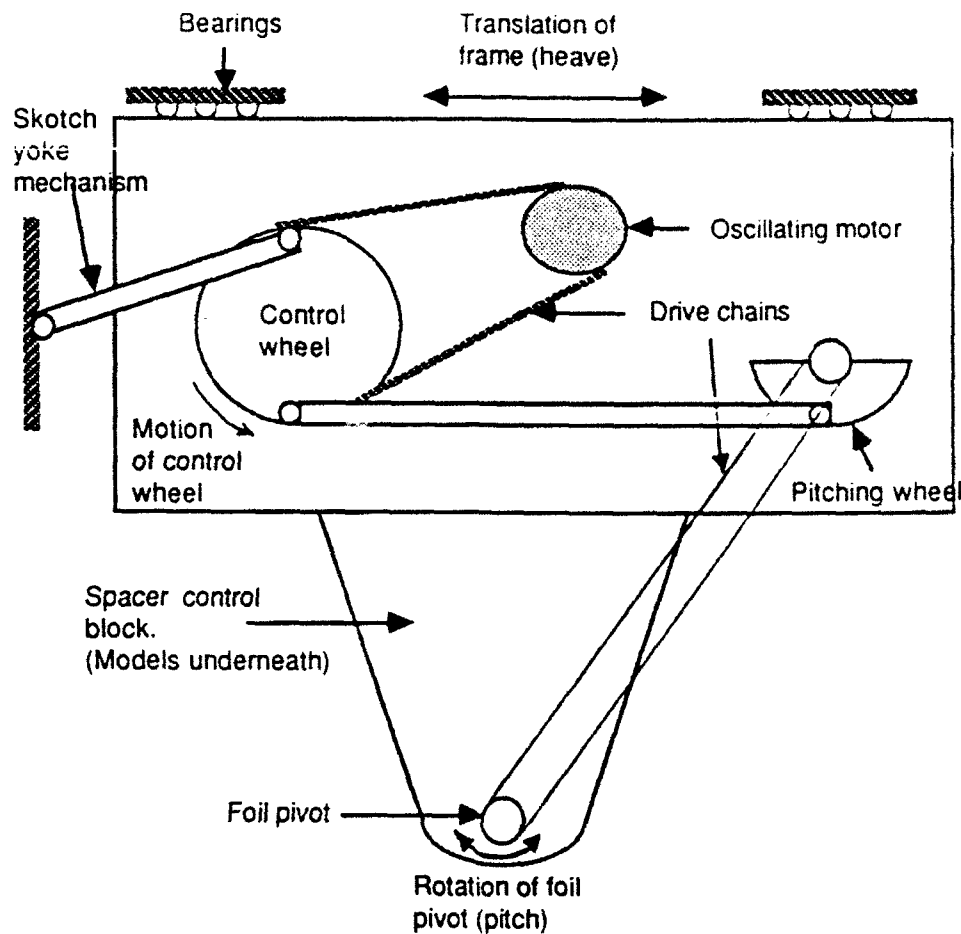


Figure 6-3: The oscillating mechanism used in the Kalliroscope-tank.

ways: by taking photographs of a TV monitor while playing back the video recordings, and also by directly using a 35mm still camera bolted on to the carriage tripod.

6.2.2 Initial experiments

Our flow visualization tests started on a disappointing note — after a number of trials, it became apparent that some modifications would be required to the apparatus. The principal difficulties that we encountered were the following:

- The presence of the foil in the wake of the circular cylinder always disrupted the lock-in vortex shedding from the cylinder, so that a strong and uniform upstream vortex street was not attainable. This behavior was a problem since it was our intention to study the vortex interaction between the cylinder and the foil, not to suppress the cylinder vortex street.

- Our original K-tank was found to be too narrow for the size of models tested. The large blockage ratio caused a distortion of the cylinder and foil vortex streets, preventing a proper interpretation of the wake behavior.

In order to overcome the above difficulties, two modifications were made. A new, wider, Plexiglas structure was acquired and installed as the Kalliroscope-tank. Fortunately, the modular nature of the towing carriage and oscillation mechanism allowed for a minimum of new parts required in order to implement the changeover. Blockage phenomena with the new tank were not detected.

To avoid the disruption of the vortex shedding by the presence of the foil in the wake, we evaluated a D-section (half-circular) bluff cylinder as our upstream Kármán vortex generator. Little information exists in the literature on the behavior of vortex-shedding from a D-section cylinder, so we first conducted a number of stationary (nonoscillating) tests with the D-section alone. We towed the model at different speeds through the K-fluid and counted the vortices shed over a given distance in order to determine the Strouhal number. Figure 6-4 shows that the behavior of the Strouhal number versus the Reynolds number for the D-section cylinder was found to be very similar to the corresponding behavior for the circular cylinder (see Figure 1-2), — the net result being that we could use the D-section in place of the circular cylinder with no changes to our selected oscillation parameters. Tests with a D-section and hydrofoil tandem arrangement proved that the D-section indeed performed its intended role of generating strong drag vortices without disruption due to the presence of the foil. An additional unanticipated benefit of the D-section was that the phase of the vortex shedding (relative to the cylinder oscillation) was found no longer to depend on the oscillation frequency (in a small range bracketing the Strouhal number); i.e. the frequency was no longer an important variable parameter. All of our further experimental runs were successfully conducted at a single cylinder Strouhal number of 0.20.

6.2.3 Successful experiments

The testing schedule, and results

Following our modifications of the flow visualization apparatus, tests were conducted at a regular testing "grid" consisting of three heave amplitude settings, three pitch amplitude settings, and twenty separation lengths. For each combination of heave and pitch amplitude,

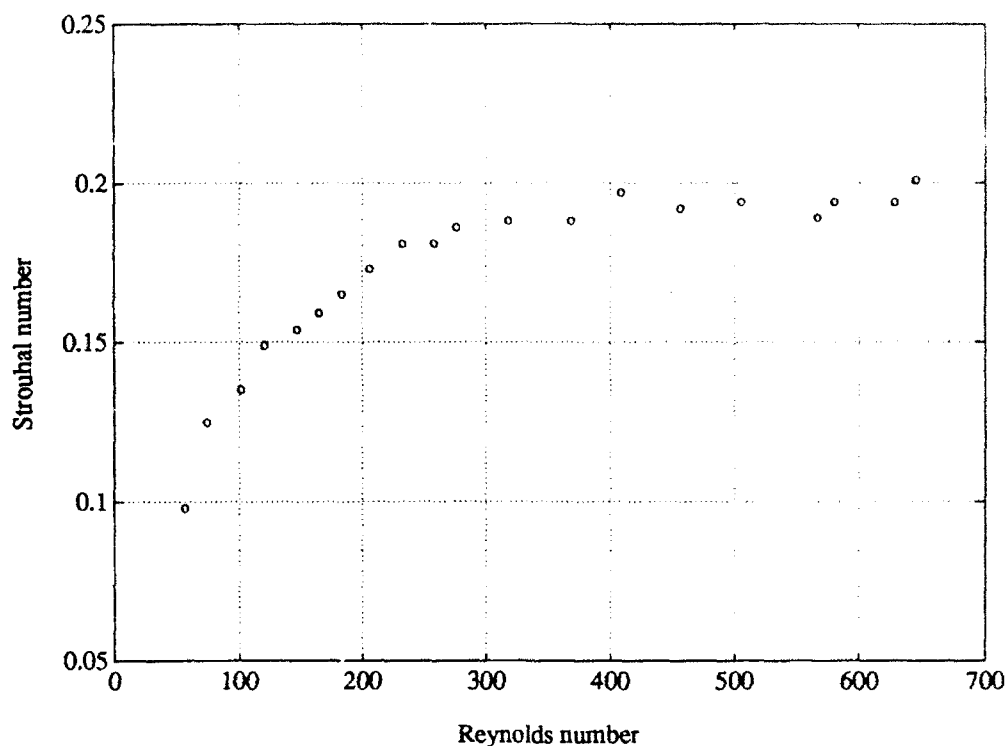


Figure 6-4: Measured Strouhal number versus Reynolds number for a D-section cylinder.

we calculated the apparent foil Strouhal number S_F (Equation 6.1) as well as the apparent foil angle of attack α , given by

$$\alpha = \tan^{-1} \left(\frac{2\pi A_F f_F}{U} \right) - \theta \quad (6.5)$$

We have used the term “apparent” since the actual flow velocity at the foil is unknown; the free-stream velocity U has been used in the calculations. We originally wished to concentrate our tests at foil Strouhal numbers $S_F \approx 0.30$, and small angles of attack $\alpha < 15^\circ$. As it turned out, we achieved very similar results for several of the values of S_F and α . Table 6.1 lists the heave and pitch amplitude combinations that we attempted; each entry of the table was repeated for 20 separation length settings.

Upon conducting the tests and reviewing the video recordings, we found that the oscillating foil did indeed have a strong effect on the cylinder vortex street. In many cases, the foil achieved a dramatic repositioning of the Kármán vortices, with the mechanism of this repositioning apparently being a suction effect as the vortices passed over the leading edge of the foil. In some situations, this repositioning effect was only temporary, as the vorticity

| Number | Heave (A_C/d) | Pitch (θ) | Strouhal # (S_F) | Angle of attack (α) |
|--------|-------------------|--------------------|----------------------|------------------------------|
| 1 | 0.500 | 15° | 0.246 | +16.86 |
| 2 | 0.500 | 30° | 0.354 | +01.86 |
| 3 | 0.500 | 45° | 0.483 | -13.14 |
| 4 | 0.667 | 15° | 0.302 | +24.65 |
| 5 | 0.667 | 30° | 0.395 | +09.65 |
| 6 | 0.667 | 45° | 0.509 | -05.35 |
| 7 | 0.833 | 15° | 0.358 | +31.01 |
| 8 | 0.833 | 30° | 0.441 | +16.01 |
| 9 | 0.833 | 45° | 0.550 | +01.01 |

Table 6.1: Heave and pitch amplitude combinations tested.

generated by the foil and the (repositioned) cylinder vortices interacted in such a manner as to quickly re-establish a drag configuration in the wake. However, we did find three distinct (and repeatable) modes wherein "beneficial" interaction occurred, in that a net reduction or elimination of the in-line wake velocity was achieved. We labeled these modes (reflecting the sequence in which we found them):

1. Vortex pairing.
2. Destructive vortex merging.
3. Constructive vortex merging.

Figure 6-5 shows the various parameter combinations at which the above modes were found. The X-axis of the figure refers to the spacing or separation length, and the Y-axis lists the heave and pitch combinations of Table 6.1. The occurrence of a mode is indicated by the number of the mode in parentheses. A number followed by an asterisk indicates that the corresponding mode was observed in a less clearly discernible fashion. Figure 6-5 shows that the spacing s/d was found to be the most important parameter, and for certain combinations of heave and pitch, it was possible to achieve more than one mode by varying s/d suitably.

In the paragraphs that follow, we shall describe each of the three modes in detail, illustrating our findings with appropriate photographs of the wake, and accompanying explanatory diagrams.

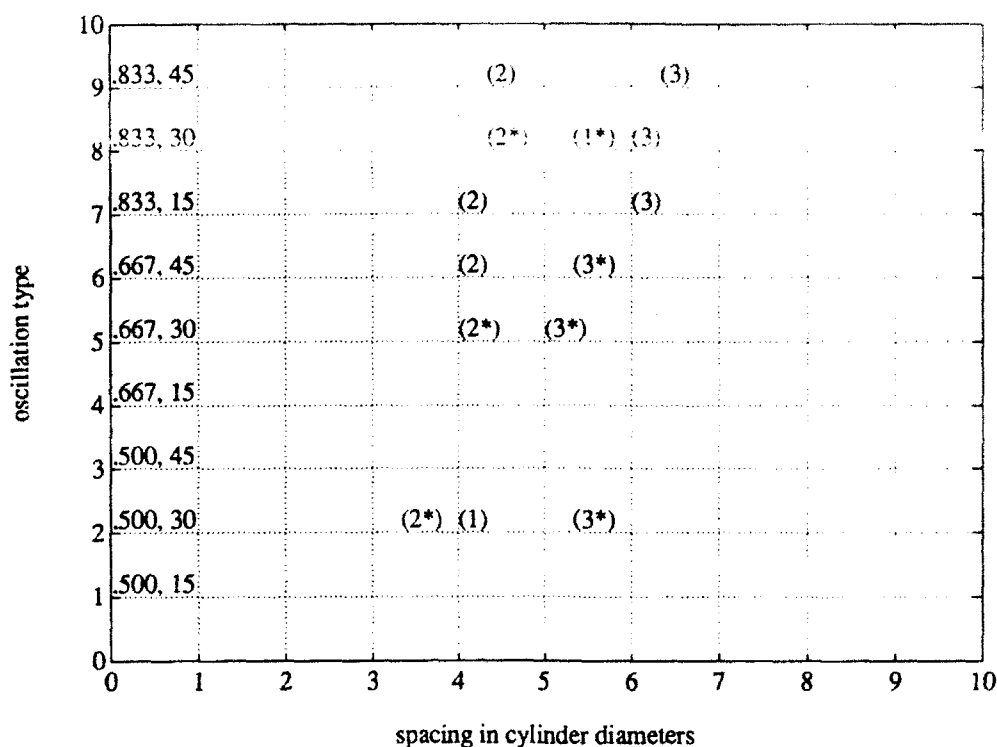


Figure 6-5: The locations of the three interaction modes observed.

Mode 1: Vortex pairing

In the "vortex pairing" mode, each cylinder vortex pairs up with a foil vortex of the opposite sign; the resulting sets of counter-rotating vortex pairs slowly drift away from the centerline of the wake. The orientation of the vortex pairs is such that there is little or no induced in-line wake velocity (i.e. in the direction of the free-stream velocity).

Vortex pairing is illustrated in Figures 6-6 and 6-7. The figures show a sequence of photographs of the wake taken at instants of time approximately $T/4$ apart, where $T = 1/f_F$ is the time period of the oscillation. The photographs focus on the region of the wake surrounding the oscillating foil, and show the vortex patterns both upstream and downstream of the foil. The direction of towing is from left to right, giving an equivalent free-stream velocity from right to left. Hand-drawn figures of the vortex positions accompany the photographs, and are useful in understanding the mechanism of the vortex pairing phenomenon. In all of the drawings, the cylinder's Kármán vortices (coming from upstream) are labeled with alphabets (A, B, C, etc.), while the foil vortices are labeled with numerals (1, 2, 3, etc.).

Figure 6-6: Wake interaction mode 1: Vortex pairing. Views I and II.

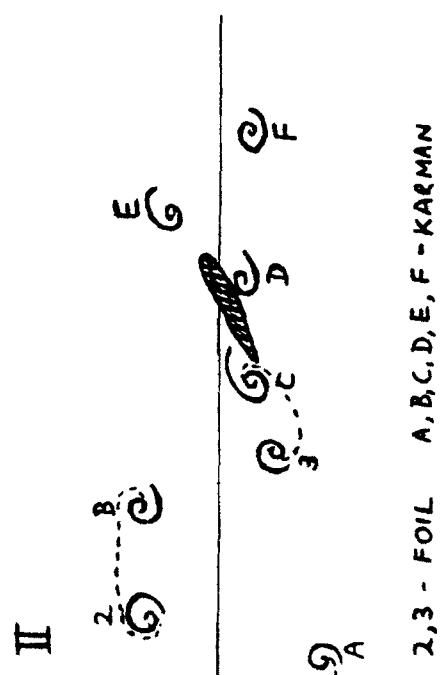
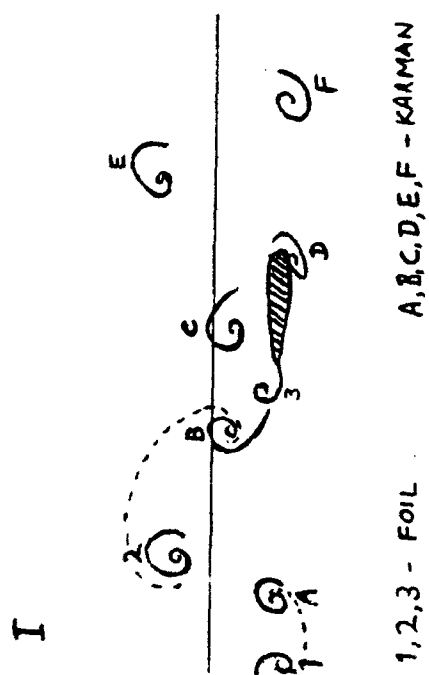
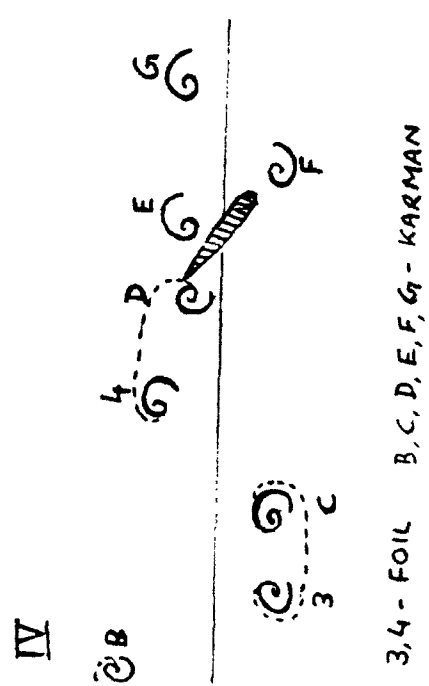
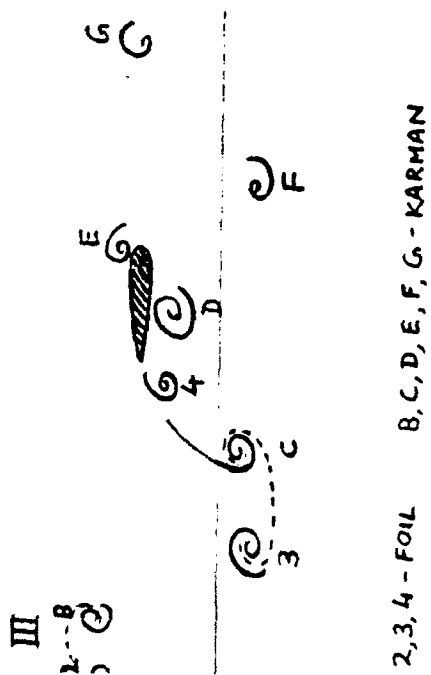


Figure 6-7: Wake interaction mode 1: Vortex pairing. Views III and IV.



We start our explanation with Figure 6-6, which illustrates the instants I and II of the cycle. During instant I, the foil is at the bottom of its heave stroke. To understand the mechanism, we concentrate on cylinder vortices C, D, and E, and foil vortices 3 and 4. In the first view, cylinder vortex C has been moved down from its upstream position (due to foil suction), while foil vortex 3 is in the process of formation. In addition, the foil has just encountered cylinder vortex D near the leading edge.

View II of Figure 6-6 shows an instant $T/4$ later, when the foil is at the centerline, moving upwards. Foil vortex 3 has been shed into the wake, and cylinder vortex C is being rolled off the trailing edge as well. Cylinder vortex D is now "trapped" by the foil suction and is moving upwards from its original position.

Figure 6-7 illustrates instants III and IV of the vortex pairing cycle. View III shows an instant of time $T/4$ later than view II of the previous figure, and the foil is now at the top center of its heave stroke. Cylinder vortex C has separated from the trailing edge of the foil, and is now paired with foil vortex 3 of the opposite rotational sign. Foil vortex 4 is in the process of formation from the trailing edge, while cylinder vortex D has been successfully repositioned by the suction of the foil.

View IV of Figure 6-7 shows the final instant of the sequence. The foil is at the centerline, moving down. Foil vortex 4 has been shed from the trailing edge, and cylinder vortex D is being swept backwards to pair with vortex 4. Downstream of the foil, the vortex pair 3-C is convecting slowly away from the wake centerline, and there is no induced wake velocity in the in-line direction. Just upstream of the foil, vortex E is trapped by the foil suction and is moving downwards; at an instant $T/4$ later it will assume the position of vortex C of view I (Figure 6-6) and the cycle will continue.

Mode 2: Destructive vortex merging

The previous mode of vortex pairing illustrated a type of behavior wherein the Kármán vortices from the cylinder and the vortices created by the foil had approximately the same circulation strengths, enabling them to form counter-rotating pairs on an equal footing (i.e. without domination by one source of vorticity). In most of the cases, however, the vortices generated by the foil were substantially stronger than the cylinder vortices. Mode 2 is the situation of "destructive vortex merging", wherein the cylinder vortices are repositioned

and then absorbed into the foil vortices of opposite rotational sign. The resulting merged vortices lie on a single line in the wake, and there is no induced in-line wake velocity.

Destructive vortex merging is illustrated by the sequence of photographs and drawings in Figures 6-8 and 6-9. As before, each figure contains two photographs taken at instants $T/4$ apart in time, for a total sequence of four views. Cylinder vortices are labeled with alphabets, while foil vortices are labeled with numbers. The free-stream velocity is from right to left.

We start with view I of Figure 6-8, where the foil is at the bottom center of its heave stroke. We concentrate on cylinder vortices C, D, and E, and foil vortices 3, 4, and 5. The strong vortex off the trailing edge in view I is foil vortex 3. Cylinder vortex C is just discernible below vortex 3, and is about to be merged into it. Cylinder vortex D is below the leading edge of the foil.

View II of Figure 6-8 shows the situation at an instant of time $T/4$ later; the foil is now at the centerline and moving up. The foil vortex 3, which has merged and destroyed cylinder vortex C, is now well into the wake. Foil vortex 4 is being formed at the trailing edge, while cylinder vortex D is trapped below the trailing edge and is being repositioned upwards. In addition, the foil is about to encounter cylinder vortex E near its leading edge.

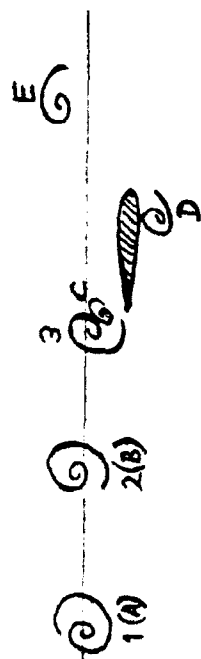
The sequence is continued in Figure 6-9, which contains views III and IV. View III, at a time $T/4$ after view II, shows the foil at the top center of its heave motion. Foil vortex 4 is prominent behind the trailing edge; cylinder vortex D can be seen just above and in front of vortex 4. Cylinder vortex E is now above the leading edge of the foil: it is partly obscured by the shadow of the foil in the photograph.

Finally, view IV of Figure 6-9 shows the foil at the wake centerline, on its way down. Vortex 4 (which now includes the merged cylinder vortex D) is well into the wake. Foil vortex 5 is in the process of formation, while cylinder vortex E is being repositioned by the foil suction. The merged vortices 3(C) and 4(B) lie on a single line in the wake (this is clearest in views I and III). While there is substantial turbulence in the wake, there is very little in-line velocity.

Figure 6-8: Wake interaction mode 2: Destructive vortex merging. Views I and II.

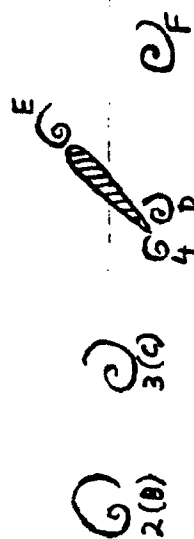


I



1, 2, 3 - FOIL (A), (B), C, D, E - KARMAN

II

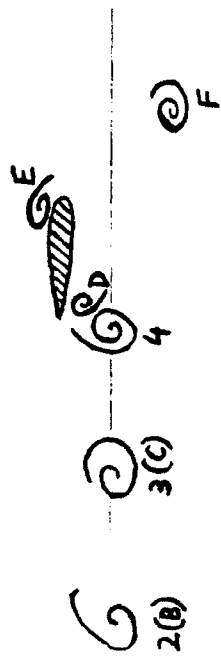


2, 3, 4 - FOIL (B), (C), D, E, F - KARMAN

Figure 6-9: Wake interaction mode 2: Destructive vortex merging. Views III and IV.

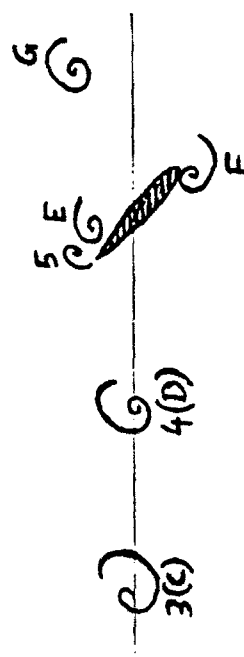


III



2, 3, 4 - FOIL (B), (C), (D), E, F - KARMAN

IV



3, 4, 5 - FOIL (C), (D), E, F, G - KARMAN

Mode 3: Constructive vortex merging

Our flow visualization showed that there were two types of vortex merging behavior – the merging of vortices of opposite sign described as mode 2, as well as the merging of vortices of the same sign. We termed this second type (the third mode, overall) “constructive vortex merging”. The sequence of photographs and associated drawings of Figures 6-10 and 6-11 illustrate mode 3, with the vortex labeling convention and flow direction as before.

The first two views are contained in Figure 6-10. We shall concentrate on the cylinder vortices (B), C, and D, and the foil vortices 2, 3, and 4. View I illustrates the situation with the foil at the bottom of the heave stroke. Clearly visible in the wake is the foil vortex 2, into which has already merged the cylinder vortex (B). (Parentheses are used to denote a vortex which is no longer visible as a distinct entity.) Cylinder vortex C is located above the foil.

View II of Figure 6-10 shows the pattern at a time $T/4$ later. The merged vortex 2(B) has moved downstream into the wake. Foil vortex 3 is forming at the trailing edge of the foil, which is now at the centerline and moving up. Cylinder vortex C is being swept back over the foil, and will eventually merge with vortex 3. Cylinder vortex D is as yet too far away to be affected by the suction of the foil.

The sequence is continued in views III and IV of Figure 6-11. View III shows the foil at the top center of its heave stroke. Foil vortex 3 has grown in size to the point that it has absorbed (merged) the cylinder vortex C. The combined vortex 3(C) is clearly on the same straight line as the previous merged vortex 2(B), which is still visible downstream.

The final photograph, view IV, shows the foil at the centerline and moving down. The merged vortex 3(C) is well into the wake. From the trailing edge, foil vortex 4 is just forming. Cylinder vortex D is being swept back below the foil, to eventually merge with vortex 4. Cylinder vortex E is as yet unaffected by the foil; during the next half-cycle it will be swept back to merge with the next foil vortex, and so on.

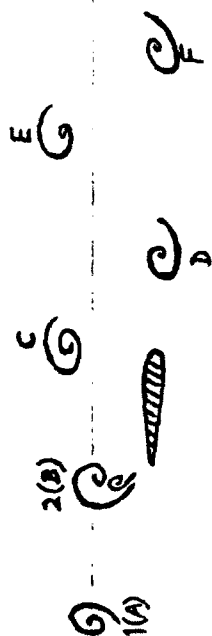
6.2.4 Conclusions from the flow visualization experiments

In the previous paragraphs, we have discussed in some detail three wake modes observed during the flow visualization tests. The oscillating foil acted (in most cases) to reposition the cylinder vortices, as well as generate strong vorticity of its own. The three modes

Figure 6-10: Wake interaction mode 3: Constructive vortex merging. Views I and II.

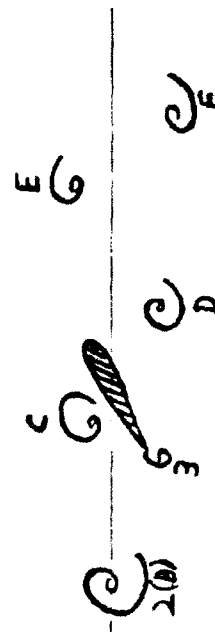


I



1, 2 - FOIL (A), (B), C, D, E, F - KARMAN

II

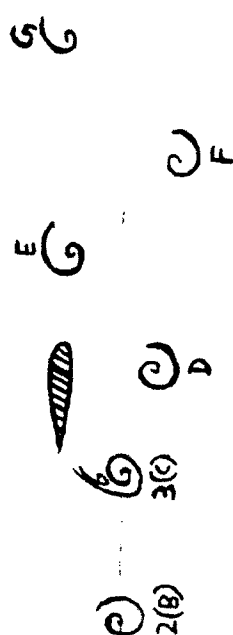


2, 3 - FOIL (B), C, D, E, F - KARMAN

Figure 6-11: Wake interaction mode 3: Constructive vortex merging. Views III and IV.



III



2,3-FOIL (B), (C), D, E, F, G - KARMAN

IV



3,4-FOIL (C), D, E, F, G - KARMAN

discussed above were those cases wherein the interaction between the foil and cylinder vortices was such as to result in little or no visible flow velocity in the wake; i.e. these were the "successful" modes.

The most important variable parameter governing the outcome in the wake was found to be the separation distance s (or the separation ratio s/d). For certain combinations of heave and pitch amplitudes, it was possible to achieve all three modes by varying the separation distance suitably. Of the three modes, "vortex pairing" was the most sensitive and difficult to reproduce. "Destructive vortex merging" and "constructive vortex merging" were found to be robust and repeatable modes.

The photographs of Figures 6-6 through 6-11 focus closely on the patterns immediately upstream and downstream of the oscillating foil, but do not show the evolution of the wake at greater downstream distances. Figure 6-12 addresses this shortcoming by including three photographs of the wake downstream from the foil. Photograph A of Figure 6-12 shows the wake when the foil is actually not present — i.e. it shows the bluff body Kármán wake behind the D-section. The familiar, staggered arrangement of vortices gives rise to a substantial in-line velocity in the wake that "follows" the cylinder. (On the photograph, the wake velocity gives the appearance of an elongated whitish region between the vortex rows.) Photograph B shows the wake during the "vortex pairing" mode. The counter-rotating pairs of cylinder and foil vortices are seen to be nearly parallel to the wake centerline. The absence (at least visually) of an in-line wake velocity is quite marked. The vortex pairs slowly convect away from the wake centerline, but do not acquire any noticeable in-line motion. Finally, photograph C shows the wake during the "constructive vortex merging" mode; the situation for the destructive merging mode is actually rather similar. The merged vortices are seen to all lie on a relatively straight line in the wake. While the visualization (in this still photograph) is rather confused due to the relatively high amount of turbulence, it appears that an in-line velocity does not exist. (The videotaped segment clearly supported this last observation.) It should be noted that a disappearance of the *visible* wake in such flow visualization tests does not necessarily prove that the wake is completely absent, and velocity measurements are required to confirm the situation. Nonetheless, it does appear that the three modes described in the last subsection do reduce the in-line wake velocity, and hence presumably the in-line drag force.

What of the reduction or enhancement of the wake signature due to the merging of the

Figure 6-12: Photographs of the wake downstream of the oscillating foil.

A



B

C



cylinder and foil vortices? From the visualization, it was clear that Mode 2 involved a destructive merging of oppositely-signed vortices, and presumably a weakened resulting vortex street; while Mode 3 involved a constructive merging of like-signed vortices and therefore a strengthened vortex street. However, due to the absence of velocity measurements, quantitative calculations of the vortex strengths were not possible, and the results of the merging behavior must be considered inconclusive.

Also inconclusive was the question of the energy costs required to bring about the in-line drag reduction, or in other words, the efficiency of the foil. In all our tests, the foil generated substantial vorticity, indicating a substantial input of energy. From the flow visualization, it was not possible to make any quantitative estimates of the work input from the foil.

To summarize, our conclusions from the flow visualization tests were the following:

- An oscillating foil acting in the wake of a bluff body can achieve a repositioning of the bluff body's Kármán vortex street.
- Due to interaction between the repositioned Kármán vortices and the foil's own vorticity, a reduction of the mean in-line wake velocity can be achieved. This reduction of the in-line wake velocity is likely to lead to a reduction of the in-line drag force on the combined system. The efficiency of this drag reduction process cannot be determined from flow visualization tests.
- Some of the interaction modes involved a constructive or destructive merging of the cylinder and foil vortices, leading presumably to an enhancement or reduction of the wake signature. The precise behavior (in a quantitative sense) could not be determined from the visualization.

6.3 Force measurement experiments

6.3.1 The apparatus and methods

In order to complement our flow visualization investigation of the tandem cylinder/foil system, we designed a series of force measurement experiments in the main testing tank facility. The requirements for our experimental apparatus were daunting, even with the reduced set of variable parameters as discussed in Section 6.1.3. We now desired the ability to oscillate a cylinder and a foil model in heave, and rotate the foil model in pitch ...

while towing the apparatus forward at a constant velocity. At least seven quantities had to be measured — lift and drag forces on the cylinder, lift and drag forces and torque on the foil, the heaving motion (identical for both models), and the foil pitching motion. In addition, the spacing (separation length) between the cylinder and foil models had to be highly adjustable.

Although these force measurement tests were conceptually just an extension to our previous cylinder tests, all of these new requirements necessitated an entirely new apparatus. After reviewing a number of possibilities, we opted for a “double-yoke” structure. Figure 6-13 illustrates this apparatus, which consisted of two inverted-U “yokes” pivoted at their upper ends. The forward yoke carried the fixed cylinder (D-section) model in a manner identical to the original apparatus, while the aft yoke carried the rotating foil model connected via a chain and pulley arrangement to a second (smaller) SEIBERCO motor that provided the pitching oscillation. (The aft yoke was similar in many ways to the apparatus used by Triantafyllou *et al.* described in [85].) Each yoke could be rotated at the pivots and held in position at any angle; thus adjustments to the separation length ratio s/d were achieved by rotating both yokes through equal and opposite angles either inwards (towards each other) or outwards (away from each other). Vertical oscillations of the entire assembly were obtained with the same SEIBERCO motor and leadscrew table combination used earlier. It should be mentioned that the double-yoke design owed a great deal to the efforts of Barrett [3].

Given our excellent experience with the piezoelectric force transducer used for the cylinder experiments, we decided to use additional sensors of the same type. Thus the lift and drag forces on the cylinder and foil models were measured with two KISTLER 9117 transducers, while a KISTLER 9065 was used to measure the pitching torque on the foil. Our original LVDT was used to measure vertical motion, and a resistance potentiometer was employed to measure the angle of rotation. Each of the above sensors was carefully calibrated using known forces and displacements. The seven data signals were transmitted to the control room, filtered, and then sampled using the same systems described in Chapter 2. An expanded version of the original experiment control program was used to provide the tracking signals for both the heave and pitch SEIBERCOs as well as the carriage motion. Rewritten versions of our MATLAB processing code were used to process the acquired data off-line.

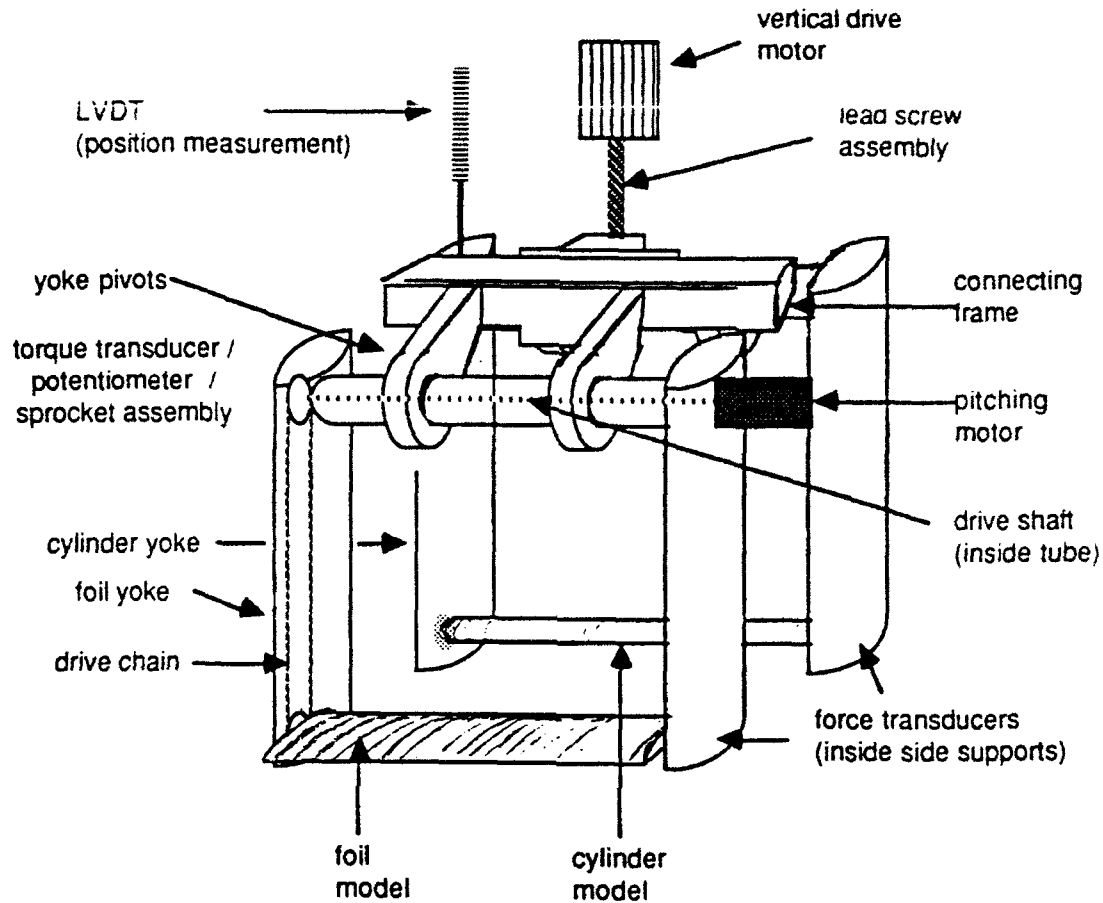


Figure 6-13: The double-yoke force measurement apparatus.

6.3.2 Experimental results

In order to conduct the force measurement experiments in a manner as similar as possible to the flow visualization tests, we used the same experimental "grid" as in Table 6.1. As an initial step, tare value tests were conducted with only the cylinder (foil removed), and then with only the foil (cylinder removed). With both models in place, we performed tests at each of the amplitude and pitch combinations of Table 6.1 and 14 separation lengths. The separation lengths were chosen to cover an entire wavelength of oscillation, equal in our case to five diameters ($\lambda = U/f_C = (1/S_C)d = 5d$).

From the test data, we extracted values of the cylinder mean drag D_{mC} , the foil thrust (or drag) T_{hF} , and hence the overall in-line drag force $D_{mC} - T_{hF}$. We defined an overall

in-line drag coefficient C_D^{overall} according to

$$C_D^{\text{overall}} = \frac{D_{mC} - T_{hF}}{\frac{1}{2}\rho d U^2} \quad (6.6)$$

where for consistency, we have used the cylinder diameter d in the normalization of both force quantities.

In addition to the in-line force, we evaluated the power input by the foil, given by

$$P_F = \langle L_F \frac{dy_F}{dt} \rangle + \langle T_F \frac{d\theta}{dt} \rangle \quad (6.7)$$

where $L_F(t)$ is the lift force (time trace) on the foil, $T_F(t)$ is the torque on the foil, and $y_F(t)$ and $\theta(t)$ are the measured heaving and pitching motions given Equations 6.3 and 6.4. As used in Chapter 5, the notation $\langle \dots \rangle$ denotes a cross-correlation at zero lag.

From the measured foil thrust force and input power, we calculated the apparent efficiency η_F of the foil, given by

$$\eta_F = \frac{T_{hF} U}{P_F} \quad (6.8)$$

As before, we have used the term "apparent" since the actual flow velocity at the foil is not known (except for the tare value tests), and the free-stream velocity U has been used in the calculations.

All of our experimental data were processed for the above quantities, which we then plotted as functions of the separation length s . With all the tests completed and the results available, we found the following results were true for every combination of pitch and heave.

- The cylinder drag force D_{mC} did not vary appreciably from the tare value conducted with the cylinder alone, nor did it vary much as a function of separation length.
- The foil thrust force T_{hF} was, in every case, considerably higher than the tare value with the foil alone. The thrust force showed a considerable dependence on the spacing. As a result of the foil thrust, the overall in-line drag coefficient on the combined system was smaller than the cylinder tare value.
- The apparent efficiency of the foil was a strong function of the spacing.

Typical examples of our results are shown in Figures 6-14 and 6-15, for the case of heave amplitude ratio $A_C/d = A_F/d = 0.833$ and pitch angle amplitude $\theta = 45^\circ$. Figure 6-14

shows the overall in-line drag force plotted against the separation distance (in terms of cylinder diameters). Also on the figure are the measured tare values for the cylinder drag (tested without the foil), and the foil thrust (tested without the cylinder). In this case the tare value of the thrust coefficient was actually negative, indicating that the foil was producing drag. With the cylinder present, the foil started producing thrust in sufficient quantities to reduce the overall drag coefficient below the cylinder tare value, with the reduction being a function of the spacing s . Figure 6-15 shows the apparent foil efficiency for the same oscillation parameters, and once again, the dependence on the separation length is clearly seen.

6.3.3 Conclusions from the force measurement experiments

Figures 6-14 and 6-15 of the previous subsection showed that the oscillating foil caused a reduction of the overall in-line drag force on the cylinder / foil system, with the foil thrust and efficiency being dependent on the separation length between the models. It is important to clarify the significance of these results, in the light of our vortex interaction study.

The fact that the foil produced drag with the cylinder absent (the tare value), but produced thrust with the cylinder present, is an interesting but not unexpected result. It should be borne in mind that the presence of the upstream cylinder causes a reduction of the mean flow velocity that the foil encounters, and hence the operating characteristics of the foil (in terms of the Strouhal number and angle of attack) are quite different in the two situations. Since the actual flow velocity at the foil is difficult to estimate (and in any case, is not uniform), we have used the freestream velocity U in all the calculations. It could be argued that the reduction in the overall in-line drag coefficient is simply the net effect of the foil thrust counteracting the cylinder drag, and is neither surprising nor significant.

The importance of our results lies in the dependence of the foil thrust and efficiency on the separation length, or spacing between the models. If no vortex interaction took place (i.e. if the foil acted as a simple thruster), one might expect a monotonic reduction of efficiency with increase of spacing, with the variation arising solely from the (monotonic) alteration of the freestream velocity (the wake defect becomes smaller with distance from the cylinder). In fact Figure 6-15 appears to indicate that there are two mechanisms at work: an average reduction of efficiency due to the variation of the average velocity, and a

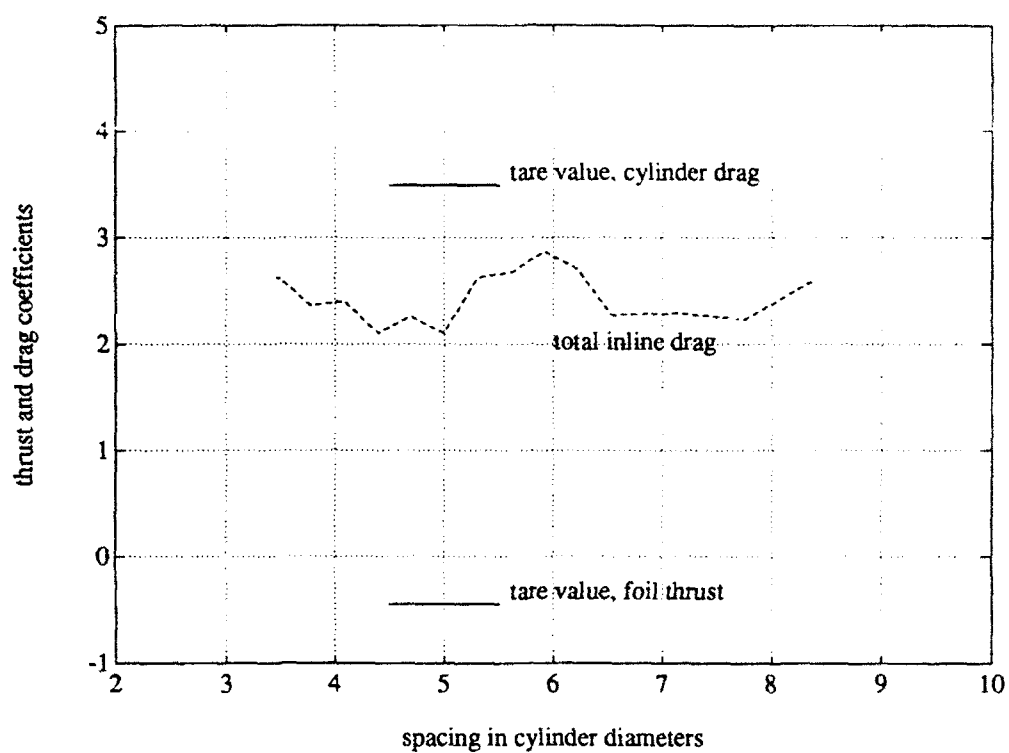


Figure 6-14: Overall in-line drag force as a function of spacing. $A_C/d = 0.833$ and $\theta = 45^\circ$.

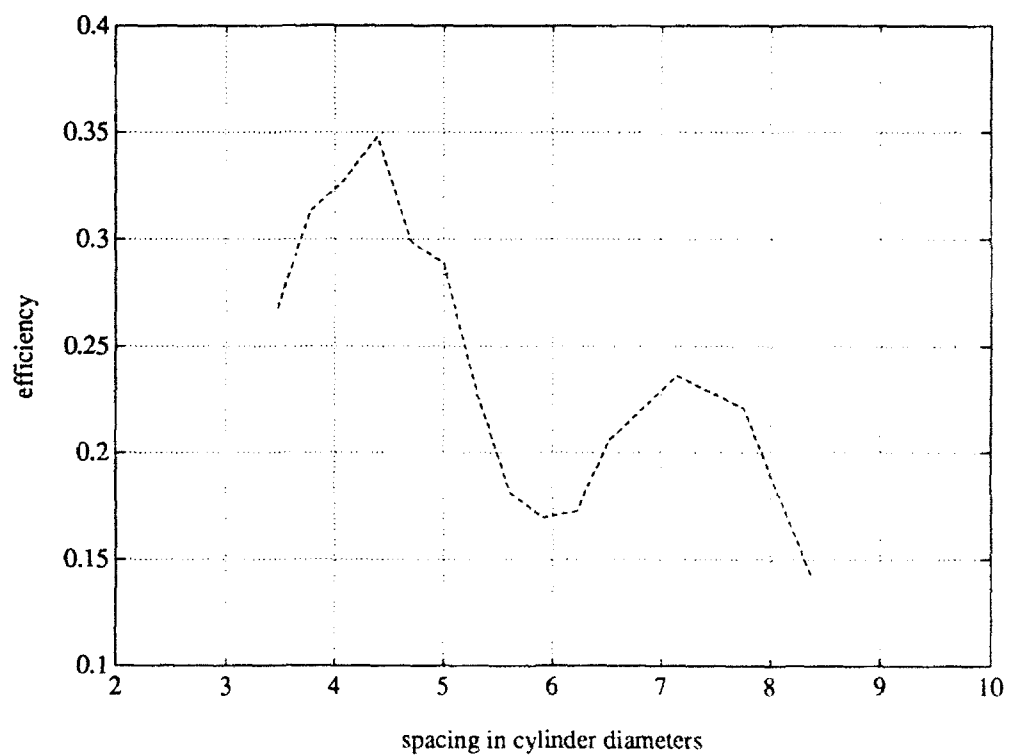


Figure 6-15: Apparent foil efficiency as a function of spacing. $A_C/d = 0.833$ and $\theta = 45^\circ$.

marked peaking behavior superimposed on this average reduction. Qualitatively identical trends were observed at all the other combinations of heave and pitch amplitudes as well. Such a peaking behavior could only mean one thing — that the operation of the foil is strongly affected by its interaction with the upstream Kármán vortex street. Since we had no means of performing flow visualization together with our force measurement apparatus, we cannot directly correlate the variation in the efficiency of Figure 6-15 with the vortex modes discussed in the previous section. It is interesting to note, however, that the two peaks in the efficiency occurred at spacings of about 4 diameters and 7 diameters respectively, corresponding well with the occurrence of modes 2 and 3 respectively during the K-tank visualization tests (Figure 6-5).

To summarize, our force measurement experiments offered the following conclusions:

- The operation of the foil behind the cylinder caused a reduction of the overall in-line drag force on the system, consistent with the reduction of the mean wake velocity observed in the flow visualization tests.
- The thrust generated by the foil, and its apparent efficiency, were found to be strongly dependent on the spacing between the models. We infer from this that the forces on the foil depend significantly on the flow interaction with the upstream vorticity.

It is important to note that the flow visualization tests described earlier in this chapter and the force measurement results above proved to be entirely consistent with each other, despite the large difference in Reynolds numbers and other obvious factors. We should also underscore that these experiments were performed on an exploratory basis, and we made no attempt to fine-tune the performance of the system. The use of an oscillating foil offers an intriguing way to alter the vortex street of a bluff body, and hence to reduce the fluid drag force acting on that body. Researchers investigating the use of oscillating foils as propulsive devices should carefully study the interaction of the devices with upstream vorticity.

Chapter 7

Conclusions

7.1 The essential conclusions of this thesis

In keeping with the broad scope of bluff body vortex wake dynamics, this thesis has attempted to shed light on a variety of related issues. With all of our experimental tests, we have tried to fill in some of the vast parameter space that exists in the areas of vortex-induced forces and vibrations — not merely in terms of raw data, but more importantly in terms of newer and better conceptual understanding. By no means do we imply that we have solved all the problems in this field! The situation can be compared to an existing brick wall representing the available knowledge on the subject that has been accumulated over the preceding several decades; this thesis adds a layer of bricks to the wall, but the wall is far from complete.

Given the relatively general nature of the work, it is important to summarize the essential conclusions of the thesis. In the next section, we shall summarize each of Chapters 3 through 6 and evaluate the various contributions therein. First, however, we will state the most important conclusions of this thesis, or in other words, the essential “message” resulting from this research.

The most important work in this thesis is that related to the original motivation — an investigation into the vortex-induced forces acting on cylinders undergoing beating oscillations. Such beating oscillations are a fundamental response of long tubulars in sheared flows, and to the best of our knowledge, this thesis contains the only laboratory-scale results applicable to these motions. Perhaps more significant than the actual force coefficient re-

sults are the comparisons to pure harmonic data — that beating causes an extension to the sinusoidal lift force excitation region, a reduction in the mean drag force, an amplification of the oscillating drag force, and that the beating wake depends in a nonlinear fashion on the instantaneous oscillation amplitude. It is hoped that these results, combined with the other important ideas in this thesis (summarized in the next section), will help scientists and engineers in applying available experimental data to the estimation and control of VIV in full-scale situations.

7.2 Principal contributions of each chapter

7.2.1 Stationary and sinusoidal oscillation tests

In Chapter 3 of this thesis, we measured and analyzed the forces acting on a smooth circular cylinder undergoing sinusoidal oscillations transverse to the free-stream (towing) velocity. Such data is far from unique, and very similar experiments have been conducted by Bishop and Hassan [6], Mercier [47], Sarpkaya [65], and Staubli [75]. Our original motivation in conducting these experiments was to lay the basis for the beating tests of Chapter 5, but as we proceeded with the tests, we began to make several novel observations. These included:

The variation of the phase angle. We noticed that the phase transition behavior was quite different for large oscillation amplitudes when compared to that for small oscillation amplitudes. This phenomenon has not been studied by any other researcher, and we believe that the outstanding sensitivity and resolution of our apparatus enabled us to capture the behavior. We believe that this “phase-flipping” phenomenon is at least partly responsible for the amplitude-limited nature of the vortex-induced lift force.

The variation of the oscillating drag force. At high frequencies of oscillation, we measured very large values of the oscillating drag force. While this behavior has been previously commented on by Mercier [47] and Sarpkaya [65], we have greatly extended their limited measurements. In addition, we evaluated the higher harmonics of the oscillating drag force and showed that the overall picture was entirely consistent with the low Reynolds number flow visualization patterns of Williamson and Roshko [95].

The lift coefficient excitation region versus the lock-in region. In a very important observation, we noted that the lift coefficient excitation region (wherein a cylinder may

be excited into oscillations by the flow) is not at all the same as the lock-in region (wherein the vortex shedding frequency is "captured" by the oscillation frequency). In the existing literature, the two concepts have been used interchangeably. We showed that excitation is determined from phase considerations, while lock-in is determined from frequency considerations, and it is important to distinguish between the two.

In addition to the observations listed above, many of our data analysis and presentation techniques provide new insight. We believe that our presentation of the large quantity of data in the form of contour maps is easier to understand and is particularly suitable for use in computer programs. Our histogrammic analysis technique may become a valuable way of identifying the wake response from force measurement data.

7.2.2 Error analysis and application to VIV predictions

Chapter 4 presented several important considerations in the applicability of our data to full-scale predictions.

Error analysis. A comprehensive error analysis showed that our measurements had very low random and systematic errors, and compared well with the existing literature.

VIV prediction. We devised a simple "back of the envelope" VIV prediction scheme using our experimental data, and showed that this scheme gave good results which compared favorably with full-scale measurements. Our model exploited the concepts of energy balance and the amplitude limited nature of the lift force. While the basic ideas are well established, we believe that they have not been used together in this fashion in any other published work.

Noncircular cross-sections. We demonstrated the versatility of our apparatus and techniques by conducting experiments with several noncircular bluff body cross-sections, including a wire-rope, a chain, a simple offshore riser section, and a haired-fairing vortex suppression device. By comparing and contrasting the data obtained with these models to smooth circular cylinder results, we illustrated the importance (and ease) of conducting dynamic oscillation tests for each cross-section of interest.

7.2.3 Beating oscillation tests

Chapter 5 presented our data on beating oscillations, important because long tubulars in sheared flows respond with complex, beating motions, and pure-sinusoidal data no longer apply. We conducted amplitude-modulated tests with several different oscillation amplitudes and frequencies, and three modulation ratios. While all of the data of Chapter 5 represented original findings, the most significant contributions included the following:

The behavior of the drag force. We showed (for the first time experimentally) that the presence of beating caused a reduction of the mean drag coefficient and an increase of the RMS oscillating drag coefficient. Our beating data, presented in the form of contour plots, can be used directly to estimate the drag coefficients in various situations. In addition, we evaluated the use of various schemes to extrapolate commonly available sinusoidal results to the beating case.

The behavior of the lift force. Our analysis of the beating lift force demonstrated that while the overall lift coefficient magnitudes remained comparable to sinusoidal data, there were substantial difficulties in measuring and interpreting the behavior of the lift coefficient phase angles. We defined equivalent lift force coefficients on the basis of direct power transfer and inertial force calculations, and presented contour maps of these equivalent coefficients. The primary excitation region for each of the beating modulation ratios considered was found to be larger in extent than the corresponding sinusoidal excitation region.

Histogrammic analysis of the wake response modes. Using time-domain histogrammic analyses of the beating force traces, we showed that the cylinder wake could respond to the amplitude-modulated excitation in any of a variety of modes. A particularly interesting mode observed was *frequency-switching*, wherein the vortex shedding frequency switched alternately between the imposed carrier frequency and the natural Strouhal frequency, thus illustrating the strong nonlinearity of the process. The modes we detected compared favorably with the flow visualization results of Nakano and Rockwell [51].

Our beating force coefficient measurements and wake response analyses are expected to be of use in a variety of full-scale situations involving long, flexible cylinders in sheared flows.

In addition, we expect that an important application of our data will be in the calibration of quasi-theoretical "wake-oscillator" models representing beating excitation, such as the one currently under development by Tjavaras [77].

7.2.4 Cylinder-foil vortex interaction

In Chapter 6 of this thesis, we performed a novel vortex interaction study. Drawing from fish observation data, we evaluated the concept of an oscillating foil acting in the wake of a bluff cylinder and interacting with the Kármán vortices shed by the cylinder so as to effect vorticity control. Such control of vorticity has two important practical applications: the reduction of the in-line wake velocity (and hence the in-line drag force) through vortex repositioning; and the reduction or enhancement of the wake "signature". A new flow visualization facility, and a new "double-yoke" force measurement apparatus were designed and used for these experiments. We obtained the following findings:

Vortex repositioning. Via suction, the foil succeeded in repositioning the cylinder vortices from their Kármán configuration. Beneficial interactions (wherein the in-line wake velocity was reduced) between the repositioned cylinder vortices and the foil vortices were achieved in three distinct modes.

The importance of the spacing ratio. Both flow visualization and force measurements showed that the separation length ratio s/d between the cylinder and the foil strongly affected the behavior of the system.

Our results from this experiment have important consequences, not the least of them being in the area of oscillating foil propulsion. Our data showed that in the presence of incoming large-scale patterns, an oscillating foil may enhance its efficiency and thrust simply by properly synchronizing its oscillation with the arrival of these patterns.

7.3 Recommendations for future work

Any work of research inevitably raises as many or more questions than it answers, and in this final section we shall suggest various avenues of research leading from this thesis. While our experimental apparatus and analysis methods gave us stable and repeatable data and proved to be efficient and versatile to use, there are further improvements that are

possible. In fact, as our experiments progressed, we noted a variety of ways to modify or extend the system to enable newer and better testing programs. Some of our suggestions in the paragraphs that follow relate to correcting these shortcomings and extending the capabilities of our apparatus, while others relate to the evaluation of promising new ideas stemming from this work.

7.3.1 Achieving higher Reynolds numbers.

Most of the experiments in this thesis were carried out at a Reynolds number Ud/ν of about 10,000. This value is well into the turbulent subcritical regime, but is still too small to be relevant to many practical situations. Many offshore flows, for instance, involve cylinder Reynolds numbers of 10^6 or higher, i.e. into the critical and supercritical regimes. It is unclear as to the extent to which even the qualitative trends in the force coefficients measured in subcritical flows are applicable to the supercritical case.

Due to the inherently finite length of the towing tank facility, higher towing speeds lead to shorter (and hence less accurate) measurement durations. It is possible to increase the Reynolds number by increasing the cylinder diameter, but this is also limited by the necessity of avoiding blockage and free-surface effects.

Are tests at higher Reynolds numbers simply not possible in this facility? We believe that it may be possible to *artificially simulate* the effects of high (i.e. supercritical) Reynolds numbers by introducing upstream flow turbulence (by towing an appropriate grid ahead of the oscillating apparatus). It is known (Blevins [7], Barnett and Cermak [2]) that free-stream turbulence in an otherwise low- Re flow can cause early transition of the cylinder boundary layers, thus giving the impression of a higher effective Reynolds number. To be sure, turbulence does not cause the same effects with all cross-sections (with sharp-edged cross-sections, there is a lowering of the effective Reynolds number — see Roberson *et al.* [62] or McLaren *et al.* [46]), and care must be taken in the interpretation of the results. We believe, nonetheless, that forced-oscillation tests in the presence of turbulence will be a useful and relatively inexpensive way of extending the capabilities of our apparatus.

7.3.2 Combined in-line and transverse oscillations.

We know that vortex shedding imposes two sets of oscillating forces on a bluff cylinder — an oscillating transverse lift force at the frequency of vortex shedding, and an oscillating in-line drag force at twice the frequency of shedding. In the case of a long tubular, the predominant response is in the transverse direction, but there is an oscillating response in the in-line direction as well. The overall motion often resembles a “Figure-8”, as has been observed in field experiments (Alexander [1], Vandiver [91]).

Attempts have been made by other researchers to conduct laboratory-scale forced-oscillation tests with combined in-line and transverse oscillations, but not very much is known about the results. Alexander’s [1] apparatus proved to be unreliable, Moe and Wu [49] have not published comprehensive results, and Pantazopoulos’ [57] data is proprietary. With our experience in motion control systems, it should not be difficult to design and implement an apparatus capable of these combined motions, preferably with the ability to reproduce amplitude-modulated oscillations in both directions. A comprehensive program of testing would then establish the extent to which the lift and drag coefficients measured with pure transverse motions (such as those presented in this thesis) are modified due to the additional in-line vibrations. Such information would doubtless be of great help to scientists and engineers alike.

7.3.3 Combined flow visualization and force measurements.

It has long been the “Holy Grail” of experimental hydrodynamicists to *successfully* combine flow visualization and force measurements with the same apparatus. (The emphasis was added in the previous sentence because many attempts have been made!) The difficulty is that good, clear, visualization is almost always possible only at low Reynolds numbers (where turbulence is small or nonexistent), while direct measurements with force transducers are possible only at higher Reynolds numbers (where the forces assume sufficient magnitude to be measurable).

The modern technique of Digital Particle Image Velocimetry (DPIV) may provide the long-awaited solution — DPIV has been used successfully to obtain “numerical snapshots” of the velocity field in relatively high-*Re* flows (Willert and Gharib [94]). A system similar to that described in the above reference is currently under installation in our Testing Tank

facility. We expect to have the capability of obtaining flow visualization together with our established force measurement techniques in the very near future.

Several of the experimental runs described in this thesis are candidates for repeat tests with the combined force / visualization system. It would be very enlightening to visualize the "phase-flipping" behavior of Chapter 3, as well as to shed light on the huge amplification of the oscillating drag force, also in that chapter. Visualization would provide excellent clues to the lift force cancellation behavior observed during tests of the riser section of Chapter 4. The beating wake response modes, inferred from the measured force traces in Chapter 5, could be confirmed from the DPIV velocity fields. And finally, simultaneous use of visualization and force measurements is exactly what is required to "tune" the operation of the tandem cylinder / hydrofoil combination studied in Chapter 6.

7.3.4 Tests with multiple cylinders

In Section 4.4.3, we studied the vortex-induced forces on a "canonical" riser section consisting of a central cylinder with two smaller satellite lines. That multiple cylinder arrangement was assumed to oscillate as a single entity, and the forces were measured on the entire group as a whole. A quite different problem, which is becoming increasingly common with the advent of deepwater oil production platforms such as TLPs, is to predict the behavior of each of a number of separate risers grouped in close proximity. The presence of the other cylinders is expected to alter the vortex-induced lift and drag forces acting on each cylinder in the group.

It is very likely that the next several years will see many attempts by researchers in the field to design forced- and free-oscillation experiments to investigate the forces acting on multiple cylinders. With our double-yoke apparatus as described in Chapter 6, we are already in the position of being able to conduct a first set of such experiments with two independent cylinders. We believe that this data will be useful in establishing a framework for future, more ambitious tests, and will likely be very interesting to engineers in the offshore field.

7.3.5 Comparative evaluation of vortex-suppression devices

In many practical engineering situations, it is necessary to reduce or suppress damaging vibrations caused by vortex shedding. In such cases, add-on devices such as splitter plates, fairings, helical strakes, axial shrouds, and the like are often employed in an attempt to interfere with the vortex shedding mechanism. A number of such devices have been reviewed by Blevins [7] and by Zdravkovich [102]. It is apparent from these reviews that reliable, quantitative comparisons of different vortex-suppression devices are very hard to obtain, since most of the systems have been developed in an ad-hoc manner by different researchers.

We believe that a comprehensive program of testing of different vortex-suppression devices under identical experimental conditions would be of great benefit. In Section 4.4.4, we discussed the evaluation of one such device (the haired-fairing), via forced-oscillation tests with our experimental system, combined with our simple energy-balance VIV prediction scheme. Given the ease with which different models can be installed in our apparatus, conducting such a comprehensive testing program would likely be inexpensive and worthwhile.

7.3.6 Further research on vortex interaction

In Chapter 6, we showed that an oscillating hydrofoil acting in the wake of a bluff cylinder could interact with the cylinder Kármán street so as to reposition the large-scale vortices and change their strengths, resulting in a reduction in the in-line wake velocity (and hence drag force). While our investigation proved the concept, we did not attempt to "tune" the various parameters to maximize the efficiency of the foil. In particular, we noticed in our experiments that the foil generated substantial vorticity of its own, indicating a substantial work input. It may well be possible to optimize the foil oscillation parameters so as to bring about the same interaction effects noticed in our tests, but with considerably less foil vortex generation.

In order to provide greater control over the cylinder and foil oscillations, it would probably be necessary to modify our double-yoke apparatus. We suggest that an updated version include two independent heave oscillation mechanisms. This would enable the cylinder and foil models to be moved at different amplitudes, with a variable phase angle between the cylinder and foil oscillations. Controlling this phase angle would control the phase of encounter of the foil with the upstream vortex street, and so would eliminate the need to

adjust the spacing between the models.

From the experimental results of Rosen [63], it is clear that parts of the fish body (in addition to the tail) participate in the repositioning of the Kármán vortices. Thus the most beneficial vortex interactions may take place with a continuous undulating surface, rather than a rigid oscillating foil. Such a device could be thought of as a "two-dimensional fish", or as an "undulating splitter plate", or as a "magic carpet mechanism". It would be fascinating to design such an apparatus and conduct flow visualization (and perhaps force measurement) experiments with it.

Bibliography

- [1] C. M. Alexander. The complex vibrations and implied drag of a long oceanographic wire in cross-flow. *Ocean Engineering*, 8(4):379-406, 1981.
- [2] K. M. Barnett and J. E. Cermak. *Turbulence Induced Changes in Vortex Shedding from a Circular Cylinder*. Technical Report 26 of Project THEMIS, Fluid Mechanics Program, Engineering Research Center, Colorado State University, Fort Collins, Colorado., January 1974.
- [3] D. Barrett. Personal Communication of equipment designed at the MIT Testing Tank Facility, June 1992.
- [4] P. W. Bearman. Vortex shedding from oscillating bluff bodies. In *Annual Review of Fluid Mechanics*, pages 195-222, Annual Reviews, Inc., 1984.
- [5] R. E. D. Bishop and A. Y. Hassan. The lift and drag forces on a circular cylinder in a flowing fluid. *Proceedings of the Royal Society of London*. Series A. 277:32-50. February 1964.
- [6] R. E. D. Bishop and A. Y. Hassan. The lift and drag forces on a circular cylinder oscillating in a flowing fluid. *Proceedings of the Royal Society of London*, Series A. 277:51-75, February 1964.
- [7] R. D. Blevins. *Flow-Induced Vibration*. Van Nostrand Reinhold Company, 135 West 50th Street, New York, NY 10020, 1990.
- [8] P. Capozucca. *Flow-Induced Vibration of a Non-Constant Tension Cable in a Sheared Flow*. Master's thesis, Massachusetts Institute of Technology, Cambridge, Massachusetts, 1988.

- [9] M. G. Chopra. Hydromechanics of lunate tail swimming propulsion. *Journal of Fluid Mechanics*, 64(2):375-391, 1974.
- [10] T-Y. Chung. *Vortex-Induced Vibration of Flexible Cylinders in Sheared Flows*. PhD thesis, Massachusetts Institute of Technology, Cambridge, Massachusetts, 1987.
- [11] M. Coutanceau and J-R. Defaye. Circular cylinder wake configurations: a flow visualization survey. In *Applied Mechanics Review*, pages 255-305, American Society of Mechanical Engineers, June 1991. ASME Book No. AMR095.
- [12] Y. Dong and J. Y. K. Lou. Vortex-induced nonlinear oscillation of tension leg platform tethers. *Ocean Engineering*, 18(5):451-464, 1991.
- [13] M. Van Dyke. *An Album of Fluid Motion*. The Parabolic Press. Stanford University. Stanford, California, 1982.
- [14] K. Engebretsen. *An Analysis of Full-Scale Experimental Data on the Dynamics of Very Long Tethers Supporting Underwater Vehicles*. Master's thesis, Massachusetts Institute of Technology, Cambridge, Massachusetts, 1988.
- [15] M. J. Every, R. King, and O. M. Griffin. Hydrodynamic loads on flexible marine structures due to vortex shedding. *Journal of Energy Resources Technology, Transactions of the ASME*, 104:330-336, December 1982.
- [16] C. C. Feng. *The Measurement of Vortex-Induced Effects in Flow Past Stationary and Oscillating Circular and D-Section Cylinders*. Master's thesis, University of British Columbia, 1968.
- [17] P. Freymuth. Propulsive vortical signature of plunging and pitching airfoils. *AIAA Journal*, 26(7):881-883, 1988.
- [18] P. Freymuth. Thrust generation by an airfoil in hover modes. *Experiments in Fluids*, 9:17-24, 1990.
- [19] R. Gopalkrishnan, M. A. Grosenbaugh, and M. S. Triantafyllou. Amplitude-modulated cylinders in constant flow: Fundamental experiments to predict response in shear flow. In *Proceedings of the Third International Symposium on Flow-Induced Vibrations and Noise*, Anaheim, California, November 1992. Paper to be presented.

- [20] R. Gopalkrishnan, M. A. Groesenbaugh, and M. S. Triantafyllou. Influence of amplitude modulation on the fluid forces acting on a vibrating cylinder in cross-flow. *International Journal of Offshore and Polar Engineering, Transactions of the ISOPE*, 2(1):32-37, March 1992.
- [21] R. Gopalkrishnan, M. A. Groesenbaugh, and M. S. Triantafyllou. Influence of amplitude modulation on the fluid forces acting on a vibrating cylinder in cross-flow. In *Proceedings of the First (1991) International Offshore and Polar Engineering Conference*, pages 132 - 139, Edinburgh, United Kingdom, August 11-16 1991.
- [22] M. Gorman and H. C. Swinney. Spatial and temporal characteristics of modulated waves in the circular Couette system. *Journal of Fluid Mechanics*, 117:123-142, 1982.
- [23] O. M. Griffin. Vortex shedding from bluff bodies in a shear flow: a review. *Journal of Fluids Engineering, Transactions of the ASME*, 107:298-306, September 1985.
- [24] O. M. Griffin. *Vortex-Induced Vibrations of Marine Cables and Structures*. Technical Report NRL Memorandum 5600. Marine Technology Division, Naval Research Laboratory, Washington, D. C., June 1985.
- [25] O. M. Griffin and G. H. Koopman. The vortex-excited lift and reaction forces on resonantly vibrating cylinders. *Journal of Sound and Vibration*, 54:435-448, 1977.
- [26] O. M. Griffin and S. E. Ramberg. Some recent studies of vortex shedding with application to marine tubulars and risers. *Journal of Energy Resources Technology, Transactions of the ASME*, 104:2-13, March 1982.
- [27] M. A. Groesenbaugh. The effect of unsteady motion on the drag forces and flow-induced vibrations of a long vertical tow cable. *International Journal of Offshore and Polar Engineering, Transactions of the ISOPE*, 1(1):18-26, 1991.
- [28] M. A. Groesenbaugh, D. R. Yoerger, M. S. Triantafyllou, and F. S. Hover. Drag forces and flow-induced vibrations of a long vertical tow cable - part II: unsteady towing conditions. *ASME Journal of Offshore Mechanics and Arctic Engineering*, 113(3):199-204, 1991.

- [29] H. T. Hansen, N. G. Skomedal, and T. Vada. Computation of vortex induced fluid loading and response interaction of marine risers. In *Eighth International Conference on Offshore Mechanics and Arctic Engineering*, pages 327-334, The Hague, The Netherlands., March 19-23 1989.
- [30] R. T. Hartlen and I. G. Currie. Lift-oscillator model of vortex-induced vibration. *Journal of the Engineering Mechanics Division, Proceedings of the ASCE*, 96(EM5):577-591, October 1970.
- [31] C. T. Howell. *Dynamics of Cables Subjected to Shear Current Excitation*. Master's thesis, Massachusetts Institute of Technology, Cambridge, Massachusetts, 1989.
- [32] W. D. Iwan and R. D. Blevins. A model for vortex-induced oscillation of structures. *Journal of Applied Mechanics*, 41:581-586, 1974.
- [33] S. P. Johnson and M. M. Zdravkovich. Optimal arrangement of a 6 + 1 satellite riser in a current. In *Proceedings of the First (1991) International Offshore and Polar Engineering Conference*, pages 164-169, Edinburgh, United Kingdom, August 11-16 1991.
- [34] G. W. Jones, J. J. Cincotta, and R. W. Walker. *Aerodynamic Forces on a Stationary and Oscillating Circular Cylinder at High Reynolds Numbers*. Technical Report NASA R-300; N69-17304, National Aeronautics and Space Administration, Washington, D.C., February 1969.
- [35] G. E. Karniadakis and G. S. Triantafyllou. Frequency selection and asymptotic states in laminar wakes. *Journal of Fluid Mechanics*, 199:441-469, 1989.
- [36] Y-H. Kim. *Vortex-Induced Response and Drag Coefficients of Long Cables in Ocean Currents*. PhD thesis, Massachusetts Institute of Technology, Cambridge, Massachusetts, 1984.
- [37] R. King. A review of vortex shedding research and its applications. *Ocean Engineering*, 4:141-171, 1977.
- [38] M. M. Koochesfahani. Vortical patterns in the wake of an oscillating airfoil. *AIAA Journal*, 27(9):1200-1205, September 1989.

- [39] M. J. Lighthill. Aquatic animal propulsion of high hydromechanical efficiency. *Journal of Fluid Mechanics*, 44:265-301, 1970.
- [40] M. J. Lighthill. Hydromechanics of aquatic animal propulsion. In *Annual Review of Fluid Mechanics*, pages 413-446, Annual Reviews, Inc., 1969.
- [41] M. J. Lighthill. *Mathematical Biofluidynamics*. Society for Industrial and Applied Mathematics (SIAM), Philadelphia, Pennsylvania, 1975.
- [42] H. J. Lugt. *Vortex Flow in Nature and Technology*. John Wiley and Sons, Inc., New York, New York. 1983.
- [43] W. A. Mair and P. K. Stansby. Vortex wakes of bluff cylinders in shear flow. *SIAM Journal of Applied Mathematics*, 28(2), March 1975.
- [44] P. Matisse and M. Gorman. Neutrally buoyant anisotropic particles for flow visualization. *The Physics of Fluids*, 27(4):759-760, April 1984.
- [45] D. J. Maull and R. A. Young. Vortex shedding from bluff bodies in a shear flow. *Journal of Fluid Mechanics*, 60(2):401-409, 1973.
- [46] F. G. McLaren, A. F. C. Sherratt, and A. S. Morton. Effect of free-stream turbulence on the drag coefficient of bluff sharp-edged cylinders. *Nature*, 223(5208):828-829, August 1969.
- [47] J. A. Mercier. *Large Amplitude Oscillations of a Circular Cylinder in a Low-Speed Stream*. PhD thesis, Stevens Institute of Technology, Hoboken, New Jersey, 1973.
- [48] G. Moe and T. Overvik. Current-induced motions of multiple risers. In *Third International Conference on the Behaviour of Offshore Structures*, pages 618-639. Massachusetts Institute of Technology, Cambridge, Massachusetts, August 2-5 1982.
- [49] G. Moe and Z. J. Wu. The lift force on a vibrating cylinder in a current. In *Eighth International Conference on Offshore Mechanics and Arctic Engineering*, pages 259 - 268, The Hague. The Netherlands., March 19-23 1989.
- [50] M. J. Moeller. *Measurement of Unsteady Forces on a Circular Cylinder in Cross Flow at Subcritical Reynolds Numbers*. PhD thesis, Massachusetts Institute of Technology, Cambridge, Massachusetts, 1982.

- [51] M. Nakano and D. Rockwell. The wake from a cylinder subjected to amplitude modulated excitation. Draft copy submitted for publication, June 1991.
- [52] R. P. Nordgren. Dynamic analysis of marine risers with vortex excitation. *Journal of Energy Resources Technology, Transactions of the ASME*, 104:14-19, March 1982.
- [53] A. Ongoren and D. Rockwell. Flow structure form an oscillating cylinder. part 1. mechanisms of phase shift and recovery in the near wake. *Journal of Fluid Mechanics*, 191:197-223, 1988.
- [54] Y. Oshima and A. Natsumi. Flow field around an oscillating airfoil. In W. Merzkirch, editor, *Flow Visualization II, Proceedings of the Second International Symposium on Flow Visualization*, pages 295-299, Hemisphere Publishing Company, Bochum, Germany, September 9-12 1980.
- [55] Y. Oshima and K. Oshima. Vortical flow behind an oscillating airfoil. *International Union of Theoretical and Applied Mechanics (IUTAM)*, 357-368, 1980.
- [56] T. Overvik and G. Moe. Added mass and in-line steady drag coefficient of multiple risers. *Journal of Energy Resources Technology, Transactions of the ASME*, 107:2-11, March 1985.
- [57] M. S. Pantazopoulos. Personal communication of laboratory experiments conducted for Exxon Production Research Company, July 1991.
- [58] N. M. Patrikalakis and C. Chrysostomidis. Vortex induced response of a flexible cylinder in a sheared current. *Journal of Energy Resources Technology, Transactions of the ASME*, 108:59-64, March 1986.
- [59] S. J. Price, M. P. Paidoussis, B. Mark, and W. N. Mureithi. Current-induced oscillations and instabilities of a multi-tube flexible riser: water tunnel experiments. In *Eighth International Conference on Offshore Mechanics and Arctic Engineering*, pages 447-454, The Hague, The Netherlands., March 19-23 1989.
- [60] A. Protos, V. W. Goldschmidt, and G. H. Toebe. Hydroelastic forces on bluff cylinders. *Journal of Basic Engineering, Transactions of the ASME*, 378-386, September 1968.

- [61] S. S. Rao. *Mechanical Vibrations*. Addison-Wesley Publishing Company, Reading, Massachusetts, 1990.
- [62] J. A. Roberson, C. Y. Lin, G. S. Rutherford, and M. D. Stine. Turbulence effects on drag of sharp-edged bodies. *Journal of the Hydraulics Division, Proceedings of the ASCE*, HY 7:1187-1203, July 1972.
- [63] M. W. Rosen. *Water Flow About a Swimming Fish*. Master's thesis, University of California, Los Angeles, California, May 1959.
- [64] T. Sarpkaya. Fluid forces on oscillating cylinders. *Journal of the Waterway, Port, Coastal and Ocean Division, Proceedings of the ASCE*, 104(WW4):275-290, August 1978.
- [65] T. Sarpkaya. *Transverse Oscillations of a Circular Cylinder in Uniform Flow*. Technical Report NPS-69SL77071-R, Naval Postgraduate School, Department of the Navy, Monterey, California., December 1977.
- [66] T. Sarpkaya. Vortex-induced oscillations : a selective review. *Journal of Applied Mechanics, Transactions of the ASME*. 46:241-258, June 1979.
- [67] Ö. Savaş. On flow visualization using reflective flakes. *Journal of Fluid Mechanics*. 152:235-248, 1985.
- [68] R. S. Schargel. *The Drag Coefficient for a Randomly Oscillating Cylinder in a Uniform Flow*. Master's thesis, Massachusetts Institute of Technology, Cambridge, Massachusetts, September 1980.
- [69] R. S. Schargel and J. K. Vandiver. *The Drag Coefficient for a Randomly Oscillating Cylinder in a Uniform Flow*. Technical Report, Department of Ocean Engineering, Massachusetts Institute of Technology, Cambridge, Massachusetts, December 1982.
- [70] W. M. Siebert. *Circuits, Signals and Systems*. The MIT Press, Massachusetts Institute of Technology, Cambridge, Massachusetts 02139, USA., 1986.
- [71] R. A. Skop and O. M. Griffin. A model for the vortex-excited resonant response of bluff cylinders. *Journal of Sound and Vibration*, 27(2):225-233, 1973.

- [72] P. K. Stansby. The effects of end plates on the base pressure coefficient of a circular cylinder. *Aeronautical Journal*, 36-37, January 1974.
- [73] P. K. Stansby. The locking-on of vortex shedding due to the cross-stream vibration of circular cylinders in uniform and shear flows. *Journal of Fluid Mechanics*, 74(4):641-665, 1976.
- [74] T. Staubli. Calculation of the vibration of an elastically mounted cylinder using experimental data from forced oscillation. *Journal of Fluids Engineering, Transactions of the ASME*, 105:225-229, June 1983.
- [75] T. Staubli. *Untersuchung der oszillierenden Kräfte am querangeströmten, schwingenden Kreiszylinder*. PhD thesis, Swiss Federal Institute of Technology, Zürich. 1983. Diss. ETH 7322.
- [76] P. J. Strykowski and K. R. Sreenivasan. On the formation and suppression of vortex shedding at low Reynolds numbers. *Journal of Fluid Mechanics*, 218:71-107. 1990.
- [77] A. Tjavaras. Personal Communication, August 1992.
- [78] G. S. Triantafyllou. Forces on a cylinder oscillating in steady cross-flow. In *Interaction of Flow-Fields with Cables, Flexible Risers, and Tethers*, MIT Sea Grant Marine Industry Collegium, Cambridge, Massachusetts., April 23-24 1991.
- [79] G. S. Triantafyllou and G. E. Karniadakis. Forces on a vibrating cylinder in steady cross-flow. In *Eighth International Conference on Offshore Mechanics and Arctic Engineering*, pages 247 - 252, March 19-23 1989.
- [80] G. S. Triantafyllou, M. S. Triantafyllou, and C. Chrysosostomidis. On the formation of vortex streets behind stationary cylinders. *Journal of Fluid Mechanics*, 170:461-477. 1986.
- [81] G. S. Triantafyllou, M. S. Triantafyllou, and C. Chrysosostomidis. Stability analysis to predict vortex street characteristics and forces on circular cylinders. *Journal of Offshore Mechanics and Arctic Engineering, Transactions of the ASME*, 109:148-154. May 1987.

- [82] M. S. Triantafyllou. Non-causal filtering in the time domain. Unpublished manuscript, Massachusetts Institute of Technology, October 1988.
- [83] M. S. Triantafyllou. Vortex-induced vibrations and drag amplification in shear flows - a tutorial paper. Unpublished manuscript, Massachusetts Institute of Technology, November 1991.
- [84] M. S. Triantafyllou, R. Gopalkrishnan, C. A. Goudey, and W. N. Upthegrove. *Experimental data from oscillating cylinders with forward speed*. Technical Report, MIT Testing Tank Facility, Cambridge, MA 02139, July 1991. Confidential Joint Industry Project report.
- [85] M. S. Triantafyllou, G. S. Triantafyllou, and R. Gopalkrishnan. Wake mechanics for thrust generation in oscillating foils. *Physics of Fluids A*, 3(12):2835-2837, December 1991.
- [86] C. W. Van Atta and M. Gharib. Ordered and chaotic vortex streets behind circular cylinders at low Reynolds numbers. *Journal of Fluid Mechanics*, 174:113-133, 1987.
- [87] J. K. Vandiver. Personal Communication, October 1991.
- [88] J. K. Vandiver. *Dimensionless Parameters Important to the Prediction of Vortex-Induced Vibration of Long Flexible Cylinders in Ocean Currents*. Technical Report MITSG 91-13, Massachusetts Institute of Technology Sea Grant Program, Cambridge, Massachusetts, 1991.
- [89] J. K. Vandiver. Drag coefficients of long flexible cylinders. In *Proceedings of the 1983 Offshore Technology Conference*, Houston, Texas, May 2-5 1983. OTC Paper No. 4490.
- [90] J. K. Vandiver. The prediction of lockin vibration on flexible cylinders in a sheared flow. In *Proceedings of the 1985 Offshore Technology Conference*, Houston, Texas, May 1985. OTC Paper No. 5006.
- [91] J. K. Vandiver and J. Y. Jong. The relationship between in-line and cross-flow induced-vibration of cylinders. *Journal of Fluids and Structures*, 1:381-399, 1987.

- [92] T. von Karman and J. M. Burgess. General aerodynamic theory: Perfect fluids. In W. F. Durand, editor, *Aerodynamic Theory, Volume 2*, Springer Verlag, Leipzig, Germany, 1935. 6 volumes.
- [93] A. K. Whitney and K. G. Nikkel. Effects of shear flow on vortex-shedding-induced vibration of marine risers. In *Proceedings of the 1983 Offshore Technology Conference*, Houston, Texas, May 2-5 1983. OTC Paper No. 4595.
- [94] C. E. Willert and M. Gharib. Digital particle image velocimetry. *Experiments in Fluids*, 10:181-193, 1991.
- [95] C. H. K. Williamson and A. Roshko. Vortex formation in the wake of an oscillating cylinder. *Journal of Fluids and Structures*, 2:355-381, 1988.
- [96] T. Y. Wu. Hydromechanics of swimming propulsion. part 1: swimming of a two-dimensional flexible plate at variable forward speeds in an inviscid fluid. *Journal of Fluid Mechanics*, 46:337-355, 1971.
- [97] T. Y. Wu. Hydromechanics of swimming propulsion. part 2: some optimum shape problems. *Journal of Fluid Mechanics*, 46:521-544, 1971.
- [98] T. Y. Wu. Hydromechanics of swimming propulsion. part 3: swimming and optimum movement of slender fish with side fins. *Journal of Fluid Mechanics*, 46:521-544, 1971.
- [99] D. R. Yoerger, M. A. Grosenbaugh, M. S. Triantafyllou, and J. J. Burgess. Drag forces and flow-induced vibrations of a long vertical tow cable - part I: steady-state towing conditions. *ASME Journal of Offshore Mechanics and Arctic Engineering*, 113(1):117-127, 1991.
- [100] M. M. Zdravkovich. A comparative overview of marine risers and heat exchanger tube banks. *Journal of Offshore Mechanics and Arctic Engineering*, 113:30-36, 1991.
- [101] M. M. Zdravkovich. On origins of hysteretic responses of a circular cylinder induced by vortex shedding. *Zeitschrift für Flugwissenschaft und Weltraumforschung*, 14:47-58, 1990.

- [102] M. M. Zdravkovich. Review and classification of various aerodynamic and hydrodynamic means for suppressing vortex shedding. *Journal of Wind Engineering and Industrial Aerodynamics*, 7:145-189, 1981.

DOCUMENT LIBRARY

March 11, 1991

Distribution List for Technical Report Exchange

Attn: Stella Sanchez-Wade
Documents Section
Scripps Institution of Oceanography,
Library, Mail Code C-075C
La Jolla, CA 92093

Hancock Library of Biology &
Oceanography
Alan Hancock Laboratory
University of Southern California
University Park
Los Angeles, CA 90089-0371

Gifts & Exchanges
Library
Bedford Institute of Oceanography
P.O. Box 1006
Dartmouth, NS, B2Y 4A2, CANADA

Office of the International
Ice Patrol
c/o Coast Guard R & D Center
Avery Point
Groton, CT 06340

NOAA/EDIS Miami Library Center
4301 Rickenbacker Causeway
Miami, FL 33149

Library
Skidaway Institute of Oceanography
P.O. Box 13687
Savannah, GA 31416

Institute of Geophysics
University of Hawaii
Library Room 252
2525 Correa Road
Honolulu, HI 96822

Marine Resources Information Center
Building E38-320
MIT
Cambridge, MA 02139

Library
Lamont-Doherty Geological
Observatory
Columbia University
Palisades, NY 10964

Library
Serials Department
Oregon State University
Corvallis, OR 97331

Pell Marine Science Library
University of Rhode Island
Narragansett Bay Campus
Narragansett, RI 02882

Working Collection
Texas A&M University
Dept. of Oceanography
College Station, TX 77843

Library
Virginia Institute of Marine Science
Gloucester Point, VA 23062

Fisheries-Oceanography Library
151 Oceanography Teaching Bldg.
University of Washington
Seattle, WA 98195

Library
R.S.M.A.S.
University of Miami
4600 Rickenbacker Causeway
Miami, FL 33149

Maury Oceanographic Library
Naval Oceanographic Office
Stennis Space Center
NSTL, MS 39522-5001

Marine Sciences Collection
Mayaguez Campus Library
University of Puerto Rico
Mayaguez, Puerto Rico 00708

Library
Institute of Oceanographic Sciences
Deacon Laboratory
Wormley, Godalming
Surrey GU8 5UB
UNITED KINGDOM

The Librarian
CSIRO Marine Laboratories
G.P.O. Box 1538
Hobart, Tasmania
AUSTRALIA 7001

Library
Proudman Oceanographic Laboratory
Bidston Observatory
Birkenhead
Merseyside L43 7 RA
UNITED KINGDOM

| | | | |
|--|------------------------------------|---|--|
| REPORT DOCUMENTATION PAGE | 1. REPORT NO. WHOI-92-38 | 2. | 3. Recipient's Accession No. |
| 4. Title and Subtitle Vortex-Induced Forces on Oscillating Bluff Cylinders | | | 5. Report Date February 1993 |
| 7. Author(s) Ramnarayan Gopalkrishnan | | | 6. |
| 9. Performing Organization Name and Address Woods Hole Oceanographic Institution Woods Hole, Massachusetts 02543 | | | 8. Performing Organization Rept. No. |
| 12. Sponsoring Organization Name and Address Funding was provided by the National Science Foundation, the Office of Naval Technology, the Sea Grant Program and the Office of Naval Research. | | | 10. Project/Task/Work Unit No. WHOI-92-38 |
| | | | 11. Contract(C) or Grant(G) No. (C) OCE-85-11431 (G) N00014-89-C-0179 NA90AA-D-SG424 |
| 15. Supplementary Notes This thesis should be cited as: Ramnarayan Gopalkrishnan, 1992. Vortex-Induced Forces on Oscillating Bluff Cylinders. Ph.D. Thesis. MIT/WHOI, WHOI-92-38. | | | 13. Type of Report & Period Covered Ph.D. Thesis |
| | | | 14. |
| 16. Abstract (Limit: 200 words) Vortex-induced forces and consequent vibration of long cylindrical structures are important for a large number of engineering applications. For a marine tubular exposed to sheared flow, the situation is particularly difficult since the vortex shedding force varies along its length, causing the response at any point to be amplitude-modulated. This thesis involves the experimental measurement of the vortex-induced forces on circular cylinders undergoing sinusoidal and amplitude-modulated oscillations. Basic concepts on vortex formation and vortex-induced vibrations, a literature review, and experimental details are introduced early in the thesis. A comprehensive program of sinusoidal oscillation tests is presented. Several novel properties are described, among them the role of the lift force phase angle in causing the amplitude-limited nature of VIV, and use of the lift force "excitation" in contrast to the quite different lift force "lock-in". Next, a data error analysis, and a simple VIV prediction scheme are described. New data on amplitude-modulated oscillations are presented, with an analysis of the behavior of the fluid forces in response to beating excitation. Finally, the control of the mean wake velocity profile via the control of the major vortical features is explored, with one application being the reduction of the in-line wake velocity. | | | |
| 17. Document Analysis a. Descriptors cable-strumming vortex-induced-vibration vortex-forces b. Identifiers/Open-Ended Terms c. COSATI Field/Group | | | |
| 18. Availability Statement Approved for publication; distribution unlimited. | | 19. Security Class (This Report) UNCLASSIFIED | 21. No. of Pages 251 |
| | | 20. Security Class (This Page) | 22. Price |